Cranfield University

Alejandro Castillo Pardo

Aeroelastic Simulation of Rotorcraft Propulsion Systems

School of Aerospace, Transport and Manufacturing

PhD Thesis

Cranfield University

School of Aerospace, Transport and Manufacturing

PhD Thesis

2017

Alejandro Castillo Pardo

Aeroelastic Simulation of Rotorcraft Propulsion Systems

Supervisor: Prof. V. Pachidis

This thesis is submitted in partial fulfillment of the requirements for the degree of Doctor of Philosophy

Acknowledgements

I would like to express my gratitude to many people who directly or indirectly contributed to this research.

First, I would like to thank my supervisor Professor V. Pachidis for giving me the opportunity to undertake this challenging project and for his constant guidance and support throughout the PhD. I would also like to thank Dr. I. Goulos for his helpful advices and recommendations regarding rotorcraft aeroelasticity.

I would like to express my gratitude to all my friends. I greatly appreciate the time that we have spent together. Among them, I specially would like to thank my handball family for the invaluable experiences we have shared, which kept me alive in the bad moments. I would also like to express my greatest gratitude to my colleagues at Cranfield University, who made this experience unique. In particular I would like to express my most sincere gratitude to Dr. J. Enconniere and Jesús Ortiz Carretero for the uncountable breaks we had and their invaluable support.

I would like to express my greatest gratitude to the medical staff from the León University Hospital. Without their help, I would have never recover my health, hope, and happiness.

Finally, I would like to dedicate this thesis to my parents, Eutiquio and María Catalina, and my sister, Laura, because without their love, encouragement, and support this would not have been possible.

Abstract

A close relationship between the aerospace technology level and the capability to model and simulate the physics involved during the flight has been identified throughout the aviation history. The continuous improvement in physical and mathematical models has provided a further understanding of the behaviour of the different components along with the complete vehicle. As a result, the performance modelling has experienced a large improvement.

The aviation industry, which is characterised by the use of cutting edge technology, requires large investments when new concepts are introduced. The application of high fidelity simulation tools reduces considerably the investment carried out prototyping and testing. This fact is also applicable to the rotorcraft industry, where a continuous increase in the employment of helicopters has been observed throughout the last decades, expecting a sharp growth within the next 20 years. The forecasted growth in the number of helicopter operations along with the increasing concern about the environmental impact of aviation, lead the governmental bodies to set up a number of goals to reduce the carbon dioxide, nitrogen oxides, and noise emissions. Three paths were identified to reduce the environmental impact and meet the proposed goals. The first one is the reduction in the number of operations. However, a sharp growth in the number of helicopter operations is expected. The second one is the optimisation of the flight procedures. Nevertheless, the potential improvement is limited. The third one is the introduction of a quieter and more efficient type of rotorcraft.

There exist two new rotorcraft configurations which show enough potential to be studied. These are the tilt-rotor and compound helicopter. Both designs improve the cruise performance using auxiliary lift and propulsive systems, while they still exploit

the vertical flight capability of helicopters. Nevertheless, the lack of reliable high fidelity models has made their development long and highly expensive.

Within this context, the necessity of a simulation framework able to simulate and predict the detailed performance of novel rotorcraft configurations is highlighted. The present work aims to lay the foundations of this comprehensive rotorcraft code by developing a computational framework for the aeroelastic simulation of propulsion systems. The tool is characterised by a high fidelity level able to predict the highly unsteady loads at a low computational cost. The first characteristic makes this tool suitable for the design stage and noise calculations; whilst the second one enables its integration into multidisciplinary optimisation procedures. The development of this framework has required a considerable contribution to the knowledge in different areas of study, these included: structural dynamics, inflow aerodynamics, blade aerodynamics, aeroelasticity, and computational acceleration techniques. The individual models have been integrated into a cost efficient aeroelastic simulation framework, which has been extensively validated with experimental data. Very good and in some cases excellent correlation with the experimental measurements has been observed.

The main contribution of this work has been the successful development of a computational framework for the aeroelastic simulation of rotorcraft propulsion systems. It accurately simulates and predicts the aerodynamic flowfield and the unsteady loads generated by the rotor and transferred to the fuselage. It is easily expandable to account for interactions with other rotors, auxiliary lift surfaces, and fuselage bodies. The simulation tool estimates high fidelity low and high frequency aerodynamic loading, which enables the calculation of impulsive noise emissions. The framework computes accurate predictions of rotor power required, which enables its use as a validation tool for lower order models. The developed framework approximates the third level of Padfield's hierarchical paradigm, providing detailed aeroelastic information necessary for design purposes. The additions of parallel computing and an acceleration scheme results in a highly computationally efficient tool suitable for optimisation methodologies. Moreover, a considerable contribution has been made in terms of modelling of: coupled modal characteristics, aeroelastic simulation; computational enhancements of inflow models and investigation of the effect of the fuselage aerodynamic interference and coupled flexible blade modelling.

Contents

List of Figures

List of Tables

Nomenclature

Roman Symbols

Symbol	Description
$[A_i]$	Global non-rotating reference frame O to rotating reference frame A_i rotation matrix, $i = 1,...N_b$
$[M]$, $[C]$, $[S]$	Mass, damping, and overall stiffness intermodal coupling matrices
$[F]$, $[G]$	Centrifugal and structural stiffness intermodal coupling matrices
$[Q(\lambda)]$	Dynamic system resultant λ-matrix
$\left[T_i^b\right]$	Global non-rotating O to blade element fixed reference frame b rotation matrix, $i = 1,...N_b$
$\{f\}$	Generalised external static loading vector
$\{\bar{q}\}_i$	ith eigenvector of λ-matrix $[Q(\lambda)]$
$\tilde{e}_x^O$, $\tilde{e}_y^O$, $\tilde{e}_z^O$	Global non-rotating reference frame O unit vectors
$\tilde{e}_x^{A_i}$, $\tilde{e}_y^{A_i}$, $\tilde{e}_z^{A_i}$	Rotating reference frame A_i unit vectors
$\tilde{e}_x^b$, $\tilde{e}_y^b$, $\tilde{e}_z^b$	Blade element fixed reference frame b unit vectors
$\mathrm{d}\tilde{f}_{cg}^O$, $\mathrm{d}\tilde{m}_{cg}^O$	Differential beam element force and moment vectors expressed in O, N, N m
$\tilde{f}_{aero}^b$, $\tilde{m}_{aero}^b$	Blade element aerodynamic force and moment per unit length vectors expressed in b, N/m, N
$\tilde{F}_i^O$, $\tilde{T}_i^O(t)$	Total force and moment vectors exerted by the ith blade, $i = 1,...N_b$, on the hub expressed in O, N, N m
$\tilde{F}_{rotor}^O$, $\tilde{T}_{rotor}^O(t)$	Total force and moment vectors exerted by the main rotor on the hub expressed in O, N, N m

$\tilde{r}$, $\tilde{V}$, $\tilde{V}_{ind}$	Position, velocity, and induced velocity vectors of a Lagrangian marker, m, $\mathrm{m\,s^{-1}}$
$\tilde{r}_{A_i/O}$	Position vector of the ith blade root/hinge A_i expressed in O, m
$\tilde{r}^{O}_{cg/O}$	Position vector of beam element $cg\,(r,t)$ relative to the origin of O expressed in O, m
$\tilde{r}^{b}_{cg/p}$, $\tilde{r}^{A_i}_{cg/p}$	Position vector of beam element $cg\,(r,t)$ relative to $p\,(r,t)$ expressed in b and A_i, m
$\tilde{r}^{A_i}_{cg/A_i}$, $\tilde{r}^{O}_{cg/A_i}$	Position vector of beam element $cg\,(r,t)$ relative to A_i expressed in A_i and O, m
$\tilde{r}^{A_i}_{p/A_i}$	Position vector of arbitrary deformed point p relative to A_i expressed in A_i, m - Section 3.2
$\tilde{r}^{A_i}_{p/A_i}$	Position vector of beam element $p\,(r,t)$ relative to A_i expressed in A_i, m - Section 3.3
$\tilde{T}_{i,offset}\,(t)$	Moment vector of the ith blade due to root/hing offset, $i = 1,...N_b$
$\tilde{T}_{i,root}\,(t)$	Moment vector of the ith blade due to root/hinge effective stiffness, $i = 1,...N_b$
$\tilde{u}_{A_i}$, $\tilde{a}_{A_i}$	Linear velocity and acceleration vectors of the origin of A_i expressed in O, $\mathrm{m\,s^{-1}}$, $\mathrm{m\,s^{-2}}$
$\tilde{u}^{b}_{cg/\phi}$, $\tilde{a}^{b}_{cg/\phi}$	Linear velocity and acceleration vectors of the beam element $cg\,(r,t)$ relative to $p\,(r,t)$ due to torsion expressed in b, $\mathrm{m\,s^{-1}}$, $\mathrm{m\,s^{-2}}$
$\tilde{u}^{A_i}_{cg/\phi}$, $\tilde{a}^{A_i}_{cg/\phi}$	Linear velocity and acceleration vectors of the beam element $cg\,(r,t)$ relative to $p\,(r,t)$ due to torsion expressed in A_i, $\mathrm{m\,s^{-1}}$, $\mathrm{m\,s^{-2}}$
$\tilde{u}^{A_i}_{cg/A_i}$, $\tilde{a}^{A_i}_{cg/A_i}$	Linear velocity and acceleration vectors of the beam element $cg\,(r,t)$ relative to A_i expressed in A_i, $\mathrm{m\,s^{-1}}$, $\mathrm{m\,s^{-2}}$
$\tilde{u}^{O}_{cg/A_i}$, $\tilde{a}^{O}_{cg/A_i}$	Linear velocity and acceleration vectors of the beam element $cg\,(r,t)$ relative to A_i expressed in O, $\mathrm{m\,s^{-1}}$, $\mathrm{m\,s^{-2}}$
$\tilde{u}^{O}_{cg}$, $\tilde{a}^{O}_{cg}$	Absolute linear velocity and acceleration vectors of the beam element $cg\,(r,t)$ expressed in O, $\mathrm{m\,s^{-1}}$, $\mathrm{m\,s^{-2}}$
$\tilde{u}_O$	Linear velocity vector of the origin of O expressed in O, $= [u_O\, v_O\, w_O]$, $\mathrm{m\,s^{-1}}$

$\tilde{\dot{u}}_O$	Linear acceleration vector of the origin of O expressed in O, $= [\dot{u}_O\, \dot{v}_O\, \dot{w}_O]$, $\mathrm{m\,s^{-2}}$
$A(r)$	Cross-sectional area, m^2
A_i	Rotating reference frame of the ith blade, $i = 1,...N_b$
A_i, b_i	Indicial functions coefficients $i = 1,...5$ - Section 3.5
$B_1^\star$, $B_2^\star(r)$	Blade cross-sectional integrals, m^6, m^5
c	Blade element chord, m
$C_{i,j}^{r,s}$	Gyroscopic intermodal coupling coefficient between the ith and jth assumed modes of the r and s DOFs
C_d, C_{d0}	Aerodynamic total drag and zero-lift drag coefficients
C_l, C_m	Aerodynamic lift coefficient and moment coefficients about 1/4 chord
C_n, C_a	Aerodynamic normal and axial force coefficients
$C_{m,\alpha}$, $C_{m,q}(s)$	Effective aerodynamic moment coefficient about 1/4 chord at time s due to time-histories of α and q
$C_{n,\alpha}$, $C_{n,q}(s)$	Effective aerodynamic normal force coefficients at time s due to time-histories of α and q
ΔC_m^α ΔC_m^q	Step change in aerodynamic moment coefficient about 1/4 chord due to step changes in α and q
ΔC_n^α ΔC_n^q	Step change in aerodynamic normal force coefficient due to step changes in α and q
C_L	Rotor rolling moment coefficient positive starboard down $= -\bar{T}^O_{rotor,x}/(\rho\pi\Omega^2R^5)$
C_M	Rotor pitching moment coefficient positive nose up $= \bar{T}^O_{rotor,y}/(\rho\pi\Omega^2R^5)$
C_P	Rotor power coefficient $= -\bar{T}^O_{rotor,z}/(\rho\pi\Omega^2R^5)$
C_T	Rotor thrust coefficient $= \bar{F}^O_{rotor,z}/(\rho\pi\Omega^2R^4)$
$cg(r,t)$	Cross-sectional centre of gravity located on the chord line at a radius r at time t
e	Blade root/hinge offset from the hub center as a fraction of rotor radius

E, $G(r)$	Material Young and shear stress moduli, Pa
e_A, $e_M(r)$	Area centroid and mass centroid offsets from the blade elastic axis, positive towards the leading edge, m
f_i^r	Centrifugal static force coefficient for the ith assumed mode of the r DOF
$F_{i,j}^{r,s}$	Centrifugal stiffening intermodal coupling coefficient between the ith and jth assumed modes of the r and s DOFs
$G_{i,j}^{r,s}$	Elastic intermodal coupling coefficient between the ith and jth assumed modes of the r and s DOFs
h	Perpendicular distance between the vortex filament and the arbitrary evaluation point, m
$I_p(r)$	Blade cross-sectional mass polar moment of inertia, kg m
I_y, $I_z(r)$	Blade cross-sectional moments of inertia about the major and minor axis, m^4
I_1, $I_2(r)$	Blade cross-sectional mass moments of inertia about the major and minor axis, kg m
$J(r)$	Blade cross-sectional torsional rigidity constant, m^4
K^r	Hinge or pitch-control system spring stiffness of the r DOF, $\mathrm{N\,m\,rad}^{-1}$
L	Actual blade length $= R\,(1 - e)$, m
$m(r)$	Blade mass per unit length, $\mathrm{kg\,m}^{-1}$
M	Mach number
$M_{i,j}^{r,s}$	Mass intermodal coupling coefficient between the ith and jth assumed modes of the r and s DOFs
N	Number of assumed mode shapes per DOF
N_b	Number of rotor blades
N_s, $N_{s,root}$	Number of span beam element in the aerodynamic efficient and root regions
$N_{\zeta_{nw}}$, $N_{\zeta_{fw}}$	Number of straight vortex segments per vortex filament in the near wake and far wake
N_ψ	Number of azimuth stations

O	Global non-rotating reference frame
$p\,(r,t)$	Arbitrary point located on the elastic axis at a radius r at time t
q	Non-dimensional pitch rate $= \dot{\alpha}c/V$, rad
Δq	Step change in non-dimensional pitch rate, rad
$q_i^r(t)$	Time-dependent generalised coordinate of the ith assumed deformation function of the r DOF
Q_i^r	Generalised force corresponding to the ith generalised coordinate of the r DOF
r	Radial coordinate, m
R	Rotor blade radius, m
r_c	Vortex core radius, m
R_{co}	Blade cut-out radius, m
RMS_{geo},	Root mean square change in blade geometry, m
RMS_{nw}	Root mean square change in wake geometry of the near wake, m
RMS_{fw}	Root mean square change in wake geometry of the far wake, m
RMS_{Γ^b},	Root mean square change in bound circulation, m
s	Reduced time $= 2/c\int_0^t V\mathrm{d}t$
$S_{i,j}^{r,s}$	Overall stiffness intermodal coupling coefficient between the ith and jth assumed modes of the r and s DOFs
t	Time, s
Δt	Time step, s
T, U	Kinetic and potential energies of the rotor blade, J
$T_{n/m,\alpha/q}$	Indicial functions time constants
$u(r,t)$	Axial ($\tilde{e}_x^{A_i}$) beam element displacement, m
$v(r,t)$	Chordwise ($\tilde{e}_y^{A_i}$) beam element displacement, m
$w(r,t)$	Flapwise ($\tilde{e}_z^{A_i}$) beam element displacement, m
x	Effective modal coordinate $= r - eR$, m
$X_{n/m,\alpha/q}^{c/nc}$, $Y_{n/m,\alpha/q}^{c/nc}(s)$	Deficiency functions, rad
$X_i^r(x)$	Shape for the ith mode of motion of the r DOF, m, rad

$x_T(r)$	Beam element radial centrifugal displacement, $= \int_0^{r-eR} \frac{\int_\lambda^L m\Omega^2(\varrho+eR)\mathrm{d}\varrho}{EA}\mathrm{d}\lambda$, m

Greek Symbols

Symbol	Description
$[\beta_{pre}]$, $[\zeta_{pre}]$	Rotor blade precone and presweep rotation matrices
$[\theta_0]$, $[\theta_c]$, $[\psi_i]$	Rotor blade collective pitch, cyclic pitch, and azimuth angle rotation matrices
$[\theta_{tw}]$, $[\lambda]$, $[\beta]$, $[\zeta]$, $[\phi]$	Beam element pretwist, sweep, flap, lag, and torsion rotation matrices
$\{\psi^r(x)\}$	Assumed mode shape vector of the r DOF $= \left[\psi_j^r(x),\, j = 1, \ldots N\right]^T$, m, rad
$\tilde{\omega}_{A_i}$, $\tilde{\dot{\omega}}_{A_i}$	Angular velocity and acceleration vectors of the ith blade root/hinge A_i, $\mathrm{rad\,s^{-1}}$, $\mathrm{rad\,s^{-2}}$
$\tilde{\omega}_O$	Angular velocity vector of the global non-rotating O reference frame $= [p_O\, q_O\, r_O]^T$, $\mathrm{rad\,s^{-1}}$
$\tilde{\dot{\omega}}_O$	Angular acceleration vector of the global non-rotating O reference frame $= [\dot{p}_O\, \dot{q}_O\, \dot{r}_O]^T$, $\mathrm{rad\,s^{-2}}$
$\tilde{\omega}_{p/A_i}^{A_i}$, $\tilde{\dot{\omega}}_{p/A_i}^{A_i}$	Angular velocity and acceleration vectors of the arbitrary point $p\,(r,t)$ located on the ith elastic axis relative to A_i expressed in A_i, $\mathrm{rad\,s^{-1}}$, $\mathrm{rad\,s^{-2}}$
$\tilde{\omega}_\phi^b$, $\tilde{\dot{\omega}}_\phi^b$	Angular velocity and acceleration vectors of the beam element $cg\,(r,t)$ relative to $p\,(r,t)$ due to torsion expressed in b, $\mathrm{rad\,s^{-1}}$, $\mathrm{rad\,s^{-2}}$
α, $\dot{\alpha}$	Angle of attack and pitch rate, rad
β	Prandtl-Glauert factor $= \sqrt{1-M^2}$ - Section 3.5
β, $\zeta\,(r,t)$	Beam element equivalent flap and lag angles rad
β_{pre}, ζ_{pre}	Precone and presweep angles, rad

Γ, Γ^b, Γ^t, Γ^v	Filament, bound, trailing, and tip vortex circulation strengths, $\mathrm{m}^2\,\mathrm{s}^{-1}$
δ	Eddy viscosity parameter
$\Delta\alpha$	Step change in angle of attack, rad
$\Delta\zeta$, $\Delta\psi$	Wake (vortex) age and azimuth discretisation resolutions, rad
ϵ_{xx}, $\epsilon_{x\eta}$, $\epsilon_{x\zeta}$	Classical strain components
ζ, ψ	Wake (vortex) age and azimuth angle, rad -Section 3.4
ζ_{nw}, ζ_{max}	Near wake truncation and maximum wake ages, rad
η, ζ	Cross-section coordinates along the major and minor principal axes, m
η_a	Leading edge suction recovery factor
$\theta(x)$	Beam element pretwist angle, rad - Section 3.2
θ_0, θ_{1c}, θ_{1s}	Collective, longitudinal cyclic, and lateral cyclic pitch angles, rad
$\theta_c\,(eR,t)$	Cyclic pitch angle at the rotor hub, rad
θ_{tw}, $\lambda\,(r)$	Beam element pretwist and sweep angles, rad - Section 3.3
λ	Eigenvalue of the λ-Matrix $[Q(\lambda)]$, $\mathrm{rad\,s}^{-1}$ - Section 3.2
ν	Kinetic viscosity, $\mathrm{m}^2\,\mathrm{s}^{-1}$
ρ	Material density, $\mathrm{kg\,m}^{-3}$
σ_{xx}, $\sigma_{x\eta}$, $\sigma_{x\zeta}$	Classical stress components, Pa
$\phi(r,t)$	Time-dependent torsional deformation angle, rad
$\phi^{c/nc}_{n,\alpha/q}$	Circulatory and non-circulatory indicial functions due to step changes in angle of attack α and pitch rate q for C_n
$\phi^{c/nc}_{m,\alpha/q}$	Circulatory and non-circulatory indicial functions due to step changes in angle of attack α and pitch rate q for C_m
$\psi^r_i(x)$	Assumed deformation function of the ith mode shape of the r DOF, m, rad
$\psi_i\,(t)$	Azimuth angle of the ith blade root/hinge at time t, $i = 1, ...N_b$, rad
Ω, $\dot{\Omega}$	Angular velocity and acceleration of the blade, $\mathrm{rad\,s}^{-1}$, $\mathrm{rad\,s}^{-2}$

Superscripts

Symbol	Description
$\dot{(\,)}$, $\ddot{(\,)}$	First and second derivatives with respect to time t
$(\,)'$, $(\,)''$	First and second derivatives with respect to radius r or modal coordinate x
$(\,)^{\phi,v,w}$	referring to torsion, lag and flap respectively
$(\,)^{r,s}$	DOF indices
$\tilde{(\,)}^{A_i}$	Vector expressed in the ith rotating reference frame A_i
$\tilde{(\,)}^{b}$	Vector expressed in the blade element fixed reference frame b
$\tilde{(\,)}^{O}$	Vector expressed in the global non-rotating reference frame O
$\hat{\tilde{(\,)}}^{n}$	Vector quantity in nth predictor step
$\tilde{(\,)}^{n}$	Vector quantity in nth corrector step

Subscripts

Symbol	Description
$(\,)_{i,j}$	Mode number indices - Section 3.2
$(\,)_0$	Referring to the root/hinge location
$\tilde{(\,)}_{/O}$	Vector relative to the origin of the global non-rotating reference frame O
$\tilde{(\,)}_{/A_i}$	Vector relative to the ith blade root/hinge A_i
$\tilde{(\,)}_{/p}$	Vector relative to the arbitrary point p on the elastic axis
$\tilde{(\,)}_{A_i/}$	Vector referring to the ith blade root/hinge
$\tilde{(\,)}_{cg/}$	Vector referring to the beam element centre of gravity $cg(r,t)$ point
$\tilde{(\,)}_{p/}$	Vector referring to the arbitrary point $p(r,t)$ on the elastic axis
$(\,)_i$	Blade number index - Section 3.3
$(\,)_i$	Azimuth index - Section 3.4
$(\,)_j$	Wake age index - Section 3.4
$(\,)_k$	Radial index

$\tilde{(\,)}_{/\phi}$	Vector quantity due to torsion
$(\,)^c$, $(\,)^{nc}$	Circulatory and non-circulatory aerodynamic quantities

Acronyms

Symbol	**Description**
BL	Baseline
DOF	Degree of freedom
FEA	Finite element analysis
GEP	Generalised eingenvalue problem
HHC	High Harmonic Control
MN	Minimum Noise
MV	Minimum Vibration
QEP	Quadratic eingenvalue problem
SEP	Standard eingenvalue problem

Chapter 1

Introduction

Since the creation of the first airline in 1919, a continuous growth in the air transportation has been observed. The increase in the number of operations has been driven by the necessity of the society to be connected with a fast and secure mean of transportation. As reported in Ref. 1, the air traffic doubled in the last 15 years and by 2036 the number of operations is expected to double again. The aforementioned growth has been enabled by the lack of restrictions on the use of petroleum-derived fuels. The continuous growth in the amount of fossil fuels used has led to an equally important pollutant share. The aviation industry was responsible for the 2% of the total carbon dioxide CO_2 emissions in 2015. Although the relative contribution of the aviation industry is small, an absolute value of 781 million tones of CO_2 was emitted (Ref. 2). In addition to the CO_2, nitrogen oxides NO_x, carbon monoxide CO, unburnt hydrocarbons UHC, and smoke are also emitted and contribute to the climate change (Ref. 3). These pollutants, specially NO_x, have been found to have a harmful effect on the human health (Ref. 4). Moreover, the emission of NO_x at high altitude exacerbates the depletion of the ozone layer and its associated consequences (Ref. 5). Furthermore, aviation noise has been identified as the most adverse consequence of the aircraft operation around airport areas. The increasing concern about the noise and chemical emissions and the depletion of fossil fuels compromise the future aviation growth.

A similar situation is presented for the rotorcraft industry. A continuous growth has been observed in the deployment of helicopters throughout the last decades. Due to their

unique capability to hover and fly at low speed, helicopters have undertaken missions not possible for fixed wing aircraft. These include: Emergency Medical Services (EMS), civil protection, Search and Rescue (SAR), police enforcement and daily transportation of people and/or goods (Ref. 6). These activities are associated with 1.5 million flight hours per year within the European region (Ref. 7). Although this figure is small compared to the 10 million flight hours of the fix wing commercial airlines, the equivalent consumption of 0.4 million tons of fuel per year will quadruplicate in 20 years if the technology level is kept constant (Ref. 8). Moreover, a large portion of these activities take place in or around densely populated areas. Consequently, the adverse effects of noise and chemical emissions on humans are intensified.

The current pollutant emission situation and the forecasted growth of aircraft operations have resulted in an increasing concern about the environmental impact of civil aviation. To restrain and reduce the environmental impact, the Advisory Council for Aeronautics Research in Europe (ACARE) has set a number of goals to be achieved by civil aviation by the year 2020 (Ref. 9). The most relevant goals are:

- 50% reduction in CO_2 emissions by reducing the fuel consumption.
- 80% reduction in NO_x.
- 50% reduction of perceived external noise emissions.
- A greener product life cycle including design, manufacturing, maintenance, and disposal/recycling.

These targets were included as part of the Vision 2020 project, which measured the success relative to the technology level of 2000. A more updated and ambitious set of goals to be met by 2050 has been set by the European Commission as part of the Flighpath 2050 initiative (Ref. 10). The goals are once again defined relative to the technology level of year 2000. These include:

- 75% reduction in CO_2 emissions per passenger and kilometre.
- 90% reduction in NO_x emissions per passenger and kilometre.

- 65% reduction in perceived external noise emissions.
- Emission-free taxiing.
- Recyclable oriented design and manufacturing.

Clarke (Ref. 11) identified 3 different alternatives to reduce the aviation environmental impact and meet the proposed goals. The first one is the reduction in the number of operations. However, the expected rotorcraft traffic growth is not compatible with the reduction in the number of operations. The second one is the improvement of the operational procedures. The optimisation of the operational procedures has been proved in Refs. 6–8, 12–17 to be the short term solution to meet the ACARE goals. However, the potential of procedures optimisation is limited and a long term solution is required, specially to meet the Flightpath 2050 goals. The third one is the introduction of a new type of rotorcraft. The introduction of a new generation of rotorcraft is associated with the deployment of a quieter and more power efficient rotorcraft, with a cleaner powerplant. The new rotorcraft would lead to a significantly smaller environmental footprint. The timescales associated with the design and certification of a new rotorcraft technology can take up to 50 years (Ref. 18). Consequently, the introduction of a new rotorcraft type is not a viable option for the fulfilment of the ACARE Vision 2020 goals. However, theses new technologies are the potential long term solutions to meet the Flightpath 2050 targets.

The challenging future of the aviation industry led to the initiation of the Clean Sky JTI (Joint Technology Initiative) in 2008 (Ref. 9). Clean Sky was a partnership between the European Commission and the aeronautical industry. The main aim of this project was the development of novel technologies to reduce the aviation environmental impact. These potentially would result in the fulfilment of the Vision 2020 goals. Innovative technologies were developed and integrated into the Clean Sky Integrated Technology Demonstrators (ITDs). Their influence on the environmental footprint was assessed by the Clean Sky Technology Evaluator. Technology solutions were given for different types of aircraft ranging from large wide body fixed wing aircraft to rotorcraft. Regarding rotorcraft research activities, Clean Sky set more realistic objectives to be fulfilled by the end of the project. These include:

- 30% reduction in specific fuel consumption, 40% reduction in CO_2 emissions, and 53% reduction in NO_x emissions for a diesel engine powered helicopter.
- 10% reduction in specific fuel consumption, 26% reduction in CO_2 emissions, and 65% reduction in NO_x emissions for a turboshaft powered helicopter.
- 10% reduction in perceived external noise emissions.
- A greener product life cycle including design, manufacturing, maintenance, and disposal/recycling.

These goals were met by the end of the programme in 2016 for conventional helicopter configurations. However, the potential of the developed technologies and procedures developed is limited and will not be able to meet the Flightpath 2050 requirements.

A new generation of rotorcraft is required to meet the 2050 goals set by the European Commission. To investigate novel configuration a new European research programme, named Clean Sky 2, is being initiated. Clean Sky 2 aims to develop and build technology demonstrators of radical innovate aircraft technologies. It will include large passenger aircraft, regional aircraft, fast rotorcraft, airframes, engines, and other systems. Within the Clean Sky 2 structure there is an Innovative Aircraft Demonstrator Platform (IADP) exclusively dedicated to the development of Fast Rotorcraft technologies. Two rotorcraft configurations are planned to be investigated, developed, built, and tested. These are the tilt-rotor and the compound helicopter. The potential of the tilt-rotor configuration is the tilting capability of its rotors. These are able to compensate the weight of the vehicle during vertical operation. Additionally, the rotors tilt during horizontal flight operation providing the thrust necessary to overcome the drag while the wings provide the necessary lift. Therefore, this configuration is able to fly faster and more efficiently than a helicopter while keeping the capability of vertical flight. The compound helicopter is characterised by the use of the main rotor to generate enough thrust to compensate the weight during vertical flight and the use of an auxiliary propulsive system to provide necessary thrust to overcome the drag during horizontal flight. Similarly to the tilt rotor configuration, wings are added to produce lift during horizontal flight. However, the main rotor is still producing part of the thrust necessary to balance the weight of the rotorcraft.

Full scale demonstrator of both configurations, named Next-Generation Civil Tilt-Rotor demonstrator (NextGenCTR) and LiferCraft Compound Rotorcraft, are planned to be built and tested by the end of the research programme.

The successful development of alternative or conceptual rotorcraft configurations, such as the ones described above, constitutes the potential long term solution to the challenging environmental impact problem. A high level of complexity is identified in both configurations. Aerodynamic interactions between rotors, auxiliary lifting surfaces, and the fuselage are likely to be present. These interactions along with the unsteady nature of the rotor operation lead to the transfer of high intensity loads and vibrations to the fuselage. The inherent complexity of these new configurations has made their development long and highly expensive.

1.1 Scope of Work

Within this context, the relevance of simulation tools able to predict the behaviour of new rotorcraft concepts is evident. However, a conflict between the level of fidelity and the computational cost has been found. Regarding the level of fidelity of helicopter simulation models, a three-level hierarchy was identified by Padfield (Ref. 19). The first level corresponds to the representation of the main rotor as a disk and the deployment of linear blade aerodynamics coupled with a first order dynamic inflow formulation. The second level is associated with the individual representation of each blade and more refined aerodynamic models. The third Padfield level corresponds to the aeroelastic modelling of the main rotor. This comprises the coupled modelling of structural properties, unsteady and nonlinear blade aerodynamics and a three-dimensional calculation of the rotor wake.

First and second hierarchy models have been extensively used for the analysis of missions and parametric studies because of its low computational cost, however, the fidelity of the results must be assessed. Third level models have been used for design purposes, where a detailed study of rotor loads and vibrations is desired. Although of different nature, the same level categorisation can be applied to the new rotorcraft concepts. Nevertheless, the increasing complexity of the aerodynamic and structural scenario presented during the operation of these configurations results in the unsuccessful prediction of the performance

of these concepts using the first and second levels. Therefore, the generation of a third hierarchy level simulation tool able to model new rotor technologies represents the next step in the development and implementation of the new configurations.

The aforementioned computational tool must fulfil some requirements:

- The level of fidelity of the model has to approximate the third level of hierarchy in order to correctly predict the complex aerodynamic flowfield and the highly unsteady loads. This capability enables the use of this tool within the design stage.
- The level of fidelity of the aerodynamic loading has to be high enough to provide low and high frequency aerodynamic characteristics required for noise calculations.
- It has to be applicable to multidisciplinary optimisation methodologies.
- The computational cost of the tool must be kept low while the fidelity of the model is increased. The successful development of a high fidelity and efficient framework enables the previous requirements to be fulfilled.

1.2 Objectives

This project aims to lay the foundations of a comprehensive rotorcraft code for the analysis of conceptual configurations. This is done by the development of the most critical component of the analysis, the propulsion system. The aims previously outlined for the rotorcraft code are converted to more specific objectives for the propulsion system aeroelastic simulation tool.

- Development of a computational framework for the aeroelastic simulation of rotorcraft propulsion systems with the following characteristics:
  - The simulation tool must be able to accurately simulate and predict the aerodynamic flowfield and the unsteady loads generated by the rotor and transmitted to the fuselage.
  - The developed framework must be easily expandable to account for potential interactions with other rotors, auxiliary lift surfaces, and fuselage bodies.

- It must be able to provide high frequency aerodynamic loading for the integration of an ongoing project on noise calculation.
- It must provide accurate predictions of rotor power required. This way, the tool can be used to validate and tune lower order models.
- It must be applicable to the design process. Consequently, a detailed aeroelastic analysis is required.
- It must be applicable to multidisciplinary optimisation methodology. Hence, the computational cost must be kept low.

The successful development of the simulation framework requires the fulfilment of more specific goals. These are:

1. Formulation of a computationally efficient method for the rapid estimation of the coupled natural frequencies and modes of vibration of modern rotor blades.
2. Development of an analytical formulation for the aeroelastic modelling of flexible rotor blades with coupled modal characteristics.
3. Implementation of an unsteady free-vortex wake aerodynamic model for the estimation of the unsteady rotor inflow.
4. Implementation of computational enhancement techniques for the minimisation of the computational overhead associated with the free-vortex wake model.
5. Implementation of a computationally efficient fuselage aerodynamic interference model to prove the ability of the framework to capture flow interactions.
6. Implementation of an unsteady blade aerodynamic model able to accurately estimate low and high frequency unsteady aerodynamics.
7. Integration of the previous areas into a cost efficient aeroelastic simulation framework.

The specific goals enumerated above correspond to different areas of study where significant progress needs to be carried out. The successful completion of this research project will result in progress on each of these areas as well as the overall simulation framework.

1.3 Thesis Structure

The present work aims to lay the foundations of a comprehensive rotorcraft code for the analysis of conceptual configurations by developing an aeroelastic simulation tool for the propulsion system. The framework, which can be easily expandable to analyse configurations with multiple rotors and auxiliary lifting surfaces, is described in this document.

This work has been organised with a conventional structure. It comprises the following chapters: introduction, literature review, methodology, results and discussion, and conclusions. The results and discussion chapter has been subdivided into four chapters: structural dynamics, integrated aeroelastic model, effect of the fuselage aerodynamic interference, and effect of coupled flexible blade modelling.

1. The first chapter presents an introduction to the context of the work, defines the aim and objectives, and outlines the structure of the thesis.

2. The second chapter presents a thorough literature review on aeroelastic rotor modelling for flight dynamics applications, including: structural modelling, inflow modelling, and existing comprehensive rotorcraft codes.

3. The third chapter describes the methodology developed in the present work. Each of the sections elaborate on the following areas: coordinate systems, structural dynamics modelling, elastic rotor blade kinematics, rotor inflow modelling, unsteady blade aerodynamic modelling, and aeroelastic modelling.

4. The fourth chapter demonstrates the predictive capability of the developed novel structural dynamic model by comparing computations with experimental measurements, finite element analysis results, and multi-body dynamics calculations for different rotor blades.

5. The fifth chapter presents an extensive validation of the proposed simulation framework by comparing computations of the present work with experimental measurements and calculations of a second comprehensive code for the HART II rotor.

6. The sixth chapter performs a thorough assessment of the effect of the incorporation of the fuselage aerodynamic interference on the operation of the rotor.

7. The seventh chapter evaluates the effect of coupled flexible blade modelling on the predictions of the rotor.

8. The eighth chapter summarises the key findings of the research project, assesses the fulfilment of the objectives, and outlines future paths of research.

9. Appendix A presents the list of publications produced by the author during the completion of this work.

1.4 Contribution

The main contribution of this work is the successful development of a computational framework for the aeroelastic simulation of rotorcraft propulsion systems. The developed framework is able to accurately simulate and predict the aerodynamic flowfield and the unsteady loads generated by the rotor and transmitted to the fuselage. The framework is easily expandable to account for potential interactions with other rotors, auxiliary lift surfaces, and fuselage bodies. An example of the latter is provided in Chapter 6. The simulation tool is able to generate high fidelity high frequency aerodynamic loading, including blade vortex interactions. The latter enables the calculation of impulsive noise, which is an ongoing research project in the institution. The framework produces accurate predictions of rotor power required, which enables its use as a validation tool for lower order models. The developed framework approximates the third level of Padfield's hierarchical paradigm, providing detailed aeroelastic information necessary for design purposes. Through the combined implementation of computational enhancement techniques the computational overhead has been kept low, which makes this tool suitable for multidisciplinary optimisation methodologies. The features of the developed framework successfully lay the foundations of a comprehensive rotorcraft code for conceptual configurations.

Moreover, a large contribution to the Clean Sky project (Ref. 9) was made in parallel to the completion of this research project. The author was actively involved in the activities undertaken by the Technology Evaluator of Clean Sky, regarding rotorcraft

performance modelling with the Green Rotorcraft Integrated Technology Demonstrator (GRC-ITD). More specifically, the author was involved in two main task. The first one was the integration of the Rotorcraft Mission Energy Management Model (RMEM) developed at Cranfield University into the Clean Sky developed PhoeniX platform (Platform Hosting Operational & Environmental Investigations for Rotorcraft) for the estimation of the power required by the onboard rotorcraft systems along the mission (Ref. 20). The second one was the assessment of the impact of novel rotorcraft technologies on fuel burn, and gaseous and noise emissions at mission, operational, and airport level (Refs. 20–22).

In addition to the development of the computational framework for the aeroelastic simulation of rotorcraft propulsion systems, contribution was made to more specific areas of research. These include:

- Analytical development of a novel mathematical formulation for modelling of coupled flap/lag bending and torsion vibration characteristics of helicopter rotor blades (Ref. 23).

- Enhancement of an existing methodology, which targets the treatment of rotor blade flexibility in helicopter aeroelasticity applications, to make it suitable for the application of coupled flap/lag bending and torsion modal characteristics.

- Computational enhancement of a free-vortex wake model for its cost effective implementation and execution. It is achieved by the combined action of parallel programming and a velocity fiel interpolation acceleration scheme.

- Investigation of the effect of the fuselage aerodynamic interference on the aerodynamic environment of the rotor, aerodynamic blade loading, blade elastic deformation, bending and torsion moments of the blade, and rotor trim parameters.

- Investigation of the effect of coupled flexible blade modelling on the aerodynamic environment of the rotor, aerodynamic blade loading, blade elastic deformation, bending and torsion moments of the blade, and rotor trim parameters.

Finally, the work undertaken during the completion of the research project has been disseminated as journal articles and conference papers. A complete list of publications can be found in Appendix A.

Chapter 2

Literature Review

The main rotor of a helicopter operates in a highly unsteady environment. Strong tip vortices are formed and trailed behind the rotor blades as a result of the high circulatory loading gradient found near the tip of the blades. This vortical structure is associated with a non-uniform three-dimensional inflow across the rotor disk. While the vortex geometry tends to be nearly axisymmetric in hover, the wake is extremely distorted in forward flight. As a consequence, the inflow associated with the tip vortices is remarkably non-uniform in this condition. Additionally, under certain flight conditions these vortices are located in the proximity of the blades, resulting in high frequency high amplitude variations of local aerodynamic conditions. The interaction of a blade with these oscillations (i.e. the vortex) is called blade-vortex interaction (BVI). BVIs are associated to unsteady impulsive loads, impulsive noise and strong vibrations. The intensity of the interaction depends on the proximity of the vortex to the blade, the orientation of the vortex relative to the blade, the viscous core radius of the vortex, the strength of the vortex, and the location of the interaction.

Besides the non-uniform flowfield, in forward flight the tangential velocity encountered by the rotor blade depends on the azimuthal and radial location. On the advancing side transonic Mach numbers can be found near the tip, while reverse flow can be observed on the retreating side near the blade root. The asymmetry and non-uniformity of the velocity flowfield encountered by the rotor blade result in highly unsteady fluctuating airloads.

As a consequence of the oscillating airloads, the rotor blade experiences flap and lead-

lag displacements and torsional deformation. Elastic deformations of the blade effectively modify the aerodynamic conditions seen by the blade, resulting in different aerodynamic loading and elastic deformations. The flapping displacements of the blade result in the modification of the orientation of the tip-path-plane (TPP) relative to the rotor shaft. The tilt of the TPP determines the spatial orientation of the thrust vector, therefore the lifting and propulsive forces. These forces must balance the gravitational and drag forces of the helicopter in steady controlled flight. That means that the TTP tilt needs to be modified to satisfy the trim condition. TPP leaning is carried out applying differential pitch control. Besides the orientation of the TTP, the magnitude of the thrust must be adjusted to obtain the amount of lift and propulsive force required. This is attained by adjusting the collective pitch of the rotor. An additional source of complexity is the strong coupling observed between the blade pitch and elastic deformations. As a consequence, the application of a control pitch input causes on-axis and off-axis response of the rotor, which needs to be accurately predicted.

The unsteady airloads described above, lead to the generation of time-dependent hub loads, which are transferred to the helicopter airframe. The correct modelling of these time-varying hub loads acts as an enabler for the accurate simulation of helicopter flight dynamics. Additionally, the accurate prediction of the BVIs is a requirement for the estimation of the main rotor noise footprint. To improve the capability to model the behaviour of the rotor blade, different interrelated fields of study have experienced substantial evolution. These are structural dynamics, aerodynamics, and flight dynamics.

Shupe (Refs. 24, 25) modelled a hingeless rotor with infinitely stiff blades in torsion and lead-lag, and the first two elastic flapping modes. The effect of the inclusion of the second flapping mode on the resultant rotor hub moment was assessed from hover to high speed flight conditions. The departure from uniform inflow during forward flight resulted in the excitation of the second flapping mode. It was concluded that the inclusion of higher order elastic modes is required for the correct prediction of hub loads in forward flight, when inflow non-uniformities in the radial and azimuthal directions are found. The magnitude of the excitation of the higher elastic modes was found to be greater at high speed conditions as a consequence of the higher non-uniformity of the inflow.

Lewis (Ref. 26) investigated the effect of using higher order modal content in the

modelling of the UH-60 articulated rotor. Although the quantified effect was small at hover, the relevance of the flexible formulation increased with flight speed. The author concluded that the flexible formulation along with a higher order aerodynamic model may improve the prediction of the off-axis response to control inputs for the particular articulated rotor studied.

He and Lewis (Ref. 27) carried out a validation study of FLIGHTLAB, originally developed by Du Val (Ref. 28), with flight test data of the UH-60A helicopter. The model used for this validation had elastic blades and the finite state dynamic inflow model proposed by Peters and He (Refs. 29, 30). Trim predictions of FLIGHTLAB for straight level flight were compared with flight test measurements. The collective pitch angle was underpredicted, while the rest of the control angles showed good agreement with flight test data. He and Lewis compared different levels of modelling in the on and off-axis response to longitudinal and lateral inputs in hover. The authors found an overprediction of the on-axis response with uniform flow, which was corrected using Peters and He finite state dynamic inflow model. The off-axis response was not captured correctly and the inclusion of elastic blades or finite state dynamic inflow did not improve the prediction.

Turnour and Celi (Ref. 31) assessed the off-axis rotor response to control inputs with the UM-GENHEL flight dynamics model (Ref. 32). It was coupled with a flexible blade model (Ref. 33) and Peters and He finite state dynamic inflow model (Ref. 29). For the particular articulated rotor studied, UH-60A, no improvement was observed as a result of the introduction of flexible blade modelling.

Celi (Refs. 34) evaluated the effect of steady stall and compressibility on the aeroelastic stability of hingeless rotors in steady turns. Flexible blades with coupled modes of vibrations were included in the analysis, inflow was modelled with Dress model (Ref. 35) and aerodynamic coefficients were obtained from steady state look-up tables with non-linearities in Mach number and angle of attack. The author concluded that lag damping was affected by compressibility effects.

Chunduru *et al.* (Ref. 36) assessed the effect of the inclusion of the ONERA stall model (Ref. 37) and Peter and He finite state dynamic inflow model (Ref. 29) on the stability of a small scale hingeless rotor. The stability characteristics predicted with this methodology correlated better than the ones calculated with quasisteady stall theory. This

was specially important for the prediction of lag damping, which is a critical property in hingeless rotor blades.

Ganguli *et al.* (Ref. 38) studied the effect of aerodynamic and inflow modelling on the prediction of vibratory hub loads. The authors concluded that the inclusion of non-uniform inflow has a large effect on the prediction of hub loads. The effect was found to magnify at high speed as a consequence of the stronger non-linearities. However, it was observed that the effect of unsteady aerodynamics on the prediction of the same loads is smaller.

Milgram *et al.* (Ref. 39) compared the vibratory hub loads calculated with UMARC and CAMRAD/JA to measurements from wind tunnel testing. The authors suggested the necessity of free-vortex wake models for the accurate calculation of vibratory hub loads, specially at low speed and transitional flight.

Nagabhushanam and Gaonkar (Ref. 40) studied the effect of inflow modelling on the aeromechanical stability of hingeless rotor helicopters in ground contact, hover, and forward flight. The use of a finite state wake model (Ref. 29) with a high number of azimuthal harmonics and radial shape functions improved the predictive capability. The authors suggested that inflow models able to capture the non-linearity of the inflow can potentially improve the prediction of aeromechanical stability characteristics of hingeless rotors.

Theodore (Ref. 41) integrated the manoeuvring free-vortex wake model developed by Bagain and Leishman (Ref. 42) and the flexible blade model from Ref. 31 into the flight dynamics model described in Ref. 43. The elastic blade rotor accounted for flexible flap-lag-torsion coupling. Theodore applied the model to two different configurations: a hingeless rotor helicopter based on the Bo105 helicopter and an articulated rotor helicopter based on the UH-60A. The effects of inflow and blade modelling on the flight dynamic characteristics of both configurations were assessed. The author found that free-vortex wake modelling improved the prediction of free flight trim, specially at low speed flight and hover. The prediction of main rotor collective and required power was improved compared with dynamic inflow model calculations, which tend to underpredict them. The author justified this behaviour by the larger average main rotor inflow obtained using free-vortex wake modelling. However, differences at high speed decreased and almost vanished. The inclusion of blade elasticity had the largest effect on the collective input required for the

trim condition. This was associated with the effective torsion deformation observed during the simulation. For the free flight on-axis response, the incorporation of free-vortex wake inflow did not improve the prediction and less sophisticated models can estimate the response correctly. It was found that for hingeless rotor helicopters, the free flight on-axis response to control inputs is insensitive to the type of inflow model and blade model. As a result, less computationally expensive methods can be employed. However, for the off-axis response, a manoeuvring free-vortex wake model and elastic blades are required. Dynamic inflow models can be used as well if they account for manoeuvring distortion and are calibrated with more sophisticated models. For the articulated rotor helicopter, the free-flight dynamic response to control inputs was found to depend on the inflow model. For this particular configuration, the dynamic response predicted with dynamic inflow was more accurate than with free-vortex wake modelling. The response of the articulated rotor was found to be independent of the blade modelling.

Brown and Houston (Ref. 44) compared two sophistication levels of inflow modelling. First order finite state dynamic inflow modelling was compared with a vorticity transport solution of the fluid domain around the helicopter. In both cases, the inflow models were linked to a rigid blade model and a flight dynamics model. The assessment of the inflow models was carried out comparing the predictions of flap angles, lag angles, pitch angles, airframe attitude angles, helicopter cross coupling derivatives, free-flight dynamic response to pilot inputs, and airframe modal characteristics. Although the incorporation of inflow models based on vorticity transport methods improved the overall flight dynamics prediction, a proportional improvement in the blade structural modelling is required to further extend the capability of the integrated model. From the above, it is concluded that the enhancement of the predicting capability of integrated flight dynamics codes is obtained through the refinement of the comprised individual models: inflow, blade aerodynamics, structural blade, and flight dynamics models.

This chapter presents a thorough review of the state-of-the-art of rotorcraft modelling. In the first place, an analysis of the previous and current structural models of rotor blades is carried out in Section 2.1. In the second place, a review of the rotor inflow models is presented in Section 2.2. In the third place, a survey of the main comprehensive rotorcraft codes is made in Section 2.3. In the last place, a summary of the state-of-the-art rotorcraft

modelling is given.

2.1 Structural Modelling

A significant evolution in structural modelling of rotor blades has taken place from the elementary beam theories to more refined modern finite element analysis (FEA) theories. Classical beam theory was deployed as a first attempt to model the structural dynamics of rotor blades. It comprised Euler-Bernoulli beam theory for the extension and bending and Saint-Venant's theory for torsion. Coupling between bending, extension, and torsion was not modelled. Timoshenko (Ref. 45) enhanced the classical theory accounting for transverse shear deformation and cross-sectional rotary inertia. This revision resulted in lower predicted natural frequencies compared with previous theories' estimations. Vlasov (Ref. 46) incorporated torsional warping restraint to the previous theory. The rotation of the blade was not accounted for and the degrees of freedom (DOFs) were treated individually. As a consequence, these theories were unsuitable for rotor blades.

During the late 1950s, Houbolt and Brooks (Ref. 47) formulated the differential equations of motion for the coupled flapwise/chordwise bending and torsion of a twisted non-uniform rotor blade subjected to linear aerodynamic loads. The theory was based on the classical engineering beam theory. It was reduced to a set of linear second order ordinary differential equations neglecting shear deformation, rotary inertia, and other non-linear terms of secondary nature. Although this theory clearly omitted the effect of non-linear terms, it provided physical insight of the problem and constituted the basis for many subsequent analyses, where approximate solutions of the set of equations were obtained. Different enhancements to the work of Houbolt and Brooks (Ref. 47) were reported by Bielawa (Ref. 48). Bielawa derived differential equations of motion for bending and torsion of a non-linearly twisted rotor blade in steady forward flight condition. The differential equations were formulated for an uncoupled case and an inertially and aerodynamically coupled case.

A non-linear set of equations of motion was derived by Hodges and Dowell (Ref. 49) during the 1970s for the coupled flapwise/chordwise bending and torsion of rotor blades. A truncation scheme, which reduced the rotor blade to a long, straight, slender, homogeneous, and isotropic beam undergoing moderate deflections, was deployed to simplify the equations. Two methods were used to derive the theory: Hamilton's principle and Newtonian methods.

The strain-displacement relations were derived from the geometrically exact transformation between the deformed and undeformed systems. Although the use of ordering schemes reduced the non-linearities considerably, several non-linear structural and inertial coupling terms still appeared in the final set of equations. These effectively represented the non-linear coupling between axial extension, flapwise/chordwise bending, and torsion. The relevance of these non-linear coupling terms for aeroelastic applications was later emphasised in Ref. 50. Crespo *et al.* (Ref. 51) modified the ordering scheme of Ref. 49 to include terms of third degree and increase the level of non-linearities modelling.

A series of new ordering schemes were developed in the 1970s and 1980s. These theories were based on small-strain approximations. They did not explicitly limit the displacements of the reference line or the rotations of the cross-section caused by deformations. This led to a generalisation of the often called "geometrically exact theories". A representative example of this type of theory is the study of the kinematics of elastic motion of Bernoulli-Euler beams subjected to large deflections carried out by Hodges *et al.* (Ref. 52). As a result, non-linear expressions relating the orientation of the deformed cross-section, torsion, local bending curvature, angular velocity, and virtual rotation with deformation variables were obtained. A posterior study carried out by the same authors (Ref. 53) extended this methodology to the dynamic analysis of pretwisted rotating beams. The assumption of moderate rotations generated by deformations was avoided in the kinematic derivation. Nevertheless, small extensional strain on the elastic axis compared with unity was assumed. References 54–57 constitute other representative theories among the described type.

Director beam theories were developed in parallel with the previous group of theories. These theories are based on the concept of directed continuum first introduced by Cosserat and Cosserat (Ref. 58). Beams are treated as 1D continua without a link to 3D material properties. The obtained set of equations does not have a link with cross-sectional distributions of 3D stress/strain and it is assumed in most of the cases. Representative examples are described in Refs. 59–63.

Asymptotic and projection beams theories are based on the deployment of projections of 3D elasticity on function spaces or asymptotic expansions in a slenderness parameter and were extensively studied during the 1970s and early 1980s. These theories can be developed with different orders. The lowest one reduces the equations to the classical beam

theories. Unlike the director beam theories, asymptotic and projection beam theories do have a connection between 1D and 3D. Representative examples of this theory can be found in Refs. 64–68.

Berdichevsky (Ref. 69) proposed the variational-asymptotic method (VAM). VAM divides the 3D geometrically non-linear elastic analysis into two different analyses: a non-linear 1D analysis and a 2D analysis. Energy functionals or variational principles are asymptotically expanded as functions of small parameters. Hodges *et al.* (Refs. 70, 71) extrapolated VAM to beams, plates and shells made of non-homogeneous composite materials. Although computationally more efficient than FEM, its computational overhead and the large amount of data required make this tool unsuitable for preliminary design.

Most of the aforementioned references are focused on the development of the kinematic expressions of a beam element. However, the equations of motion obtained have no analytical solutions. In most cases, numerical methods were developed to estimate the response of the coupled system or simplified uncoupled cases.

Murthy (Ref. 72) deployed the Transmission Matrix method (MT) to estimate the solution of the linear differential equations of Houbolt and Brooks (Ref. 47) for a twisted non-uniform blade. The TM method carries out a transformation of the differential equation of motion into first order differential equations using a state vector. Once the transformation is performed, modal characteristics are obtained for a particular set of boundary conditions. Accurate results are obtained for combined flapwise bending/chordwise bending/torsion, flapwise bending/chordwise bending, and flapwise bending/torsion.

Surace *et al.* (Ref. 73) used Green functions to calculate the coupled vibration characteristics for a rotating non-uniform pretwisted blade. Specific Green functions were imposed to satisfy the boundary conditions. Weighting matrices were required for numerical integration and differentiation. Structural influence functions are only available for hingeless beams and need to be derived for freely and spring articulated rotor blades.

2.1.1 Minimum potential energy methods

Both numerical methods presented above are based on the numerical evaluation of Houbolt and Brooks equations. However, alternative approaches based on Lagrange's method,

Rayleigh's method, and Rayleigh-Ritz procedures have also been deployed.

Fasana and Marchesiello (Ref. 74) used Rayleigh-Ritz method to study the modal characteristics of sandwich beams with constrained viscoelastic layer. Twenty simple polynomial expressions were utilised as assumed deformation functions. Up to eighty polynomial expressions were deployed to evaluate the sensibility of the results on the number of assumed deformation functions. No significant variation in the estimated results was found. The first four predicted bending natural frequencies were compared with other numerical methods estimations and good agreement was found for the lowest natural modes, nevertheless, for higher modes discrepancies between models increased considerably.

Hodges (Ref. 75) deployed a modified Ritz method to analyse non-uniform rotating beams. Radial discontinuities in bending stiffness and mass per unit length were included. The structural properties discontinuity required the use of $M + 1$ continuous segments with M discontinuities in structural properties. Hodges replaced standard polynomial expressions with power series of N terms for the formulation of the assumed deformation functions within each discrete segment. Additionally, geometric continuity was obtained at the extremes of each segment imposing boundary conditions. The relevance of the set of deformation functions assumed was emphasised by the author.

Goulos *et al.* (Ref. 76) used Lagrange's method to estimate the modal characteristics of non-uniform rotating helicopter blades. Mode shapes derived from classical beam and torsional theories were utilised as assumed deformation functions. The employed functions satisfied the structural boundary conditions for a series of hub supports. These were linearly independent and close to the actual deformation mode. The latter reduced the number of required assumed modes to attain convergence. As a result, computational times were reduced considerably leading to a computationally efficient method. The method proposed in Ref. 76 treated flapwise displacements, chordwise displacements, and torsion independently, i.e. uncoupled. However, very good agreement with the experimental measurements, FEA, and multi-body dynamics analyses was observed. Subsequently, Goulos *et al.* (Ref. 77–79) applied the proposed structural model to real-time helicopter flight dynamics integrating the proposed method into a helicopter comprehensive code.

2.2 Inflow Modelling

Helicopter rotor blades operate in a highly complex unsteady aerodynamic environment. The complexity of the flowfield encountered by the rotor blade is produced by the combination of different phenomena. The first one is the fluctuation of the tangential velocity encountered by the blade in forward flight. The second one is the time variant oscillations in control pitching angles. The third one is the elastic deformation of the blade, which derives in blade flapping and lagging motion and torsion rotation. The last source of unsteadiness is the non-uniform and unsteady rotor inflow. The combined effect of these sources results in highly unsteady changes in incident velocity and angles of attack; hence, aerodynamic loading. Although the elimination of any sources of unsteadiness from the analysis will result in deteriorated aeroelastic simulations of the rotor blade, the crux of the evaluation of the aerodynamic environment is the correct modelling of the velocity inflow across the rotor disk.

The first attempt to estimate the rotor inflow was made with the momentum theory, which was initially proposed by Rankine for axial turbines. Froude further developed the momentum theory and it was later generalised by Glauert. Momentum theory provides an average uniform inflow velocity and induced power for a given thrust requirement. Momentum theory was later combined with blade element theory (BET) to create the so-called blade element momentum theory (BEM). BEM provides a radial distribution of inflow velocity for a given rotor thrust requirement and radial distribution of blade properties. The simplicity and relative accuracy of BEM have resulted in its extensive use for preliminary calculations. However, the applicability of BEM to forward flight is limited, as the flowfield is not axisymmetric any more. BET was combined with linear inflow models for forward flight to overcome the limitation of BEM. The inflow model developed by Mangler and Squire (Refs. 80, 81) found extensive application. Mangler and Squire model provides longitudinal and lateral distributions of velocity inflow across the rotor disk. The model gives successful estimations at high advance ratios and steady flight conditions. Similar approaches can be found in Refs. 35, 82.

The next step in the evolution of inflow models was the introduction of the so-called dynamic inflow models. The basis of dynamic inflow models is the relation between

the radial and azimuthal inflow distributions, and the rotor thrust, pitching and rolling moments. A popular dynamic inflow formulation was proposed by Pitt and Peters (Ref. 83). Pitt and Peters model represents the linear inflow distribution with three inflow coefficients and three first order differential equations. The latter relate the inflow coefficients with thrust, pitch moment, and rolling moment. This model was refined to the so-called finite state wake model by Peters and colleagues (Refs. 29, 30, 84–87). Finite state wake models have a variable number of states, with Legendre functions for the representation of radial variations and Fourier series for the azimuthal distributions of inflow. The use of higher order polynomials and harmonics eliminates the limitation of linear inflow present in previous formulations (Ref. 83). Similarly to Pitt and Peters model, the number of dynamics equations is equal to the number of coefficients required to represent the inflow. The finite state wake model has found extensive application in rotor aeroelasticity and flight dynamics analyses (Refs. 36, 40, 77, 79, 88–90). This is due to its low computational cost and the ease of interfacing with flight dynamics models. However, a series of drawbacks of dynamic inflow models have been identified. The first one is the restriction in the non-uniformity of the inflow distribution, as the kind of distribution is limited to the type of radial and azimuthal mathematical functions used to describe the velocity inflow. The second one is the set of assumptions made in the development of the model. The assumption of undistorted helical structure collapses during low speed flight and transitional flight regimes where the wake is observed to bundle and distort. As a result, the accuracy of these methods during low speed flight and transitional flight is limited. The third one is the inability to simulate high frequency activity like high frequency blade vortex interaction (BVI) and high frequency vibration loads.

2.2.1 Vortex models of the rotor wake

In parallel with the study and evolution of dynamic inflow models, a large effort was made to develop the so-called vortex models. Vorticity based models do not impose a distribution of inflow velocity across the rotor disk, in contrast, the rotor wake structure is prescribed or calculated and the rotor inflow is calculated estimating the velocity flowfield induced by the vortices of the wake. As a result, the limitations of dynamic inflow models

are overcome if the structure of the wake is accurately predicted.

Rigid and prescribed wake models. The first step in the evolution of vortex wake models was the use of the so-called rigid wake models. Rigid wake models rely on the simplification of the non linear forcing term of the governing equation. This is carried out dismissing self or mutual interactions between vortices and assuming a constant average velocity forcing, which is estimated using momentum theory. As a result, the predicted geometry is composed of undistorted helical vortices. Based on the estimated wake geometry, the velocity inflow can be calculated at the rotor disk applying Biot-Savart law to all the vortex filaments. The obtained geometry captures the main effect of skewness. However, vortex interactions and wake contraction are not correctly predicted. Therefore, this model is not suitable for hover. In order to overcome the deficiency of rigid wake models in hover, Langrebe (Refs. 91, 92) developed a prescribed wake model for hovering flight. Langrebe's model prescribes the geometry of the tip vortex and the inboard sheet. The equations which define the position of the vortex filaments were derived from experimental data. A similar approach was presented by Kocurek and Tangler (Ref. 93) for experimental measurements of a subscale rotor. Egolf and Landgrebe (Ref. 94) and Beddoes (Ref. 95) developed the so-called generalised wake models for forward flight. Generalised wake models prescribe the geometry during forward flight based on the observation that in plane distorting velocities are much smaller than out of plane distorting velocities. Based on empirical data, functions which determine the out of plane distortion from the rigid wake geometry were developed. These models have found extensive application due to the low computational cost and relatively good results. However, some drawbacks have been identified. The first one is the limited applicability. The geometry is prescribed based on experimental measurements and/or momentum considerations. The geometry prescribed will be valid as long as experimental measurements of the wake are available at the specific flight condition. Therefore, the applicability is restricted to the flight conditions for which experimental measurements are available. The second one is the steady nature of the prescribed wake, as the wake is assumed to be frozen and no unsteady behaviours are included.

Free-vortex wake models. The next step in the evolution of vortex wake models was the development of free-vortex wake models. Free-vortex wake models do not prescribe

the geometry of the wake. Instead, the wake is allowed to distort based on the flight condition, blade loading, and self and mutual vortex interactions. As a result, this is the inflow formulation with less restrictions, and at least theoretically, any flight condition can be replicated. The specific numerical method used to solve the governing equation of the vortex filaments divides free-vortex wake models into relaxation methods and time-marching methods.

Relaxation free-vortex wake models.. Free-vortex wake models based on relaxation techniques enforce periodicity as a boundary condition of the problem. These methods are sometimes called iteration methods because the geometry is obtained iteratively. Based on an initial wake geometry, the overall velocity (free-stream and induced) is calculated at every location of the wake. Next, the geometry is allowed to convect and distort keeping once-per-rev (1P) periodicity. This process is repeated iteratively until convergence is attained and geometry changes are not observed between iterations. The use of relaxation techniques improves the numerical convergence of the method compared to time-marching. However, the enforcement of periodicity reduces its applicability to steady flight conditions.

The development of relaxation free-vortex wake models began in the 1970s when Clark and Leiper (Ref. 96) developed a relaxation model for the analysis of hover rotors. The wake was split in two regions: the first one comprised the tip vortices and was truncated after two revolutions, the second one comprised vortex rings and started at the vortices truncation age and lasted for thirty revolutions. The vortex rings played the role of far wake boundary condition and the resulting predictions agreement was good. Scully (Ref. 97) developed one of the most successful and used relaxation methodologies. It was based on a weight-averaging scheme for the induced velocity on a wake Lagrangian marker. The numerical stability of the method was greatly improved using the averaging technique. The method was applicable to hover and forward flight. In hover, it is well know that near the wake truncation age, the contraction of the wake vanishes and an expansion of the slipstream is present. In order to alleviate this deficiency, a far wake vortex cylinder was introduced. Each vortex was discretised into a series of straight vortex filaments. The size of the vortex core was estimated with a growth model which has been further enhanced afterwards and widely used in comprehensive analyses.

A series of relaxation free-vortex wake models were developed based on predictor-

corrector schemes. The first one was proposed by Bliss *et al.* (Ref. 98), who substituted straight line filaments with curved filaments. As a result, the self-induced velocity estimation was improved and coarser discretisation could be used. The authors suggested that better computational efficiency was attained as a result of the bigger discretisation resolution without an important increment in numerical errors. The wake was divided in two regions. The closest to the rotor was composed of tip vortices and an inboard sheet, while the furthest one comprised a set of ring vortices. Additionally, a sink singularity was added in the far field region to improve the stability of the method. Despite of the addition of the sink, the method only converged for axial climb. In order to reach convergence, Bliss *et al.* (Refs. 99) substituted the time derivatives of Ref. 98 with azimuthal and spatial derivatives and modified the far wake boundary condition having an helical filament with constant radius and pitch angle for a distance much larger than the rotor radius. Crouse and Leishman (Ref. 100,101) studied rotor/fuselage interactions with a predictor-corrector relaxation free-vortex model. A three-points central finite difference approximation was used for the representation of the spatial derivatives of the governing equations. The authors concluded that predictor-corrector schemes exhibit a much better numerical stability than explicit schemes. Bagai and Leishman (Refs. 102,103) took the method of Crouse and Leishman (Ref. 100,101) as the basis of their analysis. Bagai and Leishman developed a relaxation free-vortex wake model which made use of a pseudo-implicit correct-predictor scheme for the iterative solution of the wake geometry. A five point central finite difference approximation was used for the representation of both azimuthal and wake age domains in the governing equation. The wake was split into two region: a near wake composed of trailing and shed vortices and a far wake where a fully rolled-up vortex was modelled. The near wake was coupled with a Weissinger-L blade model to determine the aerodynamic loading and the bound vortices strengths. A centroid of vorticity method was used to determine the location and strength of the rolled-vortex. A vortex core growth model based on Lamb-Oseen approximation was deployed to estimate the size of the vortex filament. Vatista's model (Ref. 104) was used to desingularise Biot-Savart law. The model was applied to hover and forward flight and successful predictions were obtained. The numerical stability and rate of convergence of the method was greatly improved compared with other explicit schemes. The authors proved in a posterior study (Ref. 105)

the applicability of this method to multirotor configurations, thus, coaxial and tandem helicopters.The method was further enhanced in Ref. 42 including the effect of steady manoeuvres. Bagai and Leishman (Ref. 106) proposed velocity interpolation techniques to decrease the computational cost, reducing the number of Biot-Savart law evaluations per relaxation iteration while keeping the accuracy of the method. The authors showed the potential of these techniques to increase the computational efficiency while keeping the accuracy at the same level. The numerical characteristics of the pseudo-implicit predictor-corrector method of Bagai and Leishman made this methodology an excellent option for development of aeroelastic analyses, and it has been adopted in the present work.

Time-marching free-vortex wake models. Free-vortex wake models that march the solution in time are not limited to steady flight conditions, as periodicity is not enforced as a boundary condition. As a result, this is the most versatile vortex method and almost no limitations are identified. However, the numerical stability and errors have been the main difficulties to overcome in their development.

The development of time-marching free-vortex wake methods began in the 1960s. The first relevant study was made by Scully (Ref. 107) who formulated an explicit Euler time-marching scheme. Numerical instabilities and the associated lack of convergence in hover conditions limited the success of the proposed methodology. Landgrebe (Ref. 108) also used an explicit time-marching scheme to solve the geometry of the wake. Convergence in hover conditions was not attained, however, converged solutions were obtained in forward flight. The wake was split in two regions, a near wake region where velocity evaluations were carried out every iteration, and far wake where the velocity was only evaluated once to overcome the computational overhead. A coarse wake discretisation of 15 to 30 degrees was used to reduce the computational cost. The predictions obtained in forward flight showed good agreement with experimental measurements, however converged solutions were not obtained in hover. The effect of the use of curved vortex filaments instead of straight line filaments in time-marching wake models was evaluated by Bliss *et al.* (Ref. 109). The method which was implemented using a predictor-corrector scheme was deployed to study the aerodynamics of forward flight. Bhagwat and Leishman (Ref. 110) developed a time-marching free-vortex method based on a predictor-corrector scheme.

The predictor step used a five point central finite difference approximation, which was previously used by Bagai and Leishman (Ref. 102, 103), for the spatial and temporal derivatives of the governing equation. The corrector step used the same five point central finite difference approximation for the spatial derivative and a second order two step back finite difference approximation for the temporal derivative. The resultant scheme was second order accurate with implicit damping, which improved the stability of the scheme and allowed the authors to obtain converged solutions in hover. The same authors determined in Ref. 111 that straight line vortex discretisation was second order accurate if the resolution of the wake was less than five degrees. Horn and Bridges (Ref. 112) investigated the relation between the spatial and temporal resolutions, and the results and computational time. The study aimed to obtain a real time free-vortex wake analysis and the potential of parallel computing to reduce the computational overhead was highlighted.

2.2.2 CFD-based methods

The use of inflow models based on computational fluid dynamics (CFD) has been continiously increasing over the last decades. The rise in the use of CFD has been driven by the progress in computational power, which has resulted in cheaper systems with enhanced capability in speed and memory. Although the increase in computational power has enabled the rotorcraft community to use CFD, the computational cost is still orders of magnitude higher than conventional comprehensive codes with engineering models for inflow and blade aerodynamics. CFD methods are out of the scope of this work and only comparison with vortex inflow models is carried out. A detailed description of the evolution of CFD codes for rotorcraft applications can be found in Ref. 113.

The main target of the aerodynamic analysis of rotor blades is the solution of the aerodynamic loading. The first distinction can be made in terms of what inputs and outputs on each aerodynamic model are considered. The aerodynamic solution depends, among others, on the dynamic response of the rotor, which is the velocity of the rotor relative to the air, and the velocity inflow. Dynamic response and gust velocity depend on the airloads, therefore the solution is coupled. Here a clear difference between CFD methods and vortex methods can be observed. In a CFD method, the detailed flow structure around

the rotor blade is calculated. The shear layer behind the blade is captured, the roll-up of the vortices is simulated, and the general structure of the wake estimated. As a result, the disturbance of the flowfield caused by the operation of the rotor blades is modelled, which essentially is the rotor wake and its inflow. In contrast, vortex methods are inviscid and no shear layer, roll-up, or wake structure can be obtained directly from the solution of the aerodynamic problem around the rotor blades. As a consequence, the wake is modelled as a different component, which imposes a specific velocity inflow across the the rotor disk. The wake model is iteratively coupled with the aerodynamic model of the blade through conservation laws of vorticity. The second difference is the type of formulation used to describe the flow. A grid-fixed Eulerian formulation is used in CFD methods while a Lagrangian formulation is employed in vortex models.

From the above the main advantage of CFD solvers can be identified. CFD methods can potentially simulate the detailed flowfield around the blade including shockwaves, unsteadiness in blade velocity and gust, dynamic stall, shear layer shedding, roll-up, and rotor wake. In order to obtain accurate predictions, a fine computational grid is required and numerical dissipation of the vortical structures must be prevented. Two main formulations have been employed for the aerodynamic analysis of rotors using CFD: the potential Euler formulation and the Navier-Stokes formulation. Euler formulation, which is an inviscid simplification of the Navier-Stokes equations, was first used due to the smaller requirement in terms of grid resolution. However, viscous phenomena were dismissed. Navier-Stokes formulations account for viscous effects, however the numerical diffusion of the vortex structures has been identified as the major challenge to be overcome to obtain reliable solutions.

Two different approaches for the CFD solution of rotor flows have been used: first principles or direct wake capturing solutions, and partial CFD or hybrid solutions. Hybrid solutions divide the solution into two different regions, each region associated to a different type of solution. The far field is represented with vortex-wake models using a Lagrangian formulation, and a CFD solution is obtained in the flowfield around the rotor blades. Both regions are coupled through the inflow and the conservation of vorticity. Hybrid solutions were developed to mitigate the numerical diffusion of vorticity and representative examples are described in Refs. 114–118 . The increasing computational power and the

progress in CFD modelling have resulted in the departure from hybrid formulations to direct wake capturing solutions. First principles CFD methods solve the Navier-Stokes or Euler equations over the complete computational domain. The main challenge in this approach is the conservation of the vorticity, as numerical dissipation has been observed. Different approaches have been proposed to alleviate this problem. These include: local mesh refinementes in vortical regions (Refs. 119–122), higher order discretisation schemes (Refs. 123–126), vorticity confinement techniques (Refs. 127–130) and vorticity transport methods (Refs. 131, 132). CFD methods exhibit a big potential for the analysis of rotorcraft, however, the high computational cost of these techniques is prohibitive for design purposes.

2.3 Comprehensive Rotorcraft Codes

Aeromechanic and aeroelastic modelling of rotors and rotorcraft has been carried out through two different types of analyses: comprehensive codes and coupled computational structural dynamics (CSD) and computational fluid dynamics (CFD) codes. Comprehensive codes comprise different models for each of the fields of study. For the structural dynamics, finite element beam approximations of the rotor blade are usually employed. The aerodynamic model of the blade relies on experimentally derived 2D table look-up data, and semi-empirical methods for compressibility, unsteadiness, and dynamic stall. The inflow model commonly uses either a free-vortex wake model or a prescribed wake model. In some cases even a dynamic flow model can be deployed. These methods are dynamically coupled between them to obtain the aeromechanic or aeroelastic behaviour of the blade. In comparison with CFD/CSD codes, the CPU time and memory required to obtain the solution are an order or few orders of magnitude lower depending on the specific case. The increasing computational power has resulted in an increasing use of CFD/CSD codes, however they are still too computationally demanding for design purposes. In 2001 the Higher harmonic control Aeroacoustic Rotor Test (HART) II test was carried out. The data base obtained from this project was used to assess and compare the most relevant comprehensive codes. In this section the comprehensive codes used in the HART II comparison are described, as they represent the state-of-the-art of comprehensive codes.

Additionally, the Cranfield University in-house tool HECTOR is presented.

2.3.1 CAMRAD II

Comprehensive Analytical Model of Rotorcraft Aeroedynamics and Dynamics II (CAMRAD II) was originally developed by Johnson Aeronautics (Refs. 133, 134) and further developed as described in Refs. 135–138. For the prediction of the performance of the HART II hingeless rotor and comparison against the experimental data, the version described in Refs. 136, 138 was used.

The rotor blade is structurally modelled using finite non-linear elements with coupled flap, lag, and torsion degrees of freedom. The equations of motion, which contain coupling between the degrees of freedom, are solved for trim conditions (wind tunnel in this case). Bending moments are calculated using the modal method, i.e., multiplying the local curvature by the effective stiffness. Torsional moments are calculated as well using the modal method, that is the product of the first spatial derivative of the torsion and its torsional rigidity. The aerodynamic coefficients of each of the beam elements are obtained through a combination of C81 table look-up and ONERA EDLIN unsteady corrections. The local aerodynamic conditions are calculated at the 3/4 chord location. The rotor inflow is obtained from a multiple trailing vortices free-vortex wake model (Refs. 138–140). Trailing vortices are shed behind the blade and eventually merged into rolled-up vortices. The assumption made for merging vortex filaments is that consecutive vortices of the same sign roll-up together. The location of the rolled-up vortex depends on the centroid of vorticity and the circulation strength on the total vorticity contained. Wind tunnel trim is undertaken using a Newton-Raphson method, where the Jacobian matrix is computed numerically based on disturbances of the control settings. Noise is calculated at a postprocessing stage using the PSU-WOPWOP code (Refs. 141, 142), which is based on Ffowcs Williams and Hawkings formulation (Ref. 143).

2.3.2 DYMORE2.0

Georgia Institue of Technology developed a non-linear flexible multi-body dynamics code (Ref. 144). Originally it was not developed for helicopter calculations. However, the

flexibility of the multi-body formulation enabled its expansion to rotorcraft analyses.

A combination of modal reduction and finite element method is used to model the blade in the time domain. The rotor blade is aerodynamically represented by a lifting-line. Aerodynamic coefficients are calculated using a combination of Peters *et al.* method (Ref. 85) and C81 table look-up with aerodynamic conditions estimated at the 3/4 chord location. Initially, DYMORE used a Peter and He finite-state dynamic inflow (Refs. 85,86). Nevertheless, due to the limitation of dynamic inflow models to predict high frequency phenomena, a free-vortex wake model was introduced. The inclusion of Bhagwat and Leishman free-vortex wake model (Ref. 110) corrected the deficiency of dynamic inflow models and provided a tool for the calculation of BVI, necessary for noise predictions. A near wake with multiple trailing vortices is used, where some of these filaments roll-up to form a tip vortex. Squire vortex core growth model (Ref. 145) is used to estimate the size of the core radius. Similarly to CAMRAD II, the bending and torsion moments are calculated using the modal method. Trim control angles are calculated with the auto pilot method (Ref. 146). In a first phase, the loads are calculated for the prescribed control angles. From that initial solution, perturbation simulations are carried out for the collective, longitudinal, and lateral pitch angles. The Jacobian matrix is obtained from the perturbation of the initial solution. The Jacobian matrix is inverted to obtain the incremental control angles. The process is repeated until the solution of the control angles has converged. DYMORE2.0 does not include a noise model and for the HART II assessment, DLR performed the noise calculations using DYMORE2.0 airloads.

2.3.3 DYMORE4.0

DYMORE4.0 is another evolution of the original DYMORE code (Ref. 144) described in Ref. 147. The version used in the HART II assessment incorporates loose and tight coupling of the flexible multi-body dynamics code with CFD (Refs. 148–150). Additionally, the trim algorithm has been upgraded towards a more computationally efficient algorithm. In this version of DYMORE, no free-vortex wake model is included, and the inflow across the rotor is calculated using Peters and He finite-state dynamic inflow model (Refs. 85,86). The beam element aerodynamic coefficients are calculated using a combination of table

look-up and Peters *et al.* method (Ref. 85). As a result of the lack of wake model, BVI were not predicted and no noise calculations were performed.

2.3.4 HMMAP

HHMAP is the combination of five independent modules developed by ONERA to calculate the aeroelastic and aeroacoustic behaviour of rotorcraft: HOST for the rotor trim calculation, MESIR for the prediction of the wake, MENTE for the computation of the vortex roll-up process, ARHIS for the estimation of the pressure around the blade, and PARIS for the calculation of the radiated noise.

HOST comprehensive code was developed by Eurocopter (Ref. 151) for the aeroelastic response of the blades of an isolated rotor or a full helicopter. The blade is discretised in linear beam elements with flap, lag, and torsion degrees of freedom. Modal reduction is used to reduced the number of variables. Uncoupled mode shapes are used in the reduction. HOST does not have the capability to model hingeless rotor blades, in contrast these blades are approximated as equivalent spring articulated rotors. Bending moments can be calculated with the modal method or the summation method. The latter integrates the bending moments along the blade. The blade is aerodynamically modelled using a lifting line method. The local aerodynamic conditions are estimated at the 1/4 chord location, these conditions are introduced in the table look-up method to obtain the steady state compressible non-linear two-dimensional aerodynamic coefficients. Other effects such as sweep, transonic, stall, and unsteadiness are accounted for with a series of semi-empirical correction factors. The velocity inflow across the rotor is calculated with a vortex wake model. Two different steps can be distinguished in the wake mode. The first one is carried out with the METAR prescribed helical wake code (Ref. 152), which comprises vortex lattices. The circulation strength of each of them depends on the azimuthal and radial gradient of bound vortex circulation. The induced velocity and the circulation are coupled iteratively within the trim loop. The prescribed wake does not capture wake distortions present in many phases of flight. Under certain conditions, the distortion of the vortical wake results in BVI. In order to capture the BVI locations and strengths, the MESIR full span free-vortex wake model (Ref. 153) was incorporated in HOST. The coupling between

induced velocity and bound vorticity is carried out internally for each new geometry calculation. The core viscous radii are considered independent of the circulation, and are a function of the radial discretisation for the trailing vortices and the azimuthal discretisation for the shed vortices. Within the MESIR execution, the motion of the blade and trim are kept constant. In a posterior version of MESIR, the code was parallelised using OpenMP to reduce the required computational time. The trim condition is calculated in HOST, where the blade motion is represented by the sum of harmonics. In a first step, the blade is assumed to be rigid with flap, lag, and pitching degrees of freedom. Equilibrium of external and internal forces is obtained. In the second step, the effect of flexibility is taken into account using a superimposition of a limited number of harmonics. These harmonics are approximated by the product of a mode shape function of the radial location, and a generalised coordinate function of time. Based on these approximations the trim procedure determines the control angles required to obtain a given set of generalised coordinates that satisfy the trim conditions. This procedure is carried out using a Newton-Raphson gradient method. Similarly to previous codes, in Newton-Raphson gradient method, a Jacobian matrix is calculated and a direction to find the control solution obtained. For the noise calculation, the MENTHE vortex roll-up code (Ref. 154) is used to roll-up trailing vortices together under certain circumstances. MENTHE identifies regions which contain high vorticity levels with the same sign. If the vorticity level is above a threshold, the contained trailing vortices are merged into a concentrated vortex located at the centroid of vorticity. ARHIS code (Ref. 155) is an unsteady potential method used to calculate the distribution of blade pressure. The flow around the blade is assumed to be inviscid and incompressible. For each two dimensional blade section, the blade pressure is calculated with compressibility thickness and tip corrections. Then the deformation is taken into account as it is allowed to convect freely. The last step is the calculation of the noise, which is carried out using PARIS code (Ref. 156). The noise radiation code is based on the Ffowcs Williams and Hawkings equation (Ref. 143) and estimates the loading and thickness noise.

2.3.5 S4

The high resolution 4th generation rotor simulation code S4 (Ref. 157) was originally developed by the DLR in the 1970s. From the original model, many upgrades have been carried out. The effect of elasticity has been incorporated. Unsteady aerodynamics have been included. An inflow model, which takes into account high harmonics, has been developed. Additionally, a vortex wake model for the estimation of BVI events has been implemented.

S4 code divides the structural analysis in two steps. In a first step a finite element analysis (Ref. 158) based on the formulation of Houbold and Brooks (Refs. 47) calculates the coupled modal shapes and frequencies. Each shape is later represented radially as a 7th order polynomial. The coefficients of the polynomial are obtained from the dominant component of each mode obtained with FEA. The second step involves the dynamic response of the blade subjected to external loading, which is carried out with the modes previously estimated with FEA. S4 uses the modal method to calculate bending moments at any radial section. The beam section aerodynamic coefficients are calculated with a semi-empirical analytic formulation based on Leiss method for unsteady motion (Ref. 159), later upgraded to correctly model BVI. The Wagner function (Ref. 160) is used as a lift transfer function to step inputs in airfoil motion while the Küssner function (Ref. 161) is employed for gusts. In both cases, the lift transfer functions are corrected for compressibility effects. The effective angle of attack is later computed using Duhamel integral (Ref. 162). The model includes a dynamic stall formulation validated in Refs. 163–165. The parameters used in the unsteady blade aerodynamic model are obtained from steady state measured aerodynamic data. Corrections for tip loss effects are introduced as well, which modify the induced velocity. Additionally the effect of the fuselage on the velocity inflow is accounted for using an analytical formulation with coefficients derived from potential flow calculations (Ref. 166). Three different inflow models are available. The first one is the Mangler and Squire wake model (Ref. 81), which gave good predictions for performance and vibration estimation, however the inflow only depends on the steady state rotor operational condition. Therefore, any inflow variation due to high harmonic control is not captured. For noise calculations, the location of the vortices relative to the

blade is relevant. Mangler and Squire wake model (Ref. 81) was not able to capture high harmonic control effects, or non-linearities due to high speed. As a result an enhanced version of Beddoes prescribed wake model (Ref. 95) was employed. The upgraded wake model, kept the full vortex spiral with multiple trailing vortices. The wake was split in two regions, the near wake with trailing vortices forming at the extremes of each blade aerodynamic segment, and the far wake with tip, root, and inboard vortices. The modified wake model accounted for wake deflections due to high harmonic control (Ref. 167). The third inflow model is a parallelised free-wake model (Ref. 168) with trailing vortices formed at the extremes of every blade aerodynamic element, the effect of shed vorticity is also taken into account. The calculation of trim controls is carried out using a fourth-order Runge-Kutta scheme. The algorithm calculates the thrust and moments derivatives with respect to the control angles, and uses the derivative to estimate the following control angles. This process is repeated iteratively until convergence is attained. The acoustic code APSIM developed at DLR (Ref. 169, 170) is used to estimate the noise radiation. The blade loading obtained with S4 code is transferred to APSIM to calculate the noise radiation. Blade loading along with operational condition and blade motion are utilised to obtain the thickness and loading noise.

2.3.6 UMARC

The University of Maryland Advance Rotorcraft Code (UMARC) (Refs. 171, 172) was developed in the late 1980s in University of Maryland. The structural dynamics and rotor trim models are loosely coupled with a lifting line representation of the blade and a free-vortex wake model.

Blades are structurally modelled as second-order non-linear isotropic beams with flap, lag, and torsion degrees of freedom (Refs. 49, 52). Modal reduction is carried out and the dominant modes are used in a finite element time-marching algorithm. The summation method is used to obtain blade bending moments. Each blade is represented by an unsteady lifting line model. Blade element aerodynamic coefficients are calculate using a combination of table look-up of steady state two dimensional data, Weissinger-L near wake model (Ref. 173), and Leishman-Beddoes unsteady model (Ref. 174). The Parallel

Wake Analysis Module (PWAM) was used as an inflow model in UMARC (Ref. 175). The free-vortex wake model, developed at University of Maryland, divides the wake in two regions. A near wake, where trailing vortices are formed at the extremes of each aerodynamic beam element, and a far wake with tip and root vortices. The location of the tip vortex is allowed to move inboard if negative lift is present at the tip. Shed vorticity is not taken into account in any of the wake regions. The growth of the viscous core size is modelled using Squire's law (Ref. 176) and the swirl velocity is calculated using Scully's model (Ref. 177). Control angles for trim conditions are calculated using an algorithm of Ref. 178 targeting the prescribed forces and moments. Noise calculations were carried out with a University of Maryland in-house tool (Ref. 179). This tool is based on Ffowcs Williams and Hawking formulations.

2.3.7 HECTOR

The HEliCopTer Omni-disciplinary Research Platform (HECTOR) is the simulation framework developed in Cranfield University (Ref. 17). HECTOR comprises a series of modules: non-linear structural dynamics, unsteady blade aerodynamics model, finite state dynamic inflow, and an engine performance code. All these modules are coupled in an aeroelastic manner and associated to a fuselage model.

A Lagrangian method is used to obtain the uncoupled flap, lag, and torsion modal characteristics (Ref. 76). These modal characteristics are used within the aeroelastic model to approximate the non-linear elastic deflection using modal superimposition. Blade moments can be calculated using either a modal method or a summation method. Peters and He finite state dynamic inflow (Ref. 29, 30) with dynamic wake distortion (Ref. 180) and corrections for wake curvature (Ref. 181) is employed to estimate the inflow across the rotor disk. An unsteady blade aerodynamic model based on Leishman and Beddoes with corrections for dynamic stall (Ref. 174) is used for the estimation of blade element aerodynamic coefficients. The parameters used within the blade aerodynamic model are obtained from steady state two dimensional aerodynamic data. The aeroelastic model couples these modules in a time-marching manner using a fifth order accurate numerical evaluation scheme of Duhamel integral until periodicity is reached. The performance of the

rotor is coupled to a flight dynamics code and the engine performance code TURBOMATCH (Refs. 182). Control angles are calculated using a globally convergent Newton-Raphson model for either wind tunnel or free flight conditions. The code has been proven to execute in real time (Ref. 77) and has been extensively applied for mission performance analysis and dynamic response analysis (Refs. 6, 15, 183, 184).

2.4 Remarks

A thorough survey of the state-of-the-art of aeroelastic rotor modelling for flight dynamics applications has been presented in this chapter.

In the first place, the highly non-linear unsteady aerodynamic environment where the rotor operates was described. Different sources of unsteadiness and non-linearities were identified. These include: asymmetric flowfield, non-uniform inflow, and blade vortex interactions. As a consequence of the unsteady non-uniform aerodynamic conditions encountered by the rotor blade, time-varying airloads are exerted on the blade and transmitted to the rotor hub. In addition to the hub loads, the rotor blade itself experiences rigid and elastic deformations, which effectively generates another source of unsteadiness.

The necessity of the incorporation of elastic blade modelling for the accurate prediction of the time-varying hub loads was pointed out in the second place. For hingeless rotor blades, the departure from rigid to flexible blade modelling is fundamental, as the blades are excited with high order content. It was identified that the higher the non-uniformity in the radial and azimuthal direction, the larger the effect of elastic modelling. During high speed forward flight and manoeuvring flight the non-uniformity of the inflow is exacerbated, and therefore it was concluded that the use of elastic blade modelling becomes essential. For articulated rotor blades, the effect of elasticity is considerably smaller than for hingeless blades. However, blade flexibility needs to be modelled if high speed forward flight and manoeuvring flight wants to be accurately simulated.

In the third place, the influence of non-uniform inflow modelling was assessed. Although at hover it was found that the sophistication of the inflow modelling has a weak effect, during transitional flight o high speed flight sophisticated inflow models are required to capture the unsteady non-uniform physics involved. It was also pointed out that the

correct prediction of off-axis dynamic response requires a level of modelling sophistication associated with free-vortex wake methods and blade elastic formulations.

An overview of the approaches historically used for the structural modelling of elastic rotor blades was given after. Methodologies ranging from ad hoc theories to variational-asymptotic methods were reviewed. Special attention was paid to minimum potential energy methods. No computationally efficient theories able to estimate the coupled modal characteristics of rotor blades were found.

The next step was the analysis of inflow models for rotorcraft applications. Three main types were identified: dynamic inflow models, vortex models, and CFD models. Different conclusions were drawn: the computational cost associated with the use of CFD is prohibitive for its use as a design tool; dynamic inflow models are not able to capture high frequency phenomena such as BVI, and off-axis prediction can be improved with free-vortex wake models.

The last step was a detailed survey of the state-of-the-art of comprehensive rotorcraft codes. It is noted that limited information is publicly available and the published literature is focused on the validation of the codes against experimentally derived data. Additionally, a description of the Cranfield in-house comprehensive code HECTOR was given.

The present work aims to lay the foundations of a comprehensive rotorcraft code for the analysis of conceptual configurations. The first step in the elaboration of the platform is the development of a framework for the aeroelastic simulation of the propulsion system, i.e. the rotor. The developed framework must be expandable and able to capture the interactions between potential multiple rotors and/or interactions between the rotor and the fuselage or auxiliary lift systems. Time-dependent hub and section loads constitute the main inputs for the flight dynamics and noise propagation models. Therefore, an accurate calculation of these loads needs to be carried out in a fully aeroelastic manner.

To obtain reliable hub loads, the inclusion of elastic effects has been found to be essential. However, no method able to rapidly estimate the coupled vibration characteristics of helicopter rotor blades has been found. The method developed in this work is able to solve the mentioned weaknesses: model coupling between DOFs, be expressed in closed form expressions readily available for any type of hub support, require a limited amount of information, and deploy a reduce number of assumed deformation functions to enhance

the computational efficiency.

Regarding the inflow modelling, four different requirements are essential. The first one is the applicability of the model to multiple rotor configurations, where interactions between propulsion/lift systems are likely to be present. The second one is the independence of the model from external inflow prescriptions, i.e, the model must capture the physics of the problem without relying on prescribed inflow distributions. The third one is the ability to predict BVIs. Noise radiation is an increasing concern and BVIs have been identified as the main source of high intensity loading noise. The last one is the computational efficiency of the method. The computational cost must be kept low, so its use is not restricted to high performance computing facilities and its applicable to the design optimisation process. The last requirement discards CFD methods as a suitable inflow model due to its computational overhead. The accurate prediction of blade vortex interactions requires the detailed knowledge of the vortex geometry and its relative distance to the blade. As a result, only vortex models become an appropriate option. The first two requisites reduce the number of suitable inflow models to one, free-vortex wake models. A relaxation free-vortex wake model is found to be the optimum choice due to its superior convergence characteristics. As a result of its fast convergence, the computational cost is considerably smaller than time-marching methods. However, the computational overhead of the published formulations limits its applicability. In order to overcome this restriction, computational enhancements are required. The use of parallel computing and an acceleration scheme based on velocity interpolation were identified as two potential computational improvements. The combination of both techniques could potentially reduced the computational overhead of free-vortex wake models to the level of the dynamic inflow models, enabling its use for design and optimisation purposes.

Modal superimposition for aeroelastic analyses was proven in Ref. 77 to be highly computationally efficient. Uncoupled modes of vibration, dynamic inflow modelling, unsteady aerodynamics, and three-dimensional elastic kinematics were deployed at the time. The computationally efficient methodology of Ref. 77 was limited to conventional helicopters and low frequency events. However, that methodology can potentially be expanded and the limitations overcome using coupled modes of vibration and a computationally efficient free-vortex wake model.

From the above it is concluded that a computationally efficient framework for the aeroelastic simulation of rotorcraft propulsion systems applicable to conceptual rotorcraft configurations is yet to be developed. The present methodology proposes a combination of computationally efficient models for the accurate aeroelastic modelling of rotor blades. A novel mathematical formulation for the rapid estimation of coupled flap/lag bending and torsion modes of vibration is derived. A well established free-vortex wake formulation is enhanced to reduce the computational cost. Both of the previous are coupled in a computationally efficient non-linear aeroelastic manner. The generated framework has a level of fidelity high enough to obtain accurate time-dependent hub loads, which can be directly transferred to a flight dynamics code, and blade airloads including BVIs. The latter enables the calculation of high intensity loading noise. The capabilities of the developed framework along with its expandability to multirotor configurations, its easy integration into a flight dynamics code, and computationally efficiency make the proposed simulation tool an optimum choice for the multidisciplinary analysis of novel rotorcraft configurations.

Chapter 3

Methodology

This chapter describes the methodology developed in the present work. The computational model developed for the aeroelastic simulation of rotorcraft propulsion systems can be divided into different components. Each component or module deals with a different field of study, namely: structural dynamics, three-dimensional kinematics of elastic rotor blades, rotor inflow, blade aerodynamics, and aeroelasticity.

In the first place, the coordinate systems used in the present approach are described in Section 3.1. In the second place, a mathematical approach for the modelling and analysis of coupled flap-lag-torsion vibration characteristics of non-uniform rotor blades is formulated in Section 3.2. The proposed structural dynamics model estimates the coupled modal characteristics required in the aeroelastic response of the rotor. The three-dimensional kinematics of elastic rotor blades, necessary for the calculation of inertial and aerodynamic loads, are defined next in Section 3.3. The free-vortex wake model deployed for the calculation of the rotor inflow is formulated and described in Section 3.4. The acceleration strategies implemented to reduce the computational cost of the free-vortex wake model are presented and the specific treatment of viscosity effects and vortex rolling-up explained. The unsteady blade aerodynamic model is then formulated in Section 3.5. In the last place, the aeroelastic model is described in Section 3.6, the interface of this module with the previous components is explained and the implementation of the integrated method presented.

3.1 Coordinate Systems

The proposed methodology employs four right handed Cartesian coordinate systems, namely: the global non-rotating reference frame O, the rotating reference frame A_i, the blade element fixed coordinate system b and the cross-sectional coordinate system.

The origin of the global non-rotating reference frame O is located at the centre of the rotor hub, as shown in Fig. 3.1a. Its $\tilde{e}_z^O$ unit vector is aligned with the shaft of the rotor pointing upward, $\tilde{e}_y^O$ points starboard, and $\tilde{e}_x^O$ completes the right handed coordinate system. The global non-rotating reference frame O is used to define the position vector of the points of interest of the rotor blade and the Lagrangian markers of the wake. Therefore, it plays the role of interfacing the aeroelastic and the free-vortex wake models. Additionally, a non-rotating inertial coordinate system is required to account for the non-linearities present in the velocity and acceleration of rotating systems.

Figure 3.1b presents the rotating reference frame A_i, $i = 1, \cdots N_b$ where N_b is the number of blades. Its origin is located at the ith blade root/hinge. A_i accounts for the presence of rotor precone β_{pre} and presweep ζ_{pre} and the application of collective pitch θ_0. The resulting reference frame, shown in Fig. 3.1b, has its $\tilde{e}_x^{A_i}$ unit vector aligned with the undeformed elastic axis pointing radially outwards. Goulos *et al.* (Ref. 77) proposed the use of the rotation matrix $[A_i]$ to transform any vector expressed in the non-rotating reference frame O to the rotating reference frame A_i. The rotation matrix $[A_i]$ is defined as

$$[A_i] = [\theta_0]\,[\beta_{pre}]\,[\zeta_{pre}]\,[\psi_i] \tag{3.1}$$

where $[\theta_0]$, $[\beta_{pre}]$, $[\zeta_{pre}]$, and $[\psi_i]$ are the collective pitch, rotor precone, rotor presweep, and azimuthal rotation matrices respectively. Their graphical definition is presented in Figs. 3.1c and 3.1d . Mathematically, the rotation matrices are formulated as

$$[\theta_0] = \begin{bmatrix} 1 & 0 & 0 \\ 0 & \cos\theta_0 & \sin\theta_0 \\ 0 & -\sin\theta_0 & \cos\theta_0 \end{bmatrix} \tag{3.2}$$

$$[\beta_{pre}] = \begin{bmatrix} \cos\beta_{pre} & 0 & \sin\beta_{pre} \\ 0 & 1 & 0 \\ -\sin\beta_{pre} & 0 & \cos\beta_{pre} \end{bmatrix} \tag{3.3}$$

$$[\zeta_{pre}] = \begin{bmatrix} \cos\zeta_{pre} & -\sin\zeta_{pre} & 0 \\ \sin\zeta_{pre} & \cos\zeta_{pre} & 0 \\ 0 & 0 & 1 \end{bmatrix} \tag{3.4}$$

$$[\psi_i] = \begin{bmatrix} \cos\psi_i & \sin\psi_i & 0 \\ -\sin\psi_i & \cos\psi_i & 0 \\ 0 & 0 & 1 \end{bmatrix} \tag{3.5}$$

The origin of the blade element fixed coordinate system b is located at an arbitrary point $p\,(r,t)$ on the ith deformed elastic axis, as shown in Fig 3.2. $\tilde{e}_x^b$ is aligned with the deformed elastic axis and points radially outwards. $\tilde{e}_y^b$ is aligned with the cross-sectional major axis and points towards the trailing edge. $\tilde{e}_z^b$ completes the right handed coordinate system. Local inflow conditions determine the aerodynamic loads of a given blade element. Therefore it is of interest to transform the absolute velocity vectors expressed in O to the blade element fixed coordinate system b. The transformation is carried out applying a series of matrix rotations. The overall rotation matrix $\left[T_i^b\right]$ transforms any vector expressed in the global non-rotating reference frame O to the blade element fixed coordinate system b. Goulos *et al.* (Ref. 77) proposed the following definition of $\left[T_i^b\right]$

$$\left[T_i^b\right] = \begin{bmatrix} 1 & 0 & 0 \\ 0 & -1 & 0 \\ 0 & 0 & -1 \end{bmatrix} [\theta_c]\,[\beta]\,[\zeta]\,[\phi]\,[\theta_{tw}]\,[\lambda]\,[A_i] \tag{3.6}$$

where $[\theta_c]$, $[\beta]$, $[\zeta]$, $[\phi]$, $[\theta_{tw}]$, and $[\lambda]$ are blade element cyclic pitch, flap, lag, torsion, pretwist, and sweep rotation matrices respectively. The individual rotation matrices are defined as

$$[\theta_c] = \begin{bmatrix} 0 & 0 & 0 \\ 0 & \cos\theta_c\,(t) & \sin\theta_c\,(t) \\ 0 & -\sin\theta_c\,(t) & \cos\theta_c\,(t) \end{bmatrix} \tag{3.7}$$

$$[\beta] = \begin{bmatrix} \cos\beta\,(r,t) & 0 & \sin\beta\,(r,t) \\ 0 & 1 & 0 \\ -\sin\beta\,(r,t) & 0 & \cos\beta\,(r,t) \end{bmatrix} \tag{3.8}$$

$$[\zeta] = \begin{bmatrix} \cos\zeta(r,t) & -\sin\zeta(r,t) & 0 \\ \sin\zeta(r,t) & \cos\zeta(r,t) & 0 \\ 0 & 0 & 1 \end{bmatrix} \tag{3.9}$$

$$[\phi] = \begin{bmatrix} 0 & 0 & 0 \\ 0 & \cos\phi(r,t) & \sin\phi(r,t) \\ 0 & -\sin\phi(r,t) & \cos\phi(r,t) \end{bmatrix} \tag{3.10}$$

$$[\theta_{tw}] = \begin{bmatrix} 0 & 0 & 0 \\ 0 & \cos\theta_{tw}(r) & \sin\theta_{tw}(r) \\ 0 & -\sin\theta_{tw}(r) & \cos\theta_{tw}(r) \end{bmatrix} \tag{3.11}$$

$$[\lambda] = \begin{bmatrix} \cos\lambda(r) & -\sin\lambda(r) & 0 \\ \sin\lambda(r) & \cos\lambda(r) & 0 \\ 0 & 0 & 1 \end{bmatrix} \tag{3.12}$$

$\theta_c(t)$, $\beta(r,t)$, $\zeta(r,t)$, $\phi(r,t)$, $\theta_{tw}(r)$, and $\lambda(r)$ are the cyclic, equivalent flap, equivalent lag, torsion, geometrical twist, and back sweep angles. θ_c, θ_{tw}, and ϕ are considered positive for nose-up rotations. The equivalent flap and lag angles are later defined in Section 3.3, and thus, further details are not given at this point. It is noted that Eq. (3.6) is valid for a blade configuration where the cyclic pitch is applied inboard of the rotor root/hinge. An alternative formulation of $\left[T_i^b\right]$ for blades with outboard application of cyclic pitch was proposed by Goulos *et al.* (Ref. 77) as

$$\left[T_i^b\right] = \begin{bmatrix} 1 & 0 & 0 \\ 0 & -1 & 0 \\ 0 & 0 & -1 \end{bmatrix} [\zeta(eR,t)]^{-1} [\beta(eR,t)]^{-1} [\theta_c] [\beta] [\zeta] [\phi] [\theta_{tw}] [\lambda] [A_i] \tag{3.13}$$

An additional cross-sectional reference frame is used for the structural dynamics formulation. Figure 3.2b shows its definition and its relation with the rotating reference frame A_i. This cross-sectional reference frame differs from the blade element fixed coordinate system b in the sign convention of its major and minor axes. The major axis η is considered positive when moving towards the leading edge, while the minor axis ζ is positive when moving upwards, completing the orthogonal system.

3.2 Structural Dynamics Model

This section presents a mathematical formulation for the rapid estimation of the coupled vibration characteristics of helicopter rotor blades. It is capable of modelling the coupled flap/lag bending and torsion natural frequencies and mode shapes of non-uniform rotor blades. The method is based on the deployment of Lagrange's equation of motion to the three-dimensional kinematics of rotor blades. It uses mode shapes derived from classical beam and torsional theories as assumed deformation functions. These better approximate the actual deformation of the blade, accelerating the convergence of the method. As a result, the computational efficiency of the method is considerably improved.

Closed form integral expressions for the kinetic and potential energies are formulated. Lagrange's equation of motion is deployed to obtain the set of second-order ordinary differential equations. The latter is transformed into a quadratic eigenvalue problem. Its solution comprises coupled natural frequencies and mode shapes of the rotor blade.

Figure 3.3 summarises the main features of the proposed methodology. The classical beam and torsional theories are utilised to obtain the assumed mode shapes. These require inertial properties, structural properties, general dimensions, and structural boundary conditions as inputs. The derived assumed mode shapes are deployed along with blade properties, operating conditions, blade kinematics, and strain-displacement relations to fill the mass, gyroscopic, and stiffness matrices. These form the quadratic eigenvalue problem, which is solved to obtain the final natural frequencies and mode shapes.

3.2.1 Derivation of assumed deformation functions

A set of assumed deformation functions is required for each degree of freedom (DOF) within the Lagrangian formulation to derive the expressions of the kinetic and strain energies. Goulos *et al.* (Ref. 76) reported the benefits of the deployment of mode shapes derived from Bernoulli-Euler beam and classical torsional vibration theories as assumed deformation functions. To efficiently impose the structural boundary conditions, an effective modal coordinate $x = r - eR$, $x \in (0, L)$ is defined. Where $r \in (eR, R)$ is the local blade radius, e is the ratio between the hinge/root offset from the center of the rotor hub and the blade tip radius R, and $L = R(1 - e)$ is the actual blade length.

The classical Bernoulli-Euler beam theory (Eq. (3.14)) represents the time-dependent evolution of the transverse displacement $w(x,t)$ of a non-rotating beam with variable bending stiffness $EI(x)$, mass per unit length $\rho A(x)$, and load per unit length $P(x,t)$. The classical torsional theory (Eq. (3.15)) defines the time-dependent evolution of the torsion angle $\theta(x,t)$ for a non-rotating beam with variable torsional rigidity $GJ(x)$, polar moment of inertia $I_p(x)$, and torsional moment loads per unit length $M(x,t)$.

$$\frac{\partial^2}{\partial x^2}\left(EI(x)\frac{\partial^2 w(x,t)}{\partial x^2}\right) + \rho A(x)\frac{\partial^2 w(x,t)}{\partial t^2} = P(x,t) \tag{3.14}$$

$$\frac{\partial}{\partial x}\left(GJ(x)\frac{\partial \theta(x,t)}{\partial x}\right) + M(x,t) = I_p(x)\frac{\partial^2 \theta(x,t)}{\partial t^2} \tag{3.15}$$

Uniform structural properties and zero external forcing are assumed to simplify Eqs. (3.14) and (3.15). The application of separation of variables to the latter leads to the spatial solutions for transverse displacement $\Phi(x)$ and torsional deformation angle $\Theta(x)$

$$\Phi(x) = A_\Phi \sin\beta x + B_\Phi \cos\beta x + C_\Phi \sinh\beta x + D_\Phi \cosh\beta x \tag{3.16}$$

$$\Theta(x) = A_\Theta \cos\gamma x + B_\Theta \sin\gamma x \tag{3.17}$$

where β and γ are the frequency parameters for transverse displacement and torsional deformation respectively. A_Φ, B_Φ, C_Φ,D_Φ, A_Θ, and B_Θ are constants of integration determined through application of structural boundary conditions. Goulos *et al.* (Ref. 76) provided closed form expressions for the ratios between the constants of integration and frequency parameters for different boundary conditions. These include: hingeless, freely-hinged articulated, spring-hinged articulated rotor blades, and rotor blade pitch-control system with finite and infinite torsional stiffness.

The application of this procedure to flap, lag, and torsion results in the derivation of N assumed deformation functions per DOF. The deformation functions, calculated for a non-rotating beam with constant properties, satisfy the structural boundary conditions and exhibit orthogonality between each other. The deformation functions and their spatial derivatives are utilised within the Lagrangian formulation to better approximate the actual coupled mode shapes for rotating non-uniform rotor blades with coupled modes of vibration. These functions are expressed in partition vector form as $\left\{\psi^\phi(x)\right\} = [\Theta_i(x),\, i = 1,\ldots N]^T$, $\{\psi^v(x)\} = [\Phi_i^v(x),\, i = 1,\ldots N]^T$, and $\{\psi^w(x)\} = [\Phi_i^w(x),\, i = 1,\ldots N]^T$ for torsion, lag, and flap respectively. The deformation function subscript $i \in [1,\ldots N]$ refers to the ith

assumed deformation function. Similarly, the first and second spatial derivatives can be obtained in closed-form expressions. The analytical nature of these spatial derivatives bypasses the generation of numerical errors associated with numerical derivation. The spatial derivatives are expressed as the vectors $\{\psi'^r(x)\}$ and $\{\psi''^r(x)\}$, where the superscript $r \in [\phi, v, w]$ is denominated DOF index and refers to the DOF associated with the partition vector: ϕ, v, and w for torsion, lag, and flap respectively.

3.2.2 Lagrangian formulation for rotor blade dynamics

Lagrange's equation of motion. The proposed formulation accounts for inertial and elastic coupling between torsional deformation, chordwise displacement, and flapwise displacement. Lagrange's equation of motion, which is defined in Eq. (3.18), is applied to torsion, lag, and flap independently. In Eq. (3.18), T and U are the kinetic and strain energies of the complete system, Q_i^r is the generalised external force or moment, and q_i^r is the time-dependent generalised coordinate. Once again, the superscript $r \in [\phi, v, w]$ refers to the DOF index and the subscript $i \in [1, \dots N]$ the assumed deformation function index.

$$\frac{\mathrm{d}}{\mathrm{d}t}\left(\frac{\partial T}{\partial \dot{q}_i^r}\right) - \frac{\partial T}{\partial q_i^r} + \frac{\partial U}{\partial q_i^r} = Q_i^r, \quad i = 1, ...N \tag{3.18}$$

The generalised coordinates are expressed as $\{q^r(t)\} = [q_i^r(t),\, i = 1, \dots N]^T$, while the transverse displacements and torsional deformation are expressed as the dot products of the assumed deformation functions and the generalised coordinates vectors.

$$\phi(x,t) = \left\{\psi^\phi(x)\right\} \cdot \left\{q^\phi(t)\right\} \tag{3.19a}$$
$$v(x,t) = \{\psi^v(x)\} \cdot \{q^v(t)\} \tag{3.19b}$$
$$w(x,t) = \{\psi^w(x)\} \cdot \{q^w(t)\} \tag{3.19c}$$

The calculation of the rotor blade modal characteristics does not require the inclusion of external loads in the analysis. Consequently, the calculation of the generalised external force/moment, Q_i^r, is not necessary and the term is eliminated from Eq. (3.18).

Frames of reference. Transverse displacements and torsional deformation of the rotor blade are expressed in A_i, a frame of reference fixed to the blade with origin at the root/hinge. This frame of reference differs from the previously defined A_i in two aspects: zero ζ_{pre} presweep and θ_0 collective angles are assumed. The position vector of an arbitrary point p on the elastic axis before deformation is $\tilde{r}^{A_i}_{p/A_i,0} = [x\ 0\ 0]^T$. After the deformation,

the same point is located at $\tilde{r}^{A_i}_{p/A_i,1} = [x + u\ v\ w]^T$ where u, v, and w are the axial, chordwise, and flapwise displacements of p in $\tilde{e}^{A_i}_x$, $\tilde{e}^{A_i}_y$, and $\tilde{e}^{A_i}_z$ respectively. An additional cross-section reference frame defined in Section 3.1 is used to account for the deviation of the generic point from the elastic axis along the major, η, and minor, ζ, axes, and the change in orientation of the latter due to pretwist θ and torsional deformation ϕ.

Strain Energy. The application of Lagrange's equation of motion requires the formulation of the strain energy as a function of the generalised coordinates and the assumed deformation functions. Based on the assumption of uniaxial stress and the validity of the generalised Hooke's law, the strain energy is defined as

$$U = \frac{1}{2}\int_0^L \iint_A \left(E\epsilon_{xx}^2 + E\epsilon_{x\eta}^2 + E\epsilon_{x\zeta}^2\right) \mathrm{d}\zeta\, \mathrm{d}\eta\, \mathrm{d}x + \frac{1}{2}\left(K^{\phi}\phi_0^2 + K^{v}v_0'^2 + K^{w}w_0'^2\right) \quad (3.20)$$

where ϵ_{xx}, $\epsilon_{x\eta}$, and $\epsilon_{x\zeta}$ are the classical strain components, E and G are the material Young and shear stress moduli, ϕ_0 is the torsional deformation at the root/hinge, and v_0' and w_0' are the linearised chordwise and flapwise angular deformations of the hinge springs. The last group of terms on Eq. (3.20) is introduced to account for the extra strain energy due to the presence of discrete springs with $K^{v/w}$ stiffness and/or a pitch-control system with finite torsional stiffness K^{ϕ} at the root or hinge location. These discrete springs, characteristic of spring-hinged articulated rotors, contribute to the overall strain energy of the system. However, for hingeless or freely-hinged articulated rotors these terms vanish.

A series of assumptions reduce the strain-displacement relations developed by Hodges and Dowel (Ref. 49) to the classical strain components ϵ_{xx}, $\epsilon_{x\eta}$, and $\epsilon_{x\zeta}$ used in this formulation. The assumption of uniaxial stress simplifies the actual blade to a long, straight, slender, homogeneous, isotropic beam undergoing moderate displacements. For the purpose of this work, the effect of cross-section's warp is neglected, the expressions are reduced to second order, and the trigonometric functions containing the torsion angle are approximated with Maclaurin series expansions of second order. The resulting strain components are defined in Eq. (3.21) where $(\,)'$ and $(\,)''$ represent the first and second derivative with respect to x.

$$\begin{aligned}\epsilon_{xx} &= u' + \frac{v'^2}{2} + \frac{w'^2}{2} + \left(\eta^2+\zeta^2\right)\left(\theta'\phi' + \frac{\phi'^2}{2}\right) \\ &\quad - \left(v'' + w''\phi - v''\frac{\phi^2}{2}\right)(\eta\cos\theta - \zeta\sin\theta) \\ &\quad - \left(w'' - v''\phi - w''\frac{\phi^2}{2}\right)(\eta\sin\theta + \zeta\cos\theta)\end{aligned} \tag{3.21a}$$

$$\epsilon_{x\eta} = -\zeta\phi' \tag{3.21b}$$

$$\epsilon_{x\zeta} = \eta\phi' \tag{3.21c}$$

The axial displacement $u = \int_0^x u' \mathrm{d}\lambda$ is expressed as a function of the transverse displacements v and w and torsion angle ϕ through application of Eq. (3.22). This equation is an adaptation of the methodology used in Ref. 49 based on the deployment of the final equilibrium force equation on the axial direction.

$$\begin{aligned}u' = &\frac{\int_x^L m\Omega^2(\varrho + eR)\mathrm{d}\varrho}{EA} - \frac{1}{2}v'^2 - \frac{1}{2}w'^2 - \frac{J}{A}\theta'\phi' \\ &+ e_A v''\cos\theta + e_A w''\sin\theta - e_A v''\phi\sin\theta + e_A w''\phi\cos\theta\end{aligned} \tag{3.22}$$

where

$$\begin{aligned}&A = \iint_A \mathrm{d}\zeta\,\mathrm{d}\eta && m = \iint_A \rho\,\mathrm{d}\zeta\,\mathrm{d}\eta && me_M = \iint_A \rho\eta\,\mathrm{d}\zeta\,\mathrm{d}\eta \\ &B_1^* = \iint_A \left(\eta^2+\zeta^2\right)^2\mathrm{d}\zeta\,\mathrm{d}\eta && B_2^* = \iint_A \eta\left(\eta^2+\zeta^2\right)\mathrm{d}\zeta\,\mathrm{d}\eta && Ae_A = \iint_A \eta\,\mathrm{d}\zeta\,\mathrm{d}\eta \\ &I_y = \iint_A \zeta^2\,\mathrm{d}\zeta\,\mathrm{d}\eta && I_z = \iint_A \eta^2\,\mathrm{d}\zeta\,\mathrm{d}\eta && J = \iint_A \left(\eta^2+\zeta^2\right)\mathrm{d}\zeta\,\mathrm{d}\eta \\ &I_1 = \iint_A \rho\zeta^2\,\mathrm{d}\zeta\,\mathrm{d}\eta && I_2 = \iint_A \rho\eta^2\,\mathrm{d}\zeta\,\mathrm{d}\eta && I_p = \iint_A \rho\left(\eta^2+\zeta^2\right)\mathrm{d}\zeta\,\mathrm{d}\eta\end{aligned} \tag{3.23}$$

Equation (3.22) deploys cross-sectional integrals defined in Eq. (3.23). These integrals, which are functions of the material density ρ and the cross-sectional major η and minor ζ axes coordinates, are evaluated only over the structurally effective cross-sectional area. A is the cross-sectional area carrying tension, m is the blade mass per unit length, e_m and e_A are the offsets of the mass and area centroids from the elastic axis respectively, I_y and I_z are the flapwise and chordwise area moments of inertia respectively, I_1 and I_2 are the flapwise and chordwise mass moments of inertia respectively, J is the cross-sectional polar moment of inertia, I_p is the cross-sectional mass polar moment of inertia, and B_1^* and B_2^* are section constants equivalent to those of Refs. 49 and 47. It is noted

that in order to not overcomplicate the formulation with low order of magnitude terms, the cross-section is assumed to be symmetric about the major axis η. This essentially eliminates the cross-sectional integrals of odd-degree ζ polynomials. In Eq. (3.22) the first three terms have the most relevant effect on the axial displacement. The first term is directly associated with centrifugal stiffening while the following two terms are associated with the effect of transverse dislocations on the axial extension.

The final strain energy expresssion is derived by inserting Eqs. (3.21) and (3.22) into Eq. (3.20) and expressing the transverse displacement and torsional deformation as the dot products of the assumed deformation functions and the generalised coordinate vectors (Eq. (3.19)). The proposed methodology targets the rapid estimation of helicopter rotor blade vibration characteristics. To accomplish computational efficiency and make it suitable for preliminary design, the products of v, w, and/or ϕ of third degree or higher are neglected. Additionally, flap and lead-lag hinges are assumed to be coincident and their position determines the actual length of the blade L.

Kinetic energy. The second contributor to the overall energy of the system is the kinetic energy. The kinetic energy is defined in Eq. (3.24) as half of the volume integral of the density ρ times the dot product of the absolute velocity vector $\tilde{u}^{A_i}_{p/0}$ of an arbitrary point p. The latter, defined in Eq. (3.25), comprises the following terms expressed in the blade fixed reference frame A_i: the linear velocity of the root or hinge $\tilde{u}^{A_i}_{A_i}$, the deformed position vector $\tilde{r}^{A_i}_{p/A_i}$, the time derivative of the deformation position vector $\frac{\partial \tilde{r}^{A_i}_{p/A_i}}{\partial t}$, and the angular velocity vector $\tilde{\omega}^{A_i}_{A_i}$; where $\tilde{u}^{A_i}_{A_i}$ and $\tilde{\omega}^{A_i}_{A_i}$ are defined in Eqs. (3.26) and (3.27) in terms of the rotor speed Ω, root or hinge offset eR and precone angle β_{pre}

$$T = \frac{1}{2}\int_0^L \iint_A \rho \tilde{u}^{A_i}_{p/0} \cdot \tilde{u}^{A_i}_{p/0}\, \mathrm{d}\zeta\, \mathrm{d}\eta\, \mathrm{d}x \tag{3.24}$$

$$\tilde{u}^{A_i}_{p/0} = \tilde{u}^{A_i}_{A_i} + \frac{\partial \tilde{r}^{A_i}_{p/A_i}}{\partial t} + \tilde{\omega}^{A_i}_{A_i} \times \tilde{r}^{A_i}_{p/A_i} \tag{3.25}$$

$$\tilde{u}^{A_i}_{A_i} = [A_i]\left(\tilde{\omega}_{A_i} \times \tilde{r}_{A_i/O}\right) = [0 \quad \Omega e R \quad 0]^T \tag{3.26}$$

$$\tilde{\omega}^{A_i}_{A_i} = [A_i]\,\tilde{\omega}_{A_i} = [\Omega \sin\beta_{pre} \quad 0 \quad \Omega\cos\beta_{pre}]^T \tag{3.27}$$

The deformed position vector $\tilde{r}^{A_i}_{p/A_i}$ of an arbitrary point p is based on the kinematic expressions derived by Hodges and Dowel (Ref. 49) for a long, straight beam undergoing

moderate displacements. Warping is neglected and trigonometric functions containing the torsion angle are approximated using second order Maclaurin series expansions. The resulting expression for the position vector $\tilde{r}^{A_i}_{p/A_i}$ is defined as

$$\tilde{r}^{A_i}_{p/A_i} = \left\{ \begin{array}{c} x + u - (v' + w'\phi)[\eta\cos\theta - \zeta\sin\theta] - (w' - v'\phi)[\eta\sin\theta + \zeta\cos\theta] \\ v + [\eta\cos\theta - \zeta\sin\theta] - \phi[\eta\sin\theta + \zeta\cos\theta] - \frac{\phi^2}{2}[\eta\cos\theta - \zeta\sin\theta] \\ w + [\eta\sin\theta + \zeta\cos\theta] + \phi[\eta\cos\theta - \zeta\sin\theta] - \frac{\phi^2}{2}[\eta\sin\theta + \zeta\cos\theta] \end{array} \right\} \quad (3.28)$$

The final kinetic energy expression is derived by inserting Eqs. (3.25)-(3.28) into Eq. (3.24), and expressing the transverse displacement and torsional deformation as the dot products of the assumed deformation functions and the generalised coordinate vectors. Once again, the products of v, w, and ϕ of third degree or higher are neglected, and the flap and lag hinges are assumed to be coincident. However, the precone angle's trigonometric functions are approximated using Maclauring series expansions of first order.

3.2.3 Eigenproblem

Once the strain and kinetic energies have been formulated, the transverse displacements and torsional deformation are replaced by the equivalent products of assumed deformation functions and generalised coordinates (Eq. 3.19). This results in the final expressions of the kinetic and strain energies. The application of Lagrange's equation of motion (Eq. 3.18) to the strain and kinetic energies expressions leads to the following second order system of ordinary differential equations

$$\begin{bmatrix} \vdots \\ \cdots \ \left[M^{r,s}_{i,j}\right] \ \cdots \\ \vdots \end{bmatrix} \begin{Bmatrix} \vdots \\ \{\ddot{q}^r_i\} \\ \vdots \end{Bmatrix} + \begin{bmatrix} \vdots \\ \cdots \ \left[C^{r,s}_{i,j}\right] \ \cdots \\ \vdots \end{bmatrix} \begin{Bmatrix} \vdots \\ \{\dot{q}^r_i\} \\ \vdots \end{Bmatrix} + \left(\begin{bmatrix} \vdots \\ \cdots \ \left[F^{r,s}_{i,j}\right] \ \cdots \\ \vdots \end{bmatrix} + \begin{bmatrix} \vdots \\ \cdots \ \left[G^{r,s}_{i,j}\right] \ \cdots \\ \vdots \end{bmatrix} \right) \begin{Bmatrix} \vdots \\ \{q^r_i\} \\ \vdots \end{Bmatrix} = \begin{Bmatrix} \vdots \\ \{f^r_i\} \\ \vdots \end{Bmatrix} \quad (3.29)$$

or

$$[M]\{\ddot{q}\} + [C]\{\dot{q}\} + [S]\{q\} = \{f\} \quad (3.30)$$

where $[M]$, $[C]$, and $[S]$ are the mass, damping, and overall stiffness intermodal coupling matrices. The overall stiffness intermodal coupling matrix $[S]$ comprises contributions

of two different natures: structural stiffening $[G]$ and centrifugal stiffening $[F]$. $\{f\}$ is denominated external static loading forcing vector. $\{q\}$, $\{\dot{q}\}$, and $\{\ddot{q}\}$ are the generalised coordinates vector and its first and second time derivatives, respectively. In Eq. (3.29), the DOF superscripts r and s refer to a partition number (row or column) that corresponds to a DOF (ϕ for torsion, v for lag, and w for flap). It is noted that consecutive integers (1,2, and 3) are used as DOF indices in the mathematical implementation of the model. However, the use of ϕ, v, and w simplifies the description. The mode subscripts i and j correspond to row/column indices within each partition matrix. Thus, $M_{i,j}^{r,s}$ gives the mass intermodal coupling coefficient of the ith assumed deformation function of the r DOF with the jth assumed deformation function of the s DOF. It is noted that these coefficients are exclusively functions of x.

At this point, each of the above matrices is derived. The mass intermodal coupling matrix $[M]$ is symmetric and positive definite. It is associated with the kinetic energy due to time-variations of the elastic deformation of the blade. The individual components of the $[M]$ matrix are defined as follows:

$$M_{i,j}^{\phi,\phi} = \int_0^L m \int_0^x \frac{J}{A}\theta'\psi_i' \mathrm{d}\lambda \int_0^x \frac{J}{A}\theta'\psi_j' \mathrm{d}\lambda \mathrm{d}x + \int_0^L I_p \psi_i \psi_j \mathrm{d}x \tag{3.31}$$

$$M_{i,j}^{\phi,v} = M_{j,i}^{v,\phi} = \int_0^L m \left(-e_M \sin\theta \psi_i \psi_j + \int_0^x \frac{J}{A}\theta'\psi_i' \mathrm{d}\lambda \left(e_M \cos\theta \psi_j' - \int_0^x e_A \cos\theta \psi_j'' \mathrm{d}\lambda \right) \right) \mathrm{d}x \tag{3.32}$$

$$M_{i,j}^{\phi,w} = M_{j,i}^{w,\phi} = \int_0^L m \left(e_M \cos\theta \psi_i \psi_j + \int_0^x \frac{J}{A}\theta'\psi_i' \mathrm{d}\lambda \left(e_M \sin\theta \psi_j' - \int_0^x e_A \sin\theta \psi_j'' \mathrm{d}\lambda \right) \right) \mathrm{d}x \tag{3.33}$$

$$\begin{aligned} M_{i,j}^{v,v} = \int_0^L m \Bigg(& \psi_i \psi_j + \int_0^x e_A \psi_i'' \cos\theta \mathrm{d}\lambda \int_0^x e_A \psi_j'' \cos\theta \mathrm{d}\lambda \\ & - m e_M \cos\theta \left(\psi_i' \int_0^x e_A \psi_j'' \cos\theta \mathrm{d}\lambda + \psi_j' \int_0^x e_A \psi_i'' \cos\theta \mathrm{d}\lambda \right) \Bigg) \mathrm{d}x \\ & + \int_0^L \psi_i' \psi_j' \left(I_2 \cos^2\theta + I_1 \sin^2\theta \right) \mathrm{d}x \end{aligned} \tag{3.34}$$

$$\begin{aligned} M_{i,j}^{v,w} = M_{j,i}^{w,v} = \int_0^L m \Bigg(& \int_0^x e_A \cos\theta \psi_i'' \mathrm{d}\lambda \int_0^x e_A \sin\theta \psi_j'' \mathrm{d}\lambda - \psi_i' e_M \cos\theta \int_0^x e_A \sin\theta \psi_j'' \mathrm{d}\lambda \\ & - \psi_j' e_M \sin\theta \int_0^x e_A \cos\theta \psi_i'' \mathrm{d}\lambda \Bigg) \mathrm{d}x + \frac{1}{2} \int_0^L \psi_i' \psi_j' \sin 2\theta \, (I_2 - I_1) \mathrm{d}x \end{aligned} \tag{3.35}$$

$$M_{i,j}^{w,w} = \int_0^L m \left(\psi_i \psi_j + \int_0^x e_A \psi_i'' \sin\theta \mathrm{d}\lambda \int_0^x e_A \psi_j'' \sin\theta \mathrm{d}\lambda \right. \\ \left. - e_M \sin\theta \left(\psi_i' \int_0^x e_A \psi_j'' \sin\theta \mathrm{d}\lambda + \psi_j' \int_0^x e_A \psi_i'' \sin\theta \mathrm{d}\lambda \right) \right) \mathrm{d}x \\ + \int_0^L \psi_i' \psi_j' \left(I_2 \sin^2\theta + I_1 \cos^2\theta \right) \mathrm{d}x \tag{3.36}$$

The damping matrix $[C]$ is proportional to the rotational speed of the rotor Ω. It is anti-symmetric and related to the effect of Coriolis acceleration. The latter generates accelerations normal to the rotation axis and the velocity of the body. Thus, radial dislocations in the flap direction produce accelerations in the lead-lag direction and vice versa. Due to the anti-symmetry of the matrix, it does not introduce real structural or material damping and effectively acts as a rotating matrix. Therefore, the term gyroscopic will be used instead of damping within the following sections. The individual components of the $[C]$ matrix are defined as follows:

$$C_{i,j}^{\phi,\phi} = 2\Omega \int_0^L m e_M \sin\theta \left(\psi_i \int_0^x \frac{J}{A} \theta' \psi_j' \mathrm{d}\lambda - \psi_j \int_0^x \frac{J}{A} \theta' \psi_i' \mathrm{d}\lambda \right) \mathrm{d}x \tag{3.37}$$

$$C_{i,j}^{\phi,v} = -C_{j,i}^{v,\phi} = 2\Omega \int_0^L m \left(\psi_i e_M \left(\psi_j \beta_{pre} \cos\theta - \sin\theta \int_0^x e_A \psi_j'' \cos\theta \mathrm{d}\lambda \right) \right. \\ \left. + \psi_j \int_0^x \frac{J}{A} \theta' \psi_i' \mathrm{d}\lambda \right) \mathrm{d}x + \Omega \int_0^L \psi_i \psi_j' \sin 2\theta (I_2 - I_1) \mathrm{d}x \tag{3.38}$$

$$C_{i,j}^{\phi,w} = -C_{j,i}^{w,\phi} = 2\Omega \int_0^L m \psi_i e_M \sin\theta \left(\beta_{pre} \psi_j - \int_0^x e_A \psi_j'' \sin\theta \mathrm{d}\lambda \right) \mathrm{d}x \\ + 2\Omega \int_0^L \psi_i \psi_j' \left(I_2 \sin^2\theta + I_1 \cos^2\theta \right) \mathrm{d}x \tag{3.39}$$

$$C_{i,j}^{v,v} = 2\Omega \int_0^L m \left(\left(\psi_i' \psi_j - \psi_i \psi_j' \right) e_M \cos\theta + \psi_i \int_0^x e_A \psi_j'' \cos\theta \mathrm{d}\lambda - \psi_j \int_0^x e_A \psi_i'' \cos\theta \mathrm{d}\lambda \right) \mathrm{d}x \tag{3.40}$$

$$C_{i,j}^{v,w} = -C_{j,i}^{w,v} = -2\Omega \int_0^L m \psi_i \left(\psi_j \beta_{pre} + \psi_j' e_M \sin\theta - \int_0^x e_A \psi_j'' \sin\theta \mathrm{d}\lambda \right) \mathrm{d}x \tag{3.41}$$

$$C_{i,j}^{w,w} = 0 \tag{3.42}$$

The centrifugal stiffening matrix $[F]$, which is proportional to Ω^2, is symmetric and positive definite. It quantifies the stiffening of the blade due to the centrifugal force acting on it. The individual components of the $[F]$ matrix are defined as follows:

$$F_{i,j}^{\phi,\phi} = -\Omega^2 \int_0^L m \left(\int_0^x \frac{J}{A}\theta'\psi_i' \mathrm{d}\lambda \int_0^x \frac{J}{A}\theta'\psi_j' \mathrm{d}\lambda + e_M \beta_{pre} \left(\psi_i \psi_j \sin\theta \left(x + x_T + eR\right) + \cos\theta \left(\psi_i \int_0^x \frac{J}{A}\theta'\psi_j' \mathrm{d}\lambda + \psi_j \int_0^x \frac{J}{A}\theta'\psi_i' \mathrm{d}\lambda \right) \right) \right) \mathrm{d}x + \Omega^2 \int_0^L \psi_i \psi_j \cos 2\theta \left(I_2 - I_1\right) \mathrm{d}x \tag{3.43}$$

$$\begin{aligned} F_{i,j}^{\phi,v} = F_{j,i}^{v,\phi} = -\Omega^2 \int_0^L m \Bigg(& \psi_i e_M \sin\theta \left(\psi_j' \left(x + x_T + eR\right) - \psi_j \right) + \psi_j' e_M \cos\theta \int_0^x \frac{J}{A}\theta'\psi_i' \mathrm{d}\lambda \\ & - \int_0^x e_A \psi_i \psi_j'' \sin\theta \mathrm{d}\lambda \left(x + x_T + eR - \beta_{pre} e_M \sin\theta\right) \\ & - \int_0^x e_A \psi_j'' \cos\theta \mathrm{d}\lambda \left(\int_0^x \frac{J}{A}\theta'\psi_i' \mathrm{d}\lambda + \psi_i e_M \beta_{pre} \cos\theta \right) \Bigg) \mathrm{d}x \\ & - \Omega^2 \int_0^L \psi_i \psi_j' \beta_{pre} \cos 2\theta \left(I_2 - I_1\right) \mathrm{d}x \end{aligned} \tag{3.44}$$

$$\begin{aligned} F_{i,j}^{\phi,w} = F_{j,i}^{w,\phi} = & \\ -\Omega^2 \int_0^L m \Bigg(& \psi_i e_M \cos\theta \left(\psi_j \beta_{pre}^2 - \psi_j' \left(x + x_T + eR\right) - \beta_{pre} \int_0^x e_A \psi_j'' \sin\theta \mathrm{d}\lambda \right) \\ & + \left(x + x_T + eR - e_M \beta_{pre} \sin\theta\right) \int_0^x e_A \psi_i \psi_j'' \cos\theta \mathrm{d}\lambda \\ & + \int_0^x \frac{J}{A}\theta'\psi_i' \mathrm{d}\lambda \left(\psi_j \beta_{pre} + \psi_j' e_M m \sin\theta - \int_0^x e_A \psi_j'' \sin\theta \mathrm{d}\lambda \right) \Bigg) \mathrm{d}x \\ & - \Omega^2 \int_0^L \psi_i \psi_j' \beta_{pre} \sin 2\theta (I_2 - I_1) \mathrm{d}x \end{aligned} \tag{3.45}$$

$$\begin{aligned} F_{i,j}^{v,v} = -\Omega^2 \int_0^L m \Bigg(& \psi_i \psi_j - \left(x + x_T + eR - \beta_{pre} e_M \sin\theta\right) \int_0^x \psi_i' \psi_j' \, \mathrm{d}\lambda \\ & + \int_0^x e_A \psi_i'' \cos\theta \mathrm{d}\lambda \int_0^x e_A \psi_j'' \cos\theta \mathrm{d}\lambda \\ & - e_M \cos\theta \left(\psi_i' \int_0^x e_A \psi_j'' \cos\theta \mathrm{d}\lambda + \psi_j' \int_0^x e_A \psi_i'' \cos\theta \mathrm{d}\lambda \right) \Bigg) \mathrm{d}x \\ & - \Omega^2 \int_0^L \psi_i' \psi_j' \big(I_2 \cos^2\theta + I_1 \sin^2\theta \big) \mathrm{d}x \end{aligned} \tag{3.46}$$

$$F_{i,j}^{v,w} = F_{j,i}^{w,v} = -\Omega^2 \int_0^L m \left(\psi_i' e_M \cos\theta \left(\psi_j \beta_{pre} - \int_0^x e_A \psi_j'' \sin\theta \mathrm{d}\lambda \right) - \int_0^x e_A \psi_i'' \cos\theta \mathrm{d}\lambda \left(\psi_j \beta_{pre} + \psi_j' e_M \sin\theta - \int_0^x e_A \psi_j'' \sin\theta \mathrm{d}\lambda \right) \right) \mathrm{d}x - \frac{1}{2}\Omega^2 \int_0^L \psi_i' \psi_j' \sin 2\theta (I_2 - I_1) \mathrm{d}x \tag{3.47}$$

$$\begin{aligned} F_{i,j}^{w,w} = -\Omega^2 \int_0^L m \Bigg(& -\int_0^x \psi_i' \psi_j' \, \mathrm{d}\lambda (x + x_T + eR - \beta_{pre} e_M \sin\theta) \\ & + e_M \beta_{pre} \sin\theta \left(\psi_i' \psi_j + \psi_j' \psi_i \right) - \psi_i \psi_j \beta_{pre}^2 - \int_0^x e_A \psi_j'' \sin\theta \mathrm{d}\lambda \left(\psi_i \beta_{pre} + \psi_i' e_M \sin\theta \right) \\ & - \int_0^x e_A \psi_i'' \sin\theta \mathrm{d}\lambda \left(\psi_j \beta_{pre} + \psi_j' e_M \sin\theta \right) + \int_0^x e_A \psi_i'' \sin\theta \mathrm{d}\lambda \int_0^x e_A \psi_j'' \sin\theta \mathrm{d}\lambda \Bigg) \mathrm{d}x \\ & - \Omega^2 \int_0^L \psi_i' \psi_j' \left(I_2 \sin^2\theta + I_1 \cos^2\theta \right) \mathrm{d}x \end{aligned} \tag{3.48}$$

The structural stiffening matrix $[G]$ is associated with the elastic potential energy of the blade. It is symmetric and positive definite. The individual components of the $[G]$ matrix are defined as follows:

$$G_{i,j}^{\phi,\phi} = \int_0^L \left(GJ + \frac{J}{A} \int_x^L m\Omega^2 (\lambda + eR) \mathrm{d}\lambda + E\theta'^2 \left(B_1^* - \frac{J^2}{A} \right) \right) \psi_i' \psi_j' \mathrm{d}x + K^\phi \psi_{i_0} \psi_{j_0} \tag{3.49}$$

$$G_{i,j}^{\phi,v} = G_{j,i}^{v,\phi} = -\int_0^L E\theta' \cos\theta \left(B_2^* - J e_A \right) \psi_i' \psi_j'' \mathrm{d}x \tag{3.50}$$

$$G_{i,j}^{\phi,w} = G_{j,i}^{w,\phi} = -\int_0^L E\theta' \sin\theta \left(B_2^* - J e_A \right) \psi_i' \psi_j'' \mathrm{d}x \tag{3.51}$$

$$G_{i,j}^{v,v} = \int_0^L E \left(I_y \sin^2\theta + \left(I_z - A e_A^2 \right) \cos^2\theta \right) \psi_i'' \psi_j'' \mathrm{d}x + K^v \psi_{i_0}' \psi_{j_0}' \tag{3.52}$$

$$G_{i,j}^{v,w} = G_{j,i}^{w,v} = \frac{1}{2} \int_0^L E \sin 2\theta \left(\left(I_z - A e_A^2 \right) - I_y \right) \psi_i'' \psi_j'' \mathrm{d}x \tag{3.53}$$

$$G_{i,j}^{w,w} = \int_0^L E \left(I_y \cos^2\theta + \left(I_z - A e_A^2 \right) \sin^2\theta \right) \psi_i'' \psi_j'' \mathrm{d}x + K^w \psi_{i_0}' \psi_{j_0}' \tag{3.54}$$

Finally, an external static forcing vector $\{f\}$ is obtained through the application of Lagrange's equation of motion to the kinetic energy of the system. This time-invariant vector represents the static deflection associated with the centrifugal force. The deviation of the mass centre of the blade from the radially outward location where the centrifugal load is applied generates this static deflection. Therefore, coupling parameters such as pretwist, precone, and offset between mass centre and elastic axis are effectively associated with the static vector $\{f\}$. It is noted that this vector does not influence the natural vibration characteristics of the rotor blade due to the steady nature of the forcing. The individual components of the $[f]$ vector are defined as follows:

$$\begin{aligned} f_i^{\phi} = -\Omega^2 \int_0^L m \Bigg(& (x + x_T + eR - \beta_{pre} e_M \sin\theta) \int_0^x \frac{J}{A} \theta' \psi_i' \mathrm{d}\lambda \\ & + (x + x_T + eR) \psi_i e_M \beta_{pre} \cos\theta \Bigg) \mathrm{d}x - \frac{1}{2}\Omega^2 \int_0^L \psi_i \sin 2\theta \, (I_2 - I_1) \mathrm{d}x \end{aligned} \tag{3.55}$$

$$\begin{aligned} f_i^{v} = \Omega^2 \int_0^L m \Bigg(& e_M \cos\theta \left(\psi_i - \psi_i' \left(x + x_T + eR\right)\right) \\ & + \int_0^x e_A \psi_i'' \cos\theta \mathrm{d}\lambda (x + x_T + eR - \beta_{pre} e_M \sin\theta) \Bigg) \mathrm{d}x \\ & + \frac{1}{2}\Omega^2 \int_0^L \psi_i' \beta_{pre} \sin 2\theta \, (I_2 - I_1) \mathrm{d}x \end{aligned} \tag{3.56}$$

$$\begin{aligned} f_i^{w} = -\Omega^2 \int_0^L m \Bigg(& (x + x_T + eR - \beta_{pre} e_M \sin\theta) \left(\psi_i \beta_{pre} - \int_0^x e_A \psi_i'' \sin\theta \mathrm{d}\lambda \right) \\ & + (x + x_T + eR) \psi_i' e_M \sin\theta \Bigg) \mathrm{d}x + \Omega^2 \int_0^L \psi_i' \beta_{pre} \left(I_2 \sin^2\theta + I_1 \cos^2\theta \right) \mathrm{d}x \end{aligned} \tag{3.57}$$

To obtain the natural frequencies and mode shapes of vibration, an eigenvalue problem is generated and solved. Inserting a generic solution of the form $\{q\} = \{\bar{q}\} \exp(\lambda t)$ in the homogeneous part of the second order system of linear differential equations defined in Eq. (3.30) leads to the following quadratic eigenvalue problem (QEP)

$$\left(\lambda^2 [M] + \lambda [C] + [S]\right) \{\bar{q}\} = [Q(\lambda)] \{\bar{q}\} = \{0\} \tag{3.58}$$

where λ represents an eigenvalue and $\{\bar{q}\}$ the associated eigenvector. The dimension of the λ-matrix $[Q(\lambda)]$ is $3N \times 3N$, where N is the number of assumed deformation functions per DOF. The symmetry of $[M]$ and $[S]$ and skew-symmetry of $[C]$ determine the spectrum

location of the $6N$ eigenvalues in the complex plane. The eigenvalues are purely imaginary ($\Re(\lambda) = 0$) and symmetrically located with respect to the real axis as reported in Ref. 185. Hence, the eigenvalues and eigenvectors occur in pairs of conjugate complex numbers λ, $\overline{\lambda}$ and $\{\bar{q}\}$, $\overline{\{\bar{q}\}}$. To solve the QEP, a first-order λ-matrix $[Q_2(\lambda)] = [A] - \lambda[B]$ of dimensions $6N \times 6N$ is generated. This λ-matrix, called a linearisation of $[Q(\lambda)]$, constitutes the basis of the following generalised eigenvalue problem (GEP)

$$[Q_2(\lambda)]\{\bar{q}_2\} = ([A] - \lambda[B])\{\bar{q}_2\} = \{0\} \tag{3.59}$$

The applied linearisation is not unique, and the most computationally efficient linearisation needs to be chosen. Due to the aforementioned properties, a Hamiltonian/skew-Hamiltonian linearisation represents the optimal solution. The structure of the $[A]$ and $[B]$ matrices, and the right eingenvector $\{\bar{q}_2\}$ for a Hamiltonian/skew-Hamiltonian linearisation are presented in Eq. (3.60).

$$[A] = \begin{bmatrix} [0] & -[K] \\ [M] & [0] \end{bmatrix}, \quad [B] = \begin{bmatrix} [M] & [C] \\ [0] & [M] \end{bmatrix}, \quad \{\bar{q}_2\} = \begin{Bmatrix} \lambda\{\bar{q}\} \\ \{\bar{q}\} \end{Bmatrix} \tag{3.60}$$

The GEP is transformed into a Hamiltonian standard eigenvalue problem (SEP) and solved using the method proposed by Benner *et al.* (Ref. 186). Benners's method preserves the matrix structure and is considerably more efficient than the standard QZ and QR methods. The final N first mode shapes are calculated as dot products of the assumed mode shape vectors and the eigenvectors of the QEP as shown in Eq. (3.61).

$$X_i^r(x) = \{\psi^r(x)\} \cdot \{\bar{q}^r(t)\}_i, \quad i = 1, ...N \tag{3.61}$$

3.2.4 Model generation

The proposed formulation requires limited information. The required set of data is composed of general dimensions, operating conditions, boundary conditions, structural properties, and inertial properties. General dimensions such as the tip radius and root/hinge offset set the basic geometry of the rotor blade. The aim of this method is the estimation of the natural frequencies. Therefore, the only operational condition required is the rotational speed. The structural boundary conditions are imposed within the Euler-Bernoulli beam and classical torsion theories formulation. Regarding inertial and structural properties,

spanwise distributions of mass per unit length $m(x)$, mass moments of inertia $I_{1,2}(x)$, polar moment of inertia $I_p(x)$, bending stiffness $EI_{z,y}(x)$, extensional stiffness $EA(x)$, torsional rigidity $GJ(x)$, hub spring stiffness K^r, mass and area centroids offsets from the elastic axis $e_{A,M}(x)$, pretwist angle $\theta(x)$, precone angle β_{pre}, and two cross-section constants $EB^*_{1,2}(x)$ equivalent to those of Refs. 47 and 49 are required. These parameters along with the general dimensions and rotational speed are utilised to fill the mass, damping, and overall stiffness matrices. Once the matrices are filled, the QEP is linearised and the eigenvalues and eigenvectors calculated. Based on the latter, the final mode shapes are obtained for each mode of vibration.

3.3 Three-Dimensional Modelling of Elastic Rotor Blade Kinematics

The accurate simulation of the aeroelastic behaviour of the rotor requires the estimation of the aerodynamic and inertial loads exerted on the blades. These are determined by the velocity and acceleration of each blade material point. The blade's velocity and acceleration are highly nonlinear due to their dependence on the elastic deformation of the blade, applied control angles and the kinematics of the rotor itself. The treatment of the three-dimensional kinematics of the elastic rotor blade proposed by Goulos *et al.* 77 is adapted for the purpose of this work within this section.

Three different frames of reference are utilised in the kinematics formulation. These are the global nonrotating reference frame O, a rotating reference system A_i, $i = 1, \cdots, N_b$ located at the ith blade root/hinge, and the blade element fixed coordinate system b located at an arbitrary point $p(r, t)$ on the ith elastic axis. The location, alignment, and transformation matrices between each other are described in Section 3.1. In following sections, the position, velocity, and acceleration vectors of a anticlockwise rotor are formulated. It is noted that minimum changes in the reference frames and mathematical expressions are required to make the following formulation suitable for clockwise rotors. The minimum effort required for this task enables an easy expandability to configurations with clockwise rotors such as tiltrotor and coaxial helicopters.

3.3.1 Position vector

It is of interest to formulate the position vector of three different locations. These are: the ith blade root/hinge $A_i(t)$, an arbitrary point $p(r,t)$ on the deformed elastic axis of the ith blade, and the centre of gravity $cg(r,t)$ of the deformed rotor blade cross-section which contains $p(r,t)$. The position vector of the ith blade root/hinge expressed in the global nonrotating frame of reference O is given by

$$\tilde{r}_{A_i/O} = \begin{bmatrix} eR\cos\psi_i(t) & eR\sin\psi_i(t) & 0 \end{bmatrix}^T \tag{3.62}$$

where $\psi_i(t)$ is the azimuthal angle of the ith blade root/hinge at the time t. The position vector of an arbitrary point $p(r,t)$ on the ith blade's elastic axis relative to $A_i(t)$ expressed in the rotating reference system A_i is given by

$$\tilde{r}^{A_i}_{p/A_i} = \begin{Bmatrix} (r-eR)\cos\zeta(r,t)\cos\beta(r,t) \\ -(r-eR)\sin\zeta(r,t) \\ (r-eR)\sin\beta(r,t) \end{Bmatrix} \tag{3.63}$$

where $\zeta(r,t)$ and $\beta(r,t)$ are the equivalent lag and flap angles of $p(r,t)$ defined in A_i as

$$\zeta(r,t) = -\arcsin\frac{v(r,t)}{r-eR} \tag{3.64}$$

$$\beta(r,t) = \arcsin\frac{w(r,t)}{r-eR} \tag{3.65}$$

with $v(r,t)$ and $w(r,t)$ being the chordwise and flapwise transverse displacements respectively. The chordwise modal characteristics derived in Section 3.2 consider positive lead-lag transverse displacements when deformed forward. However, the equivalent lead-lag angle $\zeta(r,t)$ is assumed to be positive when moving backward. This convention justifies the presence of negative signs in front of the second element of Eq. (3.63) and Eq. (3.64). The third location to derive its position vector is the centre of gravity of the deformed blade cross section. The position vector of the centre of gravity $cg(r,t)$ relative to the arbitrary point $p(r,t)$ on the ith elastic axis expressed in the blade element fixed coordinate system b is given by

$$\tilde{r}^b_{cg/p} = \begin{bmatrix} 0 & -e_M & 0 \end{bmatrix}^T \tag{3.66}$$

where $e_m(r)$ is the chordwise mass centroid offset from the elastic axis, positive when located towards the leading edge. $\tilde{r}^b_{cg/p}$ can be expressed in the rotating reference system A_i using the following transformation

$$\tilde{r}_{cg/p}^{A_i} = [A_i] \left[T_i^b\right]^{-1} \tilde{r}_{cg/p}^{b} \tag{3.67}$$

As a result, the position vector of the centre of gravity $cg(r,t)$ relative to the ith root/hinge $A_i(r,t)$ expressed in the rotating reference system A_i is calculated as

$$\tilde{r}_{cg/A_i}^{A_i} = \tilde{r}_{p/A_i}^{A_i} + \tilde{r}_{cg/p}^{A_i} \tag{3.68}$$

The position vector $\tilde{r}_{cg/A_i}^{A_i}$ can be expressed in the global non-rotating reference frame O using the following transformation

$$\tilde{r}_{cg/A_i}^{O} = [A_i]^{-1} \tilde{r}_{cg/A_i}^{A_i} \tag{3.69}$$

Finally, the position of the centre of gravity $cg(r,t)$ relative to O expressed in the global non-rotating reference O is given by

$$\tilde{r}_{cg/O}^{O} = \tilde{r}_{A_i/O} + \tilde{r}_{cg/A_i}^{O} \tag{3.70}$$

3.3.2 Velocity vector

In the present work, the velocity of the 1/4 chord point of a given blade element along with the local rotor inflow determine the aerodynamic load exerted on the blade element. The 1/4 point is assumed to be coincident with the arbitrary point $p\,(r,t)$ on the elastic axis. At this point, the velocity vector of the centre of gravity $cg\,(r,t)$ is formulated. However, the mathematical formulation of velocity vector of the centre of gravity $cg\,(r,t)$ reduces to the one of $p\,(r,t)$ when the $\tilde{r}_{cg/p}^{b} = 0$.

$$\tilde{u}_O = [u_O \quad v_O \quad w_O]^T \tag{3.71}$$
$$\tilde{\omega}_O = [p_O \quad q_O \quad r_O]^T \tag{3.72}$$

Equations (3.71) and (3.72) define the linear and angular velocity vectors of the rotor hub expressed in the global non-rotating reference frame O. The latter along with the rotational speed of the rotor Ω determine the absolute angular velocity vector of the ith blade root/hinge $A_i\,(t)$. This is expressed in O as $\tilde{\omega}_{A_i} = [p_O \quad q_O \quad r_O + \Omega]^T$. The linear velocity of the ith blade root/hinge $A_i\,(t)$ expressed in O can now be written as

$$\tilde{u}_{A_i} = \tilde{u}_O + \tilde{\omega}_{A_i} \times \tilde{r}_{A_i/O} \tag{3.73}$$

The linear velocity vector of the centre of gravity $cg\,(r,t)$ relative to the ith blade root/hinge $A_i\,(t)$ depends on the angular velocity vector of the arbitrary point $p\,(r,t)$,

the position vector of the centre of gravity $cg\,(r,t)$ relative to $p\,(r,t)$ and $A_i\,(t)$, and the relative linear velocity vector of the centre of gravity $cg\,(r,t)$ about $p\,(r,t)$. The velocity vector of $cg\,(r,t)$ relative to $p\,(r,t)$ expressed in b is given by

$$\tilde{u}^b_{cg/p} = \tilde{\omega}^b_{cg/p} \times \tilde{r}^b_{cg/p} \tag{3.74}$$

where $\tilde{\omega}^b_{cg/p} = \begin{bmatrix} \dot{\phi} & 0 & 0 \end{bmatrix}^T$ is the angular velocity vector due to the time rate of change of the torsional deformation $\dot{\phi}\,(r,t)$ expressed in the beam element fixed reference frame b. $\tilde{u}^b_{cg/p}$ can be expressed in the rotating reference system A_i using the transformation

$$\tilde{u}^{A_i}_{cg/p} = [A_i] \left[T^b_i\right]^{-1} \tilde{u}^b_{cg/p} \tag{3.75}$$

The velocity of $cg\,(r,t)$ relative to $A_i\,(t)$ can then be expressed as

$$\tilde{u}^{A_i}_{cg/A_i} = \tilde{\omega}^{A_i}_{p/A_i} \times \tilde{r}^{A_i}_{cg/A_i} + \tilde{u}^{A_i}_{cg/p} \tag{3.76}$$

where $\tilde{\omega}^{A_i}_{p/A_i}$ is the total angular velocity vector of $p\,(r,t)$ due to flap and lead-lag displacements and the application of cyclic pitch expressed in A_i. For a hingeless rotor blade, where cyclic pitch is applied inboard of the blade root/hinge radial position, $\tilde{\omega}^{A_i}_{p/A_i}$ can be written as

$$\tilde{\omega}^{A_i}_{p/A_i} = \begin{bmatrix} \dot{\theta}_c\,(eR,t) & -\dot{\beta}\,(r,t) & -\dot{\zeta}\,(r,t) \end{bmatrix}^T \tag{3.77}$$

where $\dot{\zeta}\,(r,t)$ and $\dot{\beta}\,(r,t)$ are the first time derivatives of the equivalent lead-lag and flap angles defined in Eqs. (3.64) and (3.65). Goulos *el al.* (Ref. 77) proposed Eq. (3.78) as an alternative definition of $\tilde{\omega}^{A_i}_{p/A_i}$ for outboard blade pitch applications. Where $[\zeta\,(eR,t)]$ and $[\beta\,(eR,t)]$ refer to the lead-lag and flapping rotating matrices evaluated at the root/hinge.

$$\tilde{\omega}^{A_i}_{p/A_i} = [\zeta\,(eR,t)]^{-1}\,[\beta\,(eR,t)]^{-1} \begin{Bmatrix} \dot{\theta}_c\,(eR,t) \\ 0 \\ 0 \end{Bmatrix} + \begin{Bmatrix} 0 \\ -\dot{\beta}\,(r,t) \\ -\dot{\zeta}\,(r,t) \end{Bmatrix} \tag{3.78}$$

The velocity vector of the centre of gravity $cg\,(r,t)$ relative to A_i can now be expressed in the global nonrotating reference frame O using the following transformation:

$$\tilde{u}^O_{cg/A_i} = [A_i]^{-1}\,\tilde{u}^{A_i}_{cg/A_i} \tag{3.79}$$

The absolute velocity vector of the centre of gravity $cg\,(r,t)$ expressed in the global reference frame O is given by

$$\tilde{u}^O_{cg} = \tilde{u}_{A_i} + \tilde{u}^O_{cg/A_i} + \tilde{\omega}_{A_i} \times \tilde{r}^O_{cg/A_i} \tag{3.80}$$

3.3.3 Acceleration vector

The proposed methodology models each rotor blade as a series of discrete beam elements with differential mass mdr, located at the deformed centre of gravity of the correspondent beam element. The acceleration of this point defines the inertial load exerted on the blade throughout the time.

$$\tilde{\dot{u}}_O = [\dot{u}_O \quad \dot{v}_O \quad \dot{w}_O]^T \tag{3.81}$$

$$\tilde{\dot{\omega}}_O = [\dot{p}_O \quad \dot{q}_O \quad \dot{r}_O]^T \tag{3.82}$$

Equations (3.81) and (3.82) define the linear and angular acceleration vectors of the rotor hub expressed in the global nonrotating O reference frame. The latter along with the time derivative of the rotational speed of the rotor $\dot{\Omega}$ determine the absolute angular acceleration vector of the ith blade root/hinge $A_i(t)$. This is expressed in O as $\tilde{\dot{\omega}}_{A_i} = \left[\dot{p}_O \quad \dot{q}_O \quad \dot{r}_O + \dot{\Omega}\right]^T$. The linear acceleration of the ith blade root/hinge $A_i(t)$ expressed in O can now be written as

$$\tilde{a}_{A_i} = \tilde{\dot{u}}_O + \tilde{\omega}_{A_i} \times \left(\tilde{\omega}_{A_i} \times \tilde{r}_{A_i/O}\right) + \tilde{\dot{\omega}}_{A_i} \times \tilde{r}_{A_i/O} \tag{3.83}$$

The linear acceleration vector of the centre of gravity $cg(r,t)$ relative to the ith blade root/hinge $A_i(t)$ depends on the angular acceleration vector of the arbitrary point $p(r,t)$, the position vector of the centre of gravity $cg(r,t)$ relative to $p(r,t)$ and A_i, and the relative linear acceleration vector of the centre of gravity $cg(r,t)$ about $p(r,t)$. The acceleration vector of $cg(r,t)$ relative to $p(r,t)$ expressed in b is given by

$$\tilde{a}^b_{cg/p} = \tilde{\omega}^b_{cg/p} \times \left(\tilde{\omega}^b_{cg/p} \times \tilde{r}^b_{cg/p}\right) + \tilde{\dot{\omega}}^b_{cg/p} \times \tilde{r}^b_{cg/p} \tag{3.84}$$

where $\tilde{\dot{\omega}}^b_{cg/p} = \left[\ddot{\phi} \quad 0 \quad 0\right]^T$ is the angular acceleration vector due to the second time derivative of the torsional deformation $\ddot{\phi}(r,t)$ expressed in the beam element fixed reference frame b. $\tilde{a}^b_{cg/p}$ can be transformed to the rotating reference system A_i using the relation

$$\tilde{a}^{A_i}_{cg/p} = [A_i]\left[T^b_i\right]^{-1} \tilde{a}^b_{cg/p} \tag{3.85}$$

The acceleration of $cg(r,t)$ relative to $A_i(t)$ expressed in the rotating reference frame A_i is now given by

$$\tilde{a}^{A_i}_{cg/A_i} = \tilde{\omega}^{A_i}_{p/A_i} \times \left(\tilde{\omega}^{A_i}_{p/A_i} \times \tilde{r}^{A_i}_{cg/A_i}\right) + \tilde{\dot{\omega}}^{A_i}_{p/A_i} \times \tilde{r}^{A_i}_{cg/A_i} + 2 \cdot \tilde{\omega}^{A_i}_{p/A_i} \times \tilde{u}^{A_i}_{cg/p} + \tilde{a}^{A_i}_{cg/p} \tag{3.86}$$

where $\tilde{\omega}_{p/A_i}^{A_i}$ is the total angular velocity vector of $p\,(r,t)$ due to flap and lead-lag displacements and the application of cyclic pitch expressed in A_i. For a hingeless rotor blade, where cyclic pitch is applied inboard of the blade root/hinge radial position, $\tilde{\omega}_{p/A_i}^{A_i}$ can be written as

$$\tilde{\omega}_{p/A_i}^{A_i} = \begin{bmatrix} \ddot{\theta}_c\,(eR,t) & -\ddot{\beta}\,(r,t) & -\ddot{\zeta}\,(r,t) \end{bmatrix}^T \tag{3.87}$$

where $\ddot{\zeta}\,(r,t)$ and $\ddot{\beta}\,(r,t)$ are the second time derivatives of the equivalent lead-lag and flap angles defined in Eqs. (3.64) and (3.65). Goulos *el al.* 77 proposed Eq. (3.88) as an alternative definition of $\tilde{\omega}_{p/A_i}^{A_i}$ for outboard blade pitch applications.

$$\tilde{\omega}_{p/A_i}^{A_i} = \left[\zeta\,(eR,t)\right]^{-1}\left[\beta\,(eR,t)\right]^{-1}\begin{Bmatrix} \ddot{\theta}_c\,(eR,t) \\ 0 \\ 0 \end{Bmatrix} + \begin{Bmatrix} 0 \\ -\ddot{\beta}\,(r,t) \\ -\ddot{\zeta}\,(r,t) \end{Bmatrix} \tag{3.88}$$

The acceleration of the centre of gravity $cg\,(r,t)$ relative to A_i can now be expressed in the global nonrotating reference frame O using the following transformation:

$$\tilde{a}_{cg/A_i}^{O} = \left[A_i\right]^{-1}\tilde{a}_{cg/A_i}^{A_i} \tag{3.89}$$

The absolute acceleration vector of the centre of gravity $cg\,(r,t)$ expressed in the global reference frame O is finally expressed as

$$\tilde{a}_{cg}^{O} = \tilde{a}_{A_i} + \tilde{a}_{cg/A_i}^{O} + 2\cdot\tilde{\omega}_{A_i}\times\tilde{u}_{cg/A_i}^{O} + \tilde{\omega}_{A_i}\times\left(\tilde{\omega}_{A_i}\times\tilde{r}_{cg/A_i}^{O}\right) + \tilde{\dot{\omega}}_{A_i}\times\tilde{r}_{cg/A_i}^{O} \tag{3.90}$$

3.4 Rotor Inflow Model

The helicopter rotor wake is dominated by strong vortices formed at the blade tips. These vortices, which are convected below the rotor, determine the aerodynamic inflow through the rotor plane. Thus, the structure of the vortices dictates the loading of the blades. Modeling the rotor wake requires detailed knowledge of the location and strength of the vortices. The calculation of the wake structure is a highly complex unsteady problem as many geometric and operational factors are involved.

In the present work, a free-vortex wake model is deployed. Free-vortex wake models do not prescribe the structure of the vortices, in contrast, the geometry and strength of the vortices are part of the solution of the problem. Each vortex is discretised into a series

of vortex filaments with Lagrangian markers located at the extremes of each filament. Straight line vortex filaments are used to reconstruct the vortex. The main advantage of straight line vortices is the existence of a closed form expression for the calculation of the induced velocity with Biot-Savart law. The vorticity is assumed to be concentrated along the vortex filaments. Therefore, outside the vortex singularity, the flow is assumed to be inviscid, incompressible, and irrotational. Under these conditions, the vortex lines move along with the material lines. The position in space of the material lines is determined by the adjacent Lagrangian markers. As a results, the convection of the Lagrangian markers dictates the location of the vortex filaments. The governing equation for the position of the Lagrangian markers can be expressed as

$$\frac{\mathrm{d}\tilde{r}}{\mathrm{d}t} = \tilde{V}, \quad \tilde{r}\,(t=0) = \tilde{r}_0 \tag{3.91}$$

where $\tilde{r}$ is the position vector of a Lagrangian marker, $\tilde{V}$ is the velocity vector of the same point and $\tilde{r}_0$ is the initial location of the marker when it was released from the blade. Equation (3.91) can be written in terms of the rotational speed Ω of the rotor blade, the azimuth position ψ of the blade, and the age ζ of the vortex marker relative to the shedding from the blade. The resulting expression is given by

$$\frac{\partial\tilde{r}\,(\psi,\zeta)}{\partial\psi} + \frac{\partial\tilde{r}\,(\psi,\zeta)}{\partial\zeta} = \frac{1}{\Omega}\tilde{V}\left[\tilde{r}\,(\psi,\zeta)\right] \tag{3.92}$$

Figure 3.4 presents the variables defined above. Equation (3.92) is a partial differential equation (PDE). Its left hand side (LHS) is a one dimensional wave equation, which can be easily solved. However, the right hand side (RHS) is highly nonlinear and makes the solution of the PDE a formidable problem. Depending on the context of the problem, the velocity vector described on the RHS of Eq. (3.92) can include the free stream velocity, the velocity induced by all the vortex filaments, as well as other contributions such as manoeuvres and the effect of the fuselage.

3.4.1 Free-vortex wake model formulation

The governing equation of the convection of the Lagrangian markers (Eq. (3.92)) does not have an analytical solution and a numerical solution needs to be obtained. The pseudo-implicit predictor-corrector relaxation free-vortex method proposed by Bagai and

Leishman (Ref. 102) is implemented in the present work to solve Eq. (3.92). Periodicity is explicitly enforced and an extra pseudotime domain is introduced. The governing equation is solved iteratively in the pseudotime until convergence is obtained, resulting in zero pseudotime derivatives and a converged solution. To obtain a numerical solution, the LHS and RHS of the governing equation need to be discretised in two domains ψ and ζ. Figure 3.5a presents the five-point finite difference discretisation of both domains. The enforcement in the ψ is observed and the lines of propagation of information is illustrated. The five-point difference approximation of the LHS componentes of Eq. (3.92), originally proposed by Bagai and Leishman (Ref. 102), can be written as

$$\begin{aligned} D_\psi &\approx \left.\frac{\mathrm{d}\tilde{r}}{\mathrm{d}\psi}\right|_{\psi+\Delta\psi/2,\zeta+\Delta\zeta/2} \\ &= \frac{\left[\tilde{r}\left(\psi+\Delta\psi,\zeta+\Delta\zeta\right)-\tilde{r}\left(\psi,\zeta+\Delta\zeta\right)\right]+\left[\tilde{r}\left(\psi+\Delta\psi,\zeta\right)-\tilde{r}\left(\psi,\zeta\right)\right]}{2\Delta\psi} \end{aligned} \tag{3.93}$$

$$\begin{aligned} D_\zeta &\approx \left.\frac{\mathrm{d}\tilde{r}}{\mathrm{d}\zeta}\right|_{\psi+\Delta\psi/2,\zeta+\Delta\zeta/2} \\ &= \frac{\left[\tilde{r}\left(\psi+\Delta\psi,\zeta+\Delta\zeta\right)-\tilde{r}\left(\psi+\Delta\psi,\zeta\right)\right]+\left[\tilde{r}\left(\psi,\zeta+\Delta\zeta\right)-\tilde{r}\left(\psi,\zeta\right)\right]}{2\Delta\zeta} \end{aligned} \tag{3.94}$$

where the derivatives are evaluated at $\psi+\Delta\psi/2, \zeta+\Delta\zeta/2$, which is located in the line of propagation of the information between ψ, ζ and $\psi+\Delta\psi, \zeta+\Delta\zeta$. The direction of propagation of the information is dictated by the hyperbolic nature of the PDE. The corresponding approximation of the RHS of Eq. (3.92) is given by

$$\tilde{V}_{\psi+\Delta\psi/2,\zeta+\Delta\zeta/2} \approx \frac{1}{4}\left(\tilde{V}_{\psi+\Delta\psi,\zeta+\Delta\zeta}+\tilde{V}_{\psi+\Delta\psi,\zeta}+\tilde{V}_{\psi,\zeta+\Delta\zeta}+\tilde{V}_{\psi,\zeta}\right) \tag{3.95}$$

The complete finite difference approximation of Eq. (3.92) can now be introduced into the predictor-corrector scheme proposed in Ref. 102. The resulting pseudo-implicit predictor and corrector steps are mathematically defined in Eqs. (3.96) and (3.97).

$$\begin{aligned} \hat{\tilde{r}}^n_{i,j} = \hat{\tilde{r}}^n_{i-1,j-1} &+ \left(\frac{\Delta\psi-\Delta\zeta}{\Delta\psi+\Delta\zeta}\right)\left(\hat{\tilde{r}}^n_{i,j-1}-\hat{\tilde{r}}^n_{i-1,j}\right) \\ &+ \left(\frac{\Delta\psi\Delta\zeta}{\Delta\psi+\Delta\psi}\right)\frac{1}{2\Omega}\left(\tilde{V}^{n-1}_{i-1,j-1}+\tilde{V}^{n-1}_{i-1,j}+\tilde{V}^{n-1}_{i,j-1}+\tilde{V}^{n-1}_{i,j}\right) \end{aligned} \tag{3.96}$$

$$\tilde{r}^n_{i,j} = \tilde{r}^n_{i-1,j-1} + \left(\frac{\Delta\psi - \Delta\zeta}{\Delta\psi + \Delta\zeta}\right)\left(\tilde{r}^n_{i,j-1} - \tilde{r}^n_{i-1,j}\right) + \left(\frac{\Delta\psi\Delta\zeta}{\Delta\psi + \Delta\psi}\right)\frac{1}{4\Omega}\left(\tilde{V}^{n-1}_{i-1,j-1} + \hat{\tilde{V}}_{i-1,j-1} + \tilde{V}^{n-1}_{i-1,j} + \hat{\tilde{V}}_{i-1,j} + \tilde{V}^{n-1}_{i,j-1} + \hat{\tilde{V}}_{i,j-1} + \tilde{V}^{n-1}_{i,j} + \hat{\tilde{V}}_{i,j}\right) \tag{3.97}$$

where i and j are the azimuth and wake age subscripts respectively. $\hat{\tilde{r}}^n_{i,j}$ and $\tilde{r}^n_{i,j}$ are the predicted and corrected position vectors of a Lagrangian marker at the nth iteration. The predictor step is based on the velocity induced by the geometry of the $(n-1)$th iteration. However, the marker is convected in the corrector step by the an average velocity function of the velocity induced by the nth predicted geometry and the geometry of the $(n-1)$th iteration. Although the velocity vector $\tilde{V}_{i,j}$ can include the effect of the free stream velocity, manoeuvres, and the presence of a fuselage; it is of interest to formulate the self and mutually induced velocity vector.

$$\tilde{V}_{ind,i,j} = \tilde{V}_{ind}\left[\tilde{r}\left(\psi_i, \zeta_j\right)\right] = \sum_{l}^{N_b}\sum_{j2}^{N_\zeta} \tilde{V}_{ind}\left[\psi_i; \psi_i + (l-1)\frac{2\pi}{N_b}, \zeta_j; \zeta_{j2}\right] \tag{3.98}$$

Equation (3.98) defines the velocity vector $\tilde{V}_{i,j}$ induced at a Lagrangian point located at $\tilde{r}\left(\psi_i, \zeta_j\right)$ by all the vortex filaments. N_ζ represents the number of vortex filaments per rotor blade, which can include the tip and root vortices, near wake trailing vortices, and the bound vortex filaments. Equation (3.98) has been defined for a single rotor configuration. However, it can be easily expandable to configurations with multiple rotors. This expansion is carried out calculating the velocity of a Lagrangian marker (ψ_i, ζ_j) which belongs to the rotor q induced by all vortex filaments of every rotor. In this way the self and mutually induced velocity vector can be calculated and Eqs. (3.96-3.97) solved for each vortex filaments of all rotors under consideration. In a similar way, the velocity vector at a Lagrangian marker due to any other source can be added to the Eq. (3.98) to obtain the total velocity vector to be included in the RHS of the governing equation.

3.4.2 Free-vortex wake model implementation

In the present work, the wake is split in the near wake and far wake regions as shown in Fig. 3.4. The near wake comprises the closest region behind the trailing edge, and is composed of $N_s + 1$ trailing vortices. Each trailing vortex is discretised into $N_{\zeta_{nw}} = \zeta_{nw}/\Delta\zeta$ vortex

filaments, where ζ_{nw} is the near wake truncation age and $\Delta\zeta$ is the wake age discretisation resolution. The strength of the trailing vortex filaments is determined by the circulation radial gradient at the shedding time. The ζ boundary condition or initial position of the Lagrangian markers is dictated by the blade attachment conditions. In the present work, shed vortices are not modelled, as their effect is accounted for in the unsteady blade aerodynamic model. At the near wake truncation age, the near wake is assumed to fully rolled up into a root and a tip vortices. The roll-up model (Section 3.4.5) determines the strength and initial position of the root and tip vortices, i.e. the far wake ζ boundary condition. Each of the far wake vortices is discretised into $N_{\zeta_{fw}} = (\zeta_{max} - \zeta_{nw}) / \Delta\zeta$ vortex filaments, where ζ_{max} is the maximum wake age. The rotor blade revolution is azimuthally discretised into $N_\psi = 2\pi/\Delta\psi$, where $\Delta\psi$ is the azimuthal discretisation resolution.

Equation (3.92) accounts for unequal azimuthal and age discretisation resolutions. Unequal resolutions can reduce the computational cost if a finer discretisation is required in one of the two domain direction. However, this modifies the direction of propagation of information. In the present work equal resolutions are used, the computational cost is reduced in two ways. In the first place, the method has been written in FORTRAN 90/95 enhanced with OpenMP, which provides parallelism within a shared memory multiprocessing machine. The computational domain is split in $N_{threads}$ subdomains; each of the domains propagates the information along the characteristic directions calculating the new wake geometry. Figure 3.5a presents an example of the previously discretised computational domain where two threads are assumed. Two subdomains are therefore created and symbolised with different shadings. In the second place, the numerical acceleration scheme proposed by Bagai and Leishman (Ref. 106) based on velocity field interpolation is implemented. Along a vortex, two different types of Lagrangian markers are distinguished: free and pseudo-free collocation points. Free and pseudo-free markers are represented in Fig. 3.5b with light grey and white circles respectively. The induced velocity is explicitly calculated at the free collocation points via Biot-Savart law evaluations, while the induced velocity is interpolated at the pseudo-free points. The interpolation of the velocity field is carried out along the lines of propagation of information. After, the geometry is explicitly calculated for every marker. Figure 3.5b presents this process where the induced velocity of a pseudo-free marker in the characteristic line (dark grey circle) is

calculated by interpolation between the characteristic line adjacent free markers (black circles).

The overall implementation of the free-vortex wake module can be summarised in two flowcharts. Figure 3.6 presents the main inputs and outputs of the free-wake module. Within this module, an internal free-wake model (Fig. 3.7) is iteratively executed until convergence. For wake modelling purposes, the rotor blade is assumed to behave like a rigid blade undertaking flap and lead-lag rigid rotations. The equivalent tip flap and lag angles, $\beta(R,t)$ and $\zeta(R,t)$, along with the control angles define the position vector of the rotor blade in space and the blade attachment boundary condition. The distribution of bound circulation, aeroelastically obtained, determines the strength and core size of the vortex filaments. Based on the wake geometry of the previous iteration, vortex strengths, vortex core radii, and free stream velocity, the RHS of Eq. (3.92) is calculated. After prescribing the blade attachment boundary condition, the information is propagated along the characteristic lines of the near wake. Then, the vortex roll-up model is applied. This provides the far wake ζ boundary condition necessary to solve the far wake geometry, completing the predictor step (Fig. 3.7). Based on the predicted geometry, the new induced velocity on the wake is calculated. The new velocity flowfield is averaged with the one of the previous iteration to form the RHS of Eq. (3.92) in the corrector step. Similarly to the predictor step, the near wake geometry is solved, the far wake ζ boundary condition is calculated, and the information is propagated along the characteristic lines of the far wake (Fig. 3.7). The corrected geometry of the nth iteration is compared with the geometry of the $(n-1)$th using the L_2 norm of the wake geometry. The root mean square (RMS) change in geometry is therefore given by

$$RMS_{fw} = \frac{1}{2N_\psi\left(N_{\zeta_{fw}}+1\right)}\sqrt{\sum_{\psi:i=1}^{N_\psi}\sum_{\zeta:j=1}^{N_{\zeta_{fw}}}\left(\tilde{r}^{n}_{i,j}-\tilde{r}^{n-1}_{i,j}\right)^2} \tag{3.99a}$$

$$RMS_{nw} = \frac{1}{2N_\psi\left(N_{\zeta_{nw}}+1\right)\left(N_s+1\right)}\sqrt{\sum_{\psi:i=1}^{N_\psi}\sum_{\zeta:j=1}^{N_{\zeta_{fw}}}\sum_{r:k=1}^{N_s}\left(\tilde{r}^{n}_{i,j,k}-\tilde{r}^{n-1}_{i,j,k}\right)^2} \tag{3.99b}$$

where the RMS change is calculated for the near wake and far wake independently. The geometry is considered to be converged once the RMS change of both regions fall below a

threshold (Fig. 3.7) . The new induced velocity at the rotor disk is calculated with the converged geometry and exported along it (Fig. 3.6).

3.4.3 Treatment of viscosity effects

Free-vortex wake models assume inviscid, incompressible, irrotational flow outside the vortex filaments. The viscosity effects are therefore confined in the vortex singularities. It is of high relevance the appropriate treatment of the viscosity, as vortex strengths and core sizes determine the velocity induced at any point on the rotor disk and rotor wake. The velocity induced by a vortex filament of differential length on an arbitrary point P in space is determined by Biot-Savart law

$$\tilde{V}_{ind} = \frac{\Gamma}{4\pi} \int \frac{\mathrm{d}\tilde{l} \times \tilde{r}}{|\tilde{r}|^3} \tag{3.100}$$

where $\mathrm{d}\tilde{l}$ is a differential vortex segment, $\tilde{r}$ the position vector of P respect to the differential segment, and Γ is the circulation strength of the vortex. A closed form expression can be found for straight line vortex filaments, which can be written as

$$\tilde{V}_{ind} = \frac{\Gamma}{4\pi h} \frac{\tilde{l}_{12}}{|\tilde{l}_{12}|} \cdot \left(\frac{\tilde{r}_1}{|\tilde{r}_1|} - \frac{\tilde{r}_2}{|\tilde{r}_2|} \right) \left(\frac{\tilde{l}_{12} \times \tilde{r}_1}{|\tilde{l}_{12} \times \tilde{r}_1|} \right) \tag{3.101}$$

where $\tilde{l}_{12}$ is the vortex filament vector, and $\tilde{r}_1$ and $\tilde{r}_2$ are the position vectors of the arbitrary point P relative to the extremes of the vortex filament. The definition of these vectors can be observed in Fig. 3.8. The perpendicular distance between the arbitrary point P and the vortex filament can be calculated as

$$h = \frac{|\tilde{l}_{12} \times \tilde{r}_1|}{|\tilde{l}_{12}|} \tag{3.102}$$

Equation (3.101) is singular at $h = 0$. The singular behaviour can be corrected introducing the effect of a finite vortex core. The final expression of Biot-Savart law for a straight vortex filament with Vatista's vortex model (Ref. 104) is given by

$$\tilde{V}_{ind} = \frac{\Gamma}{4\pi} \left(\frac{h}{(r_c^{2n} + h^{2n})^{1/n}} \right) \frac{\tilde{l}_{12}}{|\tilde{l}_{12}|} \cdot \left(\frac{\tilde{r}_1}{|\tilde{r}_1|} - \frac{\tilde{r}_2}{|\tilde{r}_2|} \right) \left(\frac{\tilde{l}_{12} \times \tilde{r}_1}{|\tilde{l}_{12} \times \tilde{r}_1|} \right) \tag{3.103}$$

where r_c is the vortex core radius and $n = 1, 2$ is a superscript that defines the tangential velocity profile of Vatista's model. The vortex core radius is the radial distance from the

vortex axis to the position of maximum tangential velocity. Additionally, the core radius delimits the region where most of the vorticity is confined. The vortex core is found to experience viscous diffusion with time. This was originally modelled with the Lamb-Oseen approximation $r_c(t) = \sqrt{4\alpha\nu t}$, where $\alpha = 1.25643$ and ν is the kinematic viscosity. In the present approach the modification of the Lamb-Oseen approximation made by Squire (Ref. 145) is used.

$$r_c(\zeta) = \sqrt{r_{c_0}^2 + 4\alpha\delta\nu\frac{\zeta}{\Omega}} \tag{3.104}$$

Equation (3.104) presents this modification, where an initial finite core radius r_{c_0} was introduced to avoid the singularity of Eq. (3.103) for $h = t = 0$. An eddy viscosity parameter δ was incorporated to model the effect of turbulent mixing in the diffusion process. The eddy viscosity parameter δ is related to the vortex Reynolds number $Re^v = \Gamma^v/\nu$ by the relation $\delta = 1 + a_1 Re^v$, where a_1 is empirically determined. Typical values of $\delta \approx 10$ and $\delta \approx 1000$ were found experimentally by Bhagwat and Leishman (Ref. 177) for small-scale and full-scale rotors respectively.

3.4.4 Fuselage aerodynamic interference

The presence of a body close to the rotor, such as a fuselage, modifies the flowfield around it. Consequently, the flow structures close to the fuselage and the velocity inflow across the rotor disk are altered.

In the present work, the interference of the fuselage is taken into account implementing a semiempirical analytical formulation originally proposed by van der Wall *et al.* (Ref. 187) for its integration into the prescribed wake mode S4. The proposed methodology prescribes the fuselage induced velocity perturbation normal to the rotor plane at any point in space above a reference plane. The method utilises a generic analytical function which is evaluated at the position of interest. The generic function is the sum of the upwash u and downwash d components

$$\frac{v_i(x,y,z)}{V_\infty} = \sum_{i=u,d} \frac{A_{i0} S_{Ai}(z)}{S_{xi}(z)(x - x_{i0})^2/R^2 + S_{yi}(z)^2 (y - y_{i0})^2/R^2 + 1} \tag{3.105}$$

$$S_{Ai}(z) = \frac{1}{S_{Ai0}(z - z_0)^2/R^2 + 1}, \quad i = u, d \tag{3.106}$$

$$S_{xi}(z) = \frac{S_{xi0}}{(z - z_0)^2 / R^2}, \quad i = u, d \tag{3.107}$$

$$S_{yi}(z) = \frac{S_{yi0}}{(z - z_0)^2 / R^2}, \quad i = u, d \tag{3.108}$$

where A_{i0} is the peak magnitude of the component taken into account and S_{Ai}, S_{xi}, and S_{yi} are shape factor for each velocity component. x, y, and z are the coordinates of the point under consideration expressed in the global non-rotating frame of reference. To account for different angles of attack of the fuselage, certain model parameters are expressed as a function of it

$$A_{i0} = A_{i00} + \Delta A_{i0} \sin\alpha, \quad i = u, d \tag{3.109}$$

$$S_{xi0} = S_{xi00} + \Delta S_{xi0} \sin\alpha, \quad i = u, d \tag{3.110}$$

$$S_{yi0} = S_{yi00} + \Delta S_{yi0} \sin\alpha, \quad i = u, d \tag{3.111}$$

$$x_{i0} = x_{i00} + \Delta x_{i0} \sin\alpha, \quad i = u, d \tag{3.112}$$

Equations (3.105-3.112) require a series of model parameters. These are obtained fitting the proposed equations to a previously calculated set of data (experimental, cfd, panel methods, etc) using non-linear least-squares method. This methodology is valid for any fuselage as long as the set of data is previously generated. Once the parameters are obtained, Eqs. (3.105-3.112) are completely defined and the velocity perturbation can be evaluated at any position in space. As a result, during the simulation the flowfield around the body does not need to be calculated, instead it is prescribed reducing the computational overhead. Van der Wall *et al.* carried out this process for the HART II fuselage and the numerical values of the model parameters can be found in Ref. 187.

3.4.5 Vortex roll-up model

In the proposed formulation, the far wake region comprises tip and root vortices. The vortex roll-up model associates the near and far wake regions. In other words, it provides the far wake ζ boundary condition and the strength of the far wake vortices. Both properties, initial position vector and strength, depend on the loading of the rotor blade; i.e. on the distribution of bound circulation $\Gamma^b(r)$ along the blade. The present approach deploys an adaptation of the method developed by Rahier and Delrieux (Ref. 154) for the analysis of blade vortex interactions. Based on the distribution of bound circulation

$\Gamma^b(r)$, a distribution of local vorticity $\partial\Gamma^b(r)/\partial r$ can be calculated (Fig. 3.9). If the level of vorticity is larger than a threshold, the vorticity of the region rolls-up into a vortex of strength $\Gamma^v = \int_{r_1}^{r_2} \left(\partial\Gamma^b(r)/\partial r\right) \mathrm{d}r$, located at its centroid of vorticity.

$$r_v = \frac{\int_{r_1}^{r_2} \left(\partial\Gamma^b(r)/\partial r\right) r \,\mathrm{d}r}{\Gamma^v} \tag{3.113}$$

Equation 3.113 defines the radial position of the centroid of vorticity, a similar expression can be written for the Cartesian coordinates of the vortex. It is noted that the actual position depends on the blade loading at the time of shedding and the coordinates of the near wake at the current wake age. This process is applied at the blade cut-out and blade tip to generate the initial position and strength of the far wake structures.

3.5 Blade Aerodynamic Model

The rotor is modelled as N_b flexible blades with different hub attachments subjected to flap, lag, and torsion deformations and the application of pitch control angles. The blade cut-out divides the blade in two regions: the root and the aerodynamically effective regions. Only the latter is modelled aerodynamically, this is justified by the low order of magnitude of the aerodynamic loads generated in the root region.

The rotor blade is aerodynamically represented by a nonlinear unsteady blade lifting line model. Blade lifting line consists on the placement of a single flow singularity at the blade element quarter chord line. The singularity takes the form of a bound vortex filament of strength Γ^b_k. Vortex filaments are trailed from the extremes of each bound vortex filament towards the trailing edge. The circulatory strength of the trailing vortex is determined by the local circulation gradient, i.e. the strength difference between the two adjacent bound vortices ($\Gamma^t_k = \Gamma^b_{k-1} - \Gamma^b_k$). The intersection of the trailing vortices and the trailing edge constitutes the ζ boundary condition or releasing points of the trailing vortices of the near wake region.

In blade lifting line methods, the aerodynamic forces are determined by the incident velocity and angle of attack at the quarter chord line. The inherent simplicity of the method enables the incorporation of unsteady and nonlinear effects in the formulation. Unsteady effects are accounted for with the use of indicial functions, while nonlinear

effects are including through the use of experimentally derived aerofoil data. However, this method has a main drawback, it does not capture correctly the three-dimensional aerodynamic loading near the tip. In order to alleviate this deficiency, 2D to 3D correction factors proposed by Montgomerie (Ref. 188) for wind turbines are implemented for the blade cut-out and blade tip regions. Once the aerodynamic loading is calculated, the unsteady circulatory lift can be related with the circulation of the bound vortex using the theorem of Kutta–Joukowski.

$$\Gamma_k^b = \frac{1}{2} c_k V_k C_{l,k}^c \tag{3.114}$$

where c is the blade chord, V the normal velocity and C_l^c the circulatory lift coefficient.

3.5.1 Radial discretisation

Three different radial discretisations have been implemented in the proposed methodology. Equation (3.115) defines the position of the extremes of each blade element based on a linear discretisation. However, this discretisation is computationally inefficient as a large number of blade elements is required to capture the steep gradients present at the extremes of the blade. In order to efficiently capture these gradients, a cosine discretisation has been implemented and it is mathematically defined in Eq. (3.116). This type of discretisation places more elements near the blade cut-out and tip while a coarser discretisation is produced in the central part of the blade. An even more aggressive discretisation can be applied if the cosine discretisation presented before is biased towards the blade tip. This is mathematically defined in Eq. (3.117) and it is the strategy with the finest discretisation at the tip for a given number of blade elements N_s.

$$r_k = R\left[\frac{R_{co}}{R} + \left(1 - \frac{R_{co}}{R}\right) \cdot \left(\frac{k-1}{N_s}\right)\right], \quad k = 1, ..., N_s + 1 \tag{3.115}$$

$$r_k = \frac{R}{2}\left[\left(1 + \frac{R_{co}}{R}\right) + \left(1 - \frac{R_{co}}{R}\right) \cos\left(\pi \frac{(N_s + 1 - k)}{N_s}\right)\right], \quad k = 1, ..., N_s + 1 \tag{3.116}$$

$$r_k = R\left[\frac{R_{co}}{R} + \left(1 - \frac{R_{co}}{R}\right) \cos\left(\frac{\pi}{2} \frac{(N_s + 1 - k)}{N_s}\right)\right], \quad k = 1, ..., N_s + 1 \tag{3.117}$$

3.5.2 Two-dimensional unsteady blade aerodynamics

Rotor blades in forward flight can encounter highly unsteady angles of attack and incident velocities along a revolution. The unsteadiness of the local aerodynamic conditions is exacerbated when the tip vortices are in the proximity of the rotor blade, as these blade vortex interactions cause large variations in aerodynamic loads with time. The main difference between unsteady and quasi-steady aerodynamics is the presence of a time lag in the lift response of the unsteady model relative to the aerodynamic forcing.

In the present work, the Leishman-Beddoes indicial response method is used to model the two-dimensional unsteady aerodynamics. The implemented formulation, developed in Refs. 174, 189, 190, provides the unsteady aerodynamic lift, drag, and moment coefficients associated to an arbitrary angle of attack α and pitch rate $\dot{\alpha}$ forcing. The angle of attack α time history is a function of the pretwist, pitch control angles, non-uniform inflow, and non-linear blade element velocity (including the effect of elastic deformations). The pitch rate $\dot{\alpha}$ time history depends on the pitch control and the torsion deformation exclusively. The indicial response method models an arbitrary time history of angle of attack α as a series of consecutive step changes in angle of attack α. As a result, the response of the aerodynamic coefficients depends on the current step change in angle of attack $\Delta\alpha$ and its previous value of aerodynamic coefficients; i.e. the time-history of previous states.

$$\frac{\Delta C_n^{\alpha}(s)}{\Delta\alpha} = \frac{4}{M}\phi_{n,\alpha}^{nc}(s,M) + \frac{2\pi}{\beta}\phi_{n,\alpha}^{c}(s,M) \tag{3.118}$$

$$\frac{\Delta C_n^{q}(s)}{\Delta q} = \frac{1}{M}\phi_{n,q}^{nc}(s,M) + \frac{\pi}{\beta}\phi_{n,q}^{c}(s,M) \tag{3.119}$$

Equations (3.118) and (3.119) present the indicial normal force C_n response to step changes in angle of attack α and non-dimensional pitch rate q. The non-dimensional pitch rate is defined as $q = \dot{\alpha}c/V$, where c is the chord and V the incident velocity. An efficient time variable $s = 2/c\int_0^t V\mathrm{d}t$ is defined, which represents the distance travelled by the aerofoil in the time interval t in semichords. The Prandtl-Glauert factor $\beta = \sqrt{1-M^2}$ is introduced to account for compressibility effects. In Eqs. (3.118) and (3.119) and the rest of the section, the superscripts c and nc refer to the circulatory and non-circulatory components respectively; and the subscripts α and q refer to the response due to step change in angle of attack and non-dimensional pitch rate respectively. Therefore $\phi_{n,\alpha}^{c}$, $\phi_{n,\alpha}^{nc}$,

$\phi^c_{n,q}$, and $\phi^{nc}_{n,q}$ represent the circulatory and non-circulatory indicial functions due to step changes in α and q for the calculation of the normal force coefficient.

$$\frac{\Delta C^{\alpha}_{m}(s)}{\Delta\alpha} = -\frac{1}{M}\phi^{nc}_{m,\alpha}(s,M) + \frac{2\pi}{\beta}(0.25 - x_{ac})\,\phi^{c}_{m,\alpha}(s,M) \tag{3.120}$$

$$\frac{\Delta C^{q}_{m}(s)}{\Delta q} = -\frac{7}{12M}\phi^{nc}_{m,q}(s,M) - \frac{\pi}{8\beta}\phi^{c}_{m,q}(s,M) \tag{3.121}$$

Similar expressions are presented in Eqs. (3.120) and (3.121) for the indicial response of the moment C_m about $1/4c$ to step changes in angle of attack α and non-dimensional pitch rate q, where $\phi^c_{m,\alpha}$, $\phi^{nc}_{m,\alpha}$, $\phi^c_{m,q}$, and $\phi^{nc}_{m,q}$ are the circulatory and non-circulatory indicial functions due to step changes in α and q for the calculation of the moment coefficient.

Non-circulatory terms are sometimes denominated apparent mass because of their acceleration nature. These are directly related to the pressure forces required to accelerate the fluid in the vicinity of the aerofoil when subjected to a change in aerodynamic conditions. The non-circulatory indicial functions are approximated with rapidly decaying exponential functions. The circulatory terms are associated with the creation of circulation around the aerofoil. Changes in the aerofoil circulation result in the shedding of vorticity into the wake. Consequently, the shed vorticity affects the aerofoil effectively delaying and reducing the circulatory response of the aerofoil to the change in aerodynamic conditions. The circulatory indicial functions are approximated with exponential functions, which approach unity when s goes to infinity.

$$\phi^{nc}_{n,\alpha}(s,M) = \exp\left(\frac{-s}{T_{n,\alpha}}\right) \tag{3.122a}$$

$$\phi^{c}_{n,\alpha}(s,M) = 1 - A_1 e^{-b_1\beta^2 s} - A_2 e^{-b_2\beta^2 s} \tag{3.122b}$$

$$T_{n,\alpha}(M) = \frac{2M}{1 - M + \pi\beta M^2 (A_1 b_1 + A_2 b_2)} \tag{3.122c}$$

$$\phi^{nc}_{n,q}(s,M) = \exp\left(\frac{-s}{T_{n,q}}\right) \tag{3.123a}$$

$$\phi^{c}_{n,q}(s,M) = 1 - A_1 e^{-b_1\beta^2 s} - A_2 e^{-b_2\beta^2 s} \tag{3.123b}$$

$$T_{n,q}(M) = \frac{2M}{1 - M + 2\pi\beta M^2 (A_1 b_1 + A_2 b_2)} \tag{3.123c}$$

$$\phi^{nc}_{m,\alpha}(s,M) = A_3 \exp\left(\frac{-s}{b_3 T_{m,\alpha}}\right) + A_4 \exp\left(\frac{-s}{b_4 T_{m,\alpha}}\right) \tag{3.124a}$$

$$\phi^{c}_{m,\alpha}(s,M) = \phi^{c}_{n,\alpha}(s,M) = 1 - A_1 e^{-b_1\beta^2 s} - A_2 e^{-b_2\beta^2 s} \tag{3.124b}$$

$$\phi^{nc}_{m,q}(s,M) = \exp\left(\frac{-s}{T_{m,q}}\right) \tag{3.125a}$$

$$\phi^{c}_{m,q}(s,M) = \phi^{c}_{n,\alpha}(s,M) = 1 - A_5 e^{-b_5\beta^2 s} \tag{3.125b}$$

Equations (3.122 - 3.125) present the indicial functions and their time constants used in the indicial response method. The values of $A_i, b_i \quad i = 1, \cdots 5$ are derived from experimental unsteady experiments of oscillating aerofoils. Leishman and Beddoes (Refs. 191 and 192) proposed the use of a recurrence algorithm for the calculation of C_n and C_m to a series of step changes in α and q. In the present work the recurrence algorithm is implemented with a mid-point approximation of the indicial function. The resulting expression for the normal force coefficient due to a series of successive step changes in angle of attack is given by

$$\begin{aligned} C_{n,\alpha}(s) &= C^{nc}_{n,\alpha}(s) + C^{c}_{n,\alpha}(s) \\ &= \frac{4}{M}\Delta\alpha_e(s) + \frac{2\pi}{\beta}\alpha_e(s) = \frac{4}{M}\Delta\alpha_e(s) + C_{n_\alpha}(M)\,\alpha_e(s) \end{aligned} \tag{3.126a}$$

$$\Delta\alpha_e(s) = T_{n,\alpha}\left(\frac{\Delta\alpha_s}{\Delta s} - X^{nc}_{n,\alpha}(s)\right) \tag{3.126b}$$

$$\alpha_e(s) = \alpha(s) - X^{c}_{n,\alpha}(s) - Y^{c}_{n,\alpha}(s) \tag{3.126c}$$

$$X^{nc}_{n,\alpha}(s) = X^{nc}_{n,\alpha}(s-\Delta s)\,e^{-\Delta s/T_{n,\alpha}} + \frac{\Delta\alpha_s - \Delta\alpha_{s-\Delta s}}{\Delta s}e^{-\Delta s/(2T_{n,\alpha})} \tag{3.126d}$$

$$X^{c}_{n,\alpha}(s) = X^{c}_{n,\alpha}(s-\Delta s)\,e^{-b_1\beta^2\Delta s} + A_1\Delta\alpha_s e^{-b_1\beta^2\Delta s/2} \tag{3.126e}$$

$$Y^{c}_{n,\alpha}(s) = Y^{c}_{n,\alpha}(s-\Delta s)\,e^{-b_2\beta^2\Delta s} + A_2\Delta\alpha_s e^{-b_2\beta^2\Delta s/2} \tag{3.126f}$$

where $\alpha_e(s)$ is the circulatory effective instantaneous angle of attack seen by the aerofoil. This effective angle of attack lags an angle $X^{c}_{n,\alpha}(s) + Y^{c}_{n,\alpha}(s)$ behind the geometric angle of attack, where $X^{c}_{n,\alpha}(s)$ and $Y^{c}_{n,\alpha}(s)$ are the deficiency functions given by the recurrence algorithm. The last term of Eq. (3.126a) can be seen as the normal force coefficient read from steady state aerofoil data for the effective angle of attack $\alpha_e(s)$. Figure 3.10a presents an example of the normal force coefficient response of an idealised aerofoil to ramp change in angle of attack. A sudden increase in the non-circulatory is observed, which rapidly vanishes. The circulatory term is observed to be delayed relative to the change of angle of attack and with a smaller amplitude. However, after a short time, this term is the dominant one an slowly approaches the quasi-steady value of normal force coefficient.

Similar expressions are presented in Eqs. (3.127 - 3.129) for the recurrence algorithm implementation of the indicial response functions for the normal force coefficient due to step changes in pitch rate.

$$C_{n,q}(s) = C^{nc}_{n,q}(s) + C^{c}_{n,q}(s) = \frac{1}{M}\Delta q_e(s) + \frac{\pi}{\beta} q_e(s) \tag{3.127a}$$

$$\Delta q_e(s) = T_{n,q}\left(\frac{\Delta q_s}{\Delta s} - X^{nc}_{n,q}(s)\right) \tag{3.127b}$$

$$q_e(s) = q(s) - X^{c}_{n,q}(s) - Y^{c}_{n,q}(s) \tag{3.127c}$$

$$X^{nc}_{n,q}(s) = X^{nc}_{n,q}(s-\Delta s)\, e^{-\Delta s/T_{n,q}} + \frac{\Delta q_s - \Delta q_{s-\Delta s}}{\Delta s} e^{-\Delta s/(2T_{n,q})} \tag{3.127d}$$

$$X^{c}_{n,q}(s) = X^{c}_{n,q}(s-\Delta s)\, e^{-b_1\beta^2\Delta s} + A_1\Delta q_s e^{-b_1\beta^2\Delta s/2} \tag{3.127e}$$

$$Y^{c}_{n,q}(s) = Y^{c}_{n,q}(s-\Delta s)\, e^{-b_2\beta^2\Delta s} + A_2\Delta q_s e^{-b_2\beta^2\Delta s/2} \tag{3.127f}$$

$$C_{m,\alpha}(s) = C^{nc}_{m,\alpha}(s) + C^{c}_{m,\alpha}(s) = -\frac{1}{4}C^{nc}_{n,\alpha}(s) + \frac{2\pi}{\beta}(0.25 - x_{ac})\,\alpha_e(s) \tag{3.128}$$

$$\begin{aligned} C_{m,q}(s) &= C^{nc}_{m,q}(s) + C^{c}_{m,q}(s) \\ &= -\frac{1}{4}C^{nc}_{n,q} - \frac{1}{3M}\Delta q_e(s) - \frac{\pi}{8\beta}\left(q(s) - X^{c}_{m,q}(s)\right) \end{aligned} \tag{3.129a}$$

$$\Delta q_e(s) = \frac{T^2_{n,q}}{2M}\left(\frac{\Delta q_s}{\Delta s} - X^{nc}_{m,q}(s)\right) \tag{3.129b}$$

$$X^{nc}_{m,q}(s) = X^{nc}_{m,q}(s-\Delta s)\, e^{-2M\Delta s/T^2_{n,q}} + \frac{\Delta q_s - \Delta q_{s-\Delta s}}{\Delta s} e^{-M\Delta s/\left(T^2_{n,q}\right)} \tag{3.129c}$$

$$X^{c}_{m,q}(s) = X^{c}_{n,q}(s-\Delta s)\, e^{-b_5\beta^2\Delta s} + A_5\Delta q_s e^{-b_5\beta^2\Delta s/2} \tag{3.129d}$$

It is noted that the last term of Eq. (3.128) can be interpreted as the moment coefficient read from steady state aerofoil data for the effective angle of attack $\alpha_e(s)$. Once the circulatory and non-circulatory indicial responses are known, the overall normal coefficient can be calculated as

$$C_n(s) = C_{n,\alpha}(s) + C_{n,q}(s) \tag{3.130}$$

$$C_a(s) = C^{c}_{n}(\alpha_e(s))\tan\alpha_e(s) \tag{3.131}$$

Equation (3.131) presents the chordwise force coefficient. It is a function of the normal force circulatory component $C^{c}_{n}(s) = C^{c}_{n,\alpha}(s) + C^{c}_{n,q}(s)$ and the effective angle of attack α_e (Ref. 193). The expressions of the final lift, drag, and moment coefficient can be written as

$$C_l(s) = C_n(s)\cos\alpha(s) + C_a(s)\sin\alpha(s) \tag{3.132}$$

$$C_d(s) = C_{d_0} + C_n(s)\sin\alpha(s) - \eta_a C_a(s)\cos\alpha(s) \tag{3.133}$$

$$C_m(s) = C_{m,\alpha}(s) + C_{m,q}(s) \tag{3.134}$$

where η_a is the leading edge suction recovery factor and C_{d_0} is the zero lift drag coefficient. The latter is sometimes called viscous or shear stress drag and is a function of the Mach number and can be assumed to be constant for low angles of attack (Ref. 193). In Eq. (3.133), $C_n(s)\sin\alpha(s) - \eta_a C_a(s)\cos\alpha(s)$ can be interpreted as the pressure drag coefficient. For steady potential flow, the pressure drag coefficient vanishes. In contrast ,the real flow is not able to recover the complete magnitude of leading edge suction C_a and the leading edge suction recovery factor η_a is introduced to model this deficiency (Ref. 193). The effect of both parameters is presented in Fig. 3.10b in terms of aerofoil steady flow polar curves. If no viscous drag is modelled and perfect leading edge suction recovery is assumed, the drag coefficient will be zero for any lift coefficient. The addition of C_{d_0} essentially increases the value of drag coefficient by a constant value. The inability to recovery the 100% of leading edge suction is modelled reducing the value of η_a. In Fig. 3.10b it can be observed that the lower this value, the higher the drag coefficient will be for a given lift coefficient.

3.6 Aeroelastic Model

The present works aims to aeroelastically simulate the behaviour of a rotor blade. The components necessary for the formulation of the aeroelastic model have been derived in the previous sections. In the first place, the coupled modes of vibration of the rotor blade *in vacuo* were obtained in Section 3.2. These are important as the rotor blade tends to elastically oscillate in a combination of these mode shape when externally excited. In the second place, the three-dimensional kinematics of the elastic rotor blade were formulated in Section 3.3. This provides the velocity vector of the blade necessary for the calculation of the aerodynamic loads and the acceleration vector required for the estimation of the inertial loads. In the third place, the velocity flowfield induced by the wake at the rotor disk was calculated in Section 3.4. The rotor inflow along with the velocity vector of the blade determine the local aerodynamic conditions encountered by the rotor blade. In the fourth place, the unsteady blade aerodynamics were formulated in Section 3.5. This provides an estimation of the unsteady aerodynamic forces when excited with an arbitrary

time-variation of local aerodynamic conditions. The steady state aerofoil data required by the unsteady blade aerodynamic model is imported from externally defined files. In this way compressibility and non-linear effect can be incorporated into the analysis.

The above described modules need to be aeroelastically connected. This section presents the formulation for the combination of these components. As a starting point, the main inputs and outputs of the aeroelastic model are shown in Fig. 3.11. The control angles are imposed either externally by the user or by the rotor trim model, while the free stream velocity is defined by the wind tunnel testing conditions. The modal characteristics are obtained from the structural dynamics model. The last input to the model is the rotor inflow induced by the rotor wake. Local flap, lag, and torsion deformations and their time and spatial derivatives are obtained from the aeroelastic model. As a result, the equivalent rigid flap and lag angles are calculated, which are needed for the calculation of the blade attachment boundary condition in the free-vortex wake model. Additionally, the kinematics of the blade can be fully evaluated and the aerodynamic and inertial loads calculated. Once the aerodynamic loading is obtained, the bound circulation distribution can be estimated and fed back to the free-vortex wake model.

3.6.1 Structural dynamics interface

The structural dynamics model presented in Section 3.2 accounts for the effect of gyroscopic coupling. However, the integration of the structural dynamics model into the aeroelastic model is carried out without it. The exclusion of the gyroscopic matrix $[C]$ reduces the quadratic eigenvalue problem (Eq. (3.58)) to a generalised problem

$$\left(\left[S\right] - \lambda^2 \left[M\right]\right) \left\{\bar{q}\right\} = \left[Q\left(\lambda\right)\right] \left\{\bar{q}\right\} = \left\{0\right\} \tag{3.135}$$

The eigenvectors solution of the GEP, $X_i^r\left(x\right) = \left\{\psi^r\left(x\right)\right\} \cdot \left\{\bar{q}^r\left(t\right)\right\}_i$, $i = 1, ..., N$, are orthogonal to each other, property lost when the gyroscopic matrix is accounted for. As a results of the orthogonality of the modal characteristics, the response of the system to arbitrary external loading can be approximated with modal superimposition. Although the gyroscopic effect is dismissed in the modal characteristics, it is fully accounted in the formulation of the inertial loading. Consequently, the gyroscopic effect is restored as an inertial load externally applied.

3.6.2 Three-dimensional kinematics interface

The position, velocity, and acceleration vectors derived in Section 3.3 require the prior knowledge of the lag, flap, and torsion elastic deformations (v, w, ϕ) and their first $(\dot{v}, \dot{w}, \dot{\phi})$ and second $(\ddot{v}, \ddot{w}, \ddot{\phi})$ time derivatives. The proposed aeroelastic model marches in time, therefore the time is discretised and numerical approximations of the time derivatives are obtained using finite difference schemes. In the present work two finite difference approximations schemes are used, there will be denoted as S1 and S2.

The first scheme, S1, is a second-order accurate backward-difference approximation, which only requires knowledge of the discrete values of the variable at the time of evaluation and previous time-steps. The first and second time derivatives approximation for the flap displacements can be written as

$$\frac{\partial w\left(r,t\right)}{\partial t} \approx \frac{3w\left(r,t\right) - 4w\left(r,t-\Delta t\right) + w\left(r,t-2\Delta t\right)}{2\Delta t} \tag{3.136}$$

$$\begin{aligned}\frac{\partial^2 w\left(r,t\right)}{\partial t^2} \approx & \frac{9w\left(r,t\right) - 24w\left(r,t-\Delta t\right) + 22w\left(r,t-2\Delta t\right)}{4\Delta t^2} \\ & + \frac{-8w\left(r,t-3\Delta t\right) + w\left(r,t-4\Delta t\right)}{4\Delta t^2}\end{aligned} \tag{3.137}$$

The second scheme, S2, is a second-order accurate backward-difference approximation originally developed by Bhagwat and Leishman (Ref. 110) and later modified by Goulos *et al.* (Ref. 77). The approximation was proved in Ref. 110 to be stable with positive damping. However, the calculation of the derivative at a time t requires the knowledge of the variable at a time step $t + \Delta t$, which under some circumstances is not possible. The approximations of the first and second time derivative is given by

$$\frac{\partial w\left(r,t\right)}{\partial t} \approx \frac{3w\left(r,t+\Delta t\right) + 2w\left(r,t\right) - 4w\left(r,t-\Delta t\right) - 2w\left(r,t-2\Delta t\right) + w\left(r,t-3\Delta t\right)}{8\Delta t} \tag{3.138}$$

$$\begin{aligned}\frac{\partial^2 w\left(r,t\right)}{\partial t^2} \approx & \frac{9w\left(r,t+\Delta t\right) - 6w\left(r,t\right) - 17w\left(r,t-\Delta t\right) + 12w\left(r,t-2\Delta t\right)}{16\Delta t^2} \\ & + \frac{7w\left(r,t-3\Delta t\right) - 6w\left(r,t-4\Delta t\right) + w\left(r,t-5\Delta t\right)}{16\Delta t^2}\end{aligned} \tag{3.139}$$

Although the previous time derivatives have been presented for flapwise displacement, the same equations are applicable for lead-lag displacement and torsional deformation.

The knowledge of the deformations and their time derivatives enables the calculation of the local aerodynamic conditions and inertial forces of a blade element.

3.6.3 Rotor inflow interface

The present approach couples the non-uniform rotor inflow from the free-vortex wake model with the time-marching aeroelastic model. Once the geometry of the wake has converged, the rotor inflow is calculated at each radial and azimuthal location. This inflow distribution is fed into the aeroelastic model and kept constant. If the azimuthal resolution of the aeroelastic model is finer than the one of the inflow model, spline interpolation is used. For the rotor inflow calculation, the rotor blade is assumed to be rigid and it undertakes rigid flap and lag rotations. Torsion is not taken into account in the calculation of the wake geometry and its rotor inflow. The equivalent rigid tip lag and flap angles expressed in A_i are given by

$$\zeta\left(R,t\right) = -\arcsin\frac{v\left(R,t\right)}{R-eR} \tag{3.140a}$$

$$\beta\left(R,t\right) = \arcsin\frac{w\left(R,t\right)}{R-eR} \tag{3.140b}$$

The aerodynamic loading resulting from the aeroelastic model determines the bound circulation distribution, which is fed back into the rotor inflow model to recalculate the wake geometry and rotor inflow.

3.6.4 Blade aerodynamics interface

The blade aerodynamic model provides the aerodynamic forces resulting from a time-dependent local aerodynamic excitation. The velocity of the blade element depends on the rigid and elastic motion of the blade as shown in Section 3.3. The velocity of the blade element along with the rotor inflow at the same location are expressed in the blade element fixed coordinate system b, whose orientation in space depends on the local flap, lag, and torsion angle. Consequently, the local aerodynamic conditions fed into the aeroelastic model are able to account for the effect of non-uniform inflow and time-dependent elastic deformation.

3.6.5 Numerical time-marching scheme

Figure 3.12 presents the flowchart correspondent to the numerical time-marching solution of the aeroelastic model. The proposed approach uses a predictor-corrector scheme for the solution of each time step. In the predictor step at the instant t, the first and second time derivatives of the flap, lag, and torsional deformations (and their spatial derivatives) are calculated with the finite difference approximation scheme S1. Based on the elastic deformations and their derivatives at the instant t, the aerodynamic and inertial loads are calculated using

$$\mathrm{d}\tilde{f}_{cg}^{O} = \left[T_i^b\right]^{-1} \left\{ \tilde{f}_{aero}^{b} - m\left(r\right) \tilde{a}_{cg}^{b} \right\} \mathrm{d}r \tag{3.141}$$

$$\mathrm{d}\tilde{m}_{cg}^{O} = \left[T_i^b\right]^{-1} \left\{ \tilde{m}_{aero}^{b} - I_p\left(r\right) \dot{\tilde{\omega}}_{\phi}^{b} - m\left(r\right) \left(\tilde{r}_{cg/p}^{b} \times \tilde{a}_{cg}^{b} \right) \right\} \mathrm{d}r \tag{3.142}$$

where $\mathrm{d}\tilde{f}_{cg}^{O}$ and $\mathrm{d}\tilde{m}_{cg}^{O}$ are the differential force and moment exerted on a differential beam element expressed in the global non-rotating frame of reference O. $\tilde{f}_{aero}^{b}$ and $\tilde{m}_{aero}^{b}$ are the aerodynamic force and moments expressed in the blade element fixed coordinate system b. The next step is the calculation of the generalised loads for flap, lag, and torsion. Great attention is paid to avoid double counting inertial loads already taken into account in the calculation of the modal characteristics. The generalised loads along with the modal characteristics of the rotor blade are incorporated into the convolution integral. The predicted elastic deformation at the instant $t + \Delta t$ is the solution of the dynamic response of the system, which is obtained using a fifth-order accurate numerical recurrent evaluation of the convolution integral (Ref. 194). It was found that a better and more stable approximation of the elastic deformations time derivatives was achieved if they were approximated using the finite difference approximation scheme S2. This was done in the corrector step, which uses the scheme S2 to approximate the time derivatives. This scheme requires the knowledge of the deformation at $t + \Delta t$, which is possible thanks to the prediction of the deformations done in the predictor step. Based on the better approximation of the time derivatives, the new generalised loads are calculated. The corrected elastic deformation at $t + \Delta t$ is obtained solving the convolution integral with an average of the generalised loads calculated with the predictor and corrector steps. The solution is marched in time until once-per-rev (1P) periodicity is reached. The periodicity

criteria used in the present work is the reduction of the RMS change in blade geometry between two consecutive revolutions below a threshold. The RMS change in blade geometry can be expressed as

$$RMS_{geo} = \frac{1}{N_\psi \left(N_s + N_{s,root}\right)} \sqrt{\sum_{\psi:i=1}^{N_\psi} \sum_{r:k=1}^{N_s+N_{s,root}} \left(\tilde{r}^O_{p/O,i,k} - \tilde{r}^O_{p/O,i-N_\psi,k}\right)^2} \tag{3.143}$$

where $N_{s,root}$ is the number of beam elements contained in the region delimited by the blade root/hinge and the blade cut-out, and $\tilde{r}^O_{p/O}$ is the position vector of an arbitrary point p on the ith elastic axis expressed in the global non-rotating reference frame O. Although the use of a predictor-corrector scheme multiplies by two the number of operations per time step, the better stability of the scheme enables the use of larger azimuthal discretisation and an overall reduction in computational cost.

3.6.6 Integrated rotor loads

The total time-dependent rotor force $\tilde{F}^O_{rotor}(t)$ and moment $\tilde{T}^O_{rotor}(t)$ can be obtained summing the contribution of each individual blade at an instant t. The resulting expressions are given by

$$\tilde{F}^O_{rotor}(t) = \sum_{i=1}^{N_b} \tilde{F}^O_i(t) \tag{3.144}$$

$$\tilde{T}^O_{rotor}(t) = \sum_{i=1}^{N_b} \tilde{T}^O_i(t) \tag{3.145}$$

$$\tilde{F}^O_i(t) = \int_{eR}^{R} \mathrm{d}\tilde{f}^O_{cg}, \quad i = 1, ...N_b \tag{3.146}$$

where $\tilde{F}^O_i(t)$ and $\tilde{T}^O_i(t)$ are the force and moment vectors exerted by an individual blade on the rotor hub. The total blade force $\tilde{F}^O_i(t)$ is independent of the rotor blade hub support boundary condition. The moment $\tilde{T}^O_i(t)$ can be split in two components $\tilde{T}^O_i(t) = \tilde{T}^O_{i,offset}(t) + \tilde{T}^O_{i,root}(t)$. The first one, $\tilde{T}^O_{i,offset}(t)$, is independent of the type of hub support and is generated by the offset between the origin O and the root/hinge $A_i(t)$, where the overall blade force $\tilde{F}^O_i(t)$ is applied. The resulting expression for this component is $\tilde{T}^O_{i,offset}(t) = \tilde{r}_{A_i/O} \times \tilde{F}^O_i(t)$. The second component, $\tilde{T}^O_{i,root}(t)$ is the moment vector produced on the rotor blade and transmitted to the root/hinge due to its stiffness.

Therefore, it depends on the type of blade hub support. For a hingeless rotor blade, two different approaches are possible to obtain $\tilde{T}^{O}_{i,root}(t)$.

$$\tilde{T}^{O}_{i,root}(t) = [A_i]^{-1} \left\{ \begin{array}{c} GJ(eR)\,\phi'(eR,t) \\ -EI_y(eR)\,w''(eR,t) \\ EI_z(eR)\,v''(eR,t) \end{array} \right\}, \quad i = 1, ...N_b \tag{3.147}$$

Equation (3.147) presents the first method, which is denominated modal method, and is based on the product of the root stiffness and the second spatial derivative of modal deflection at the root for flap and lag, and the first spatial derivative for torsion. This method is numerically efficient, however, numerical differentiation can lead to numerical errors. These errors can be amplified if a reduced number of vibration modes is used. As an alternative, a force summation method can be deployed, where the total loads exherted on the blade are integrated along the blade. The summation method can be expressed as

$$\tilde{T}^{O}_{i,root}(t) = \int_{eR}^{R} \tilde{r}^{O}_{cg/A_i} \times \mathrm{d}\tilde{f}^{O}_{cg} + \int_{eR}^{R} \mathrm{d}\tilde{m}^{O}_{cg}, \quad i = 1, ...N_b \tag{3.148}$$

If the rotor is equipped with spring articulated rotor blades, $\tilde{T}^{O}_{i,root}(t)$ is due to the discrete stiffness of the springs and the respective local flap/lag angles. If the rotor is freely articulated about an axis, no moment is transferred to the hinge about that axis. If the presence of a lead-lag damper is required, the moment consequence of this mechanisim needs to be added. In the present work, the methodology proposed by Titurus and Lieven (Ref. 195) is used to model the behaviour of the lag damper.

3.6.7 Integrated trim-aeroelastic model

Figure 3.13 presents the flowchart of the integrated trim-aeroelastic model. It can be divided in two main modules. These are the integrated aeroelastic model and the rotor trim model. For a given set of control pitch angles $(\theta_0, \theta_{1c}, \theta_{1s})$, the integrated aeroelastic model calculates the resultant total rotor force and moment vectors, $\tilde{F}^{O}_{rotor}(t)$ and $\tilde{T}^{O}_{rotor}(t)$, and the equivalent tip flapping angles. The integrated aeroelastic model comprises two main modules. In the first place, the wake geometry is solved for the prescribed rotor loading. Once the geometry of the wake is converged, the rotor inflow is calculated and fed into the aeroelastic model which is run until one-per-rev (1P) periodicity is reached. Once

periodicity is reached, the distribution of bound circulation, total rotor force and moment vectors, and flapping angles are calculated. The new distribution of bound circulation is fed into the free-vortex wake model and the geometry and inflow updated. This process is repeated until the bound circulation has converged. The distribution of bound circulation is considered to be converged when the RMS change between two consecutive iterations falls below a threshold. The RMS change in circulation is defined as

$$RMS_{\Gamma^b} = \frac{1}{N_\psi N_s}\sqrt{\sum_{\psi:i=1}^{N_\psi}\sum_{r:k=1}^{N_s}\left(\Gamma^b_{i,k} - \Gamma^b_{i-N_\psi,k}\right)^2} \tag{3.149}$$

The converged rotor force and moment vectors are fed into the rotor trim model. A globally-convergent Broyden's method has been implemented in the present work to obtain the control angles which satisfies the wind tunnel rotor trim. The latter consists on the generation of rotor hub moments and thrust equal to the prescribed values.

3.7 Conclusions

This chapter has described the methodology developed in the present work. As a starting point, the reference frames used in the proposed methodology were defined, and rotation matrices for the transformation of vectorial quantities between frames were formulated. After, a mathematical formulation for modelling of coupled flap-lag bending and torsion vibration characteristics of helicopter rotor blades was presented. The model was formulated based on the application of Lagrange's equation of motion to the three-dimensional kinematics of a non-uniform rotating blades. Spatial solutions of classical theories were deployed as assumed deformation functions to enhance the computational efficiency of the method. The method was reduced to a set of closed-form integral expressions compatible with different structural boundary conditions. The next step was the formulation of the three-dimensional kinematics of elastic rotor blades. The derived expressions account for the effect of manoeuvres, application of cyclic pitch, elastic deformations, and non-linearities associated with rotating systems. After, the free-vortex wake model used to estimate the rotor inflow was formulated. The computational implementation utilised to enhance the computational efficiency was presented. The approach chosen to include the

effect of viscosity and fuselage interferences on the inflow model was described and the roll-up vortex model formulated. The next step was the formulation of the blade aerodynamic model, a non-linear unsteady lifting line. The unsteady aerodynamic loads, calculated using the Leishman-Beddoes indicial response functions, were linked with the distribution of bound circulation using the theorem of Kutta-Joukowski. This links the aerodynamic loading with the geometry of the wake and its inflow. Next, the time-marching aeroelastic model was presented. The aeroelastic model was coupled with the rotor inflow, three-dimensional kinematics, modal characteristics, and blade aerodynamic model with the use of the convolution integral. The convolution integral was solved using a combination of a predictor-corrector scheme and a fifth-order accurate numerical recurrent evaluation of the Duhamel's integral. In the last place, the integrated loads of the converged aeroelastic model were coupled with a globally convergent Broyden's method for the solution of the rotor trim.

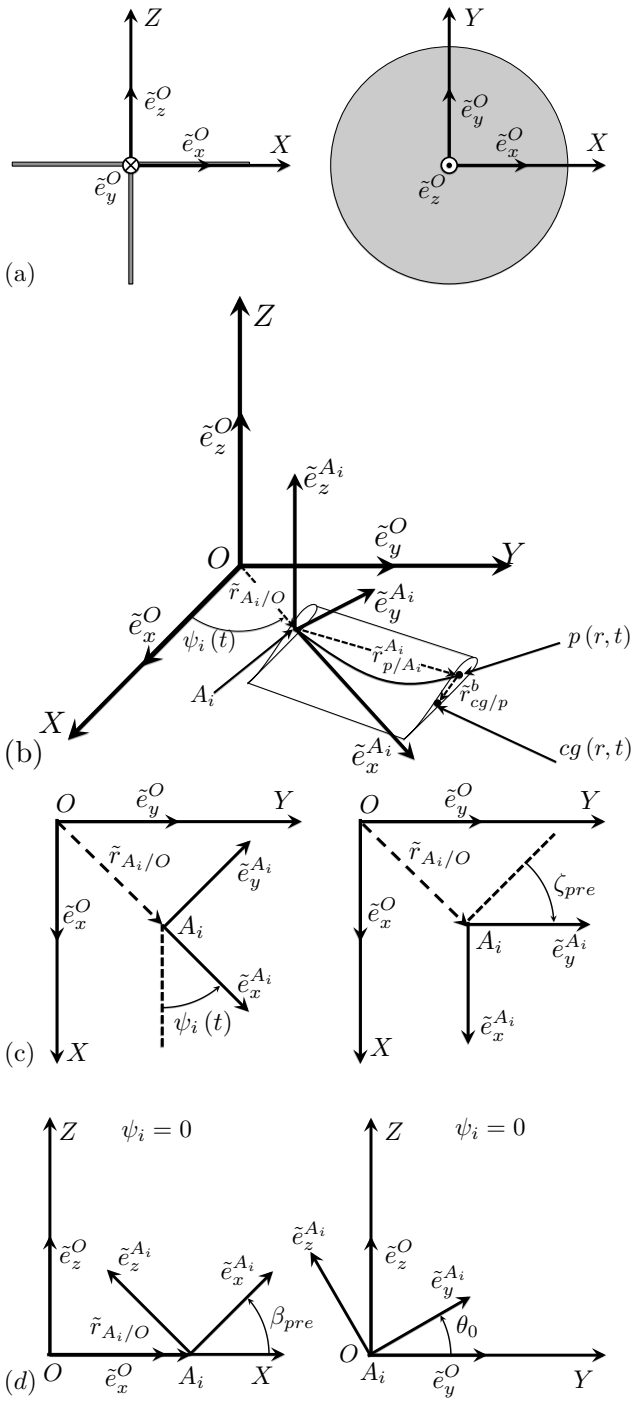

Figure 3.1: Reference frames: (a) global non-rotating frame O, (b) rotating frame A_i, (c) azimuth and presweep angles definition, (d) precone and collective pitch angles definition.

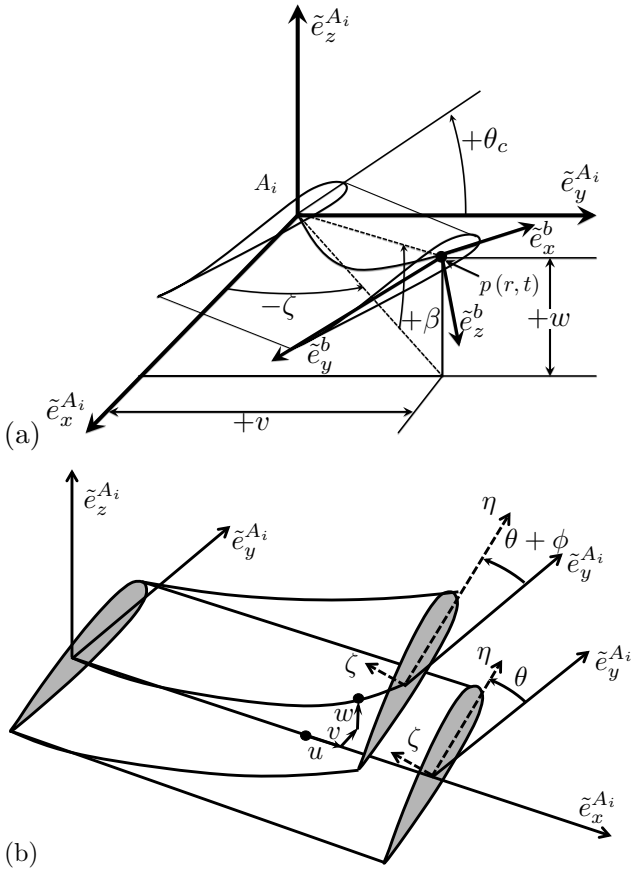

Figure 3.2: Reference frames: (a) blade element fixed b reference frames, (b) cross-section frame of reference.

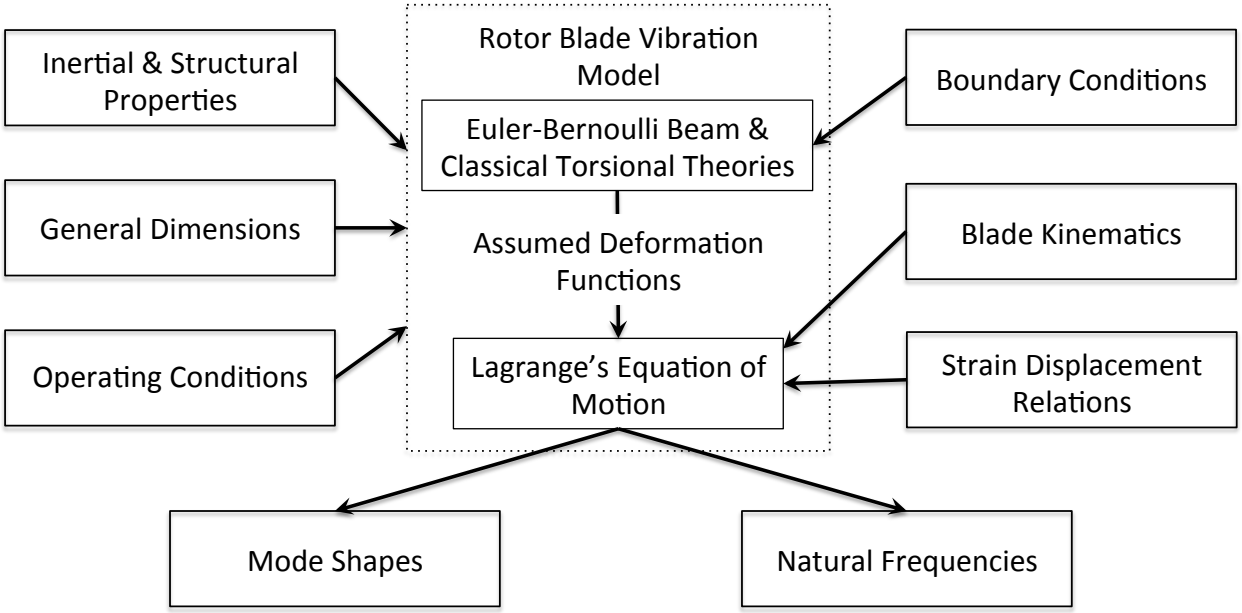

Figure 3.3: Rotor blade vibration model flowchart.

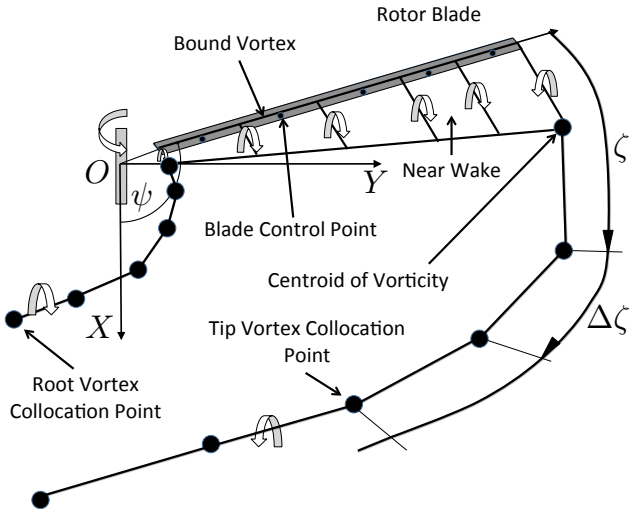

Figure 3.4: Sketch of the Lagrangian discretisation of the vortex filaments trailed from one blade.

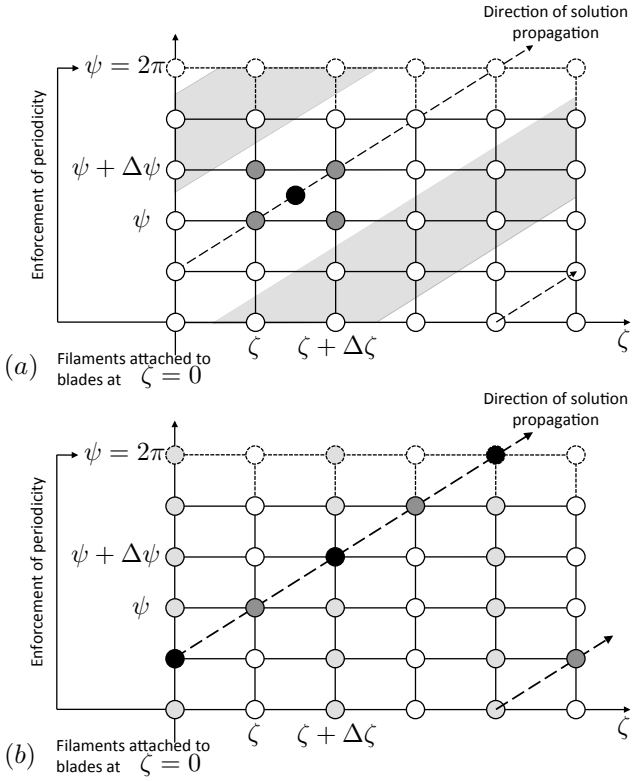

Figure 3.5: Discretised wake computational domain: (a) five-points finite difference stencil and computational subdomains, (b) different types of Lagrangian markers in velocity interpolation scheme.

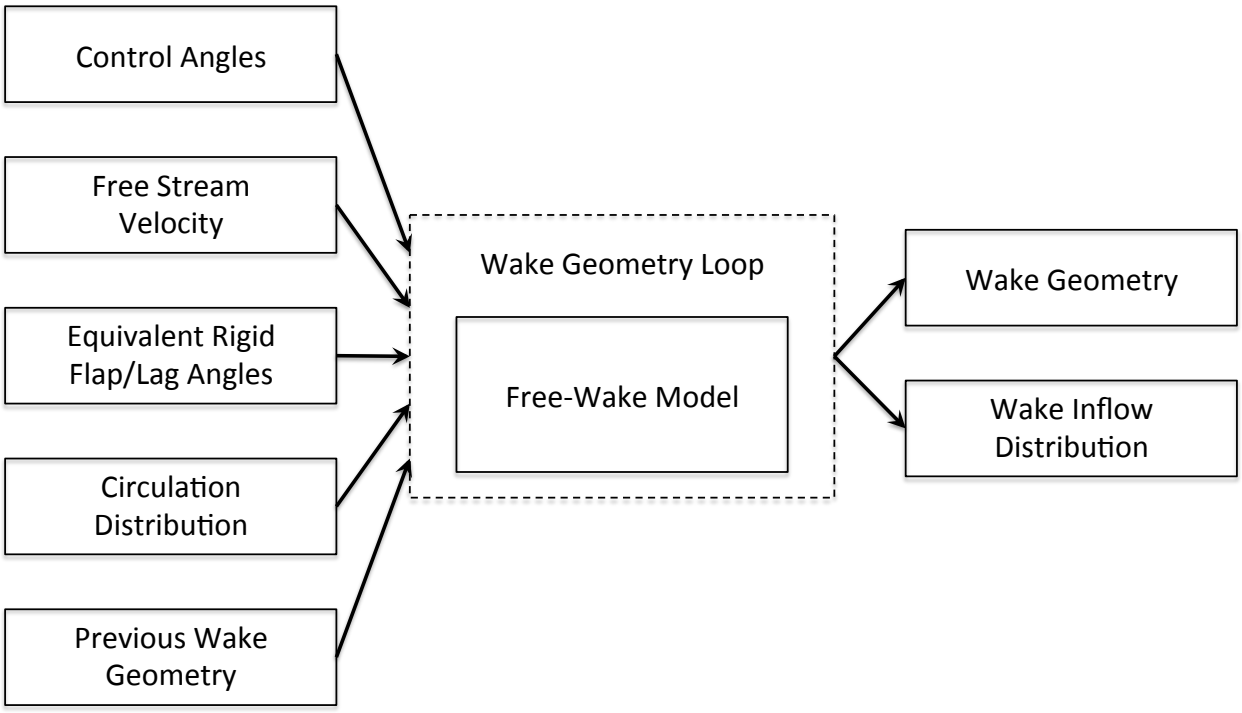

Figure 3.6: Free-vortex wake model inputs and outputs.

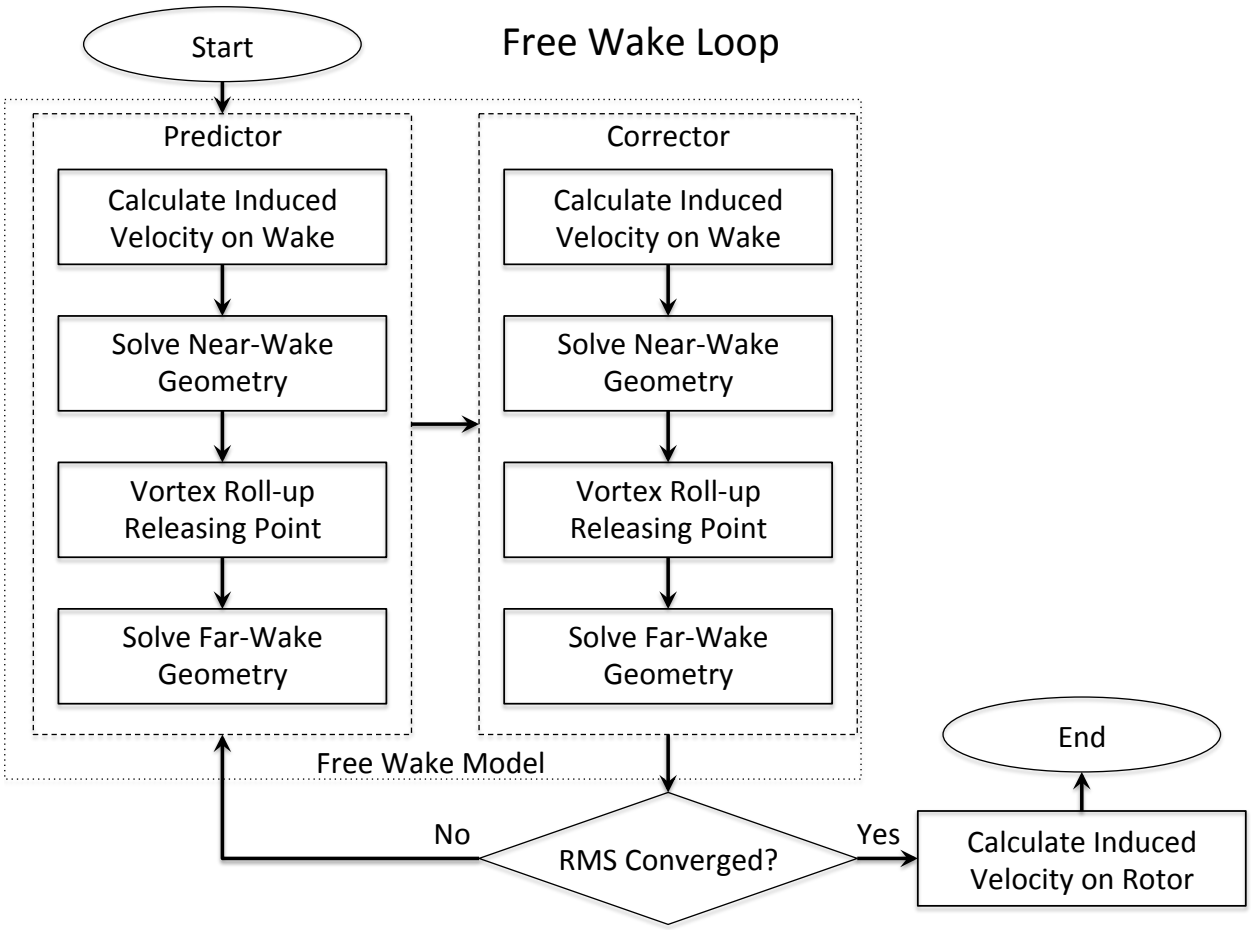

Figure 3.7: Free-vortex wake model flowchart.

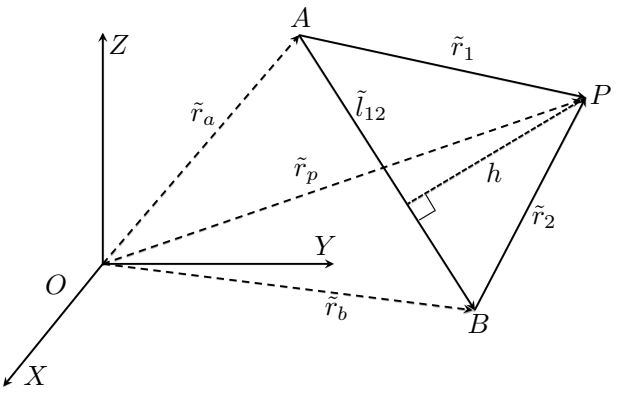

Figure 3.8: Definition of position vectors for the induced velocity calculation using Biot-Savart Law.

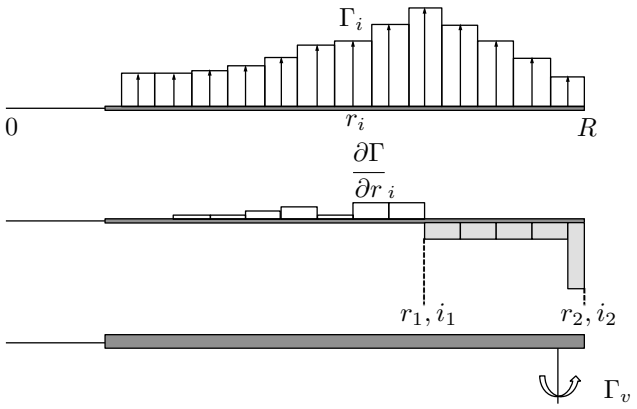

Figure 3.9: Sketch of the vortex roll-up model.

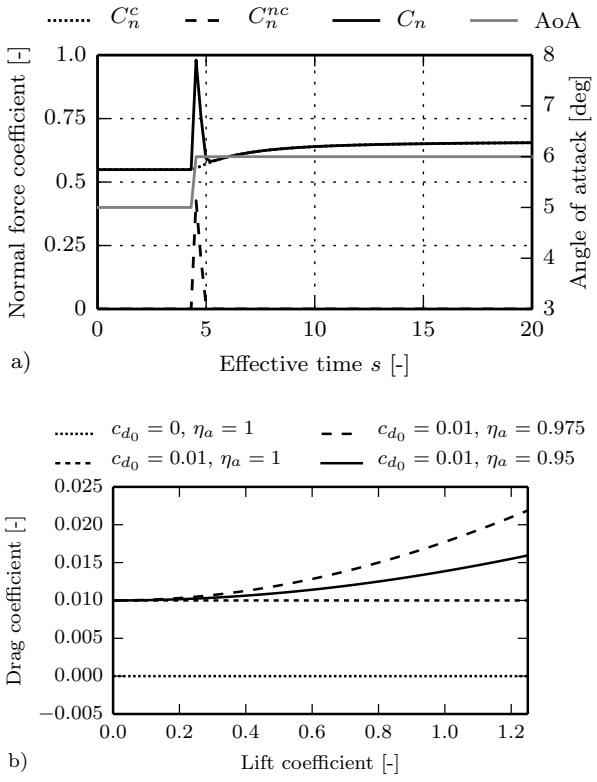

Figure 3.10: Two-dimensional blade aerodynamics: (a) sketch of the evolution of the normal force coefficient with time after a step change in angle of attack, (b) effect of leading edge suction recovery factor and zero lift drag coefficient on the aerodynamic polar.

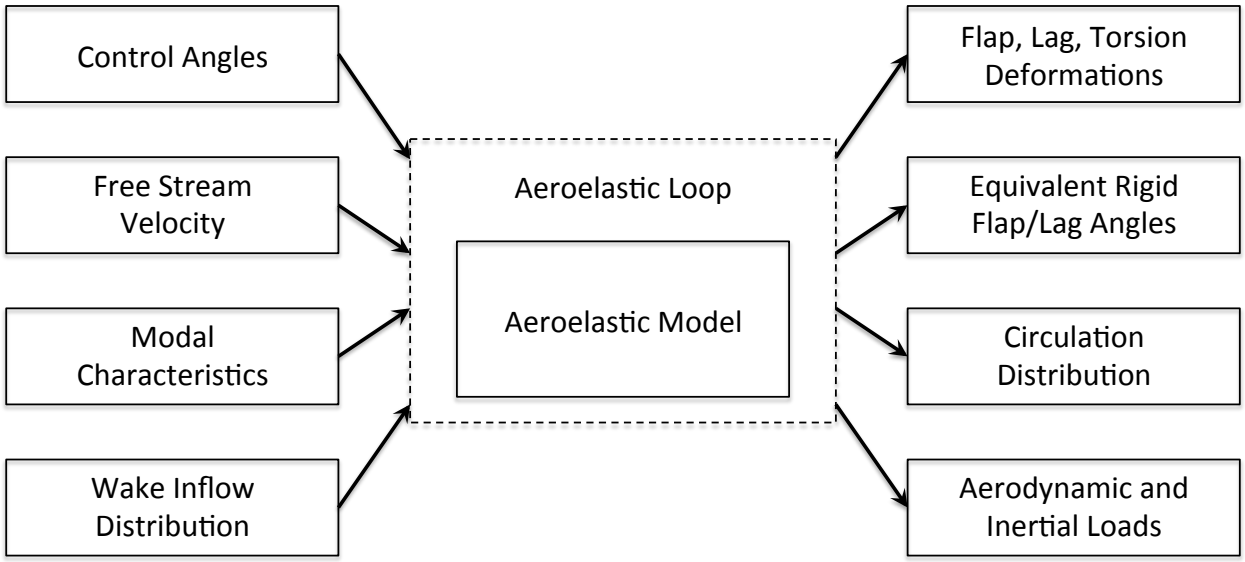

Figure 3.11: Aeroelastic model inputs and outputs.

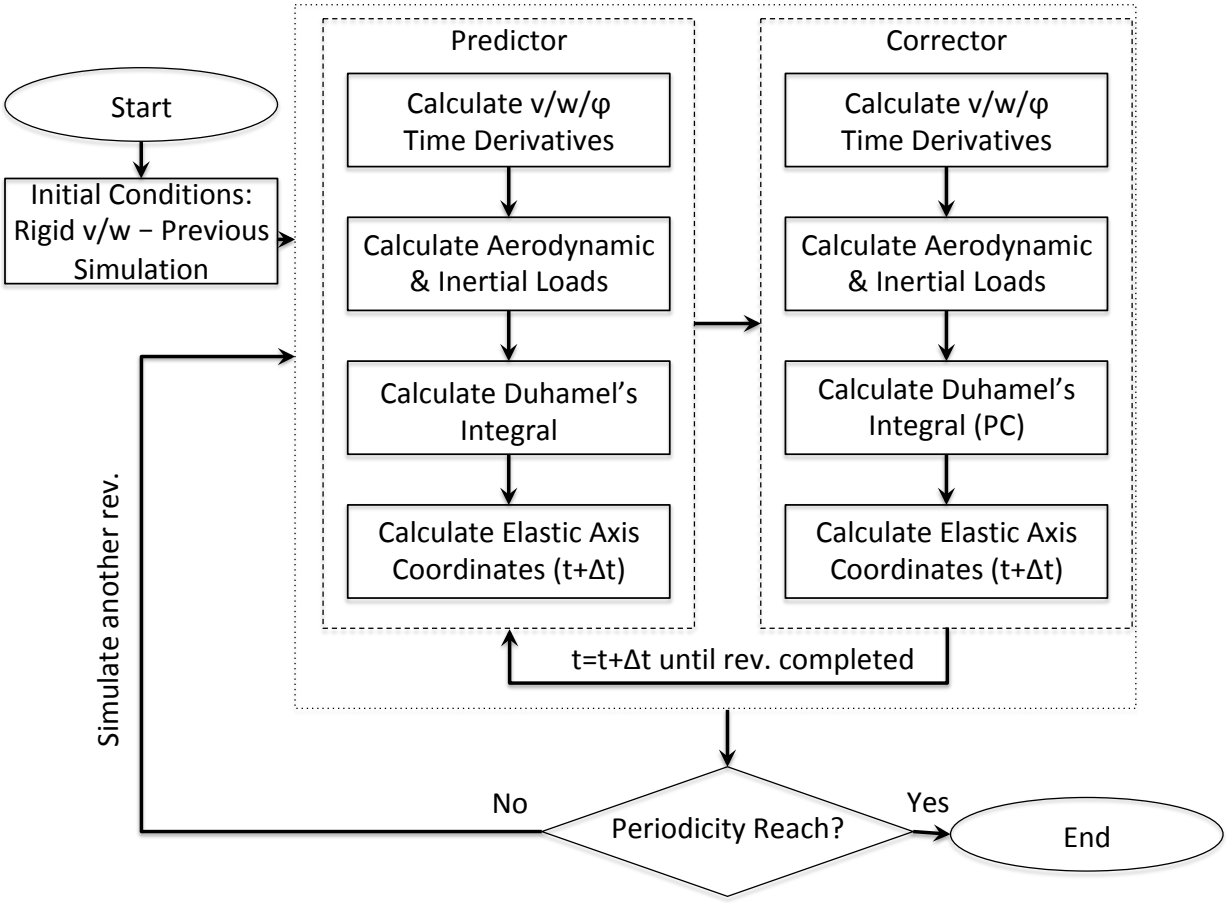

Figure 3.12: Aeroelastic model flowchart.

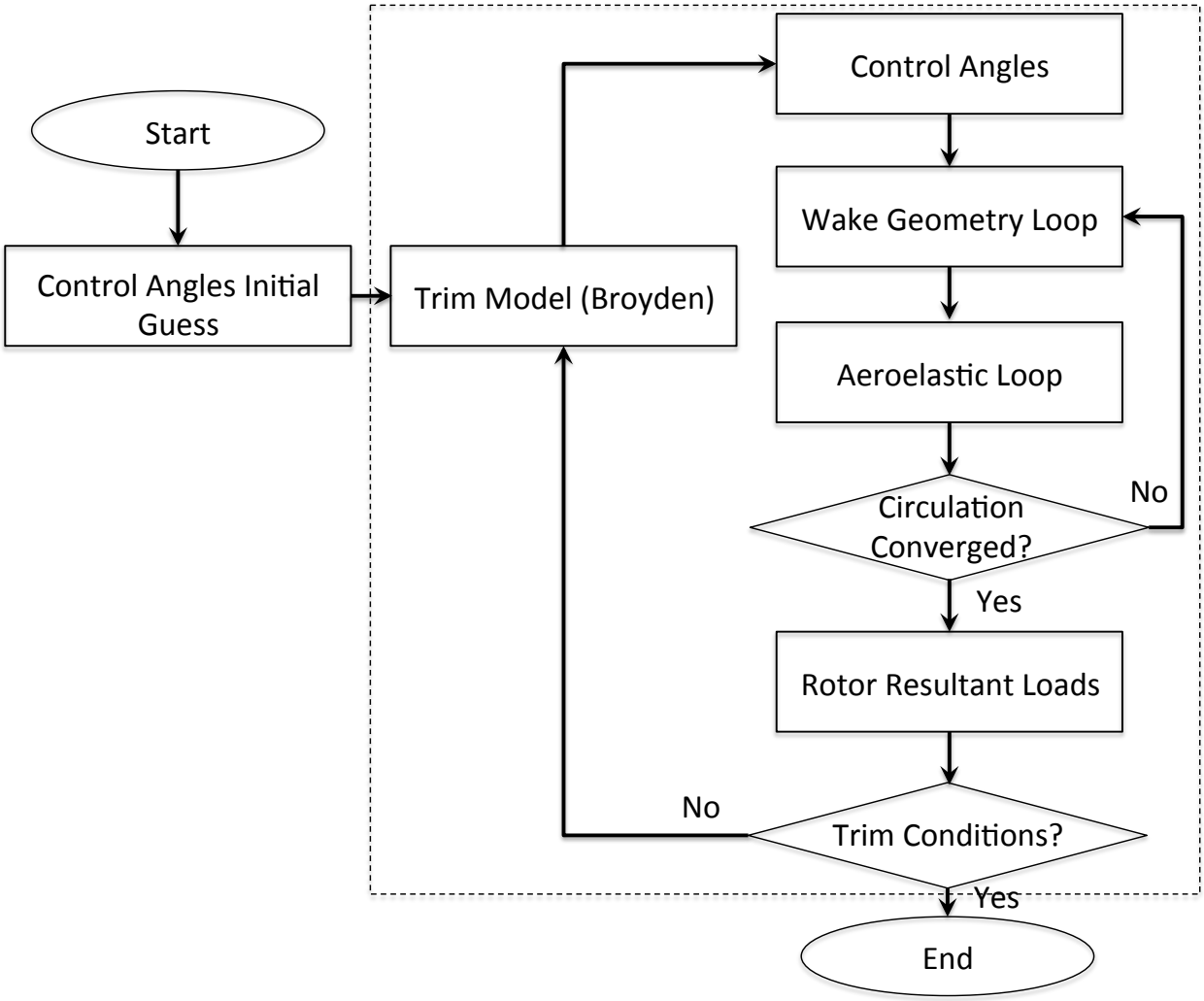

Figure 3.13: Integrated trim-aeroelastic model flowchart.

Chapter 4

Results and Discussion: Structural Dynamics

A novel mathematical formulation for modelling of coupled flap/lag bending and torsion vibration characteristics of helicopter rotor blades was presented in Section 3.2. This formulation solves the weakness of previous methods: it models coupling between DOFs, it is expressed in closed form expressions readily available for any type of hub support, it requires a limited amount of information, and it deploys a reduced number of assumed deformation functions to enhance the efficiency. The proposed formulation is implemented in FORTRAN 90/95 and its performance and predictive capability are evaluated in this chapter.

In the first place, the performance of the model is assessed numerically and computationally for a small scale hingeless rotor blade and a full scale articulated rotor blade. In the second place, the predictive capability of the method is compared with experimental measurements and FEA calculations for two small scale hingeless rotor blades. After, a comparison between the results obtained with the proposed formulation and multi-body analysis methods is presented for a small scale hingeless rotor blade and a full scale articulated rotor blade. In the last place, the effect of different geometrical parameters on the coupling between modes of vibration is assessed and the dependence of the method's prediction on the gyroscopic coupling is evaluated.

4.1 Numerical Performance

The numerical performance of the proposed method has been assessed by analysing the impact of the number of assumed deformation functions per DOF on the convergence of the natural frequencies. Two different rotor blade models have been used for this study: the full scale articulated Aérospatiale SA330 helicopter main rotor described in Ref. 196 and the hingeless HART II rotor blade. The HART II rotor blade is a 40% Mach scaled model of the hingeless BO-105 helicopter rotor blade used in the Higher harmonic control Aeroacoustics Rotor Test program HART II. The main objective of the HART II program was to generate a comprehensive database of rotor loads, pressure distributions, blade deformations, acoustic radiations, and wind tunnel data for the small scale rotor during descending flight. A detailed description of the HART II test and rotor blade can be found in Refs. 197–201 and Refs. 202, 203 respectively.

Figure 4.1a presents the influence of the number of assumed deformation functions per DOF on the convergence of the natural frequencies for the hingeless HART II rotor blade. The natural frequencies were normalised with the nominal rotorspeed, $\Omega_0 = 109.13\,\mathrm{rad\,s^{-1}}$. In Fig. 4.1a, the label refers to the dominant DOF. The first two natural modes (1L and 1F) are highly independent of the number of assumed deformation functions. Convergence of the normalised natural frequencies is attained with only two assumed deformation functions per DOF, and no further variation is observed as a result of the inclusion of a higher number of assumed deformation functions. The estimation of the first 8 flap and lag dominant natural modes of vibration (1L, 1F, 2F, 2L, 3F, 4F, 3L, and 5F) is attained with the use of 4 modes per DOF. The calculation of torsional vibration modes requires the deployment of a larger number of assumed deformation functions, e.g. 8 assumed deformation functions per DOF are required to reach convergence on the first 2 torsional vibration modes (1T and 2T).

Figure 4.1b presents the impact of the number of assumed deformation functions per DOF on the convergence of the natural frequencies for the full scale articulated Aérospatiale SA330 helicopter main rotor blade. The natural frequencies were normalised with the nominal rotorspeed, $\Omega_0 = 27.0\,\mathrm{rad\,s^{-1}}$. Once again, the label refers to the dominant DOF. The first two natural modes (1L and 1F) correspond to rigid modes of vibration, and

the natural frequency is completely independent of the number of assumed deformation functions. Convergence on the solution of these modes is reached with the use of one assumed deformation function per DOF. The calculation of elastic modes of vibration requires a higher number of assumed deformation functions. For the first 10 natural modes of vibration, convergence on the natural frequencies is obtained with the use of 6 modes per DOF with the exception of the second and third flap modes (2F and 3F). The convergence of these modes is attained using 10 assumed deformation functions.

Thus, the method proposed for the rapid estimation of helicopter modal characteristics has been proven to exhibit excellent numerical behaviour. A relatively small number of assumed deformation functions per DOF is required for the convergence of the final natural frequencies. This is highly associated with the deployment of assumed deformation functions derived from classical methods. These better approximate the actual mode shape accelerating the convergence of the method. The analytical availability of the first and second assumed deformation function spatial derivatives does not introduce any numerical error. As a result, an infinite number of vibration modes can be theoretically calculated. Additionally, the lack of numerical instabilities found in the analyses carried out, presents this method as a robust approach for the structural treatment of helicopter rotor blades.

4.2 Computational Performance

The computational performance of the method has been evaluated by analysing the dependence of the required computational time on the number of assumed deformation functions. The small scale hingeless HART II rotor blade described in Refs. 202, 203 and the full scale articulated Aérospatiale SA330 helicopter main rotor blade described in Ref. 196 have been used as study cases. The measured computational time comprises the allocation of system variables, solution of the classical methods, population of the dynamic system matrices, solution of the QEP, eigenvector normalisation, and calculation of the final mode shapes. The method has been implemented in serial FORTRAN 90/95 code. The calculations have been carried out on a personal computer equipped with 8 Gigabytes (GB) of Random Access Memory (RAM) and a Central Processing Unit (CPU) operating at 1.7 Gigahertz (GHz) without parallel processing.

Figure 4.2a presents the evolution of the required computational time with the number of assumed deformation functions for the hingeless HART II rotor blade. A quadratic relation is identified. Thus, the convergence of the method needs to be quick to avoid computational overhead. Figure 4.1a shows that the first 10 natural modes can be estimated with the use of 8 assumed modes per DOF. This fairly quick convergence requires a computational time of 0.6 seconds.

Figure 4.2b presents the relation between the required computational time and the number of assumed deformation functions for the articulated Aérospatiale SA330 helicopter main rotor blade. A quadratic relation is identified as well for the articulated rotor blade. Figure 4.1b shows that 10 assumed deformation functions per DOF are required to obtain the first 10 modes of vibration, which essentially means that a converged solution can be calculated in only 0.6 seconds. Even though the number of assumed deformation functions is higher for this case than in the HART II case, the required computational time is the same. This is justified by the lower magnitude of the natural frequencies of the articulated rotor blade. Thus, the required time to obtain the assumed deformation functions is smaller, and the required computational time to obtain the final coupled modal characteristics is reduced.

Excellent computational performance has been identified for the proposed method for the rapid estimation of helicopter modal characteristics. Fully converged solutions with 10 modes of vibration have been obtained in 0.6 seconds for a small scale hingeless rotor blade and a full scale articulated rotor blade on a low-end personal computer. The excellent computational performance enables an efficient integration of the method into the aeroelastic model.

4.3 Comparison with Experiment and FEA

The agreement of the proposed method results with experimental measurements and FEA results is assessed for two small scale hingeless rotor blades. These are the previously presented HART II rotor blade described in Refs. 202, 203 and a torsionally soft untwisted blade. The latter is a small scale, 1.92m diameter, torsionally soft, untwisted hingeless helicopter rotor. The blade was designed to have uniform properties from 9.5% of the

blade radius to the tip. The two bladed rotor was tested in Ref. 204 at hover conditions at different rotor speeds ranging from 0 to 1000rpm. The objective of Ref. 204 was to quantify the modal frequencies, steady blade bending moments, and lead-lag damping.

Figure 4.3 presents the resonance chart calculated for the small scale, torsionally soft, hingeless rotor described in Ref. 204. Natural frequencies and rotorspeed have been normalised with its nominal rotorspeed, $\Omega_0 = 105\,\mathrm{rad\,s^{-1}}$. Solid and dashed lines represent the natural frequencies predicted with the present approach and FEA respectively. Experimental measurements in vacuum reported in Ref. 205 have been labelled as Exp. Excellent agreement between experimental measurement and results calculated with the proposed method is observed. The averaged relative errors between both experimental measurements and the calculations of the proposed method across the whole rotorspeed range are of the order of 0.3%, 1.6%, 0.5%, 1.7%, and 0.5% for the first 5 vibration modes respectively. The comparison of calculations of the proposed method with FEA results reported in Ref. 205 leads to the identification of average relative errors of the order of 1.1%, 1.0%, 1.3%, 0.5%, and 0.5%. The order of magnitude of these relative errors is representative of a method with excellent agreement with FEA.

The proposed method is able to predict transitions between modes of vibration, i.e. changes in the dominant DOF for a given natural mode of vibration. The transition between 2F and 1T modes can be observed in the magnified area of Fig. 4.3 as the convergence and posterior divergence of the frequencies of both modes. Apart from the convergence-divergence of the natural frequencies, the flapping amplitude is reduced whilst the torsional deformation is increased for the 3rd natural mode in the convergent region. This process continues in the divergent region until torsion becomes the dominant DOF. The opposite phenomenon takes place for the 4th natural mode. This can only be predicted with methods able to model coupling between modes of vibration such as the proposed approach.

Figure 4.4 presents the calculated dominant mode shapes for the first 5 modes of vibration of the hingeless rotor described in Ref. 204 at zero speed. Excellent agreement with experimental and FEA data reported in Ref. 205 is observed for all modes presented. The calculated dominant mode shapes for the first 5 modes of vibration of the hingeless rotor described in Ref. 204 at nominal speed, $\Omega_0 = 105\,\mathrm{rad\,s^{-1}}$, are presented in Figure 4.5.

Very good agreement with experimental and FEA data reported in Ref. 205 is observed for all modes except for the 1st flap mode where a significant variation in mode shape is noticed.

Figure 4.6 presents the resonant chart calculated for the small scale hingeless HART II rotor blade. Natural frequencies and rotorspeed have been normalised with the nominal rotorspeed $\Omega_0 = 109.13\,\mathrm{rad\,s^{-1}}$. Solid lines represent natural frequencies calculated with the present approach. Experimental measurements from Refs. 200,206 taken in vacuum for the 2nd to 10th vibration modes have been superimposed in Fig. 4.6 as Exp. Experimental tests have been only undertaken at non-rotating conditions and no comparison can be done at higher rotorspeeds. It is noted that the experimental measurements of the 1st torsion mode present scatter. This has been attributed to variations in blade weight consequence of the attachment of instrumentation to the blade (Ref. 203). The calculated natural frequencies exhibit very good agreement with the experimental measurements. Relative errors of the order of 0.2%, 0.74%, 0.78%, 0.64%, 2.24%, 0.96%, 2.94%,0.72,% and 2.0% are observed for the 2nd to 10th natural modes respectively. For this particular configurations five different transitions between modes of vibration are observed. The 1st one involves 1F and 1L. The 2nd one relates 1T and 3F. The 3rd transition connect 2L and 4F. The 4th one associates 2T and 5F. Finally a 5th transition between 3L and 5F is identified.

Potential sources of errors between the estimated frequencies and the experimental measurements and FEA results can be identified. The first one is the truncation scheme deployed during the derivation of the presented formulation, terms involving transverse displacements and/or torsion deformations of order cubic or higher have been eliminated. This leads to the omission of certain nonlinear terms which might be relevant at high speed conditions. Shear deformation, rotary inertia, and other secondary nature nonlinear terms have also been neglected. Those could lead to significant variations in predicted natural frequencies at high speed. A third source of error is the normalisation condition applied to the assumed deformation functions, for small scale rotors the assumption of generalised mass equal to 1.0 can lead to a potential breakdown of the linearisation associated with the small displacement formulation as reported in Ref. 76. A fourth source of error is the uncertainty of some inertial and structural properties not readily available in the public domain, which have been estimated based on sensible best guess engineering criteria.

These include: blade cross-sectional integrals $B_{1,2}$, area centroid offset from the elastic axis e_A, extensional stiffness EA, and blade mass moments $I_{1,2}$. A fifth source of error is the uncertainty of the experimental measurements themselves. The introduction of instrumentation can cause variations in the vibration characteristics of the rotor blade. Additionally, a deficient vacuum isolation can lead to deviation in the modal characteristics due to aerodynamic damping.

4.4 Comparison with Multi-Body Analysis Methods

The proposed approach is compared with multi-body analysis methods extensively used in comprehensive rotorcraft codes. To carry out this comparison, resonant charts are calculated for the small scale hingeless HART II rotor described in Refs. 202, 203 and the full scale articulated Aérospatiale SA330 helicopter main rotor blade described in Ref. 196. Additionally, the dominant mode shapes are calculated and compared for the HART II rotor blade at its nominal rotational speed.

Figure 4.6 presents the resonant chart for the HART II rotor. Natural frequencies and rotational speed have been normalised with the nominal speed, $\Omega_0 = 109.13\,\mathrm{rad\,s^{-1}}$. Solid and dashed lines represent predictions of the proposed method and CAMRAD calculations respectively. The averaged relative errors across the rotorspeed range are of the order of 3%, 2%, 2%, 2%, 2%, 3%, 4%, 2%, 3%, and 5% for the first 10 natural frequencies. The larger deviations from CAMRAD calculations can be justified by the deployment of different sets of mass and structural properties. The calculations carried out with CAMRAD, reported in Ref. 207, were based on the original set of structural data (Ref. 200). However, Jung *et al.* (Ref. 203) further studied the structural properties and found that the initial documentation overestimated the properties by 5 to 15%. The structural properties obtained by Jung *et al.* (Ref. 203) have been used in the present work. The excellent agreement of the Lagrangian estimation with the experimental measurements shown in Fig. 4.6 justifies the use of the newest set of structural properties.

Figure 4.7 shows the calculated dominant mode shapes for the first 10 modes of vibration of the small hingeless HART II rotor blade at its nominal speed, $\Omega_0 = 109.13\,\mathrm{rad\,s^{-1}}$. The calculations carried out with the Lagrangian method and CAMRAD essentially superimpose

for the three first flap mode shapes. A slight phase discrepancy is observed for the 4th and 5th flap modes shapes which is attributed to the differences in structural properties. Despite the small discrepancy in phase angle, the agreement between both methods in the shape and amplitude is excellent. The three first lag modes calculated by both means completely superimpose, leading to an excellent agreement between methods. Torsion modal characteristics exhibit excellent agreement between multi-body and Lagrangian calculations. Small differences are observed near the root, which can be attributed to the use of different root boundary conditions. Overall, excellent agreement in the shape and amplitude of the modes estimated with the proposed approach and multi-body analysis methods is observed for all the natural modes.

Figure 4.8 presents the resonant chart for the articulated Aérospatiale SA330 helicopter main rotor. Natural frequencies and rotational speed have been normalised with the nominal speed, $\Omega_0 = 27.0\,\mathrm{rad\,s^{-1}}$. Solid lines represent Lagrangian predictions. CAMRAD calculations at nominal rotorspeed, which were reported in Ref. 196, have been superimposed in Fig. 4.8 as CMRD. Excellent agreement between the values calculated with the Lagrangian formulation and CAMRAD is observed. The discrepancies between both methods are smaller than 1% for the first 6 natural modes.

The natural frequencies estimated with the proposed approach exhibit good agreement with those calculated with multi-body dynamics codes. Discrepancies of the order of 3%, justified by the use of different structural properties, have been identified for the first 10 natural frequencies of the small scale HART II rotor. Excellent correlation between mode shapes calculated with both methods is observed. Excellent agreement between Lagrangian and CAMRAD natural frequencies predictions for the full scale articulated Aérospatiale SA330 helicopter main rotor is found, with discrepancies smaller than 1% for the first 6 natural modes. The overall very good agreement of both techniques makes the proposed approach a computationally efficient alternative to multi-body dynamics.

4.5 Coupling Analysis

As a consequence of the symmetry of the mass and stiffness matrices and the antisymmetry or the gyroscopic matrix, pairs of complex conjugate eigenvalues and eigenvectors are obtained solving the QEP of Eq. (3.58). If the gyroscopic matrix is eliminated and a solution of the form $\{q\} = \{\bar{q}\} \sin \lambda t$ is assumed, the QEP is reduced to the following GEP

$$\left([S] - \lambda^2 [M] \right) \{\bar{q}\} = [Q(\lambda)] \{\bar{q}\} = \{0\} \tag{4.1}$$

where λ is a real eigenvalue and $\{\bar{q}\}$ the associated real right eigenvector. Equation (4.2) presents the resultant undamped mode equation as meant to be introduced in the forced response of the dynamic system, where λ_i and $X_i^r(x)$ are real numbers representing the eigenvalues and final mode shapes calculated with Eq. (3.61).

$$\chi_i^{r,U}(x,t) = X_i^r(x) \cos \lambda_i t \tag{4.2}$$

In Eq. (4.2), $\chi_i^{r,U}(x,t)$ is the undamped (U) time-dependent transverse displacement/torsional deformation for the ith natural mode and r DOF.

If the gyroscopic matrix is included in the analysis, pairs of complex conjugate eigenvalues (λ_i, $\overline{\lambda_i}$) and mode shapes ($X_i^r(x)$, $\overline{X_i^r}$) are obtained. The superimposition of pairs of complex conjugate time-dependent functions ($X_i^r(x) \exp(\lambda_i t)$, $\overline{X_i^r}(x) \exp(\overline{\lambda_i} t)$) leads to Eq. (4.3). Where $\chi_i^{r,D}(x,t)$ represents the damped (D) time-dependent transverse displacement/torsional deformation for the ith natural mode and r DOF.

$$\chi_i^{r,D}(x,t) = |X_i^r(x)| \cos \left(\Im\left(\lambda_i\right) t + \arctan \frac{\Im\left(X_i^r(x)\right)}{\Re\left(X_i^r(x)\right)} \right) e^{\Re(\lambda_i) t} \tag{4.3}$$

As previously discussed in Section 3.2.3, a QEP with symmetric mass and stiffness matrices, and skew-symmetric gyroscopic matrix is associated with pairs of purely imaginary ($\Re\left(\lambda_i\right) = 0$) eigenvalues. As a result, the time-dependent decay term $\exp(\Re\left(\lambda_i\right) t) = 1$ and no damping is present. Although the gyroscopic matrix does not introduce any time-dependent decay, it introduces a phase angle $\varphi_i^r(x) = \arctan \frac{\Im\left(X_i^r(x)\right)}{\Re\left(X_i^r(x)\right)}$ which depends exclusively on the phase angle of the complex number $X_i^r(x)$. The variation of the phase angle $\varphi_i^r(x)$ across the blade leads to a time-dependent mode shape variation. Therefore, the mode shape is not constant with a sinusoidal amplitude oscillation as it was observed for the undamped system. In addition to the non-uniformity along the span, the phase angle $\varphi_i^r(x)$ depends on the DOF r and phase delays between DOFs can be found.

Table 4.1 quantifies the effect of the inclusion of the gyroscopic matrix on the normalised natural frequencies of the small scale hingeless helicopter rotor blade model described in Ref. 204. The analyses were carried out at the nominal speed, $\Omega_0 = 105.0\,\mathrm{rad\,s^{-1}}$. Normalised frequencies obtained from the QEP are shown in columns labelled as Q $\left(\frac{\omega}{\Omega_0}\right)$ whilst the solutions of the GEP are presented as percentage deviations from the QEP data and labelled as G (%). The uncoupled case refers to a case study with zero offset between the centre of gravity and the elastic axis (e_M), blade pitch angle (θ_0), pretwist (θ'). and precone (β_{pre}). Whilst the coupling source of the other cases is specified in the top row.

For the uncoupled case, small discrepancies between the QEP and GEP frequencies are observed for the first torsion (1T) and second flap (2F) modes of vibration. That suggests a soft gyroscopic coupling between flapwise displacement and torsional deformation. To corroborate this assumption, Hinton diagrams of the mass, gyroscopic and overall stiffness matrices are presented in Fig. 4.9 for this case study. A Hinton diagram represents the magnitude and sign of each matrix element with a square. The area of the square is proportional to the absolute value of the matrix element, while the sign of the element is determined by the color (white for positive values and black for negatives). As previously stated, each matrix comprises 9 partitions. These have been arranged as follows: 1st partition column/row corresponds to torsion, 2nd partition column/row to lead-lag, and 3rd partition column/row to flap. From Fig. 4.9 it is easy to observe the symmetry of the mass and overall stiffness matrices and the anti-symmetry of the gyroscopic matrix. Thus, $M^{r,s}_{i,j} = M^{s,r}_{j,i}$, $S^{r,s}_{i,j} = S^{s,r}_{j,i}$, and $C^{r,s}_{i,j} = -C^{s,r}_{j,i}$. In Fig. 4.9 only the diagonal blocks are non-zero for the mass and stiffness matrices. However, a non-diagonal block appears in the gyroscopic matrix which couples flap and torsion. The coupling strength increases with the proximity of the flap and torsion modes in the frequency spectrum and therefore the intensity of the coupling is higher for the coupling between 1T and 2F for this particular case of study.

Note in Fig. 4.9 the absence of gyroscoping coupling between flap and lag. The gyroscopic effect can be explained in terms of conservation of angular momentum. If zero net torque is applied to the system, the angular momentum of a particle or system remains constant. Consequently, a reduction in the effective radial position of a particle results in a rise of the tangential velocity to keep the angular momentum constant. For this particular

case, the effect of a inwards radial dislocation produces a lag dislocation in the direction of the rotation which increases the relative velocity. As a result, the angular momentum is kept constant. The radial dislocation or axial displacement u of was defined in terms of its first spatial derivative u' (Eq. (3.22). For the uncoupled case the axial displacement reduces to

$$u\left(x\right)=\int_{0}^{x}\left(\frac{\int_{x}^{L}m\Omega^{2}(\varrho+eR)\mathrm{d}\varrho}{EA}-\frac{1}{2}v'^{2}-\frac{1}{2}w'^{2}\right)\mathrm{d}\lambda \tag{4.4}$$

The first term of Eq. (4.4) does not change with time and is associated with centrifugal stiffening, the second term is the axial displacement due to a lag transverse dislocation, and the third one is the due to a flap transverse movement. Although the second and third terms are not negligible in terms of order of magnitude, the assumption of neglecting products of v, w,and ϕ of third degree or higher eliminates these terms from the gyroscopic matrix $[C]$. Consequently, the fundamental gyroscopic coupling due to radial dislocations is not correctly captured. This trend is constant throughout the next analysed cases and no further comment is given. This particularity does set a limitation in the applicability of the structural dynamics model. Nevertheless, as it was stated in Section 3.6.1, within the aeroelastic model the gyroscopic effect is applied as an external inertial load. Therefore, the effect of the gyroscopic coupling initially dismissed is fully restored in the aeroelastic simulation.

As a result of the inclusion of an offset between the center of gravity and the elastic axis of 5%, certain coupling between flap and torsion is generated. It can be observed in Table 4.1, where the first torsion and second flapping frequencies are affected. It can be observed as well in Fig. 4.10, where blocks coupling flap and torsion appear in the mass and stiffness matrices. Although of low order of magnitude, intermodal coupling between lead-lag assumed deformation functions are observed in the gyroscopic matrix.

The inclusion of blade pitch angle results in coupling between flapwise and chordwise displacements. It can be easily observed in the mass and stiffness matrices of Fig. 4.11, where blocks linking flap and lag are present. This leads to discrepancies between QEP and GEP frequencies as shown in Table 4.1. Certain gyroscopic coupling is further generated between lead-lag and torsion. However, the effect is fairly weak due to the distance between torsion and lead-lag frequencies in the frequency spectrum. Although of different nature,

the effects of pretwist along the blade observed in Fig. 4.12 are similar to the pitching angle effects identified in Fig. 4.11 and further discussion is not carried out.

The inclusion of precone has the strongest effect on the gyroscopic coupling as observed in Table 4.1. Large intermodal coupling coefficients between lag and flap appear in the partition matrices' diagonals (i.e., $C^{v,w}_{i,i} = 2\Omega \int_0^L m\psi_i^v \psi_i^w \beta \mathrm{d}x = -C^{w,v}_{i,i}$) due to the Coriolis acceleration. This generates considerable coupling between assumed modes of vibration with the same mode index i. This coupling strengthens with the proximity of the flap and lead-lag frequencies in the frequency spectrum. For this particular case of study, the 1st lag and flap modes are closely located. As a result, the effect of the inclusion of the gyroscopic matrix is much larger for these two modes of vibration. Although of smaller magnitude, gyroscopic coupling between flap and torsion does still exist and certain coupling between lag and torsion is observed in the stiffness matrix.

The effect of the inclusion of the gyroscopic matrix in the analysis of modal characteristics has been assessed. Initially, the generation of time-dependent variations on mode shapes has been mathematically demonstrated. Secondly, the relevance of the gyroscopic matrix has been assessed in terms of discrepancies between frequencies obtained from the QEP and GEP for different study cases. The assumptions made in the generation of the model have been identified as the cause of the lack of gyroscopic coupling due to axial displacement associated to transverse dislocations. The presence of precone has been found as a key factor in generation of gyroscopic coupling between flap and lag. Additionally, the effect of other coupling factors on the coupling between modes of vibration has been assessed, and the magnitude quantified.

4.6 Conclusions

The mathematical formulation for modelling of coupled flap/lag bending and torsion vibration characteristics of helicopter rotor blades proposed in Section 3.2 has been assessed in this chapter.

Excellent numerical performance based on the use of assumed deformation functions derived from classical methods has been demonstrated for a small scale hingeless rotor blade and a full scale articulated rotor blade. Definite fast convergence with a theoretical

infinite number of obtainable modes of vibration has been shown. As a result of the enhanced convergence, converged results are obtained with the deployment of a low number of assumed deformation functions. As a consequence, the computational efficiency has been highly improved. Excellent agreement of the experimental measurements and FEA results with the natural frequencies prediction has been demonstrated for two small scale hingeless rotor blades. Very good agreement between the predicted dominant mode shapes and the experimental measurements has been found, with the exception of the first flap mode. Good and very agreement between natural frequencies predicted by the proposed method and nonlinear multi-body dynamics calculation has been observed for a full scale and small scale rotor blades. Additionally, excellent agreement between the predicted dominant mode shapes and multi-body calculations has been identified for the small scale hingeless rotor. The effect of the gyroscopic matrix on the vibration predictions has been assessed. Time-dependent variations in mode shapes have been associated with the inclusion of the gyroscopic effect in the analysis. A limitation in the applicability of the structural dynamics model for the gyroscopic coupling has been identified. However, this limitation is not propagated to the aeroelastic model and the deficiency is restored externally.

The proposed method has been demonstrated to accurately estimate the first ten modes of vibration in a fraction of a second. Its computational efficiency and the very limited required information present this method as an efficient alternative to FEA or multi-body dynamics for the structural analysis of rotor blades during the preliminary design phase. Its further integration into an aeroelastic code acts as an enabler for the generation of comprehensive codes for the analysis of novel rotorcraft configuration where strong coupling between modes of vibration is present.

	Uncoupled		$e_M = 5\%c$		$\theta_0 = 5$deg		$\theta' = -5$deg		$\beta_{pre} = 5$deg	
	Q $\left(\frac{\omega}{\Omega_0}\right)$	G(%)	Q $\left(\frac{\omega}{\Omega_0}\right)$	G(%)	Q $\left(\frac{\omega}{\Omega_0}\right)$	G(%)	Q $\left(\frac{\omega}{\Omega_0}\right)$	G(%)	Q $\left(\frac{\omega}{\Omega_0}\right)$	G(%)
1F	1.176	0.000	1.176	0.000	1.170	0.000	1.174	0.000	1.173	1.555
1L	1.516	0.000	1.516	0.002	1.521	0.001	1.517	0.000	1.540	-1.530
1T	2.864	0.002	2.839	0.002	2.862	0.001	2.865	0.002	2.864	0.002
2F	3.341	-0.002	3.398	-0.002	3.340	-0.002	3.343	-0.002	3.340	0.018
3F	7.064	0.001	6.971	0.000	7.064	0.001	7.054	0.001	7.064	0.003

Table 4.1: Influence of the gyroscopic matrix on the normalised modal frequencies of the model described in Ref. 204.

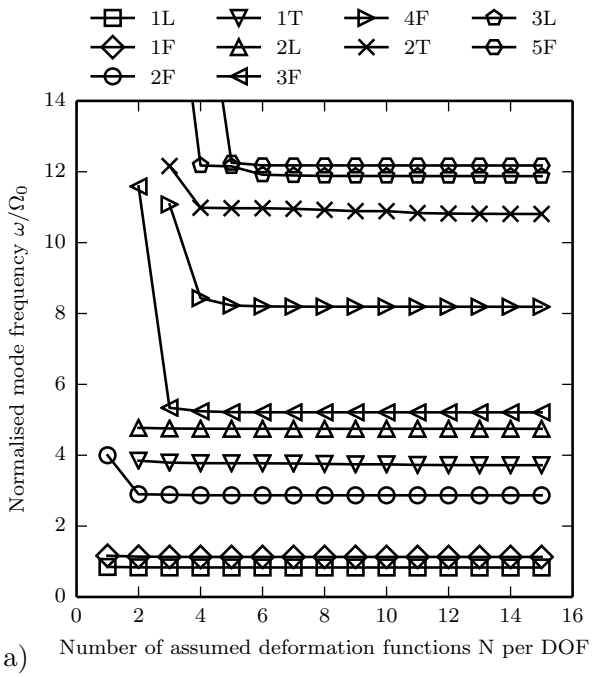

Figure 4.1: Influence of the number of assumed deformation functions on the convergence of the normalised modal frequencies for: (a) hingeless HART II rotor blade described in Refs. 202, 203 (b) articulated SA330 helicopter main rotor blade described in Ref. 196.

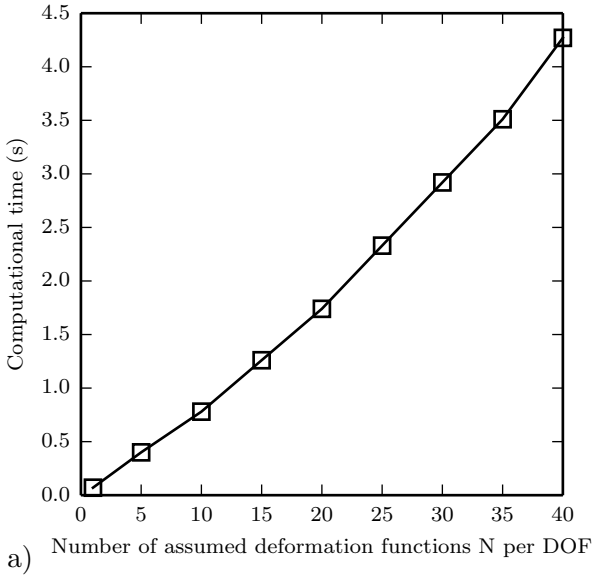

a)

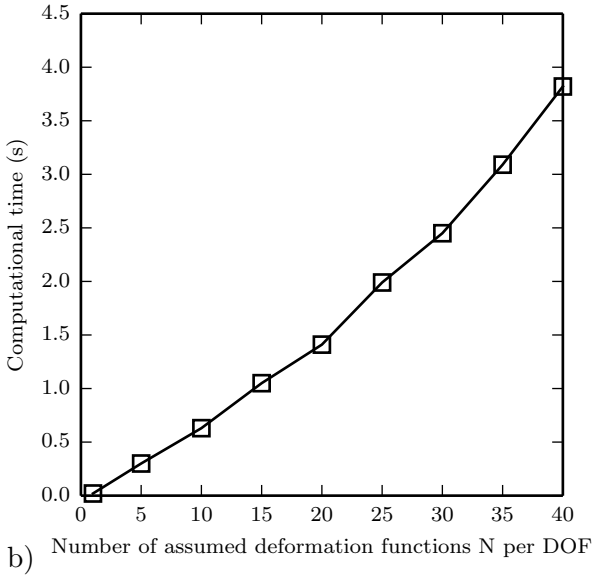

b)

Figure 4.2: Influence of the number of assumed deformation functions on the required computational time for a personal computer with a 1.7GHz CPU and 8GB of RAM for: (a) hingeless HART II rotor blade described in Refs. 202, 203 (b) articulated SA330 helicopter main rotor blade described in Ref. 196.

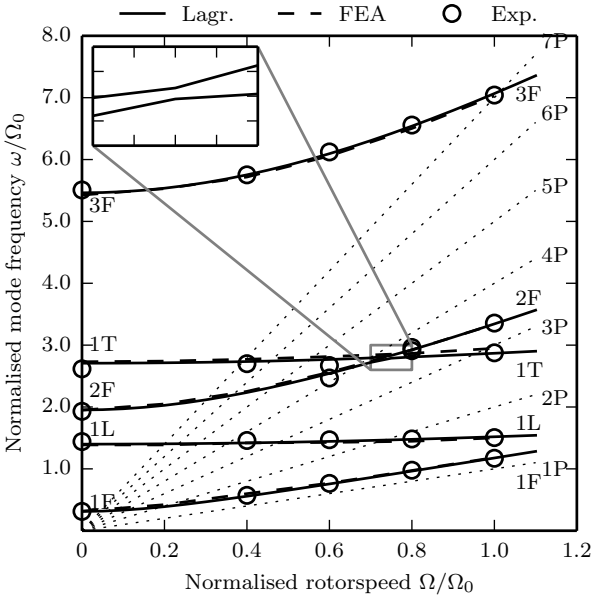

Figure 4.3: Calculated resonance chart for the hingeless rotor blade model described in Ref 204: comparison with experimental measurements and finite element analysis results from Ref. 205. Solid and dashed lines denote Lagrangian and finite element analysis predictions, respectively.

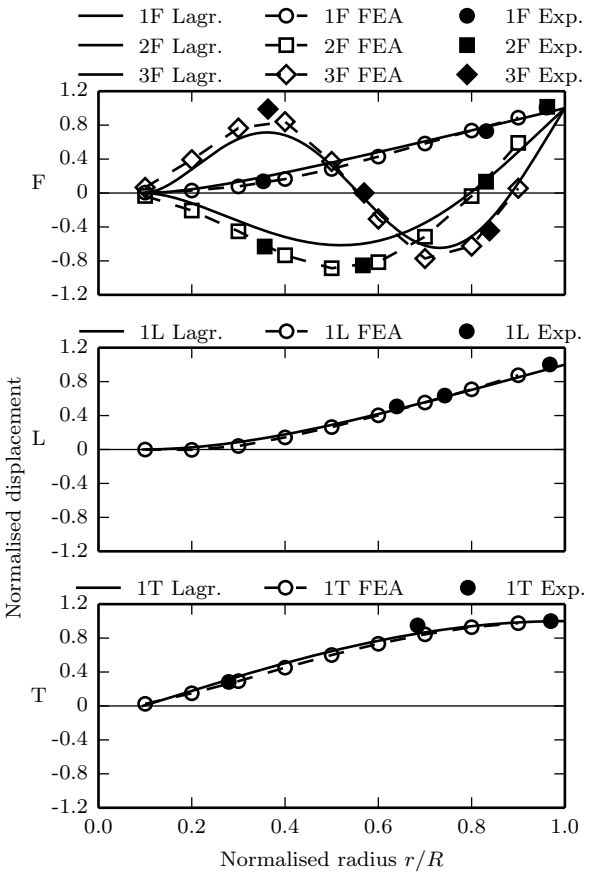

Figure 4.4: Normalised dominant mode shapes for the hingeless rotor blade model described in Ref. 204, $\Omega = 0\mathrm{rad\,s^{-1}}$: comparison with experimental measurements and finite element analysis results from Ref. 205.

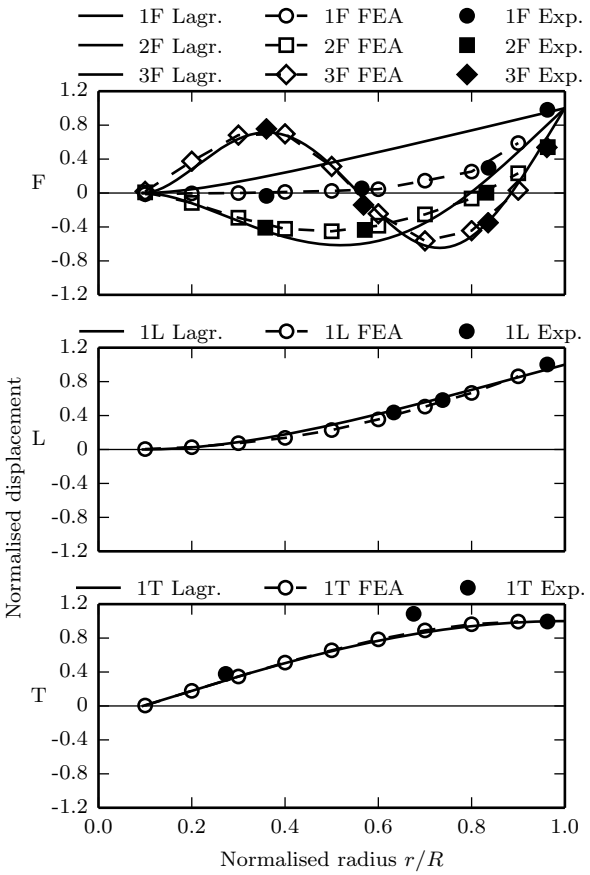

Figure 4.5: Normalised dominant mode shapes for the hingeless rotor blade model described in Ref. 204, $\Omega = 105\text{rad}\,\text{s}^{-1}$: comparison with experimental measurements and finite element analysis results from Ref. 205.

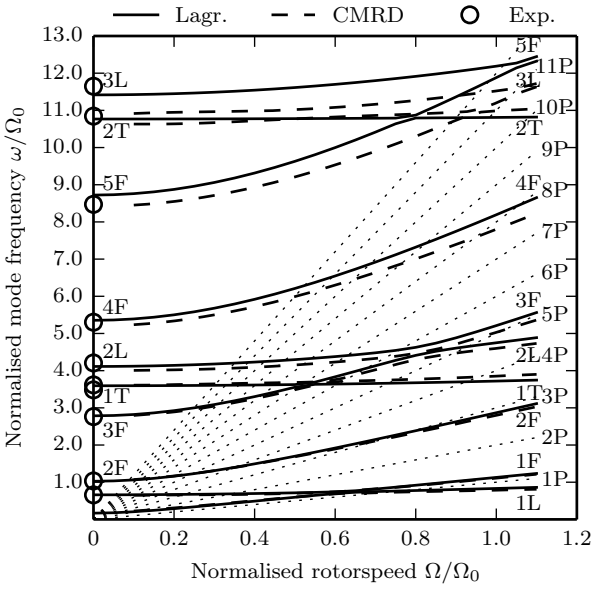

Figure 4.6: Calculated resonance chart for the hingeless HART II rotor blade described in Refs. 202, 203: comparison with CAMRAD calculations from Ref. 207 and experimental measurements from Refs. 200, 206. Solid and dashed lines denote Lagrangian and CAMRAD predictions, respectively.

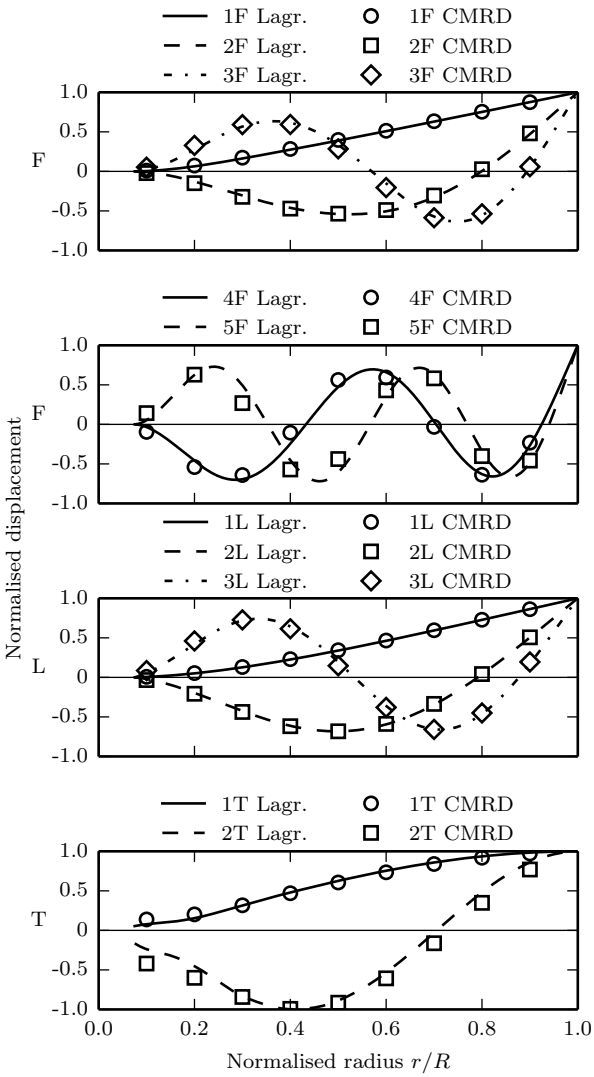

Figure 4.7: Normalised dominant mode shapes for the hingeless HART II rotor blade described in Refs. 202, 203, $\Omega = 109.13\mathrm{rad\,s^{-1}}$: comparison with CAMRAD calculations from Ref. 202, 203.

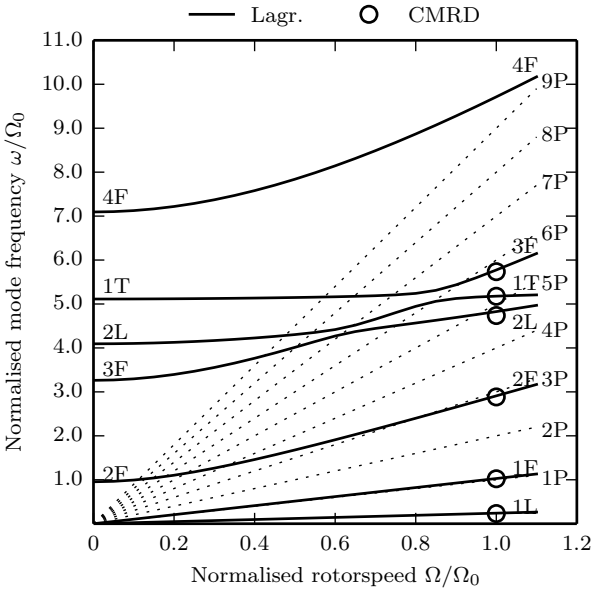

Figure 4.8: Calculated resonance chart for the articuated SA330 main rotor blade described in Ref 196: comparison with CAMRAD calculations from Ref. 196. Solid lines denote Lagrangian predictions.

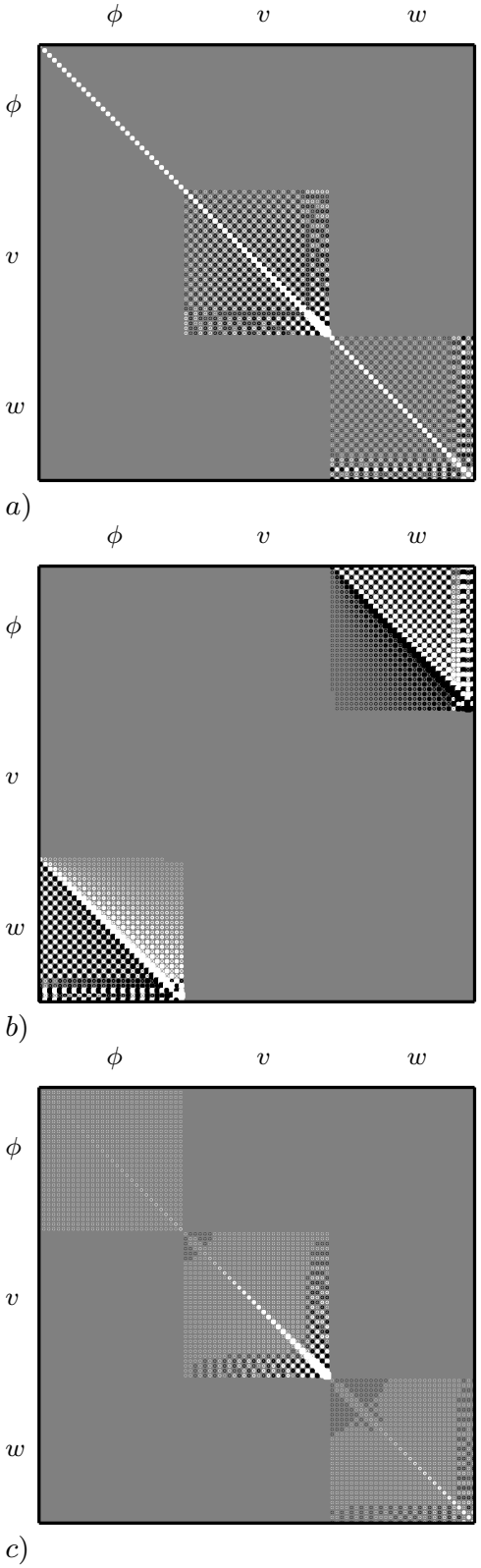

Figure 4.9: Hinton diagrams computed for the hingeless rotor blade model described in Ref. 204. Uncoupled: (a) mass matrix, (b) gyroscopic matrix, (c) overall stiffness matrix.

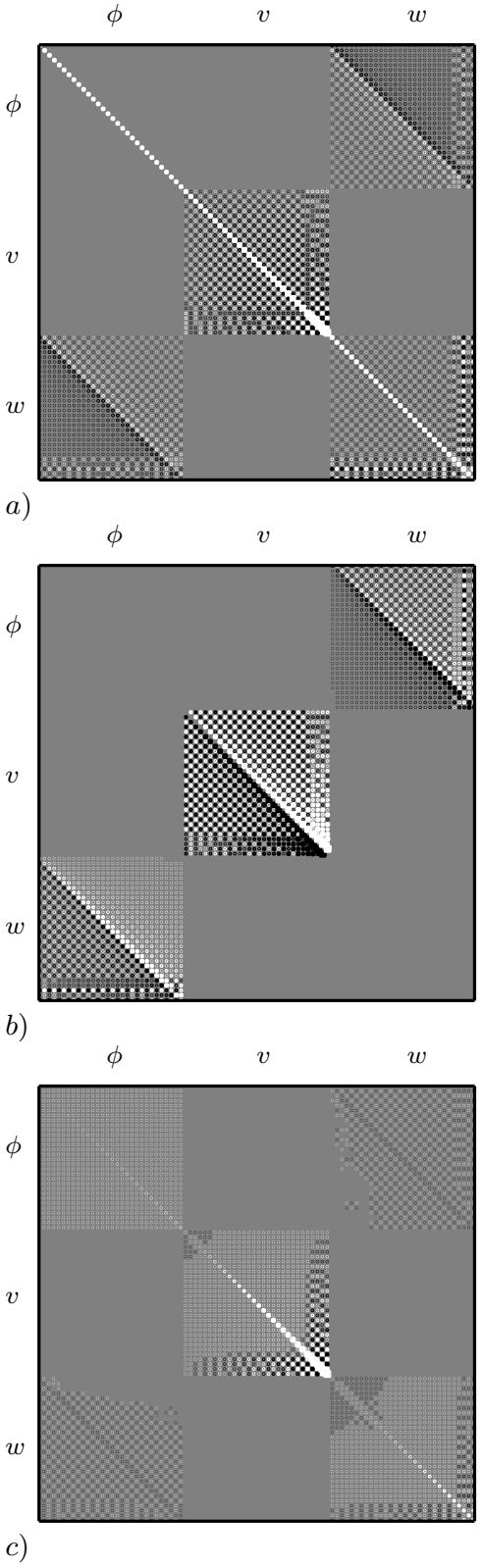

Figure 4.10: Hinton diagrams computed for the hingeless rotor blade model described in Ref. 204. $e_M = 5\%c$: (a) mass matrix, (b) gyroscopic matrix, (c) overall stiffness matrix.

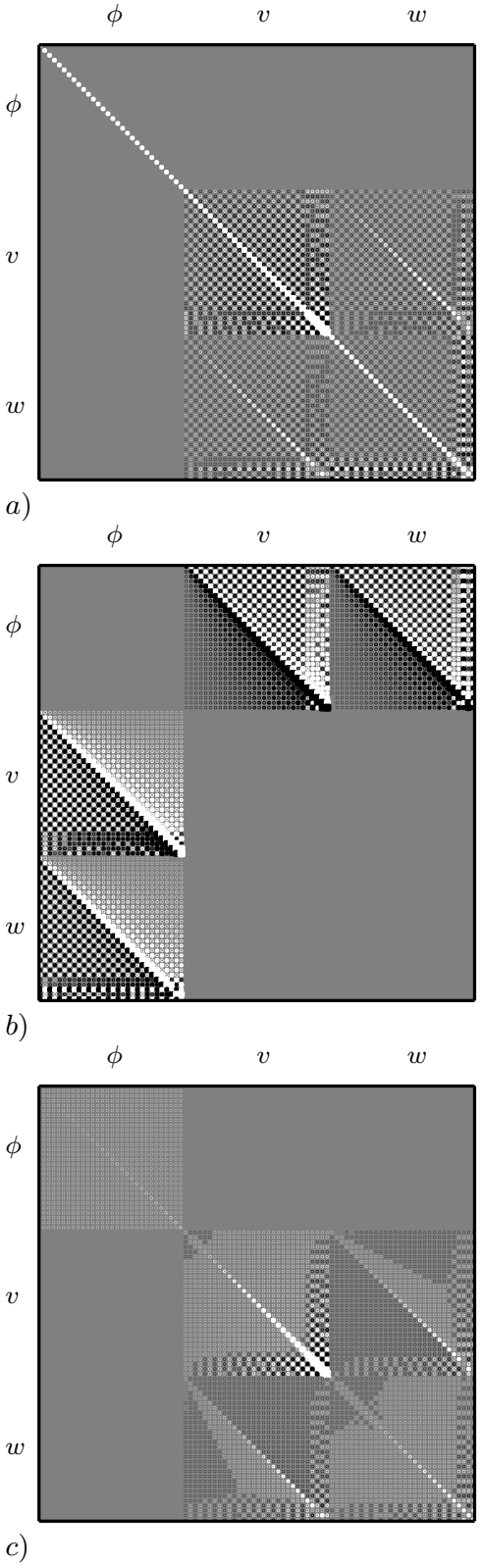

Figure 4.11: Hinton diagrams computed for the hingeless rotor blade model described in Ref. 204. $\theta_0 = 5$deg: (a) mass matrix, (b) gyroscopic matrix, (c) overall stiffness matrix.

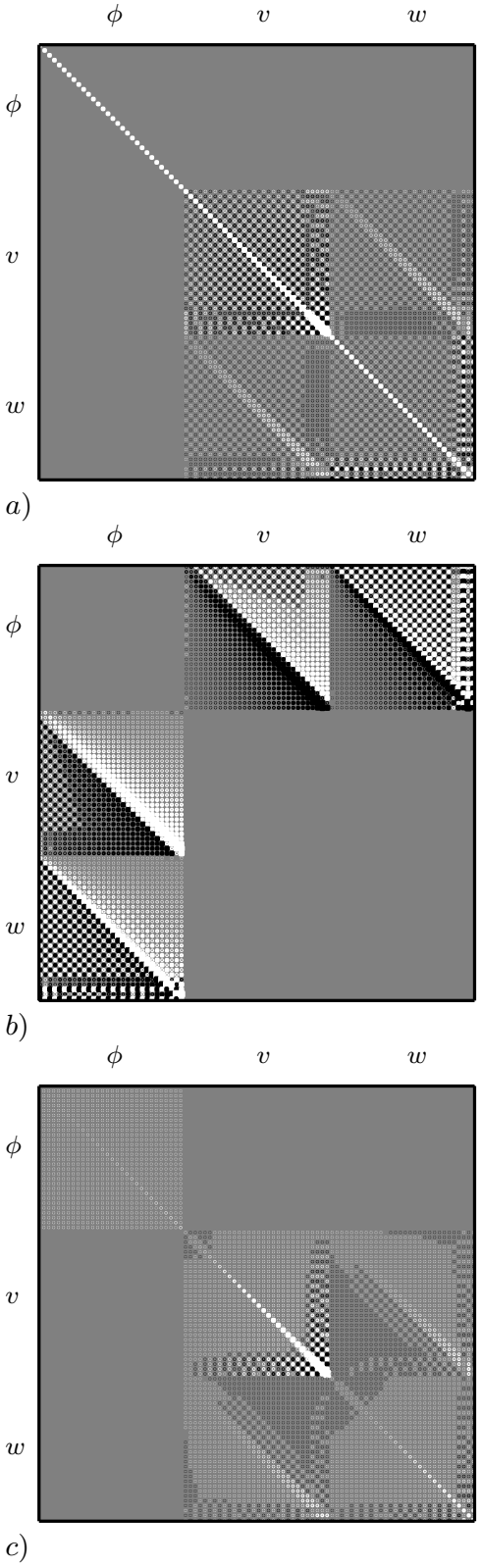

Figure 4.12: Hinton diagrams computed for the hingeless rotor blade model described in Ref. 204. $\theta' = -5$deg: (a) mass matrix, (b) gyroscopic matrix, (c) overall stiffness matrix.

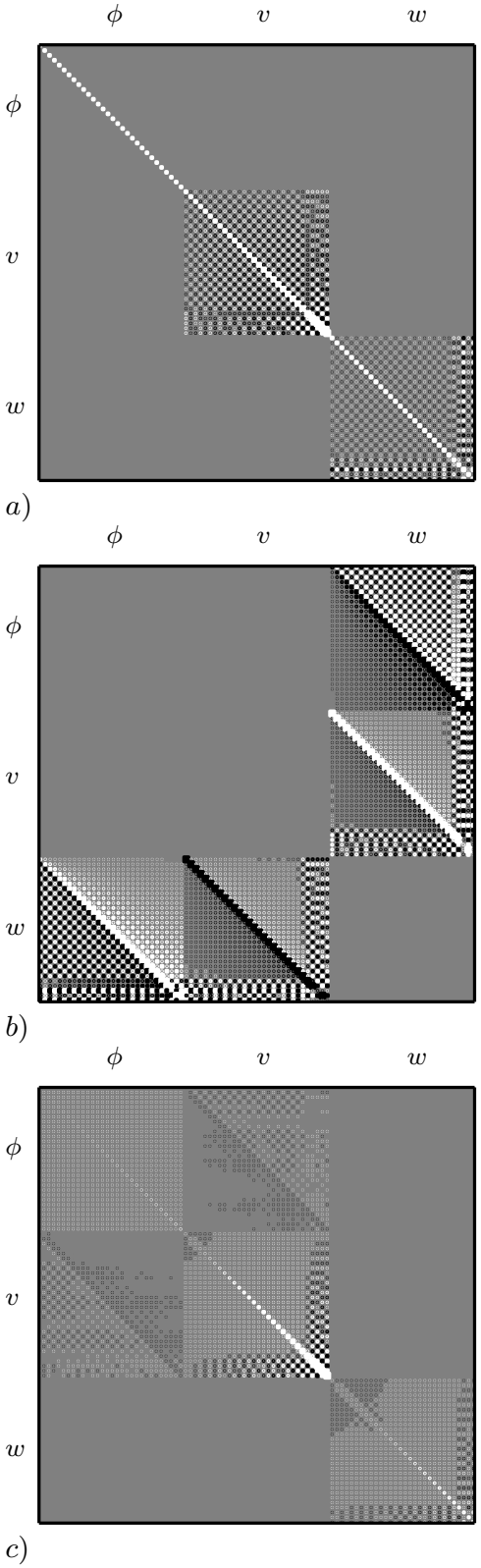

Figure 4.13: Hinton diagrams computed for the hingeless rotor blade model described in Ref. 204. $\beta_{pre} = 5$deg: (a) mass matrix, (b) gyroscopic matrix, (c) overall stiffness matrix.

Chapter 5

Results and Discussion: Integrated Aeroelastic Model

The predictive capability of the integrated aeroelastic model has been assessed by comparing its calculations with experimental measurements and calculations of a well established comprehensive rotorcraft code named CAMRAD. The hingeless HART II rotor is the model used for this study. The HART II rotor blade is a 40% Mach scaled model of the hingeless BO-105 helicopter rotor used in the Higher harmonic control Aeroacoustics Rotor Test program HART II. The main objective of the HART II program was to generate a comprehensive database of rotor loads, pressure distributions, blade deformation, acoustic radiations, and wind tunnel measurements for the small scale rotor during descending flight. A detailed description of the HART II test can be found in Refs. 197–201. However, a summary of the geometrical characteristics, wind tunnel conditions, and operational conditions is provided in Table 5.1. It is noted that the steady state aerodynamic properties measured in the ARA wind tunnel (Refs. 208, 209) for the NACA23012 aerofoil are used in the aerodynamic model of the present methodology.

The HART II test was carried out in the cross-section open jet configuration of the DNW wind tunnel. In the baseline case (BL) the rotor was operated with a rotor shaft angle $\alpha_s = 5.3$deg nose-up and an advance ratio $\mu = 0.151$. As a result of the wind tunnel interference, the rotor thrust caused a modification of the slip stream. That effectively changed the rotor shaft angle to an effective shaft angle $\alpha_{eff} = 4.5$deg nose-up. It was

predicted a further −0.2deg interference due to the presence of the fuselage, however, this effect was not taken into account in the computations. The tested flight condition constitutes a representative example of descending flight with strong BVIs at approximately $\psi = 50$deg and $\psi = 300$deg.

To assess the effect of high harmonic control (HHC) on the noise radiation and vibration generation, a minimum noise (MN) and a minimum vibration (MV) cases were tested. The MN case corresponds to the application of a three-per-rev (3P) harmonic of amplitude $\theta_3 = 0.8$deg with a phase angle $\psi_3 = 300$deg to the pitch control angle. The phase angle was shifted to $\psi_3 = 180$deg for the MV setup.

$$\theta_{geo}(r,\psi) = \theta_{tw}(r) + \phi(r,\psi) + \theta_0 + \theta_{1s}\sin\psi + \theta_{1c}\cos\psi + \theta_3\cos(3\psi - \psi_3) \quad (5.1)$$

Equation (5.1) presents the geometric pitch angle at any radial station and azimuthal location. The overall geometric pitch angle comprises the effects of pretwist (θ_{tw}), elastic torsion (ϕ), collective pitch (θ_0), longitudinal cyclic pitch (θ_{1s}), lateral cyclic pitch (θ_{1c}), and the 3P cyclic pitch (θ_3). The rotor has been trimmed (θ_0, θ_{1s}, and θ_{1c}) to match the prescribed thrust, rolling moment, and pitching moment coefficients for each setup. The computational predictions obtained with the proposed method presented in this chapter include the effect of fuselage induced velocity perturbations to better replicate the experimental test setup. The effect of the fuselage interference on the present work predictions is analysed in depth in chapter 6.

Within the next sections, the predictions obtained with the integrated aeroelastic model developed in this work are extensively compared with experimental measurements from Refs.197–199, 201, 207 and CAMRAD calculations from Ref. 207 to assess its predictive capability.

5.1 Computational Performance

The effectiveness of the numerical and computational enhancements implemented in the integrated aeroelastic model to reduce the execution time is assessed by quantifying the relative computational speedup. In Section 3.4.2 two approaches were described to reduce the time required to obtain a free-vortex wake solution. The first one is the use of parallel programming combining FORTRAN 90/95 and OpenMP. This combination provides

parallelism within a shared memory multiprocessing machine. The level of parallelism will be limited by the processor core number. The second one is the implementation of a numerical acceleration scheme based on velocity field interpolation.

Figure 5.1a presents the evolution of the computing speedup with the number of threads used in the computation. Squares, diamonds, and triangles refer to wake, aeroelastic, and ideal speedups respectively. Within this context, speedup is defined as the ratio of the required computational time without parallel computing to the required computational with parallel computing. The wake speedup accounts exclusively for the execution of an iteration of the free-wake model. In contrast, the aeroelastic speedup accounts for the calculation of the complete integrated aeroelastic model. These are compared with the ideal speedup. The presented computations were carried out using a personal computer with an eight cores 3.4GHz CPU and 16GB of RAM. Initially, a linear correlation between the number of threads used and the speedup is observed, however after four cores the efficiency of the parallelism is reduced. This can be attributed to the need of synchronisation between cores, heterogeneous or unbalance computational loading of the cores, and memory bandwidth limitations. Additionally, a further reduction in the efficiency is found when the number of threads approaches the number of cores. This is related to the need of sharing processors between the operating system and the code itself. As a result, the execution of some of the cores is delayed. Additionally, the number of cores sets up a limitation in the attainable speed up. In this case the limitation takes the form of a plateau once eight cores are used. Maximum speedups of 5.8 and 5.6 are identified for the wake and aerolastic model respectively. That means that the time required to obtained a complete converged aeroelastic solution is reduced by 82% just by using parallel computing.

Figure 5.1b presents the evolution of the computing speedup with the ratio of age to azimuth resolution. The ratio of age to azimuth resolution is defined here as $\Delta\zeta_f/\Delta\zeta_{ps}$, where $\Delta\zeta_f$ and $\Delta\zeta_{ps}$ are the wake age discretisation resolution of the free and pseudo-free collocation points respectively. As described in Section 3.4.2, the current implementation uses equal age and wake discretisation resolutions, which essentially makes $\Delta\zeta_{ps} = \Delta\psi$. The ratio of age to azimuth resolution is the main driving parameter in the numerical acceleration scheme based on velocity field interpolation. This scheme is used in the calculation of the wake geometry. Therefore, only the wake speedup is shown in Fig.

5.1b. Squares and diamonds represent wake and ideal speedups respectively. However, the calculation of the wake is the main contributor to the total execution time of the aeroelastic model. The assessment of the effect of the ratio of age to azimuth resolution is carried out for an azimuthal discretisation of $\Delta\psi = 1$deg which is a very fine discretisation valid for noise calculations. Speedups of 4.7 and 9.0 are identified for ratios of 5 and 10 respectively. These correspond to reductions in computational time of 79% and 89% respectively.

The combined effect of both approaches has been assessed by comparing the computational time required to obtained a converged solution with parallel computing (8 threads) and the acceleration scheme switched on with the same simulation with serial computing and without velocity interpolation. Reductions of 95% and 97% have been attained for age to azimuth resolution ratios of 5 and 10 respectively, which correspond to total execution times of 230.3min and 120.7min. Unless noise calculations are required, the azimuth resolution is increased to $\Delta\psi = 5$deg with age to azimuth ratios of 1 and 2, or $\Delta\psi = 10$deg with a ratio of 1. The respective execution times are 19.5min, 13.3min, and 3.2min respectively.

The computational efficiency of the integrated aeroelastic model has been enhanced by the implementation of two approaches. The use of parallel computing leads to reductions in the required computational time of 82%. The reduction in the number of Biot-Savart evaluations by means of velocity interpolations results in reductions of up to 89%. The combined effect of both techniques leads to reductions of up to 97% for a case with fine azimuth discretisation. A 97% reduction in the execution time reduces the time to 120.7min. The use of a coarser discretisation can potentially reduce the required computational time to only 3.2min. Therefore, the proposed approach exhibits an excellent computational performance, with execution times close to dynamic inflow models and few orders of magnitude lower than CFD. This enables its use for design purposes as well as detailed noise calculations.

5.2 Modal Characteristics

Prior to the presentation of the aeroelastic comparison, the modal characteristics *in vacuo* of the rotor blade should be presented. A detailed comparison between the modal characteristics calculated with the proposed Lagrangian method, experimental measurements, and multi-body analysis (CAMRAD) calculations was presented in Sections 4.3 and 4.4 respectively. Therefore, further detail is not given.

5.3 Rotor Trim

The HART II database was generated for specific trim conditions. The control angles were modified to experimentally match the prescribed thrust, rolling moment and pitch moment coefficients. This process was carried out for a given combination of wind speed and rotor shaft angle. As a result of the operation of the rotor inside the wind tunnel, a wind tunnel interference was observed and the effective rotor shaft angle modified. Details of the wind tunnel and operating conditions are given in Table 5.1.

Control angles. Table 5.2 presents the collective θ_0 (at $r = 0.75R$), lateral cyclic θ_{1c}, and longitudinal cyclic θ_{1s} pitch angles needed to trim the rotor to the prescribed force and moments coefficients. The calculated control angles are compared with experimental values and CAMRAD calculations from Ref. 207.

The present method underpredicts the collective pitch angle θ_0 by an average of 0.8deg in every case. The magnitude of the collective pitch angle alone cannot be used to determine the accuracy of the model. Elastic twist needs to be taken into account because a negative value of elastic torsion reduces the effective collective angle. Therefore, the sum of the collective pitch angle and the mean tip elastic torsion, which is denominated here effective collective pitch angle, better represents the static aeroelastic behaviour of the rotor. Table 5.3 presents the comparison between the proposed approach, experimental measurements, and CAMRAD calculations for this parameter. It is noted that three experimental values are provided: minimum, mean, and maximum. This is justified by the differences in mean elastic torsion measurements between blades. The values calculated by the proposed approach are slightly lower (0.3deg) than the minimum values experimentally

obtained. CAMRAD predictions, although higher, are still located at the lower end of the experimental range. Van der Wall *et al.* (Ref. 207) related this trend to an underprediction of the velocity normal to the rotor disk. This could be caused by an underestimation of the wind tunnel interference or by an underrating of the average induced velocity. The latter could be associated with the truncation of the wake. A second conclusion can be drawn from Table 5.3, the increase in effective collective pitch angle observed in the MN case is captured. Similarly, the decrease in effective collective pitch angle measured in the MV case is correctly predicted. Therefore, the model has been able to correctly predict relative changes in effective collective pitch angle associated with the introduction of HHC in the cases analysed.

The lateral pitch angle θ_{1c} is underpredicted in every case by an average of 0.3deg. The average discrepancy in lateral pitch angle obtained with the proposed model shows better agreement with experimental measurements than CAMRAD calculations, which underestimates the lateral pitch angle by an average of 0.6deg. The better agreement found in the present work can be explained by the inclusion of fuselage velocity disturbances in the analysis. This model, generates an upwash velocity perturbation at the front of the disk and a downwash interference at the back of the disk. The incorporation of this velocity differential in the longitudinal direction needs to be balanced by the control system, resulting in an increase in lateral cyclic pitch angle. In addition to the effect of fuselage disturbances, the underestimation of the wind tunnel interference angle can be identified as the second possible source of error in the lateral pitch angle predictions.

An average offset of 0.3deg is found between the calculated longitudinal pitch angles θ_{1s} and the experimental measurements. For this particular variable, CAMRAD calculations show better agreement with an average error of 0.05deg. Similarly to previous control variables, the underestimation of wind tunnel and fuselage interferences can be identified as possible sources of error.

The discrepancies between control pitch angles calculations and experimental measurements are contained within the 0.3deg margin for all three cases: BL, MN, and MV. Hence, overall very good agreement in the trim control angles is observed between the proposed model and experimental measurements.

Power. Table 5.4 presents the comparison between the predicted rotor power required,

experimental measurements from Ref. 210, and CAMRAD calculations from Ref. 210. The required rotor power predicted with the present method shows and excellent agreement with the experimental measurements in every case. Discrepancies of only 0.91kW, 2.61kW, and 0.84kW are observed for the BL, MN, and MV cases respectively. The low order of magnitude of the discrepancies contrasts with the 10kW average discrepancy observed in the calculations carried out with CAMRAD. It is as well of interest to assess the relative change in rotor power required consequence of the application of HHC. The experimental measurements of power taken in the MN and MV cases show a relative increase in rotor power of 1.5kW and 0.5kW respectively. This trend is correctly predicted by the proposed approach with relative changes of 3.15kW and 0.39kW for the MN and MV setups respectively. Instead, CAMRAD estimates relative rotor power changes of 1.69kW for MN and 1.01kW for MV. Despite the more accurate prediction of the change in rotor power obtained with CAMRAD in the MN case, the high order of magnitude of the power prediction discrepancy reduces the level of confidence on its rotor power estimations.

5.4 Elastic Deformations

The motion of the blade has been quantified by measuring the elastic deformation of the blade tip relative to the undeformed rotor blade in the flap and lag directions and relative to the pitch control angle in the pitch direction. The instrumentation of the blades during the experimental test resulted in non-identical blade structural and inertial properties. Consequently, blade to blade differences in dynamic behaviour and elastic deformations are observed.

Elastic flap deflections. Flap tip elastic deformations are measured in the out of plane direction relative to the undeformed preconed rotor. Figure 5.2 presents elastic flap deformations in the baseline, minimum noise, and minimum vibration cases. Elastic flap deflections have been normalised with the rotor radius, $R = 2$m. Solid and dashed black lines denote elastic deflections predicted with the present approach and CAMRAD (Ref. 207) respectively. Experimental measurements of each blade from Ref. 207 are presented with grey lines. A strong once-per-rev (1P) flap oscillation is observed in the

BL case. The maximum and minimum positive out of plane deflections are located at approximately 280deg and 100deg respectively. The location of the maximum and minimum flap deflections dictates the forward and starboard tilt of the tip path plane (TTP). The relative orientation of the TTP is in accordance with the positive rolling and negative pitching rotor hub moments. The average flap tip deflection is negative, which symbolises a trim thrust smaller than the design point thrust. Excellent agreement is observed between the presented method predictions, CAMRAD calculations, and experimental measurements; with discrepancies in the range of blade to blade differences.

In the MN setup, a three-per-rev (3P) flapping component is identified. This is attributed to the inclusion of a 3P HHC. Very good agreement is observed between predicted deflections, CAMRAD calculations, and experimental measurements. The proposed method slightly overpredicts the 3P content at approximately $\psi = 180$deg, which is associated with a higher aerodynamic loading on the advancing side. Despite the overestimation of the 3P response, the magnitude of the discrepancy relative to the experimental data is in the range of blade to blade differences and excellent phase agreement is observed. Regarding the MV case, considerable high order content in the flapping deflection is observed for the second and third blade which is not found in the response of the first and fourth blades. The predictions of the proposed methodology show excellent agreement with the calculations carried out with CAMRAD and the experimental values of the first and fourth blades. If the calculated flapping deflections are compared with the deflections of the second and third blade, the discrepancies found are mainly associated with the high frequency content. Even for the latter, the discrepancies are in the range of blade to blade differences and overall very good agreement in amplitude and phase is observed.

Elastic torsion twist. The elastic tip torsion twist is measured in the pitching direction relative to the pretwisted blade with applied control angles. The comparison between predicted values, CAMRAD calculations, and experimental measurements is presented in Fig. 5.3 for the BL, MN, and MV cases. Solid and dashed black lines symbolise elastic deflections predicted with the present approach and CAMRAD (Ref. 207) respectively. Experimental measurements of each blade from Ref. 207 are presented with grey lines. In the BL case a strong 2P component is observed in the experimental measurements.

Although of smaller magnitude, CAMRAD captures the 2P component of the time-dependent torsion deformation. Coupling between the first torsion mode and the second flapping mode can be identified as the main cause of the 2P torsion component. The proposed approach fails to predict the 2P torsional behaviour and a less dynamic elastic tip torsion twist is predicted. The discrepancies could be attributed to a limitations on the applicability of the structural dynamic model. However, the natural frequency of the first torsion mode and the 1P frequency are located relatively far in the frequency spectrum. As a result, the response of the blade torsion follows the external forcing, i.e. aerodynamics loading, in amplitude and phase. As a consequence, the discrepancies between the prediction of the proposed approach and the experimental measurements could be attributed to the set of aerofoil data used and not to the dynamics of the blade itself.

As a result of the application of HHC, the dynamics of torsion raise significantly as illustrated in Fig. 5.3 for the MN and MV cases. Regarding the MN case, excellent agreement between the phase of the predicted deformation, CAMRAD calculations, and experimental measurements is observed. In terms of the torsion magnitude, the present work slightly underestimates the dynamics of torsion leading to an underprediction of the torsion angle at approximately $\psi = 180$deg. In contrast, CAMRAD tends to overpredict the magnitude of the torsion deformation. Similar comments are applicable to the MV case, where excellent agreement is observed in the calculated phase and very good acorrelation in amplitude is identified with a small underprediction of the torsion twist at approximately $\psi = 30$deg and $\psi = 150$deg. For this specific case, CAMRAD calculations exhibit excellent agreement with experimental measurements in terms of magnitude and phase.

Overall very good agreement of the predictions of the proposed method with experimental measurements and CAMRAD calculations has been observed in the analysed cases. The only identified deficiency of the method is a systematic underprediction of the dynamic content of the torsional deformation.

Elastic lag deflections. Lag deflections are measured relative to the undeformed blade in the in plane direction, with positive sign against rotation. Fig. 5.4 presents the dynamic evolution of the lag deflection, mean removed, for the proposed approach, experimental measurements from Ref. 207, and CAMRAD calculations from Ref. 207.

Elastic lag deflections have been normalised with the rotor radius. Solid and dashed black lines correspond to elastic deflections predicted with the present approach and CAMRAD respectively. Experimental measurements of each blade are denoted by grey lines. The predicted deflections virtually superimpose the experimental values and CAMRAD calculations for every setup. A strong 1P content is observed in all cases and little high order content is identified. Regarding the mean value of the lag deflection, large discrepancies between codes and experimental measurements are shown in Table 5.5. However, a repeated error higher than 1% in the measured lag displacements was found. Therefore, a reliable comparison can not be made regarding this parameter.

5.5 Bending Moments

During the HART II test, the flap and lag bending moments and the torsion moment were experimentally measured at $r = 0.17R$ and $r = 0.33R$ respectively. Experimental measurements of flap bending and torsion moments are available for all four blades, while lag bending moments are not available for the third blade.

Flap bending moments. Figure 5.5 presents the predicted flap bending moments, experimental measurements, and CAMRAD calculations. The mean value of flap bending moment has been subtracted in every case. Solid and dashed black lines symbolise flap bending moments predicted with the present approach and CAMRAD (Ref. 207) respectively. Experimental measurements of each blade from Ref. 207 are illustrated with grey lines. In general the predictions of the proposed approach and CAMRAD exhibit little correlation with the experimental measurements. The only case where good agreement between the predictions of the present work and experimental is found is in the MN case, where magnitude and phase of the experimental bending moments are matched. Van der Wall *et al.* (Ref. 207) attributed the lack of correlation between CAMRAD predictions and experimental measurements to the prescribed rotor trim moments. The low order of magnitude of these moments leads to very small flap bending moments and a general bad agreement between code predictions and experimental data.

Torsion moments. In contrast with flap bending moments, the agreement between code predictions and experimental data is much better for torsion moments as shown in

Fig. 5.6. Solid and dashed black lines correspond to flap bending moments predicted at $r = 0.33R$ with the present approach and CAMRAD (Ref. 207) respectively. Experimental measurements of each blade from Ref. 207 are presented with grey lines. A low order of magnitude 1P component in the torsion moment is observed in the experimental measurements in the BL case. This evolution is well captured with CAMRAD. However, the present work does not capture correctly the dynamics of the torsion moments, which is accordance with the underestimation of the dynamic torsion twist previously presented in Fig. 5.3.

The introduction of 3P HHC results in an increase in the excitation of the first torsion mode. This is justified by the proximity of the first torsional moment and the 3P frequency in the frequency spectrum. In both cases, MN and MV, excellent agreement between the predicted values, experimental measurements, and CAMRAD calculations is observed. A small underestimation of the torsional moment at approximately $\psi = 180$deg and $\psi = 150$deg is found in the MN and MV cases respectively. However, the overall prediction exhibits very good agreement with the experimental measurements in magnitude and phase.

Lag bending moments. Figure 5.7 presents the calculated lag bending moments, experimental measurements from Ref. 207, and CAMRAD calculations from Ref. 207. The mean value of lag bending moment has been removed in every case to better show the dynamic content. Solid and dashed black lines denote flap bending moments predicted with the present approach and CAMRAD respectively. Experimental measurements are illustrated with grey lines. The present work predicts correctly the 1P content in both magnitude and phase. The low magnitude high frequency content is not captured, as CAMRAD does. However, the magnitude of these components is much lower than the 1P component and the discrepancy of the total moment prediction with the experimental measurements is in the range of blade to blade measurements.

Overall very good agreement is observed between the bending and torsion moments calculated with the proposed method, experimental measurements, and CAMRAD estimations. The low order of magnitude of the total rotor moments results in poor agreement between predictions of flap bending moment and experimental values. Very good agreement of torsional moments was observed with a small underestimation on the dynamics

of torsion. In the last place, excellent correlation between prediction and experimental measurements has been found for lag bending moments.

5.6 Aerodynamic Loading

The blade number one of the HART II rotor was instrumented at $r = 0.87R$ with pressure sensors to obtain blade pressure distributions, which were later used to calculate normal force and moment coefficients. It was observed in Figs. 5.2 and 5.3 that the blade number one has a higher mean flap position and stronger dynamic oscillations of the pitch angle compared with the other blades. As a result, the magnitude of the measured aerodynamic loading is expected to be higher in mean value and dynamic content than the computed aerodynamic loading where identical blades are simulated. Consequently, this source of error will magnify the aerodynamic loading discrepancies between experimental measurements and computations.

Normal force coefficient.. The mean values of normal force coefficient calculated at $r = 0.87R$ are presented in Table 5.6 along with the respective experimental measurements and CAMRAD calculations from Ref. 207. An underprediction of about 4% relative to the experimental measurements is observed in the normal force coefficient calculated with the present methodology in the BL case. Similarly, CAMRAD underpredicts the normal coefficient by about 6%. In the HHC cases the trend is similar and the computed section loading is underestimated by 12% and 16% in MN and MV cases respectively. These values show better correlation than CAMRAD, which underpredicts the section loading by 17% and 20% respectively. The underprediction of the aerodynamic loading is in accordance with the higher experimental loading expected due to the stronger dynamic oscillations exhibited by the instrumented blade.

Figure 5.8 presents the calculated dynamic, mean removed, normal force coefficients at $r = 0.87R$ along with the correspondent experimental measurements from Ref. 207 and CAMRAD calculations from Ref. 207. Solid and dashed black lines denote normal force coefficients predicted with the present approach and CAMRAD respectively. Experimental measurements are presented with grey lines. In every case, strong high frequency fluctuations in aerodynamic loading associated with BVIs are observed at approximately

$\psi = 50$deg and $\psi = 300$deg. In the BL case, a 2P oscillation in aerodynamic loading is identified. Overall very good agreement between predictions and experimental measurements is observed for the low frequency content of the normal force coefficient except at the minimum aerodynamic loading location, $\psi = 160$deg, where the predicted value has an offset in phase and amplitude. This discrepancy can be attributed to the underprediction of the dynamics of torsion identified in the proposed method and the overestimation of the elastic motion of the blade number one previously observed in Fig. 5.3. CAMRAD calculations exhibit slightly better correlation with experimental measurements at the aerodynamic loading minimum position, which can be explained by the better prediction of torsion twist observed in Fig. 5.3.

Regarding the MN and MV setups, a combination of 2P and 3P oscillations is observed in Fig. 5.8. Excellent correlation between code calculations and experimental measurements is observed. In the MN case, the predictions match the experimental values in both, amplitude and phase. A small underprediction of the loading is found at approximately $\psi = 110$deg and $\psi = 170$deg, which can be explained by the discrepancies in torsion angles observed in Fig. 5.3. The latter is exacerbated in the MV case, where larger discrepancies in torsion predictions were previously observed.

In order to show the further study the BVI loading, the high frequency content of the aerodynamic loading is presented. The normal force coefficient previously shown in Fig. 5.8 is high-pass filtered and only signals with frequency higher than 10P are obtained and presented in Fig. 5.9. The calculated values are compared with experimental measurements from Ref. 207 and CAMRAD calculations from Ref. 207. Solid and dashed black lines correspond to the normal force coefficients predicted with the present approach and CAMRAD respectively. Experimental measurements are denoted by grey lines. The BVIs can now be clearly identified. In the BL case, the present work matches the experimental phase of the advancing side BVIs. However, the magnitude of the interactions is overestimated. Similar behaviour in the calculations of CAMRAD is observed. Regarding the retreating side BVI, the prediction of the magnitude is improved at the expense of deteriorated phase agreement. During the analysis of the data it was found that the magnitude and phase of the BVI was greatly influenced by the strength and size of the root vortex, which is sensitive to the rotor trim conditions.

In the MN case, fair correlation between the calculations of the present method and the experimental measurements is found on the advancing side. The experimental advancing side BVIs are characterised by one strong vortex interaction and several smaller interactions. The predictions of both, CAMRAD and this work, fail to predict the strong vortex interaction and estimates a series of relative strong interactions instead. The agreement between the predicted interactions and the experimental measurements is greatly improved on the retreating side where the interactions are well capture in magnitude. In the last place, very good correlation between experimental measurements and predicted values is observed in the MV setup. On the advancing side the magnitude of the BVIs are correctly estimated and only a small offset in the phase is identified. On the retreating side, the magnitude is once again correctly predicted, and the fluctuations are slightly offset in the azimuth direction.

Loading noise predictions are highly dependent on the time derivative of the aerodynamic loading (Ref. 191). As a result, areas with high time derivatives are associated with strong loading noise. Figure 5.10 illustrates the relation between the time derivative of the normal force coefficient and the BVIs locations. Markers symbolise locations with BVI miss distance smaller than the blade chord. Black and red colours refer to above and below rotor interactions respectively. Four different BVI locations are identified. At the rear and front of the disk, the directions of the vortex and blade are normal and no impulsive loading is found. At the advancing ($\psi = 30 - 100$deg) and retreating sides ($\psi = 280 - 330$deg), the vortices and the blades are parallel and large oscillations in aerodynamic loading are observed. From the above is concluded that the accurate prediction of the BVI locations and strengths enables the correct estimation of the aerodynamic loading time derivatives and loading noise predictions.

In order to quantify the capability to predict loading noise, Fig. 5.11 presents the time derivative of the normal coefficient for the proposed approach, experimental measurements from Ref. 207, and CAMRAD calculations from Ref. 207 at $r = 0.87R$. Solid and dashed black lines correspond to the first time derivative of the normal force coefficients predicted with the present approach and CAMRAD respectively. Experimental measurements are denoted by grey lines. In the BL case, both codes overpredict the magnitude of the time derivatives on the advancing side. However, the phase angle is accurately predicted.

In contrast on the retreating side the derivatives are underestimated in magnitude and a phase offset is identified. Regarding the MN case, on the advancing side the strong interaction observed in the experimental measurements is underpredicted, while the weaker interactions are overpredicted. As a result fair agreement is observed in this region. The prediction on the retreating side is improved and the magnitude and phase predictions are closer to the experimental values. In the MV setup, good correlation between the present predictions and experimental measurements is observed for the magnitude on the advancing side whilst the signal exhibits some offset in the azimuth direction. On the retreating side, the strong interaction is not correctly modelled. Nevertheless, the rest of the interactions show good correlation with the experimental data in magnitude an phase. Overall good agreement between code predictions and experimental measurements has been observed in the prediction of the time derivative of the aerodynamic loading.

Moment coefficient. The mean values of moment coefficient calculated at $r = 0.87R$ are presented in Table 5.6 along with the respective experimental measurements and CAMRAD calculations from Ref. 207. Although the coarse instrumentation attached to the blade at this blade section is fine enough to correctly measure the normal force coefficient, the level of confidence for the estimation of the moment coefficient drops. This is due to the sensitivity of the aerodynamic moment to the position of the pressure sensors. As a result, a definitive answer can not be drawn from the comparison between experimental measurement and code predictions of the moment coefficient. Nevertheless, very good agreement between the results calculated with the proposed method and CAMRAD is observe for all three cases. The agreement is as well very good with the experimental value of BL. However, the discrepancies in the MN and MV cases are much higher.

The dynamic content of the aerodynamic moment coefficients calculated at $r = 0.87R$ with the proposed method is presented in Fig. 5.12 along the experimental measurements and CAMRAD calculations. Solid and dashed black lines represent moment coefficients computed with the present methodology and CAMRAD (Ref. 207) respectively. Experimental measurements from Ref. 207 are presented with grey lines. Similarly to the normal force coefficient, strong BVIs are identified at approximately $\psi = 50$deg and $\psi = 300$deg. In the BL case, a superimposition of a 2P oscillation and high frequency oscillations associated with BVIs is observed. The present work accurately predicts the magnitude and

phase of the BVIs. However, the low frequency contents at $\psi = 180$deg is not correctly modelled. This discrepancy is once again related to the underestimation of the dynamic torsion angle at this location. In contrast, CAMRAD does not model BVIs and only the low frequency content is estimated with fairly good agreement with the experimental data.

As a result of the introduction of 3P HHC, the moment coefficient exhibits a strong 3P component. For the MN setup, excellent correlation between the calculated moment coefficient and the experimental measurements is observed for the low frequency content. Very good agreement is found between CAMRAD calculations and the experimental measurements. Regarding the MV case, the 3P oscillation is correctly captured by the presented code and only a small underestimation of the moment coefficient is observed at approximately $\psi = 100$deg. Similarly to the previous case, very good correlation between CAMRAD and experimental measurements is identified for the low frequency content.

Figure 5.13 presents the high frequency content, 10P high-pass filtered, of the calculated moment coefficients. Solid and dashed black lines represent moment coefficients predicted with the present approach and CAMRAD respectively. Experimental measurements are denoted by grey lines. The calculated values are compared with experimental measurements and CAMRAD calculations from Ref. 207. The BVIs can now be clearly observed. Note that CAMRAD does not have a model for the calculation of the moment coefficients associated with BVIs and no high frequency content is predicted. In the BL case, excellence agreement between the predicted and experimental values is observed in both magnitude and phase. Regarding the MN case, the magnitude of the BVI matches the experimental measurements. However, there is a phase difference in the calculated moment coefficients. For the MV setup, the magnitude of the interactions are correctly capture on the advancing side with a phase discrepancy. In contrast, on the retreating side the phase angle is accurately modelled and the magnitude of only one of the vortex interactions is not matched.

Overall very good agreement is observed between the predicted aerodynamic loading and the experimental measurements. The complexity of the flowfield associated with the descending flight condition is associated with strong BVIs. The presence of strong fluctuations constitutes a challenge for code predictions and the proposed method has been proven to predict the physics of the problem with high level of fidelity.

5.7 Wake Geometry

The present work employs a free-vortex wake model to estimate the velocity inflow across the rotor disk. Hence, the structure of the wake plays a crucial role in the accurate determination of the aeroelastic behaviour of the rotor blades. Within this section a general overview of the wake geometry predicted for the HART II test conditions is first given. After, an extensive comparison of the computed values with experimental measurements and CAMRAD calculations is carried out to assess the accuracy of the inflow model.

Figure 5.14 presents a general view of the wake geometry predicted for the BL setup. Solid black and grey lines correspond to tip and root vortices respectively. For clarity purposes the trailing vortices of the near wake are only shown in the top view. Tip and root vortices are observed to behave differently. Root vortices convect downwards relatively fast as a result of the overall downwash generated by the wake. However, the tip vortices lay close to the rotor disk plane leading to BVIs. Additionally, tip vortices strongly interact between them at the lateral extremes resulting in larger size bundle vortices. As a consequence of the self and mutual vortex interactions, the geometry of the wake is highly distorted and high level of non-uniformity in the inflow is generated. This highlights the complexity of the wake geometry in descending flight, and the inherent difficulty to mathematically capture the physics of the problems.

Top view. Figure 5.15 presents the top view of the vortical structure predicted with the proposed approach, experimental measurements from Ref. 207, and CAMRAD calculations from Ref. 207 in the BL case. Solid and dashed lines denote tip vortices predicted with the present approach and CAMRAD respectively. Experimental measurements have been superimposed as Exp. The colour of the tip vortex refers to the blade number where the vortex was originally released: 1=blue, 2=red, 3=fuchsia, and 4=green. Top and bottom subfigures of Fig. 5.15 refer to the vortex system observed for two different azimuth positions of the blade number one: $\psi = 70$deg and $\psi = 20$deg. The agreement between the wake geometry predictions of the proposed approach and CAMRAD is excellent, and both geometries are close to superimpose each other in the top view. Very good agreement between the calculations of the present work and experimental measurements is found in

the first and fourth quadrants, whilst excellent correlation with the experimental data is observed in the second and third quadrants.

Figure 5.16 presents the top view of the vortex system predicted with the proposed approach and experimental measurements from Ref. 207 in the MN case. No CAMRAD calculations are available for this case. Solid lines represent the predicted geometry while experimental measurements have been superimposed as Exp. for conventional rotation direction vortices (clockwise vortices) and Exp. CCW for counter-rotating vortices (counter clockwise vortices). Distinction between clockwise and counter clockwise vortices is made here due to the presence of negative lift at the tip region over some part of the azimuth. As a result of the tip negative lift, a counter clockwise vortex is trailed at the tip and a clockwise vortex is emitted further inboard. The proposed approach estimates the tip vortex emission location based on the vorticity criteria. However, a single vortex is modelled and no dual vortex system is captured. Very good agreement between the calculations of the present work and experimental measurements is found in the first and fourth quadrants. Excellent correlation with the experimental data is observed in the second and third quadrants, specially for early wake ages.

Figure 5.17 presents the top view of the vortex system predicted with the proposed approach and experimental measurements from Ref. 207 for the MV setup. No CAMRAD calculations are available for this case. Solid lines denote the predicted geometry while experimental measurements have been superimposed as Exp. for conventional rotation direction vortices and Exp. CCW for counter-rotating vortices. Very good agreement between the calculations of the present work and experimental measurements is found in the fourth quadrant, while excellent correlation with the experimental data is observed in the first, second, and third quadrants, specially for early wake ages.

Overall very good and in some cases excellent correlation between predictions and experimental measurements has been observed in the top view of the vortex system. The best correlation has been found at early wake age, where the vortex has not been strongly deformed yet. Cases with dual vortex configurations have been approximated with a single vortex whose releasing position is adapted based on vorticity considerations. This led to very good agreement of the geometry of the vortex even when subjected to negative lift loading. The very good agreement observed in the top view increases the level of

confidence on the calculations. However, it does not guarantee the accurate prediction of BVIs because of the strong dependence of BVIs on the vertical distance between the blade and the vortex.

Side view. The relative vertical distance between the blade and the vortex is a critical factor in the determination of the BVI strength. In order to assess the capability of the present work to predict the relative vertical between blade and vortex, experimental measurements taken at two lateral planes have been compared with computational predictions. The planes chosen for this analysis are located at $y = \pm 0.7R$, which are representative of BVIs at the most relevant azimuth positions. The experimental measurements were always taken of the vortex emitted from the blade number one, which was shown in Section 5.4 to have a higher mean flapping location than the rest of the blades. Consequently, the position of the measured vortices are expected to be higher than the computed locations.

Side view: advancing side. Figure 5.18 presents the vortex system predicted with the proposed approach, experimental measurements from Ref. 207, and CAMRAD calculations from Ref. 207 for the lateral plane located on the advancing side. Solid and dashed black lines correspond to tip vortices predicted with the present approach and CAMRAD respectively. Experimental measurements have been superimposed as Exp. for conventional rotation direction vortices and Exp. CCW for counter-rotating vortices. The open marker indicates the position of the blade one at emission time. In the BL case, the experimental measurements are located above the predictions of the present method by an average of 0.5 chords. The computational underprediction of the vortex location can be partially justified by the average higher flapping location of the releasing blade. Very good agreement between both computational methods is observed, with slightly better results with the present methodology. For the MN setup, the introduced 3P phase angle results in a higher lift loading. Consequently, an increasing downwash in the advancing side is observed which pushes the vortex system further down. The agreement between the predicted geometry and the experimental measurements is excellent in shape and height. In contrast, CAMRAD calculations show an underestimation of the vortex vertical position. The phase angle applied to the HHC in the MV case leads to the opposite situation. A dual vortex system is observed which essentially pushes the vortices upwash increasing the main height of the vortex. As a result, the BVI miss distance is reduced. CAMRAD

is able to capture the trend correctly. Nevertheless, an underprediction of the vertical position is observed. The proposed method does not account for dual vortex systems and the predicted vortex is located at an intermediate position between the clockwise and counter clockwise vortices predicted with CAMRAD.

Side view: retreating side. Figure 5.19 presents the vortex system predicted with the proposed approach, experimental measurements from Ref. 207, and CAMRAD calculations from Ref. 207 for the lateral plane located on the retreating side. Solid and dashed black lines denote tip vortices predicted with the present approach and CAMRAD respectively. Experimental measurements have been superimposed as Exp. The open marker indicates the position of the blade one at emission time. The vortex geometry obtained with the present work in the BL case exhibits and excellent agreement with the experimental measurements in shape and height, and a virtual superimposition is observed. CAMRAD slightly underpredicts the vertical position of the vortex. Nevertheless of the underestimation, excellent correlation is identified. In the MN case, the excellent agreement between the experimental measurements and the proposed approach is repeated, and virtual superimposition is observed. A larger discrepancy in height between CAMRAD and the experimental dataset is found. However, the correct shape is captured. In last place, excellent correlation between the calculations carried out with the present work and the experimental measurements is observed in the MV case. Regarding CAMRAD, the shape of the vortex geometry is not correctly captured, although the average height corresponds to the average height of the experimental measurements.

Two different conclusions can be drawn from the vortex system lateral cuts. The agreement observed on the advancing side has ranged from good in the MV case to excellent in the MN case. However, certain discrepancies in height and physics have been identified. In contrast, on the retreating side excellent correlations between the predicted values and the experimental measurements have been observed. The accurate estimation of the BVIs miss distances is critical for the precise prediction of the interactions themselves. The present methodology has been proven to provide the level of confidence required to obtain a reliable prediction of the vortex geometry and consequently the BVIs miss distances.

5.8 Conclusions

An extensive assessment of the developed integrated aeroelastic model has been presented in this chapter. In the first place, the computational performance of the method was evaluated. The combined effect of using parallel computing and a velocity interpolation based acceleration scheme was shown to lead to a reduction in the required computational time of up to 97% for a given level of discretisation. As a result, fully converged simulation were obtained in 120.7min, 48.9min, 13.3min, and 3.2min for azimuth discretisation of $\Delta\psi = 1$deg, $\Delta\psi = 2$deg, $\Delta\psi = 5$deg, and $\Delta\psi = 10$deg respectively in a personal computer. Consequently, the execution time of the method was slightly higher than low order method while keeping an order of fidelity only improved by CFD codes, which are considerably more expensive computationally. This enables its multidisciplinary use, including design purposes as well as detailed noise calculations.

In the second place, the modal characteristics of the HART II rotor blade calculated with the proposed approach were compared with experimental measurements and multi-body analysis results. Excellent agreement between experimental data and the calculations was observed. The predicted values showed better agreement than the results obtained with the multi-body code. Nevertheless, a favourable comparison between computations of the proposed formulation and multi-body analysis was also identified.

In the third place, the trim control angles and rotor power required were analysed. Overall very good agreement between experimental measurements and predicted values was observed, with average discrepancies of the order of 0.3deg. Regarding the rotor power required, very good correlation with the experimental measurements was shown. This favourable correlation contrasts with the much larger discrepancies observed for a second comprehensive code.

In the fourth place, tip elastic deformations predicted with the present methodology were compared with experimental data. Excellent agreement between calculated and experimental flap deflections was identified, with maximum discrepancies in the range of blade to blade differences. The dynamics of torsion were slightly underpredicted. However, overall very good correlation was shown as well for torsion twist. Lag deflection obtained by both means virtually superimpose in the cases analyses. Hence, excellent agreement

between the deformation computed with the present methodology and experimental measurements was demonstrated.

In the fifth place, the capability of the code to predict bending and torsion moments was assessed by comparing its calculations with experimental values. The low order of magnitude of the rotor moments resulted in poor good agreement between predictions of flap bending moments and experimental values. Very good agreement of torsional moments was observed with a small underestimation of the dynamics of torsion. Excellent correlation between predictions and experimental measurements was found for lag bending moments.

In the sixth place, the accuracy of the aerodynamic loading predictions was evaluated. Overall very good agreement was observed between the predicted aerodynamic loading and the experimental measurements. The complexity of the flowfield associated with the descending flight condition is associated with strong BVIs. The presence of strong fluctuations constitutes a challenge for code predictions and the proposed method was proven to predict the physics of the problem with high level of fidelity.

In the last place, the capability of the code to predict the geometry of the tip vortices was assessed. Overall very good and in some cases excellent correlation between predictions and experimental measurements was observed in the top view of the vortex system. The best correlation was found at early wake ages, where the vortex has not been strongly deformed yet. Cases with dual vortex configurations were approximated with a single vortex whose releasing position was adapted based on vorticity considerations. This led to very good agreement of the geometry of the vortex even when subjected to negative lift loading. Regarding the side views. The agreement observed on the advancing side ranged from good in the MV case to excellent in the MN case. However, certain discrepancies in height and physics were identified. In contrast, on the retreating side excellent correlations between the predicted values and the experimental measurements were observed. The accurate estimation of the BVI miss distance is critical for the precise prediction of the interaction itself. The present methodology was proven to provide the level of confidence required to obtain a reliable prediction of the vortex geometry and consequently the BVI miss distance.

From the above, it is concluded that very good and in some cases excellent agreement

between the computations carried out with the present work and the experimental measurements has been observed. The favourable comparison proves the predictive capability of the presented methodology for the most challenging flight condition, descending flight. As a result, a high fidelity aeroelastic simulation tool has been created. The generated tool is able to represent the highly complex physics of the problem and provide accurate time-dependent calculations of elastic deflections, bending and torsion moments, and aerodynamic loading. The latter acts as an enabler for the estimation of the radiation of impulsive noise associated with BVIs. The additions of parallel computing and an acceleration scheme has resulted in a highly computationally efficient tool which can generated fully converged solutions in less than an hour for a really fine azimuthal resolution. If a slightly coarser discretisation is used, the solution can be obtained in only 3.2min with a low end personal computer.

Parameter	Value	Unit
Rotor Geometry		
Number of blades	4	–
Blade radius	2.0	m
Blade chord	0.121	m
Rotor solidity	0.077	–
Non-dimensional blade cutout	0.22	–
Non-dimensional blade root	0.075	–
Blade linear twist per span	-8	deg
Precone	2.5	deg
Aerofoil	NACA23012	–
Wind tunnel data		
Air pressure	100.97	kPa
Air temperature	290.45	K
Air density	1.2055	$\mathrm{kg\,m^{-3}}$
Wind speed	32.9	$\mathrm{m\,s^{-1}}$
Mach number	0.0963	–
Operational data		
Rotational speed	109.12	$\mathrm{rad\,s^{-1}}$
Rotor shaft angle of attack	5.3	deg
Wind tunnel interference angle	-0.8	deg
Advance ratio	0.151	–
Thrust coefficient	4.57×10^{-3}	–
Rolling coefficient (+ starboard-down)	1.386×10^{-5}	–
Pitching coefficient (+ nose-up)	-1.386×10^{-5}	–

Table 5.1: Rotor geometry, wind tunnel conditions, and operational conditions of the HART II rotor model described in Ref. 207.

	θ_0 [deg]			θ_{1c} [deg]			θ_{1s} [deg]		
	Sim.	Exp.	CMRD	Sim.	Exp.	CMRD	Sim.	Exp.	CMRD
BL	3.01	3.8	3.95	1.63	1.92	1.38	-1.17	-1.34	-1.43
MN	3.15	3.9	4.05	1.75	2.00	1.36	-1.11	-1.35	-1.40
MV	2.93	3.8	3.88	1.65	2.00	1.35	-1.01	-1.51	-1.52

Table 5.2: Calculated control angles for the HART II rotor: comparison with experimental measurements and CAMRAD calculations from Ref. 207.

	$\theta_0 + \phi_{tip}$ [deg]				
	Sim.	Exp. min.	Exp. mean	Exp. max.	CMRD
BL	2.19	2.50	2.71	3.11	2.59
MN	2.32	2.49	2.73	3.17	2.69
MV	2.10	2.27	2.62	2.71	2.48

Table 5.3: Calculated sum of collective pitch angle and elastic tip torsion: comparison with experimental measurements and CAMRAD calculations from Ref. 207.

	Rotor Power [kW]		
	Sim.	Exp.	CMRD
BL	19.25	18.3	28.65
MN	22.40	19.8	30.34
MV	19.64	18.8	29.66

Table 5.4: Calculated rotor power required: comparison with experimental measurements and CAMRAD calculations from Ref. 210.

	$100v/R$				
	Sim.	Exp. min.	Exp. mean	Exp. max	CMRD
BL	0.14	1.29	1.40	1.49	-0.67
MN	0.18	1.33	1.46	1.58	-0.66
MV	0.14	1.34	1.47	1.58	-0.67

Table 5.5: Calculated mean blade tip elastic lag motion: comparison with experimental measurements and CAMRAD calculations from Ref. 207.

	C_nM^2			C_mM^2		
	Sim.	Exp.	CMRD	Sim.	Exp.	CMRD
BL	0.086	0.090	0.084	-0.0031	-0.0026	-0.0029
MN	0.088	0.101	0.084	-0.0030	-0.0058	-0.0029
MV	0.086	0.102	0.082	-0.0031	-0.0051	-0.0029

Table 5.6: Calculated mean normal force and moment coefficients at $r = 0.87R$: comparison with experimental measurements and CAMRAD calculations from Ref. 207.

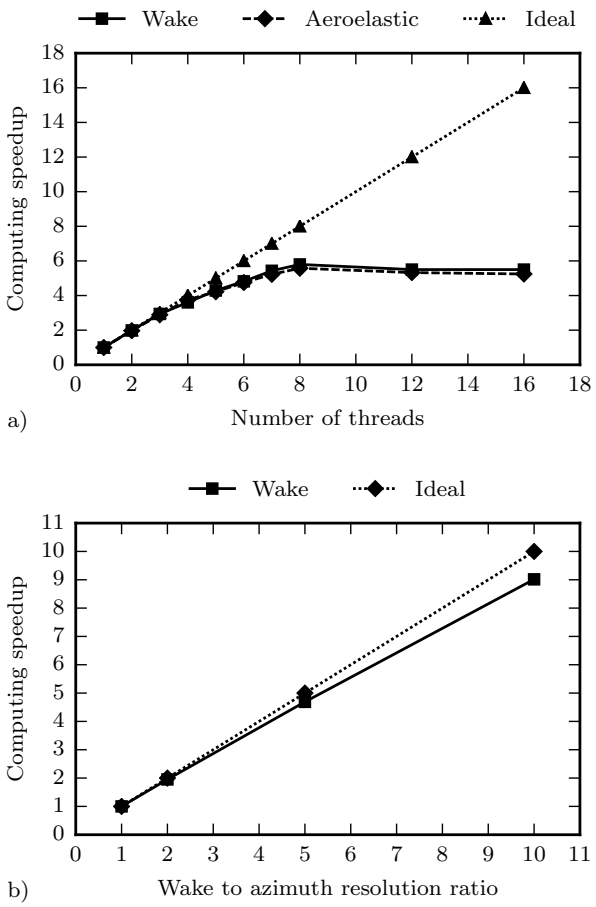

Figure 5.1: Influence of: (a) number of threads, (b) wake to azimuth resolution ratio; on the code execution speedup for a personal computer with a 3.4GHz CPU and 16GB of RAM.

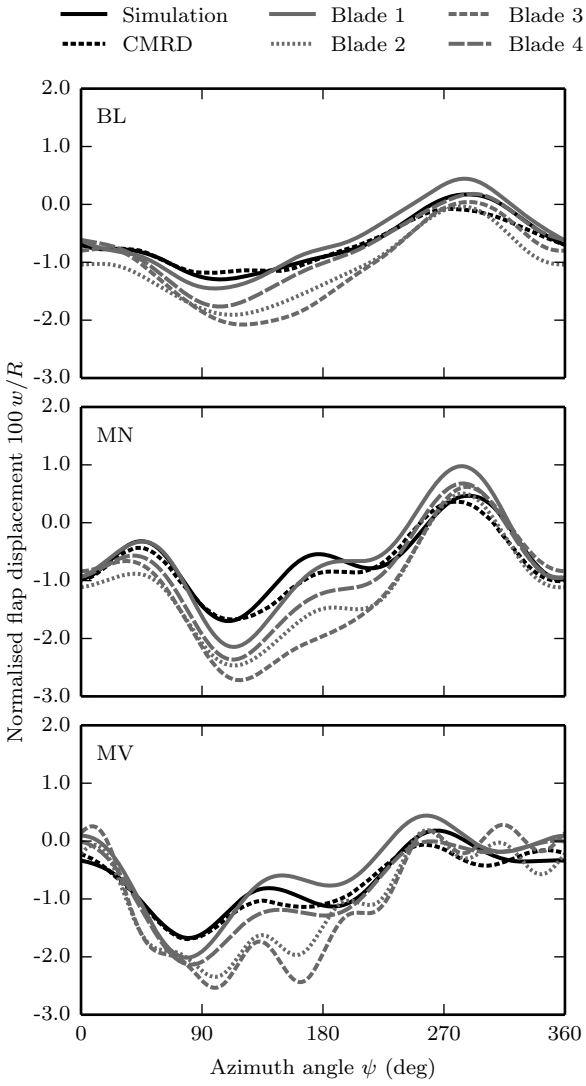

Figure 5.2: Calculated blade tip elastic flapping motion relative to precone: comparison with experimental measurements and CAMRAD calculations from Ref. 207.

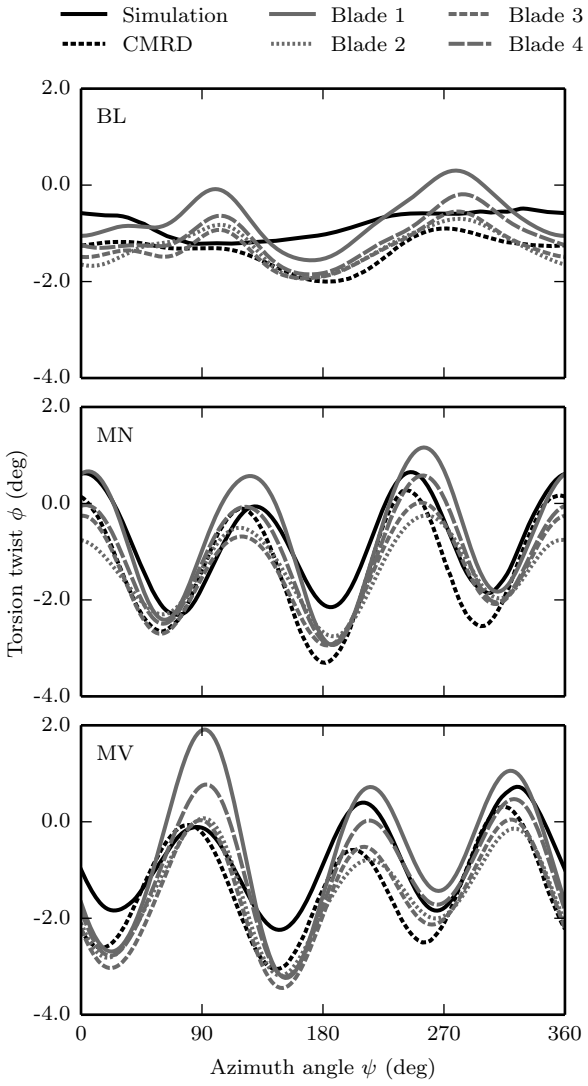

Figure 5.3: Calculated blade tip elastic torsion motion relative to control and pretwist: comparison with experimental measurements and CAMRAD calculations from Ref. 207.

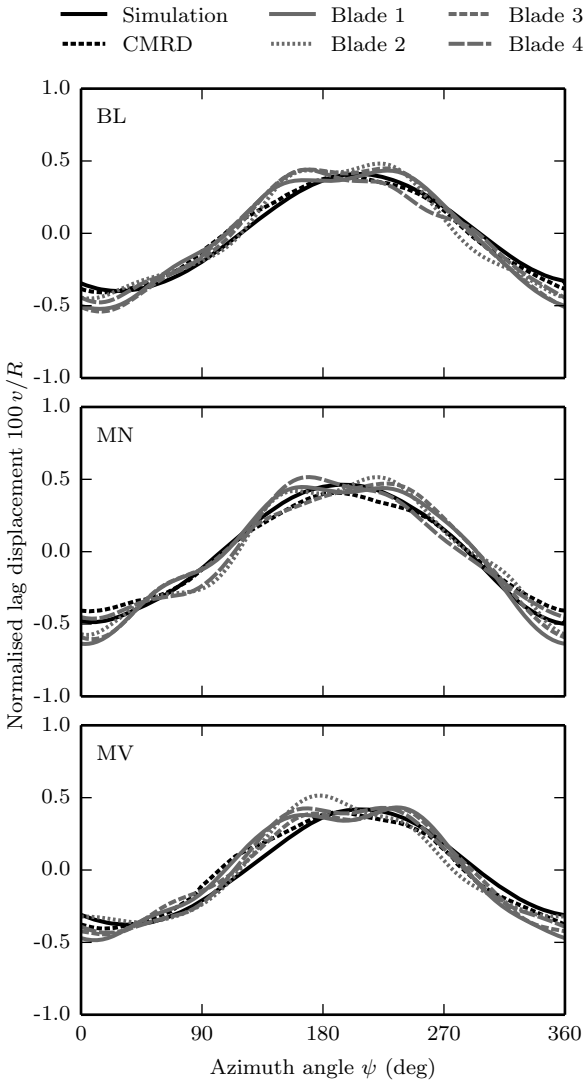

Figure 5.4: Calculated blade tip elastic lag motion, mean value removed: comparison with experimental measurements and CAMRAD calculations from Ref. 207.

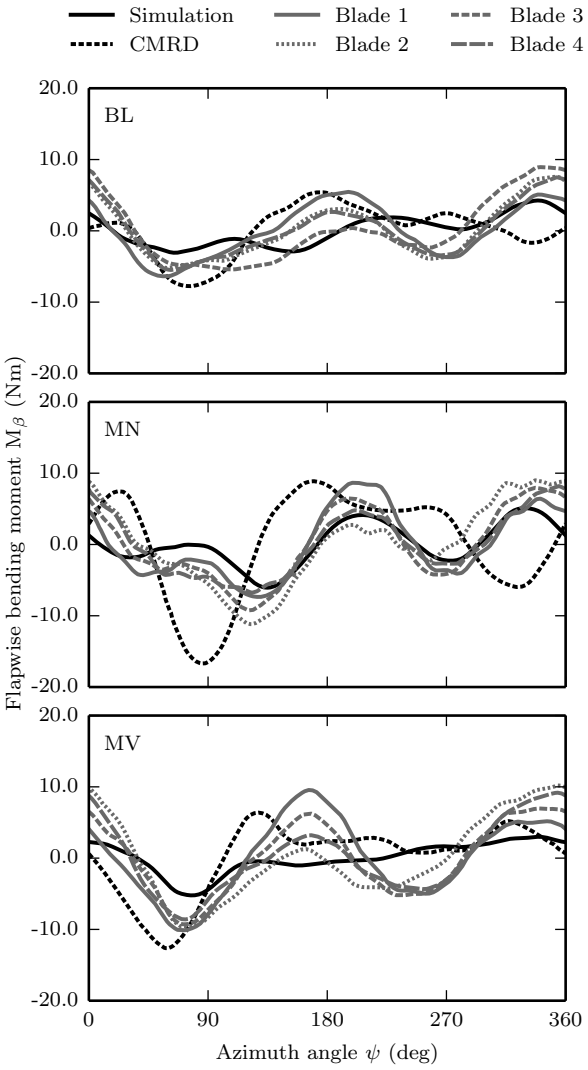

Figure 5.5: Calculated flapping bending moments at $r = 0.17R$, mean value removed: comparison with experimental measurements and CAMRAD calculations from Ref. 207.

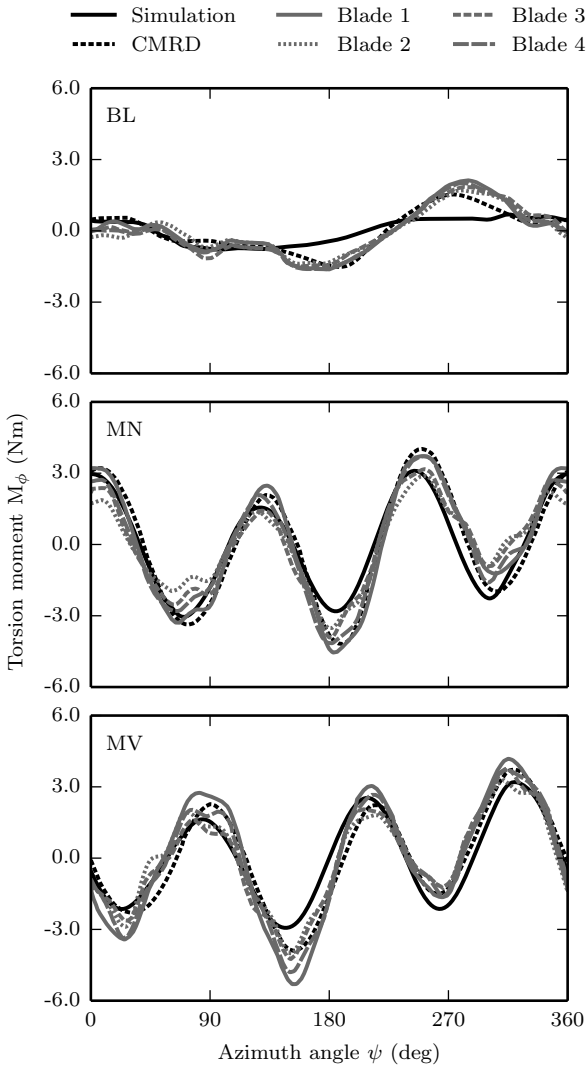

Figure 5.6: Calculated torsion moments at $r = 0.33R$, mean value removed: comparison with experimental measurements and CAMRAD calculations from Ref. 207.

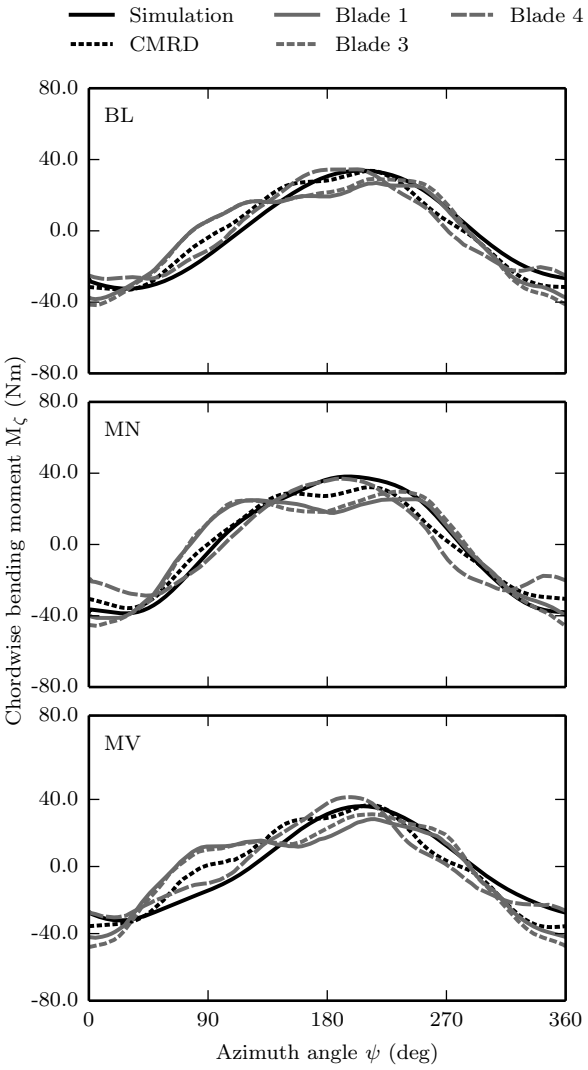

Figure 5.7: Calculated lag bending moments at $r = 0.17R$, mean value removed: comparison with experimental measurements and CAMRAD calculations from Ref. 207.

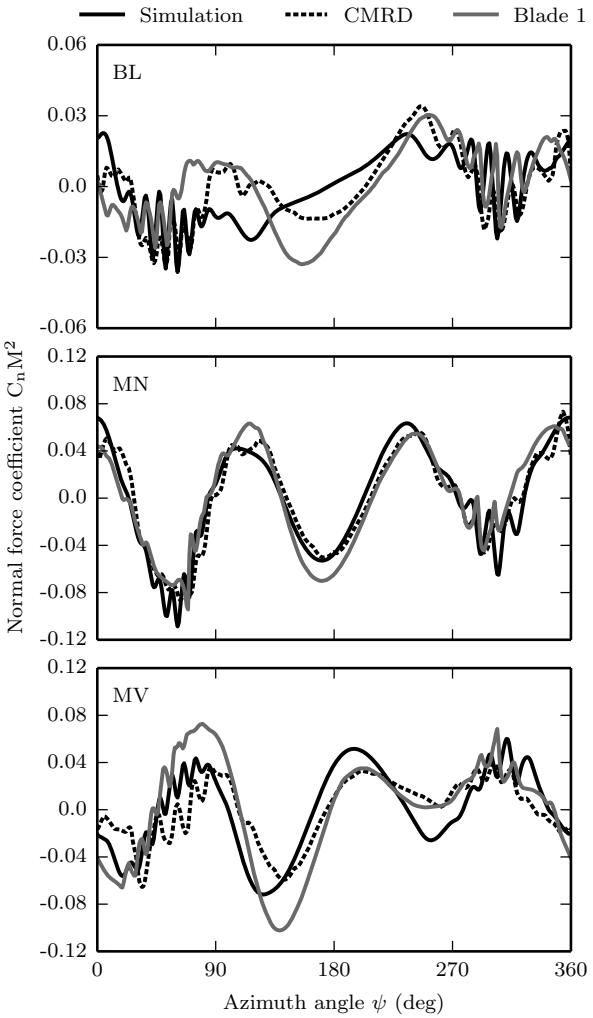

Figure 5.8: Calculated normal force coefficient at $r = 0.87R$, mean value removed: comparison with experimental measurements and CAMRAD calculations from Ref. 207.

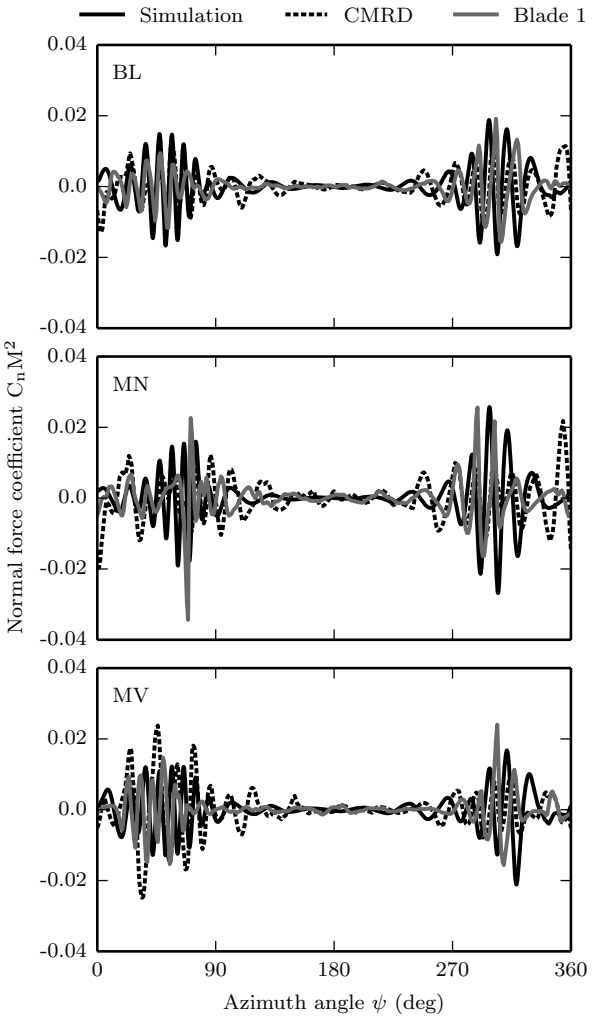

Figure 5.9: Calculated normal force coefficient at $r = 0.87R$, 10/P high-pass filtered: comparison with experimental measurements and CAMRAD calculations from Ref. 207.

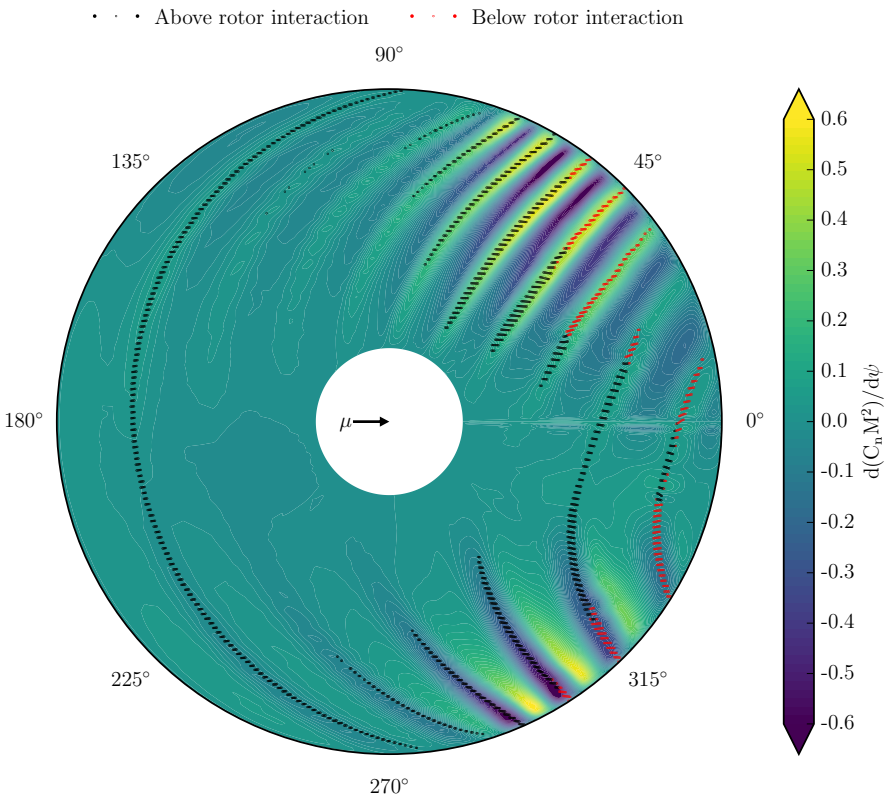

Figure 5.10: Calculated normal force coefficient time derivative and BVI locations, baseline (BL).

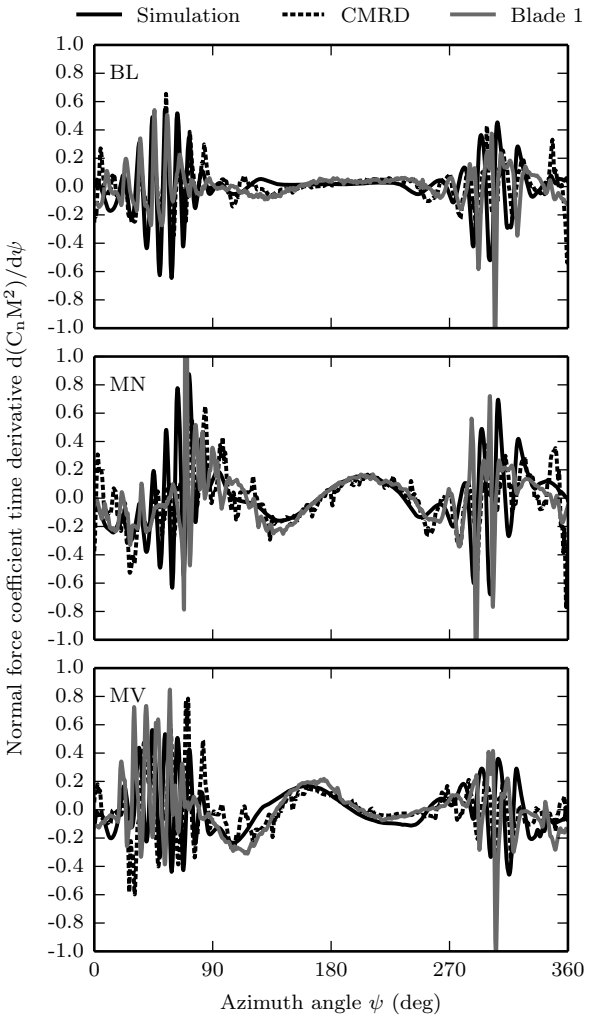

Figure 5.11: Calculated time derivative of normal force coefficient at $r = 0.87R$: comparison with experimental measurements and CAMRAD calculations from Ref. 207.

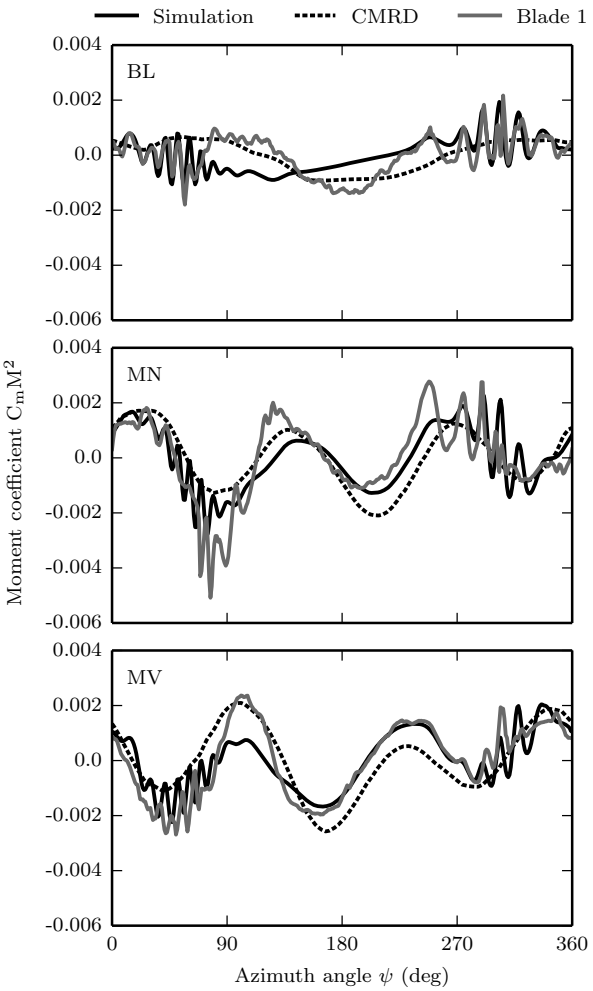

Figure 5.12: Calculated moment coefficient at $r = 0.87R$, mean value removed: comparison with experimental measurements and CAMRAD calculations from Ref. 207.

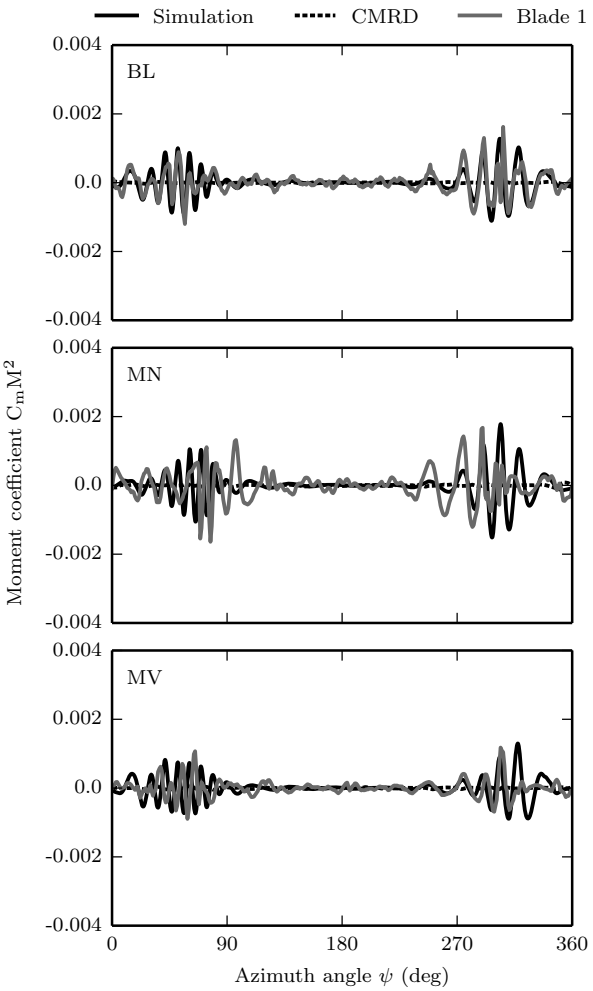

Figure 5.13: Calculated moment coefficient at $r = 0.87R$, 10/P high-pass filtered: comparison with experimental measurements and CAMRAD calculations from Ref. 207.

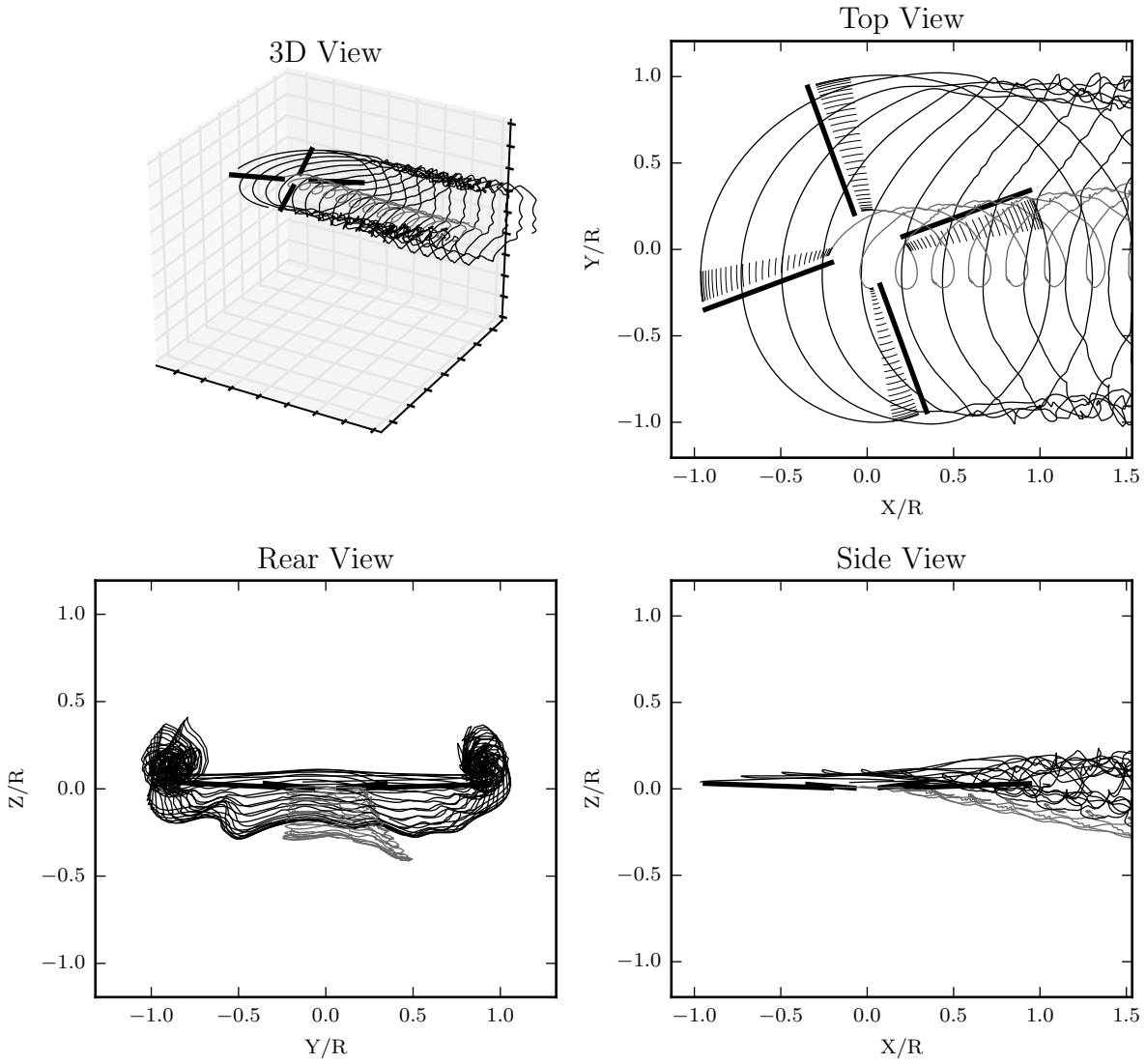

Figure 5.14: Overview of the calculated wake geometry - baseline (BL).

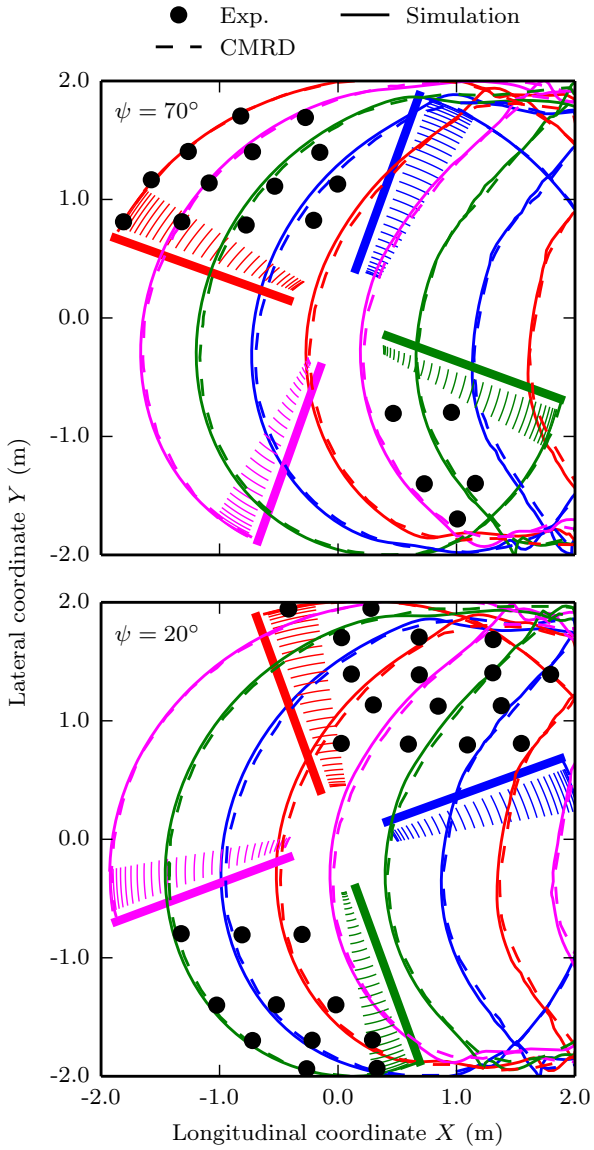

Figure 5.15: Top view of the calculated wake geometry - baseline (BL): comparison with experimental measurements and CAMRAD calculations from Ref. 207.

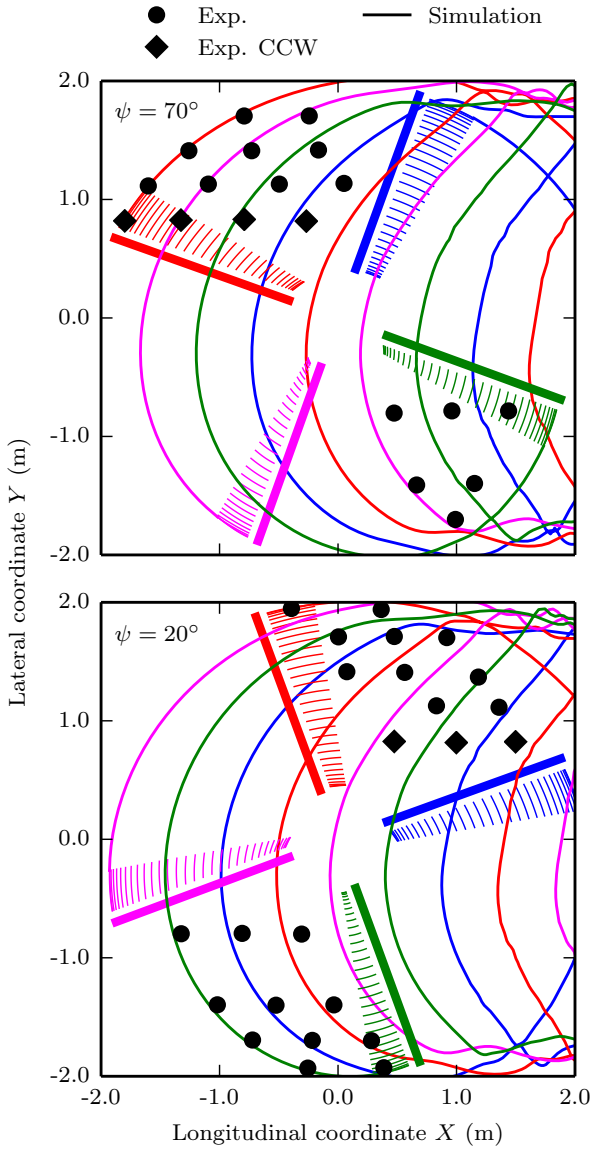

Figure 5.16: Top view of the calculated wake geometry - minimum noise (MN). Comparison with experimental measurements from Ref. 207.

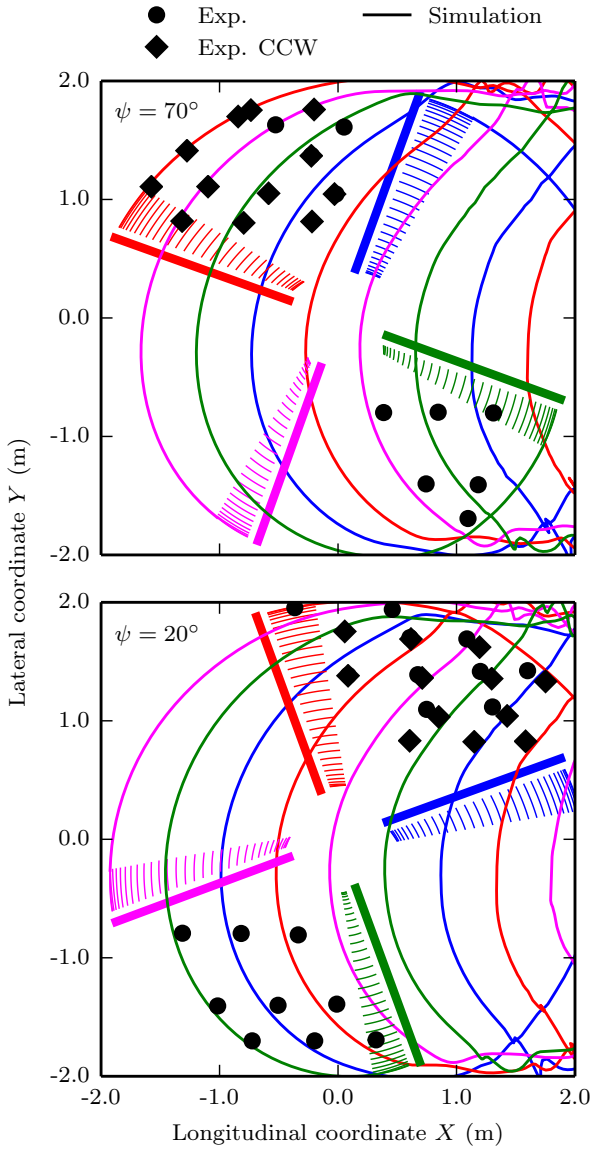

Figure 5.17: Top view of the calculated wake geometry - minimum vibration (MV). Comparison with experimental measurements from Ref. 207.

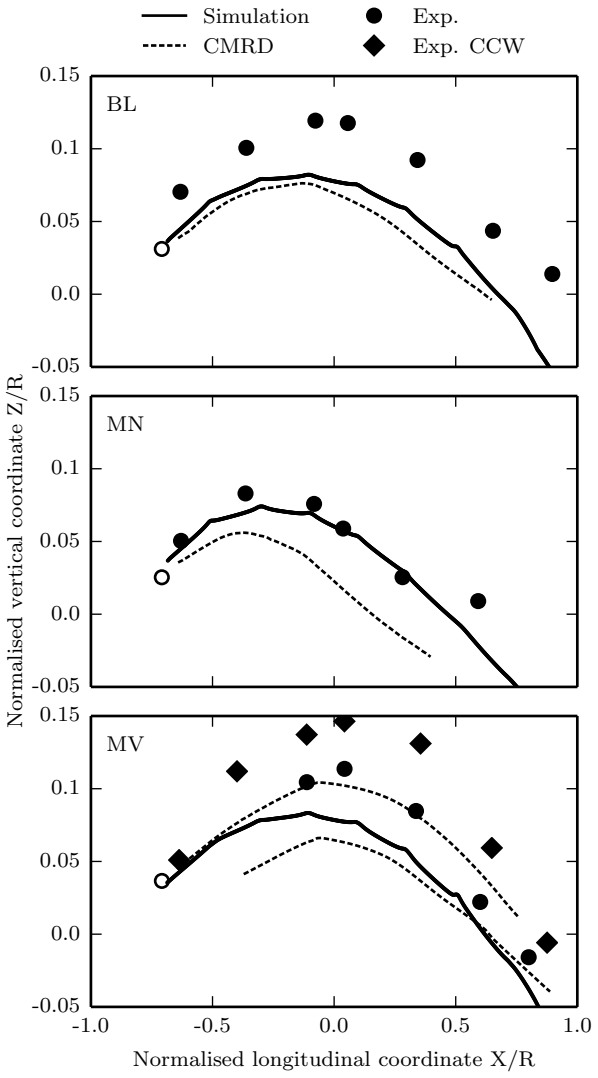

Figure 5.18: Side view of the calculated wake geometry, advancing side: comparison with experimental measurements and CAMRAD calculations from Ref. 207.

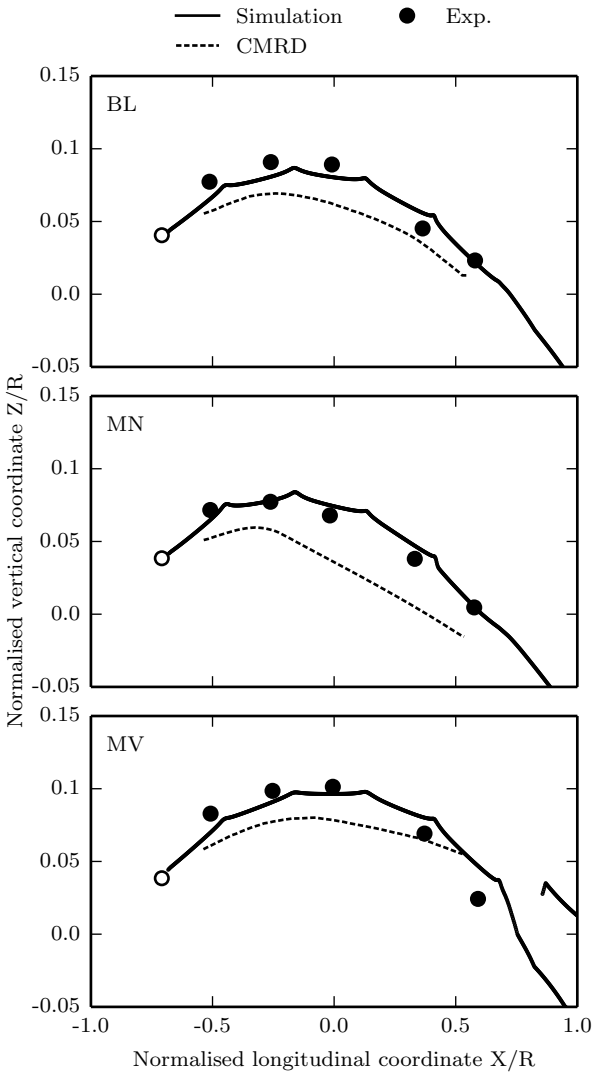

Figure 5.19: Side view of the calculated wake geometry, retreating side: comparison with experimental measurements and CAMRAD calculations from Ref. 207.

Chapter 6

Results and Discussion: Effect of Fuselage Aerodynamic Interference

A computationally efficient semiempirical analytical fuselage formulation has been implemented in the present work to estimate the fuselage induced velocity perturbations consequence of the existence of a fuselage in a free-stream. The incorporation of the fuselage aerodynamic model has two direct consequences highly coupled between them: modification of the rotor disk inflow and alteration of the vortex system geometry. The variation of any of the above leads to a further change in the second one. As a result, the fuselage induced velocity perturbation needs to be applied simultaneously to the rotor disk inflow and the wake geometry. The modification of the rotor disk inflow alters the environment where the rotor blades operate. Ultimately, this leads to a further change in the aerodynamic loading. Consequently, the dynamic response of the rotor blade and the rotor trim state are altered.

From the above it is clear the inherent coupling between all the aerodynamic and dynamic aspects of the rotor operation. Hence, the incorporation of fuselage induced velocity perturbations leads to the modification of the complete rotor behaviour. This chapter assesses the effect of the introduction of the fuselage aerodynamic model on the performance of the rotor and its different modelling components. In the first place, the fuselage induced velocity perturbations are presented along with the change in rotor disk inflow. In the second place, the effect of the fuselage interference on the trim state is

evaluated. In the third place, the variation of the vortex system associated with the introduction of the fuselage model is assessed. In the fourth place, the influence of the fuselage interference on the dynamic response of the rotor blades is examined, first in terms of the elastic deflections and after in terms of the bending and torsion moments. In the last place, the variation in low and high frequency aerodynamic loading linked to the incorporation of the fuselage induced velocity perturbations is evaluated.

6.1 Induced Velocity Flowfield

The first step in the analysis of the effect of the fuselage induced velocity perturbations on the operation of the rotor is the presentation of the velocity perturbations themselves. The implemented fuselage aerodynamic formulation prescribes a value of velocity perturbation normal to the rotor disk at any point in space above a reference plane parallel to the rotor disk. In this particular case of study, the reference height was set to $z/R = -0.3$. Figure 6.1 presents the fuselage induced velocity perturbation component normal to the rotor disk at for different horizontal planes: $z/R = 0.1$, $z/R = 0.0$, $z/R = -0.1$, and $z/R = -0.2$. The vertical positions of these planes have been identified as the possible locations of the rotor blades and the vortex system closest to the rotor. The induced velocity perturbations, which are considered positive for downwash, have been normalised with the blade tip velocity in every case. Compressibility effects are not accounted in the formulation and the proposed set of equations is valid for any flight speed within the incompressible flow regime. Two different regions can be distinguished in Fig. 6.1. At the front of the disk an upwash region can be identified while a downwash area is observed at the rear of the disk. For every plane, the positions of maximum upwash and downwash are located next to the rotor hub in the central plane $y/R = 0.0$, zero side-slip angle is assumed. A large variation in the magnitude of the maximum upwash/downwash perturbation velocity with height is observed. The smaller the relative distance between the plane and the reference plane, the larger the maximum upwash/downwash. This is clearly observed in the individual contour scales.

The prescribed distribution of fuselage induced velocity perturbations normal to the rotor disk presented in Fig. 6.1 has two direct effect: modification of the rotor disk inflow

and variation of the vortex system geometry. Figure 6.2 presents the total induced velocity component normal to the rotor disk for the baseline case with fuselage interference (Fig 6.2a) and the isolated rotor case (Fig. 6.2b). In both cases the velocity, which is considered positive for downwash, is normalised with the blade tip speed. A highly non-uniform velocity inflow is observed. The high level of non-uniformity is associated with the specific operational condition tested, where the vortex system lays close to the rotor and strong BVIs are present. The first of the direct effects, the direct modification of the rotor disk inflow, can be observed around the central plane $y/R = 0.0$ and close to the rotor hub. A weaker inflow, associated with the fuselage upwash, is identified at the front of the disk in Fig. 6.2a which is not found in Fig. 6.2b. The opposite effect is observed at the rear of the back, where the inflow is higher than in the reference setup. In addition to the local modification of the velocity inflow consequence of the direct addition of the fuselage induced velocity perturbation, the geometry of the wake is altered (full details in Section 6.3). The variation of the geometry wake leads to a further modification of the velocity inflow as shown in Figure 6.2. The most relevant changes associated with the modification of the vortex geometry is the increase in the amplitude of the induced velocity oscillations observed on the advancing side for the isolated case as a result of the smaller BVI miss distances. As a consequence, larger BVIs will be predicted if the fuselage interference is not accounted. Similar results have been obtained for the MN and MV cases. Hence, they are not presented here due to their similarity to the BL case.

The fuselage induced velocity perturbations have been proven to directly influence the normal inflow across the rotor disk, specially in the inboard region; and the overall inflow distribution as a result of the change in wake geometry.

6.2 Rotor Trim

As a consequence of the incorporation of a fuselage model for the estimation of fuselage induced velocity perturbations, the induced flowfield across the rotor disk is modified as shown in the previous section. The trim control angles required to obtain the same prescribed prescribed thrust, rolling moment, and pitch moment coefficients must vary to balance the new velocity inflow.

Control angles. Table 6.1 presents the collective θ_0 (at $r = 0.75R$), lateral cyclic θ_{1c}, and longitudinal cyclic θ_{1s} pitch angles needed to trim the rotor to the prescribed force and moments coefficients. The calculated control angles are presented for the reference case with fuselage interference and compared with the values obtained for an isolated rotor with the present approach and experimental measurements from Ref. 207.

In every case tested, the introduction of the fuselage aerodynamic model results in a marginal decrease of the collective pitch angle θ_0. The reduction could be attributed to a slightly higher average inflow velocity. However, due to the low magnitude of the change, no conclusion can be drawn. During the analysis, the mean tip elastic torsion was found to be virtually the same for the isolated rotor and the rotor with fuselage interference. As a result, the effective collective pitch angle remains the same and the specific value is not presented here for brevity.

The prediction of the lateral cyclic pitch angle θ_{1c} is greatly improved as a result of the inclusion of fuselage velocity perturbations. An average reduction of 0.35deg in the discrepancy between the proposed method predictions and the experimental measurements is observed in Table 6.1.

Regarding the longitudinal cyclic pitch angle θ_{1s}, an average reduction of 0.12deg in the error between the present predictions and the experimental measurements is identified as a result of the inclusion of fuselage induced velocity perturbations in the analysis.

The introduction of fuselage interferences has been proven to have a large effect on the trim control angles. Although no appreciable difference in the collective pitch angle is identified, the cyclic pitch angles prediction is greatly improved. This highlights the necessity of the calculation of fuselage aerodynamic interferences for the accurate modelling of the rotor trim condition.

Power. Table 6.2 presents the comparison between the rotor power required predicted with and without fuselage induced velocity perturbations and experimental measurements from Ref. 210. Substantial improvement in the prediction of the required rotor power is identified as a consequence of the inclusion of fuselage velocity perturbations. The rotor power is overestimated by the model without fuselage by 4.7kW, 4.8kW, and 4.4kW in the BL, MN, and MV cases respectively. The incorporation of the fuselage interference leads to a reduction of the discrepancies to only 0.9kW, 2.6kW, and 0.84kW for BL, MN, and

MV respectively. In both cases, the relative changes in rotor power required consequence of the application of HHC are assessed. The experimental measurements of rotor power required taken for the MN and MV cases show relative increments in rotor power of 1.5kW and 0.5kW respectively. This trend is correctly predicted with the model without fuselage interferences, with relative changes of 1.63kW and 0.19kW in MN and MV cases respectively. The same trend is observed in the case where fuselage velocity perturbations are included. In this case the relative changes become 3.15kW and 0.39kW for MN and MV respectively. The overall effect of the incorporation of fuselage interferences is an improvement on the prediction of the rotor power required. The HHC changes of rotor power relative to the BL case are correctly predicted in both cases.

6.3 Wake Geometry

The second direct consequence of the incorporation of the fuselage induced velocity perturbations is the modification of wake geometry. This effect is expected to be larger on the region closer to the rotor hub where the velocity perturbations are stronger. A significant effect is expected as well on the advancing side, as the vortex structure has previously gone trough the central area.

Top view. Figure 6.3 presents the top view of the vortical structure calculated with the proposed approach with and without fuselage perturbations and experimental measurements from Ref. 207 for the BL case. Solid and dashed lines denote tip vortices predicted with and without fuselage interference respectively. Experimental measurements have been superimposed as Exp. The colour of the tip vortex refers to the blade number where the vortex was originally released: 1=blue, 2=red, 3=fuchsia, and 4=green. Top and bottom subfigures of Fig. 5.15 correspond to the vortex system observed for two different azimuth positions of the blade number one: $\psi = 70$deg and $\psi = 20$deg. The predictions made with and without a fuselage aerodynamic model virtually superimpose in the top view. This is explained by the nature of the fuselage formulation, which only prescribes perturbations normal to the rotor disk. As a result, the largest differences between both models are expected to be seen on the vertical direction. Very good agreement between the calculations of the present work and experimental measurements is found in the first

and fourth quadrants, whilst excellent correlation with the experimental data is observed in the second and third quadrants. The virtual superimposition in the top view of the geometry predictions obtained with and without fuselage perturbations is repeated in the MN and MV cases and no further detail is given.

Side view. The relative vertical distance between the blade and the vortex dictates the strength of the BVI. In order to assess the effect of fuselage velocity perturbations on the relative vertical between blade and vortex, experimental measurements taken at two lateral planes have been compared with computational predictions with and without fuselage interference. The planes chosen for this analysis are located at $y/R = \pm 0.7$, which are representative of BVIs at the most relevant azimuth positions and the central plane $y/R = 0.0R$, which represents the location with the strongest velocity perturbations. The experimental measurements were always taken of the vortex emitted from the blade number one, which was shown in Fig. 5.2 to have a higher mean flapping location than the rest of the blades. Consequently, the position of the measured vortices are expected to be higher than the computed locations.

Side view: central plane. Figure 6.6 presents the vortex system predicted with and without fuselage perturbations for the central plane. Solid black and grey lines denote tip vortices predicted with the present approach with and without interference respectively. A slightly higher initial position is observed in the isolated case compared with the case with fuselage. This is associated with the different trim state previously identified, which leads to differences in elastic blade deflections. The upwash perturbation observed previously in Fig. 6.1 generates the movement of the tip vortex upwards at the front of the disk, as shown in Fig. 6.6. The fuselage produces a downwash region at the rear of the disk. As a result, the tip vortex is pushed downward for positive values of X. Hence, the overall effect of the introduction of fuselage induced velocity perturbations is the increase in the trajectory curvature, resulting in higher vertical positions in the central area of the central plane and lower locations outside it. The same trend is observed in Fig. 6.1 for the MN and MV cases and no further details are given.

Side view: advancing side. Figure 6.7 presents the vortex system calculated with and without fuselage induced velocity perturbations and experimental measurements from Ref. 207 for the lateral plane located on the advancing side. Solid black and grey lines

correspond to tip vortices predicted with the present approach with and without fuselage perturbations respectively. Experimental measurements have been superimposed as Exp. for conventional rotation direction vortices and Exp. CCW for counter-rotating vortices. The open marker indicates the position of the blade one at emission time. In the BL case, the initial location of the blade tip vortex computed with both model superimpose, which is linked to similar flap deflections at approximately $\psi = 135$deg for both simulations. The introduction of the fuselage interference leads to an average higher vertical location of the vortex system. This is a consequence of the combination of the advance ratio and the upwash perturbation located at the from of the disk. The vortex structure whose intersections are plotted in Fig. 5.18 has previously gone through the upwash perturbation region. Consequently, their location is higher in the lateral plane. The higher position of the vortices, better matches the experimental measurements and increases the BVIs miss distance. The latter ultimately decreases the intensity of the advancing side BVIs. Regarding the HHC cases, the incorporation of the fuselage aerodynamic model leads to the same trends observed for the BL case.

Side view: retreating side. Figure 6.8 presents the vortex system computed with and without fuselage interference and experimental measurements from Ref. 207 for the lateral plane located on the retreating side. Solid black and grey lines denote tip vortices calculated with the present approach with and without fuselage perturbations respectively. Experimental measurements have been superimposed as Exp. The open marker indicates the position of the blade one at emission time. For the BL case, the initial position of the tip vortex is observed to be higher for the isolated rotor case. The larger elastic deflection of the isolated rotor blade at this location justifies this behaviour. As the vortex becomes older, it spends more time on the upwash region of the disk and it is pushed upwards. However, this effect is much weaker on the retreating side. This is due to the decrease of the order of magnitude of the fuselage perturbations as the distance from the central plane increases. The same trend is observed for the MN and MV cases, with minimum differences in the predicted geometry between both computational models. Despite of the low order of magnitude of the discrepancy, the introduction of the fuselage perturbations leads to better agreement between computational predictions of the vortex geometry and correspondent experimental measurements.

From the above it is concluded that the incorporation of the fuselage induced velocity perturbations results on an increment of the vortex trajectory curvature. It leads to higher positions on both lateral positions, advancing and retreating side, which ultimately increase the BVI miss distance. Therefore, the incorporation of a fuselage aerodynamic model dictates the BVIs miss distances and the strength of the interactions.

6.4 Elastic Deformations

The incorporation of the fuselage interference has been proven to influence the trim state of the rotor. As a result, the dynamic response and elastic deformation of the rotor blade are expect to vary. In this section the effect of the fuselage perturbations on the motion of the blade is quantified by measuring the elastic deformation of the blade tip relative to the undeformed rotor blade. These predictions are compared with the experimental measurements to assess the predictive capability.

Elastic flap deflections. Flap tip elastic deformations are measured in the out of plane direction relative to the undeformed preconed rotor. Figure 6.9 presents the elastic flap deformations for the BL, MN, and MV cases. Elastic flap deflections have been normalised with the rotor radius. Solid and dashed black lines represent elastic deflections predicted with the present approach with and without fuselage induced velocity perturbations respectively. Experimental measurements of each blade from Ref. 207 are denoted by grey lines. A strong 1P flapping oscillation is observed for the BL case with and without the interference of the fuselage. The magnitude and location of the maximum and minimum flap deflections are not altered by the introduction of the fuselage model. Nevertheless, flapping deflections are modified at the front and back of the rotor disk. In order to satisfy the rotor trim conditions, a large increment in lateral cyclic pitch angle θ_{1c} was applied. As a result, a larger flap forcing is generated at the back of the disk, whilst the flap excitation is reduced at the front of it. The generated differential loading results in the variation of the elastic flap deflections shown in Fig. 6.9. Both predictions exhibit excellent agreement with the experimental data, and are located within the blade to blade difference range.

In the MN case, 3P flapping component is identified. This is attributed to the inclusion of a 3P HHC. Very good agreement is observed between both predictions and experimental

measurements. The proposed method slightly overpredicts the 3P content at approximately $\psi = 180$deg. The discrepancy at this location is reduced when the fuselage induced velocity perturbations are incorporated into the analysis. It is once again explained by the larger lateral cyclic pitch angle θ_{1c} required to satisfy the trim conditions, which leads to higher and lower flapping locations at the back and front of the rotor disk respectively. Despite the overestimation of the 3P response, the discrepancies of both implementations relative to the experimental data are in the range of blade to blade differences and excellent phase agreement is shown.

Regarding the MV case, considerable high order content is observed in the experimental flap deflection for the second and third blades, which is not found in the response of the first and fourth blades. The computations with fuselage interference show excellent agreement with the experimental values of the first and fourth blades. If the flap deflections are calculated with the isolated rotor model the lower flap position at the back of the disk leads to larger discrepancies relative to the experimental measurements. Even for the latter, the discrepancies are in the range of blade to blade differences and overall excellent agreement in magnitude and phase is identified in both cases.

Elastic torsion twist. The elastic tip torsion twist is measured in the pitching direction relative to the pretwist blade with applied control angles. The comparison between computations with and without fuselage induced velocity pertubations and experimental measurements is presented in Fig. 6.10 for BL, MN, and MV. Solid and dashed black lines denote predicted elastic deflections with and without aerodynamic fuselage interference respectively. Experimental measurements of each blade from Ref. 207 are presented with grey lines. In the BL case a strong 2P component is observed in the experimental measurements. Coupling between the first torsion and the second flap modes can be identified as the source of the 2P torsion component. The introduction of the fuselage has a minimum impact on the torsion response, and their predictions virtually superimpose. In both cases, the proposed approach fails to predict the 2P response and a less dynamic tip torsion twist is predicted.

As a result of the application of HHC, the dynamics of torsion raise significantly as shown in Fig. 6.10 for the MN and MV cases. In the MN case, excellent agreement between the phase of the reference computations and experimental measurements is

observed. In terms of the torsion amplitude, the present work slightly underestimates the dynamics of torsion leading to an underprediction of the torsion angle at approximately $\psi = 180$deg. No substantial differences in the prediction of torsion are observed as a result of the incorporation of the fuselage induced velocity perturbations. Similar comments are applicable to the MV case. Excellent agreement is observed in the calculated phase and very good agreement in amplitude is identified, with an underprediction of the torsion angle at approximately $\psi = 30$deg and $\psi = 150$deg.

Overall excellent agreement of the predictions between the proposed method with experimental measurements has been observed in the analysed cases. No dependence of the torsion dynamics on the fuselage interference has been found. A systematic underprediction of the torsion dynamics previously identified in this model dominates the torsional behaviour of the blade.

Elastic lag deflections. Lag deflections are measured relative to the undeformed blade in the in plane direction, with positive sign against rotation. Fig. 6.11 presents the dynamic evolution of the lag deflection, mean removed, for the proposed method with and without fuselage perturbations and experimental measurements from Ref. 207. Elastic lag deflections have been normalised with the rotor radius. Solid and dashed black lines represent elastic deflections computed with and without fuselage perturbations respectively. Experimental measurements of each blade are denoted by grey lines. A larger dynamic oscillation is generated as a result of the inclusion of fuselage velocity perturbations. These predictions virtually superimpose with the experimental values for all three cases and the discrepancies are confined to the blade to blade differences range.

6.5 Bending Moments

Bending moments along with elastic deflections characterise the dynamic response of the rotor blade to external loading. The effect of the fuselage induced velocity perturbations on the elastic deflections has been previously analysed. Hence, the effect of the fuselage interference on the bending moments is assessed in this section. Experimental measurements of bending and torsion moments were taken at $r = 0.17R$ and $r = 0.33R$ respectively.

Flap bending moments. Figure 6.12 presents the flap bending moments predicted with

and without fuselage induced velocity perturbations and experimental measurements. The mean value of flap bending moment has been subtracted in every case. Solid and dashed black lines correspond to flap bending moments computed with and without fuselage interferences respectively. Experimental measurements of each blade from Ref. 207 are denoted by grey lines. The lack of correlation between computed flap bending moments and experimental measurements previously justified in Section 5.5 impedes the author to assess the positive or negative effect of the inclusion of the fuselage model on the prediction of flap bending moments. However, calculations carried out with and without the fuselage interferences show good correlation between them and only a weak discrepancy is observed. Therefore minimum effect of the fuselage perturbations on the flap bending moments is identified.

Torsion moments. The agreement between code predictions and experimental data is analysed in Fig. 6.13, where solid and dashed black lines correspond to flap bending moments predicted with an without fuselage velocity perturbations respectively. Experimental measurements of each blade from Ref. 207 are presented with grey lines. A low order of magnitude 1P torsion moment fluctuation is observed in the experimental measurements for the BL case. The dynamics of torsion are underpredicted with the proposed approach. This discrepancy is equally observed for calculations with and without the fuselage interferences. In Section 5.5, possible sources of error for the underestimation of the dynamic torsion moments were provided and further details are not given.

The introduction of 3P HHC results in an increase in the excitation of the first torsion mode. This is justified by the proximity of the first torsional moment and the 3P frequency in the frequency spectrum. Excellent agreement between computations and experimental measurements is observed. In both cases, MN and MV, the calculations carried out with and without fuselage velocity perturbations virtually superimpose each other.

Lag bending moments. Figure 6.14 presents the calculated lag bending moments with and without fuselage velocity perturbations and experimental measurements from Ref. 207. The mean value of lag bending moment has been removed in every case to better show the dynamic content. Solid and dashed black lines denote flap bending moments predicted with and without fuselage interference respectively. Experimental measurements of each blade are presented with grey lines. The present work predicts correctly the 1P

content in both amplitude and phase with both implementations. The calculations made with the isolated rotor leads to a slightly less dynamic moments. However, the magnitude of the difference is in the range of blade to blade differences.

Overall very weak effect of the fuselage induced velocity perturbations on the bending and torsion moments has been identified. Virtual superimposition was observed for flap bending and torsion moments whilst a small increase in the dynamics content of the lag bending moment was found.

6.6 Aerodynamic Loading

Within the previous sections the relation between the incorporation of fuselage induced velocity perturbations, dynamic response of the blade, wake geometry, and rotor disk inflow has been described. Changes in these variables are associated with changes in aerodynamic loading. This section presents the comparison between computational predictions of aerodynamic loading obtained with and without fuselage interference and experimental measurements. It was observed in Figs. 5.2 and 5.3 that blade number one has a higher mean flap position and stronger dynamic oscillations of the pitch angle compared with the other blades. As a result, the magnitude of the measured aerodynamic loading should be higher in mean value and dynamic content than the computed one, where identical blades are simulated. Consequently, this will magnify the discrepancies of low frequency aerodynamic loading between experimental measurements and computations.

Normal force coefficient. The mean value of normal force coefficient at $r = 0.87R$ calculated with and without fuselage velocity perturbations is presented in Table 6.3 along with the respective experimental measurements from Ref. 207. An underprediction of about 4% relative to the experimental measurements is observed in the normal coefficient calculated with fuselage velocity perturbations in the BL case. In the HHC cases, the trends are similar and the computed aerodynamic loading is underestimated by 12% and 16% in the MN and MV cases respectively. Differences between code implementations are lower than 1% and a weak effect of the fuselage on the mean value of normal force coefficient.

Figure 6.15 presents the dynamic, mean removed, normal force coefficient calculated at

$r = 0.87R$ along with the correspondent experimental measurements from Ref. 207. Solid and dashed black lines denote normal force coefficients predicted with and without fuselage interference respectively. Experimental measurements are presented with grey lines. In every case, strong high frequency fluctuations in aerodynamic loading associated with BVIs are observed at approximately $\psi = 50$deg and $\psi = 300$deg. In the BL case, a 2P oscillation in aerodynamic loading is observed. Discrepancies between the predictions with and without fuselage interferences are identified in the low frequency content of the normal coefficient. An underprediction of the loading is observed for the isolated rotor in the first and fourth rotor quadrants, while the slightly higher values of normal force coefficient are found at the front of the disk. Different sources of discrepancies can be identified. The first one is the change in cyclic control angle. As a result, there are differences in geometric pitch angle along the azimuth with maximum variations of ± 0.37deg . The second source of discrepancy is the change in flap elastic motion. As a consequence of the change in flap motion, the relative distance between the tip vortices and the blade is modified varying the rotor inflow. Additionally, elastic motion contributes to the effective angle of attack. The third source of discrepancy is the difference in rotor disk inflow. The addition of the fuselage induced velocity perturbation clearly modifies the rotor disk inflow, along with its variation due to to changes in wake geometry. The intertwinement of these effect results in the final modification of the normal force coefficient shown in Fig. 6.15. Overall better agreement between computations and experimental measurements is found as a result of the introduction of the fuselage interference.

Regarding the MN and MV cases, combinations of 2P and 3P oscillations are observed in Fig. 6.15. Excellent correlation between calculations and experimental measurements is observed. In the MN case, the predictions match the experimental values in both: amplitude and phase. Differences between the isolated rotor and the fuselage interference cases are only appreciable at the 3P loading peaks. These differences are once again low frequency discrepancies with sources of error similar to the ones of the BL case. However, because of the relatively high amplitude of the 3P control, these discrepancies become relatively small. Overall better agreement between the computations and the experimental measurements is observed if fuselage velocity perturbations are accounted for, except at the loading peak located at approximately $\psi = 110$deg. Nevertheless, excellent correlation

between the proposed approach calculations and experimental measurements is found. A similar situation takes place in the MV case, where the incorporation of the fuselage model results in a small improvement in the correlation of the 3P loading peaks located at approximately $\psi = 130$deg and $\psi = 190$deg. However, excellent agreement between both calculations and the experimental measurements is observed.

Figure 6.16 presents the high frequency content, 10P high-pass filtered, of the calculated normal force coefficient. The calculated values are compared with experimental measurements from Ref. 207. Solid and dashed black lines correspond to normal force coefficients predicted with and without fuselage interference respectively. Experimental measurements are denoted by grey lines. BVIs can now be clearly identified. In the BL case, the present work matches the experimental phase of the advancing side BVIs. However, the magnitude of the interactions is overestimated. Small differences between predictions made with and without fuselage velocity perturbations are identified. For the earlier azimuth angles, the higher flapping position of the case with fuselage observed in Fig. 6.9 leads to a slightly shorter BVI miss distance and a stronger interaction. For older azimuth angles, the higher vertical position of the vortex predicted with fuselage perturbations along with the lower flapping position increase the BVI miss distance, leading to weaker interactions relative to the isolated rotor setup. No phase difference between computations is identified, this is associated with the virtual superimposition of both geometry predictions in the top view (Fig. 6.3). Regarding the BVIs of the retreating side, the magnitude prediction is improved at the expense of deteriorated phase agreement. The effect of the incorporation of the fuselage interference on the amplitude of the BVI is the opposite to the one found on the advancing side. As a result, BVI predictions with fuselage perturbations are weaker at the earlier azimuth angles and stronger at the oldest. Even if there is a change in the magnitude of the BVI, the order of magnitude of this change is considerable smaller than one observed in the low frequency content. The same trends identified for the BL case resulting from the incorporation of the fuselage interference are valid in the MN and MV cases. Once again the order of magnitude of these variations are considerably smaller than the ones of low frequency content.

Impulsive noise is highly influenced by the time derivative of the aerodynamic loading. Figure 6.17 presents the relation between the time derivative of the normal force coeffi-

cient and the BVI locations for the BL case with and without fuselage induced velocity perturbations. In accordance with the changes observed in the high frequency content of the normal force coefficient, the location of the strongest interactions is shifted as a result of the fuselage interference. As it was previously explained, the amplitude of the BVI becomes larger at early azimuth when the fuselage is considered. That can be observed in Fig. 6.17 where steeper gradients are identified at approximately $\psi = 30 - 50$deg in the top figure. In contrast the derivatives at older azimuth angles $\psi = 60 - 100$deg are reduced, which corresponds to the smaller interaction amplitudes in Fig. 6.16. The opposite effect is observed on the retreating side. The derivatives become stronger at the back of the rotor disk while a weakening of the aerodynamic derivatives takes place at approximately $\psi = 270 - 300$deg. These trends are in accordance with the changes in amplitude previously identified in Fig. 6.16.

The trends presented for the time derivative of the normal force coefficient are now quantify in Fig. 6.18, where the time derivative of the normal force coefficient predictions obtained with and without the fuselage interference, 10P high-pass filtered, are compared with the experimental values from Ref. 207. Solid and dashed black lines correspond to the first time derivative of the normal force coefficients computed with and without fuselage interferences respectively. Experimental measurements are denoted by grey lines. In the BL case, both implementations overpredict the magnitude of the time derivatives on the advancing side. However, the phase angles are accurately predicted. The biggest differences between the predictions obtained with and without the fuselage interferences are located between $\psi = 60$deg and $\psi = 90$deg, where the overprediction observed for the isolated rotor is reduced and better correlation with the experimental measurements is obtained. On the retreating side the predictions show a phase offset relative to the experimental measurements. Small reductions in the time derivative of the normal force coefficients are observed as a result of the introduction of the fuselage perturbations. The incorporation of the fuselage aerodynamic model to the HHC analyses results in similar relative changes in normal force coefficient time derivatives. Even though the amplitude prediction is improved with the fuselage perturbations, the magnitude is still overpredicted. Nevertheless, overall good agreement between code predictions and experimental measurements has been observed in the prediction of the time derivative of

the aerodynamic loading.

Moment coefficient. Table 6.3 presents the mean value of the moment coefficient calculated at $r = 0.87R$ with and without fuselage induced velocity perturbations along with the respective experimental measurements from Ref. 207. The predictions done with and without the fuselage interference are virtually the same and no difference is noticed. Very good agreement with the experimental value in the case of BL is observed, whilst larger discrepancies are identified in the MN and MV cases. The coarse resolution of the experimental sensors does not provide a definitive comparison between experimental and computation. However, the computations have been proven to be independent of the fuselage induced velocity perturbations.

The dynamic content of the moment coefficient at $r = 0.87R$ is presented in Fig. 6.19 for the proposed method and experimental data. Solid and dashed black lines denote moment coefficients computed with and without fuselage induced velocity perturbations respectively. Experimental measurements from Ref. 207 are presented with grey lines. Similarly to the normal force coefficient, strong BVIs are identified at approximately $\psi = 50$deg and $\psi = 300$deg. In the BL case, superimposition of a 2P oscillation and high frequency oscillations associated with BVIs is observed. Both code implementations accurately predicts the magnitude and phase of the BVIs. However, the low frequency contents at approximately $\psi = 180$deg is not correctly modelled. This discrepancy is once again related to the underestimation of the dynamic torsion angle at this location. Predictions made accounting for fuselage effects show a slightly higher moment coefficient in the first two quadrants than computations with the isolated rotor. The opposite effect is observed in the third and fourth quadrants. The same sources of discrepancies identified for the normal force coefficients are applicable to this analysis.

As a result of the introduction of 3P HHC, the moment section exhibits a strong 3P component. In the MN case, excellent correlation between the calculated moment coefficient and the experimental measurements is observed for the low frequency content. Regarding the MV case, the 3P oscillation is correctly captured by the presented code and only a small underestimation of the moment coefficient is observed at approximately $\psi = 100$deg. Similarly to the BL case, there is a very small effect of the fuselage interference on the moment coefficient for the HHC cases. Once again the small discrepancies are of

different signs depending on the azimuth angle.

Figure 5.13 presents the high frequency content, 10P high-pass filtered, of the calculated moment coefficient. BVIs interactions can now be clearly observed. In the BL case, excellence agreement between the predictions with both implementations and experimental values is observed in magnitude and phase. A minimum reduction in the amplitude of the advancing side BVIs is observed as a consequence of the introduction of the fuselage interference. Regarding the MN case, the magnitude of the BVI matches the experimental measurements. However, there is a phase difference in the calculated moment coefficient. In the MV case, the magnitude of the interactions are correctly capture with both implementations on the advancing side, with a phase discrepancy. In contrast, on the retreating side the phase angle is accurately modelled and the magnitude of only one of the vortex interactions is not matched. This behaviour is independent of the fuselage interference, as no substantial difference has been identified as a result of the inclusion of the fuselage induced velocity perturbations.

Overall very good and in some case excellent agreement is observed between the predicted aerodynamic loading and the experimental measurements. A better prediction of the aerodynamic loading has been obtained as a result of the inclusion of the fuselage aerodynamic model into the analysis. This improvement is specially notable in the low frequency content of the normal force coefficient. Additionally, the alteration of the vertical position of the vortex structure slightly modifies the location and strength of the BVIs.

6.7 Conclusions

A computationally efficient semiempirical analytical fuselage formulation has been implemented in the present work to estimate the fuselage induced velocity perturbations consequence of the existence of a fuselage in a free-stream. This chapter has assessed the effect of the introduction of the fuselage aerodynamic model on the performance of the rotor and its different modelling components.

In the first place, the fuselage induced velocity perturbations estimated with the implemented model were presented and their influence on the normal inflow across the rotor disk was described. The influence on the rotor inflow was identified to be associated

to two sources. The first one is the direct superimposition of the velocity perturbations on the rotor disk inflow. The second one is related to the change in wake geometry generated by the inclusion of fuselage induced velocity perturbations.

In the second place, the introduction of the fuselage interference was proven to have a large effect on the trim control angles. Although no appreciable difference in the collective pitch angle was identified, the cyclic pitch angle prediction was largely affected, specially the lateral cyclic pitch angle. The prediction of rotor power required was greatly improved as a result of the incorporation of the fuselage model. This highlighted the necessity of the inclusion of the fuselage interference in the analysis for the accurate modelling of the rotor trim state.

In the third place, the effect of the fuselage interference on the geometry of the wake was quantified. No appreciable effect on the geometry as seen in the top view was found. However, a considerable effect on the vertical position of the wake filaments was observed. It essentially increases the vortex trajectory curvature. Leading to higher position of the vortices on both lateral position, advancing and retreating side. This ultimately increases the BVIs miss distance. Therefore, the inclusion of the fuselage induced velocity perturbations varies the BVIs miss distances and the strength of the interactions.

In the fourth place, the dependence of the blade elastic deformations on the fuselage interference was evaluated. A weak effect of the fuselage induced velocity perturbations on the flap elastic deflections was identified, with the only noticeable prediction improvements located at the front and rear of the rotor disk. The elastic twist was found to be independent of the fuselage interference. A better agreement between the elastic lag predictions and the experimental measurements, with more dynamic behaviour, was generated by the inclusion of fuselage induced velocity perturbations in the analysis.

In the fifth place, a very weak effect of the fuselage induced velocity perturbations on the bending and torsion moments was identified. Virtual superimposition was observed for flap bending and torsion moments whilst a small increase in the dynamic content of the lag bending moment was found.

In the last place, the effect of the inclusion of the fuselage interference on the aerodynamic loading was assessed. The agreement between low frequency content of the normal force coefficient calculated with the present work and experimental measurements was

improved when the fuselage velocity perturbations were considered. As a result of the alteration of the wake geometry, the BVIs miss distance was modified. Consequently, the intensity of the high frequency content of the normal force coefficient was altered. Alightly better agreement with the experimental measurements for the BVIs was found as a result of the incorporation of fuselage perturbations. However, a very weak effect of the fuselage interference was found for the moment coefficient.

From the above, it is concluded that fuselage induced velocity perturbations modify different aspects of the rotor operation. The alteration of the rotor disk inflow results in a modification of the rotor hub moments, which is cancelled through a change in the control angles. As a result, a large improvement in the prediction of cyclic control angles is observed. An equally important change in wake geometry was identified. The combined effect of the changes in control angles and wake geometry was observed to result on a modification of the aerodynamic loading. However, the effect on the dynamic response of the rotor was found to be weak.

	θ_0 [deg]			θ_{1c} [deg]			θ_{1s} [deg]		
	Fuselage	Isolated	Exp.	Fuselage	Isolated	Exp.	Fuselage	Isolated	Exp.
BL	3.01	3.06	3.8	1.63	1.27	1.92	-1.17	-1.07	-1.34
MN	3.15	3.22	3.9	1.75	1.37	2.00	-1.11	-0.98	-1.35
MV	2.93	2.94	3.8	1.65	1.315	2.00	-1.01	-0.872	-1.51

Table 6.1: Calculated control angles with fuselage interference and isolated rotor: comparison with experimental measurements from Ref. 207.

	Rotor Power [kW]		
	Fuselage	Isolated	Exp.
BL	19.25	23.02	18.3
MN	22.40	24.65	19.8
MV	19.64	23.21	18.8

Table 6.2: Calculated rotor power required with fuselage interference and isolated rotor: comparison with experimental measurements from Ref. 210.

	C_nM^2			C_mM^2		
	Fuselage	Isolated	Exp.	Fuselage	Isolated	Exp.
BL	0.086	0.085	0.090	-0.0031	-0.0031	-0.0026
MN	0.088	0.087	0.101	-0.0030	-0.0030	-0.0058
MV	0.086	0.084	0.102	-0.0031	-0.0031	-0.0051

Table 6.3: Calculated mean normal force and moment coefficients at $r = 0.87R$ with fuselage interference and isolated rotor: comparison with experimental measurements from Ref. 207.

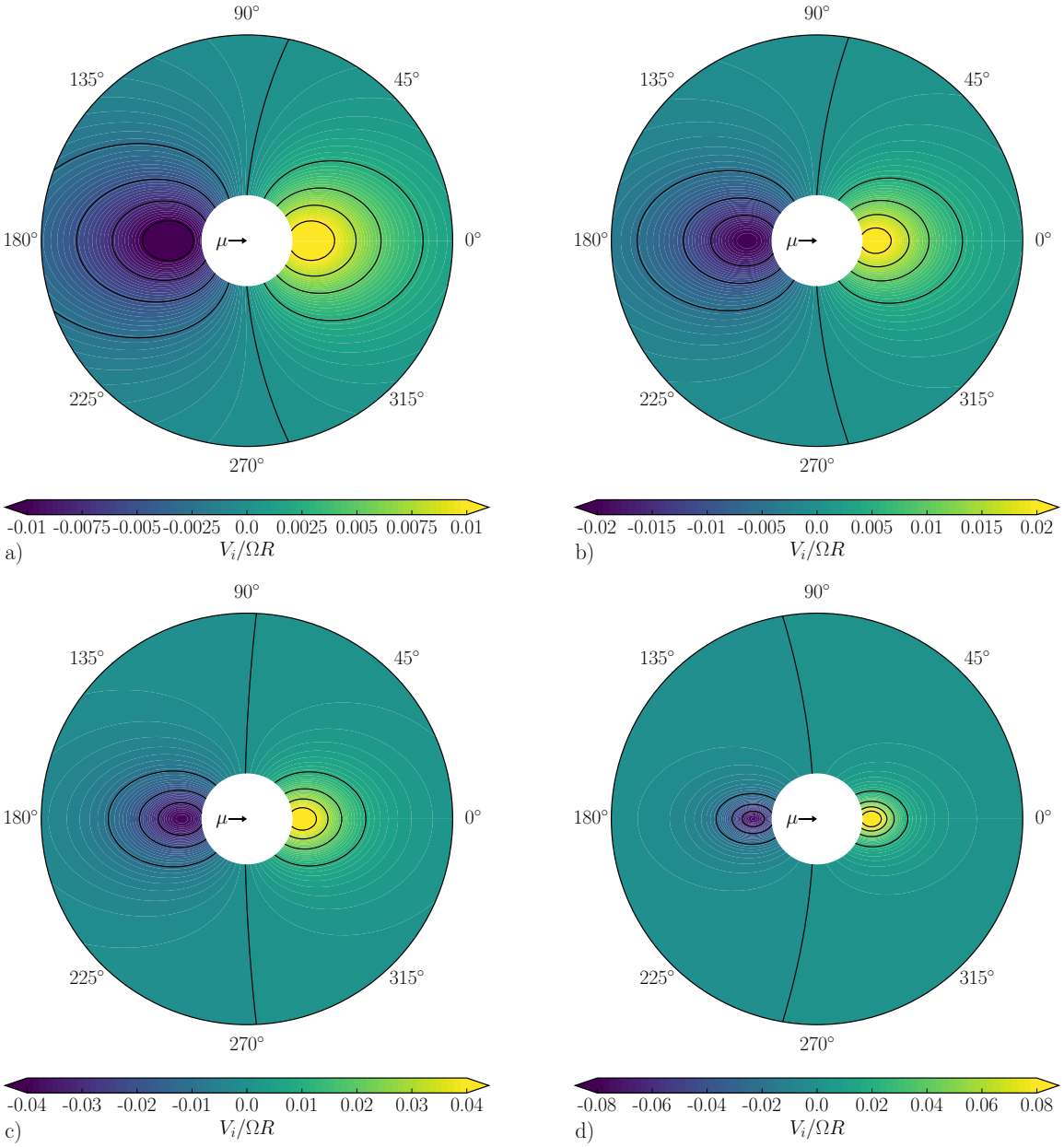

Figure 6.1: Normalised induced velocity perturbation component normal to the rotor disk at plane: (a) $z/R = 0.1$, (b) $z/R = 0.0$, (c) $z/R = -0.1$, (d) $z/R = -0.2$.

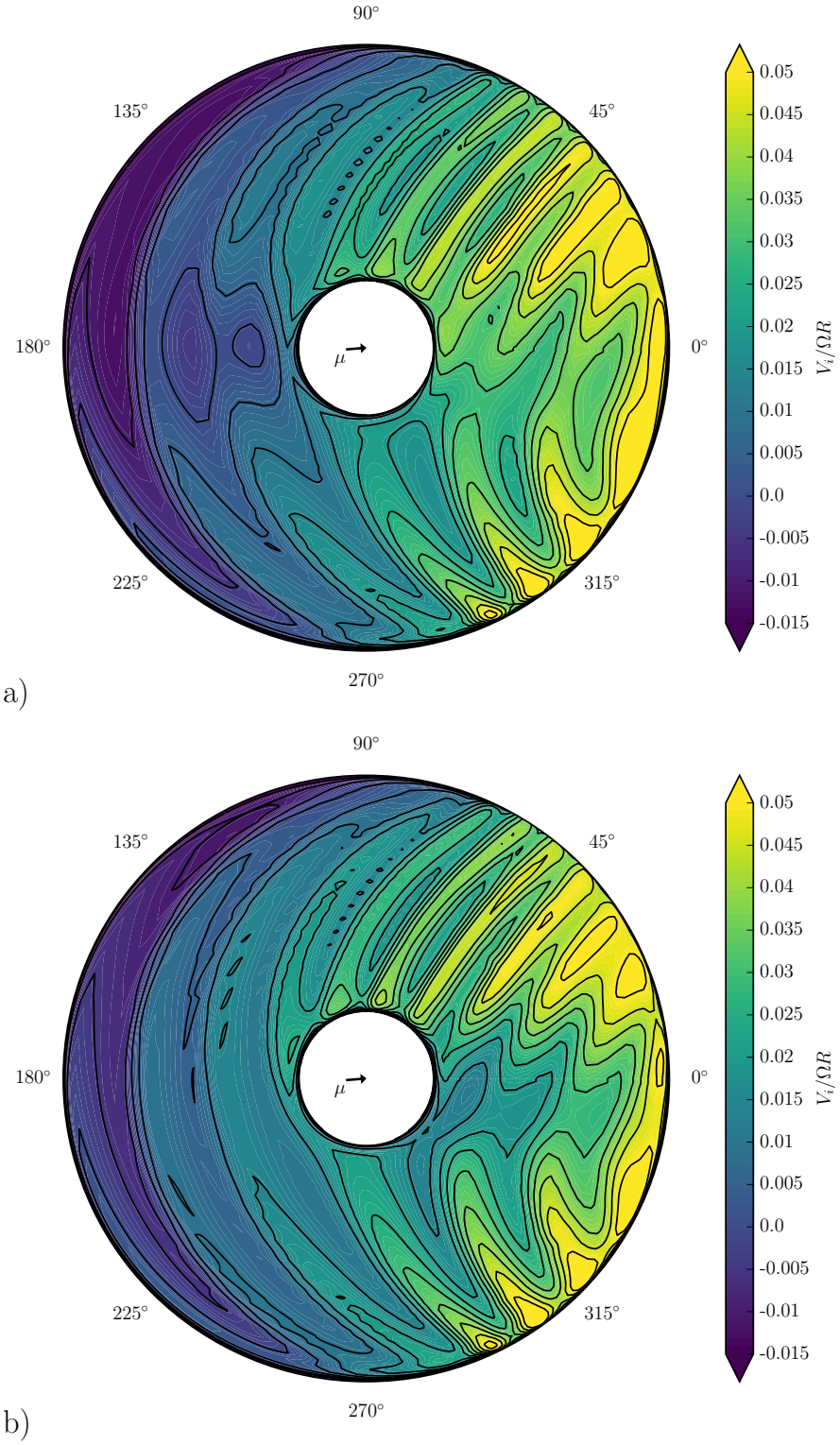

Figure 6.2: Normalised induced velocity component normal to the rotor disk - baseline (BL): (a) fuselage interference, (b) isolated rotor.

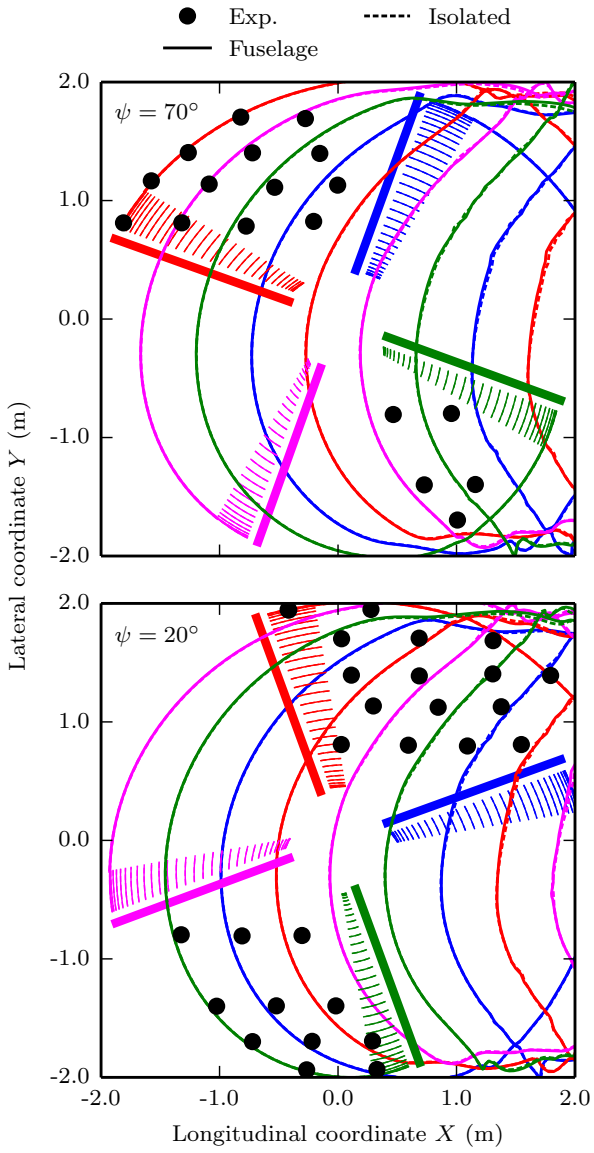

Figure 6.3: Top view of the calculated wake geometry with fuselage interference and isolated rotor - baseline (BL). Comparison with experimental measurements from Ref. 207.

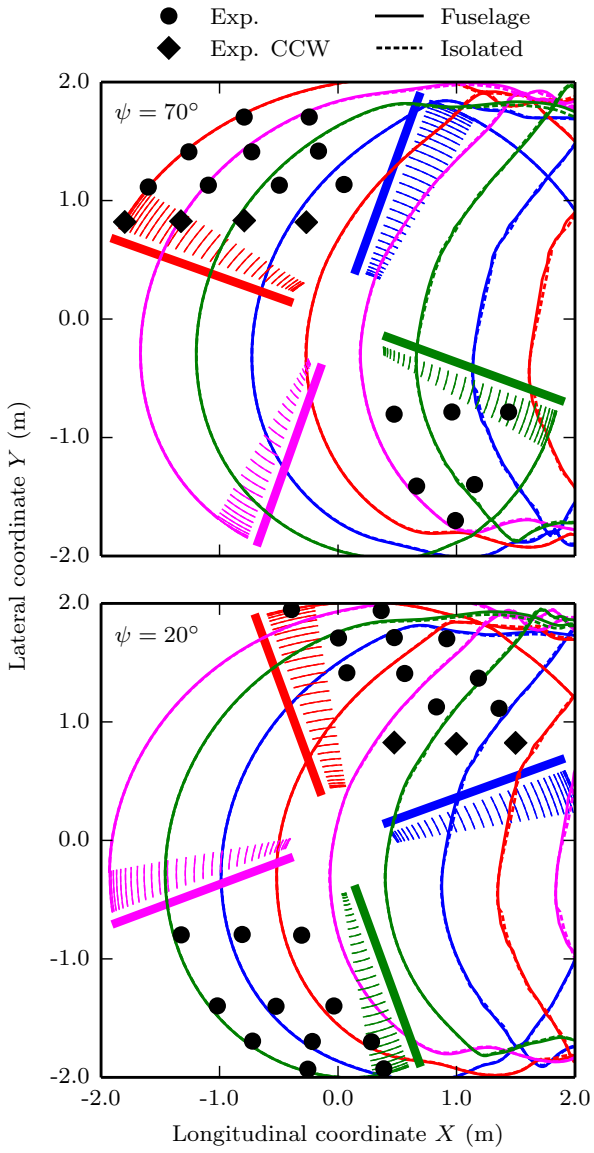

Figure 6.4: Top view of the calculated wake geometry with fuselage interference and isolated rotor - minimum noise (MN). Comparison with experimental measurements from Ref. 207.

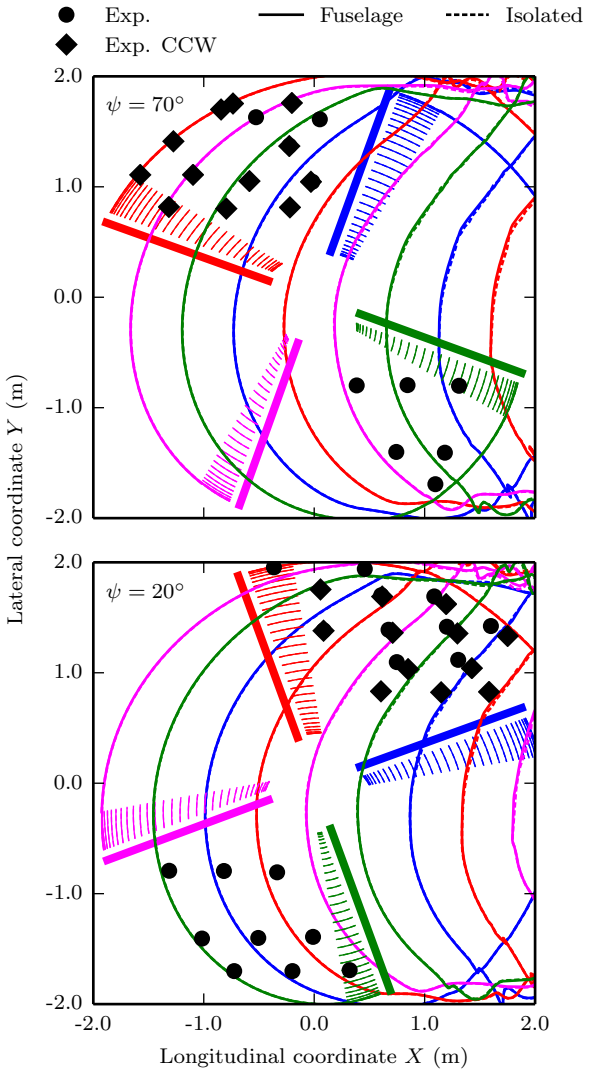

Figure 6.5: Top view of the calculated wake geometry with fuselage interference and isolated rotor - minimum vibration (MV). Comparison with experimental measurements from Ref. 207.

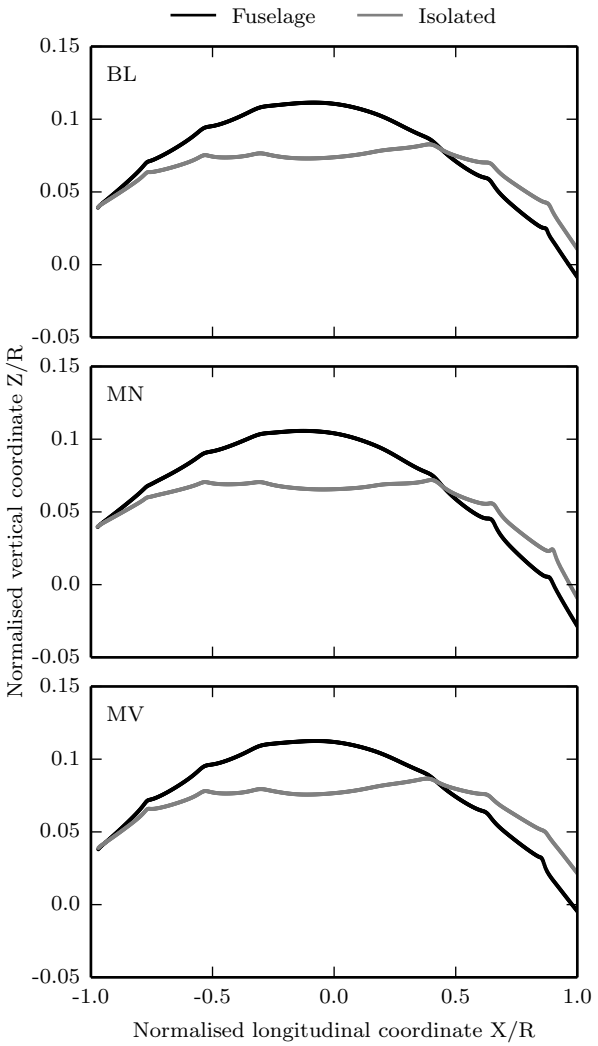

Figure 6.6: Side view of the calculated wake geometry with fuselage interference and isolated rotor - $y/R = 0.0$.

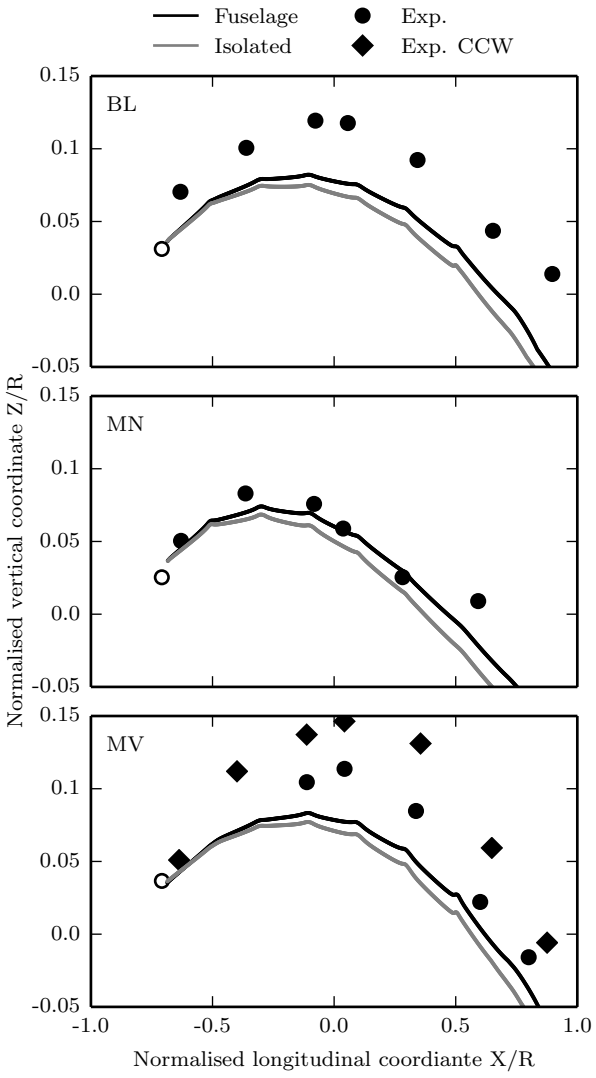

Figure 6.7: Side view of the calculated wake geometry with fuselage interference and isolated rotor - $y/R = 0.7$. Comparison with experimental measurements from Ref. 207.

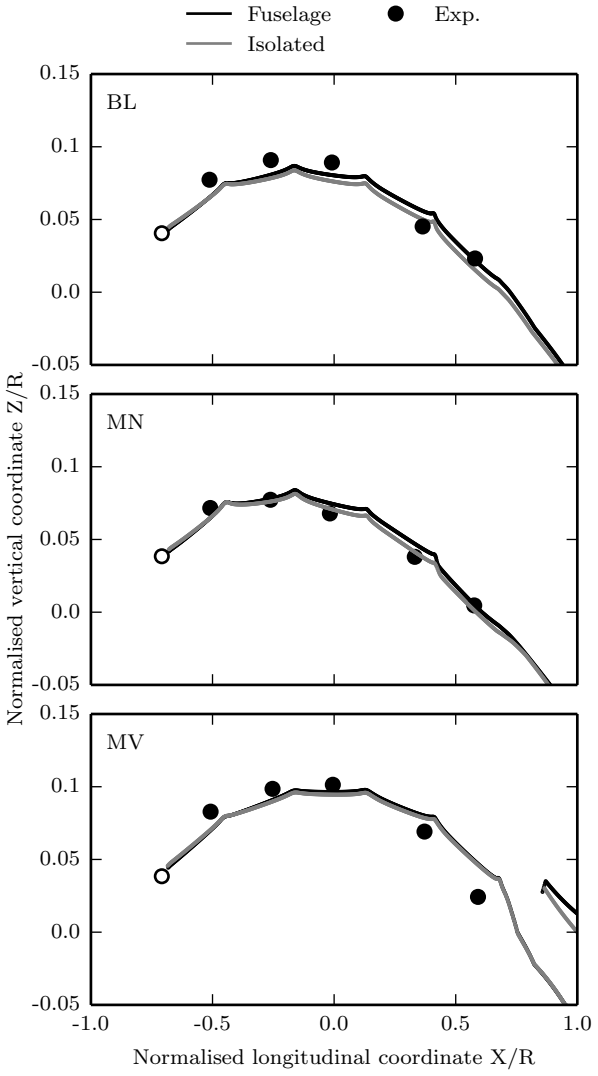

Figure 6.8: Side view of the calculated wake geometry with fuselage interference and isolated rotor - $y/R = -0.7$. Comparison with experimental measurements from Ref. 207.

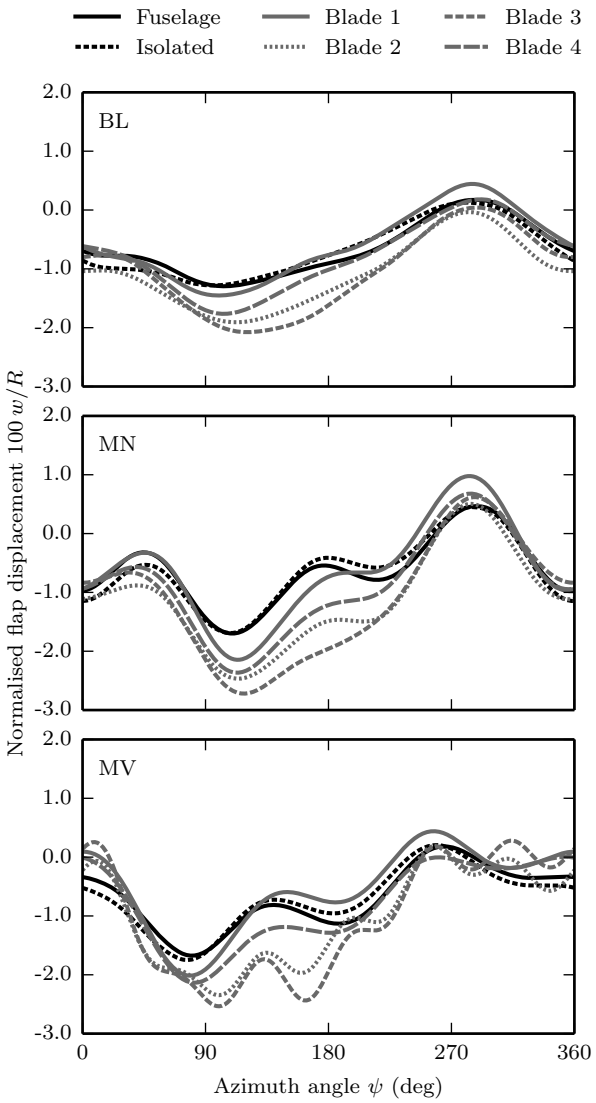

Figure 6.9: Calculated blade tip elastic flapping motion relative to precone with fuselage interference and isolated rotor. Comparison with experimental measurements from Ref. 207.

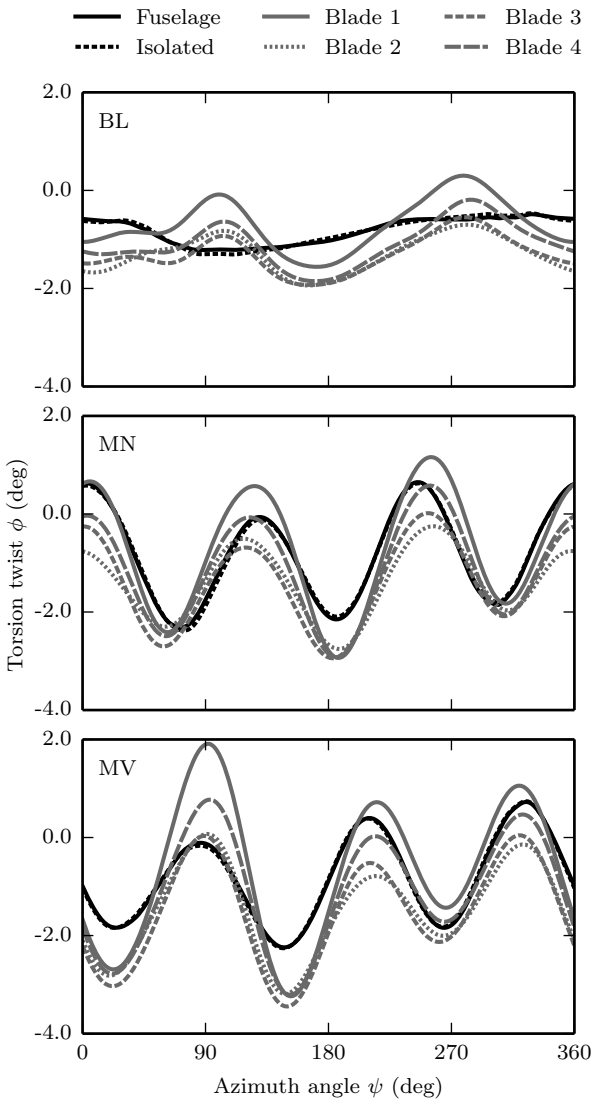

Figure 6.10: Calculated blade tip elastic torsion motion relative to control and pretwist with fuselage interference and isolated rotor. Comparison with experimental measurements from Ref. 207.

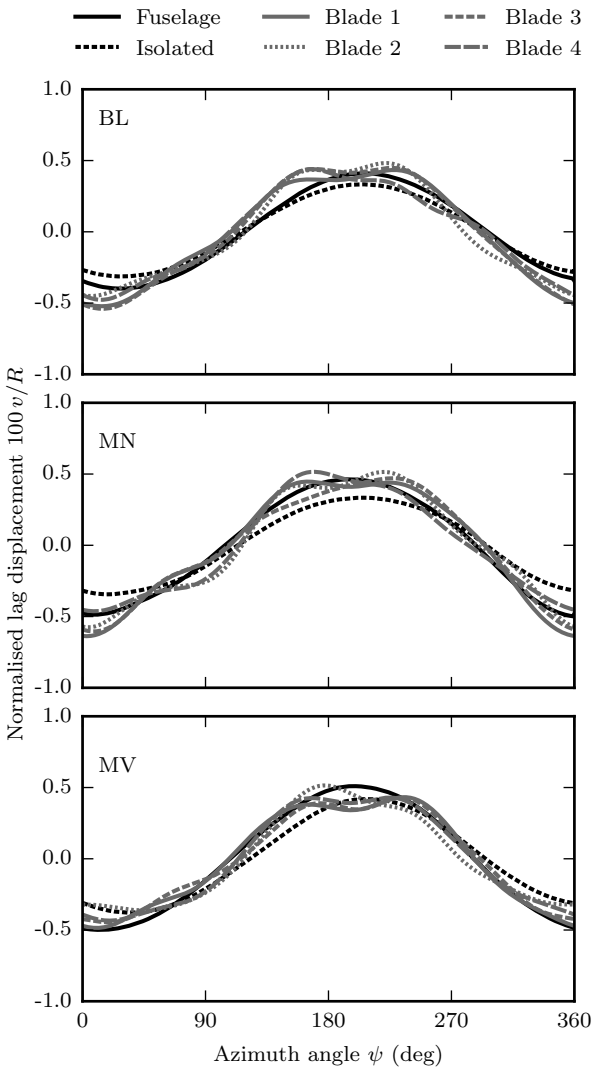

Figure 6.11: Calculated blade tip lag elastic motion with fuselage interference and isolated rotor, mean value removed. Comparison with experimental measurements from Ref. 207.

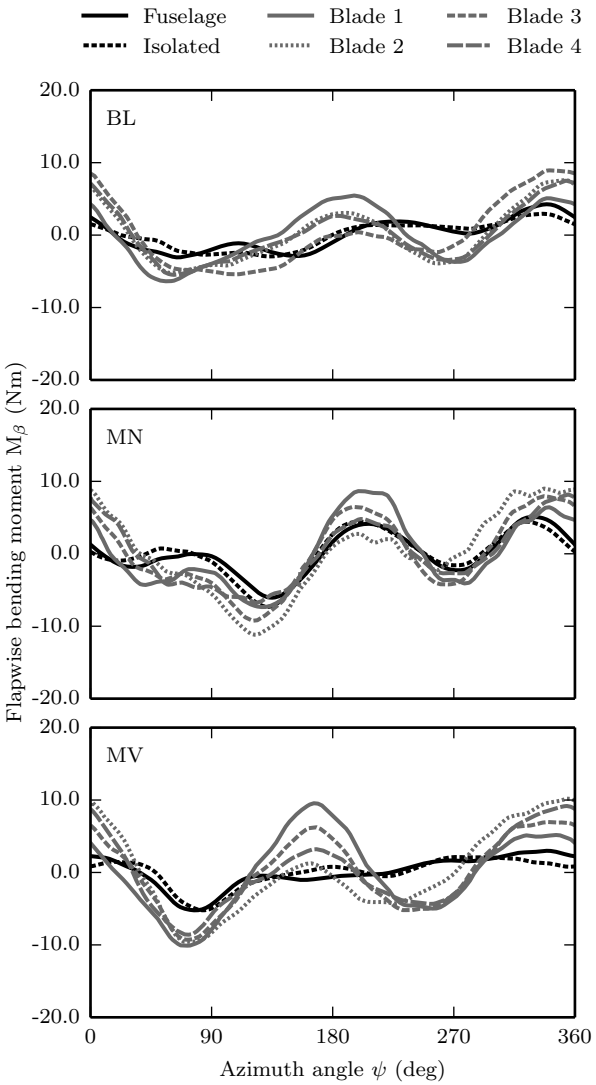

Figure 6.12: Calculated flapping bending moments at $r = 0.17R$ with fuselage interference and isolated rotor, mean value removed. Comparison with experimental measurements from Ref. 207.

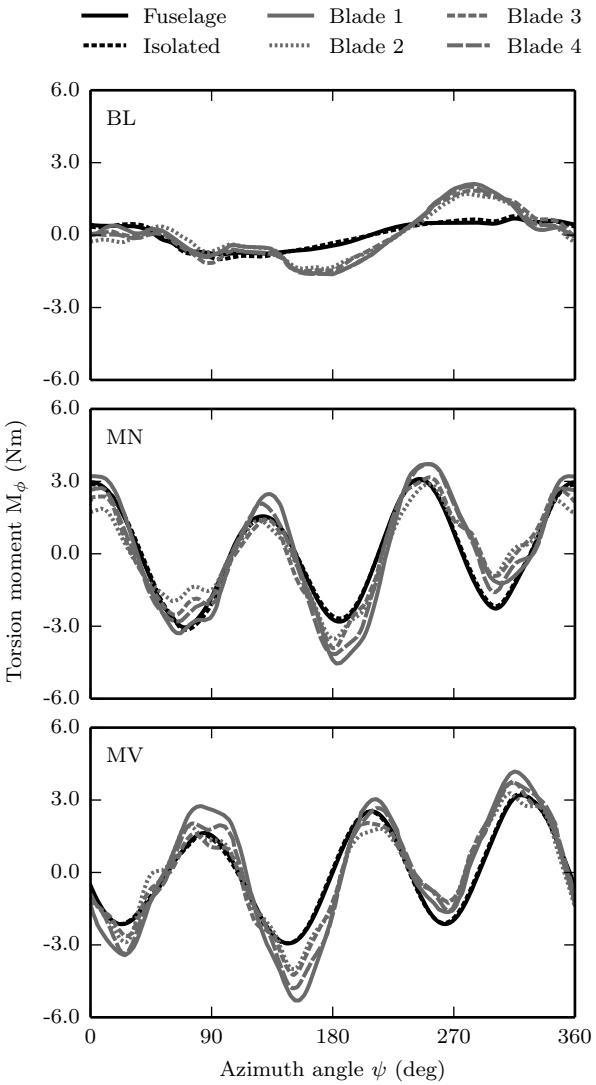

Figure 6.13: Calculated torsion moments at $r = 0.33R$ with fuselage interference and isolated rotor, mean value removed. Comparison with experimental measurements from Ref. 207.

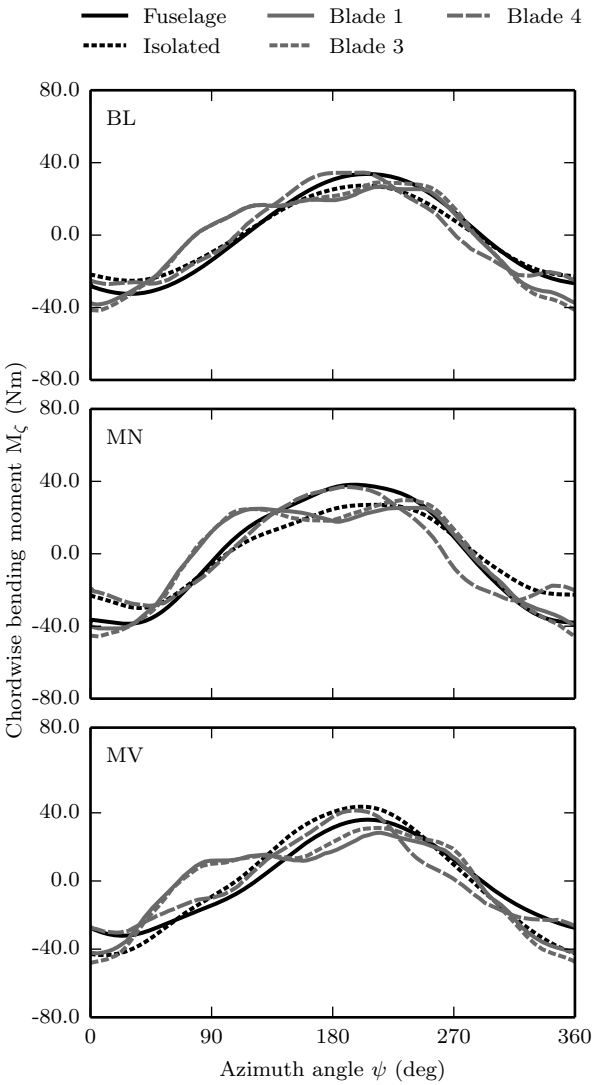

Figure 6.14: Calculated lag bending moments at $r = 0.17R$ with fuselage interference and isolated rotor, mean value removed. Comparison with experimental measurements from Ref. 207.

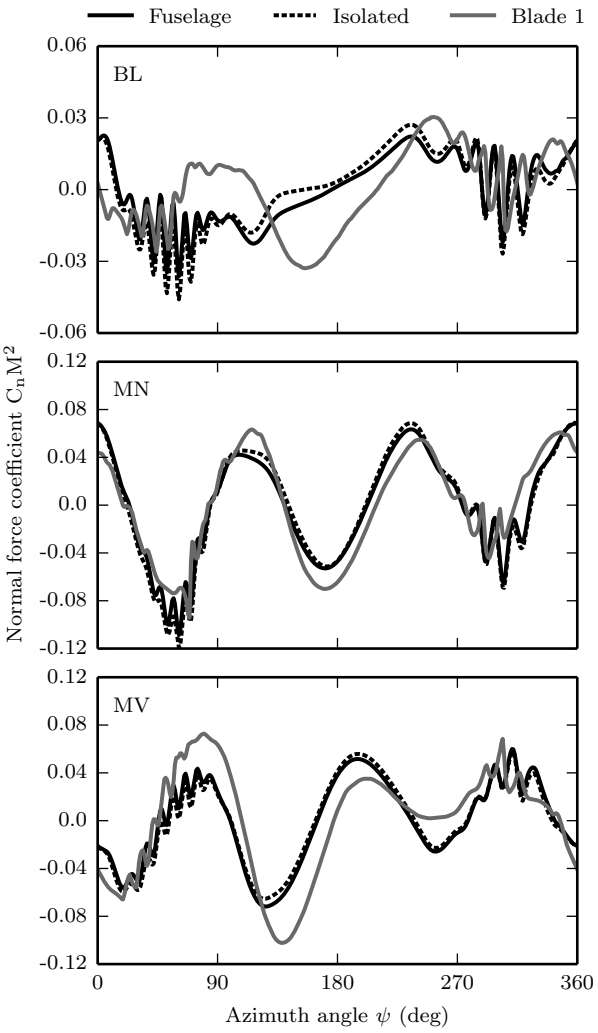

Figure 6.15: Calculated normal force coefficient at $r = 0.87R$ with fuselage interference and isolated rotor, mean value removed. Comparison with experimental measurements from Ref. 207.

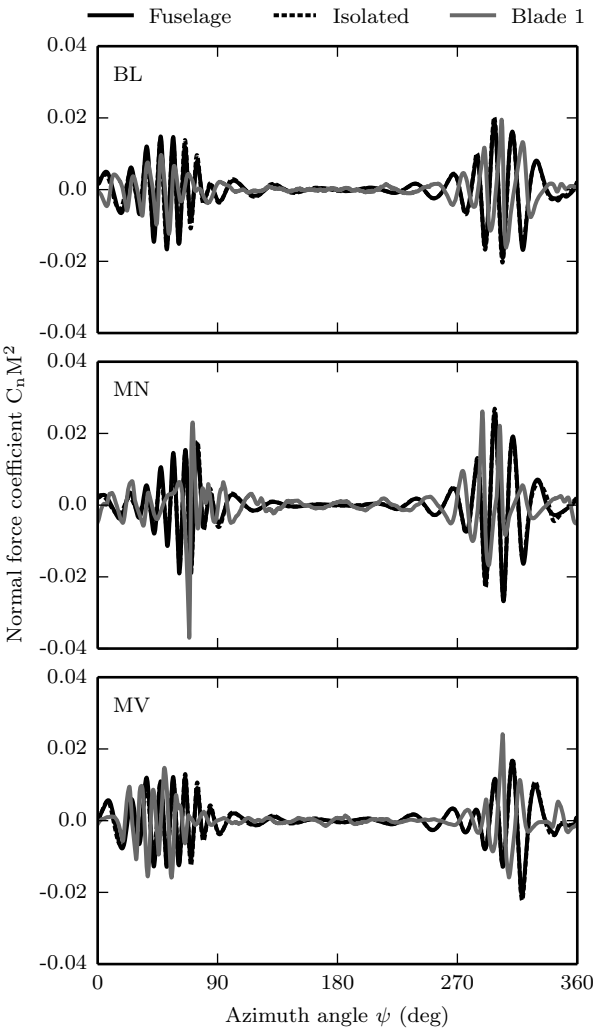

Figure 6.16: Calculated normal force coefficient at $r = 0.87R$ with fuselage interference and isolated rotor, 10/P high-pass filtered. Comparison with experimental measurements from Ref. 207.

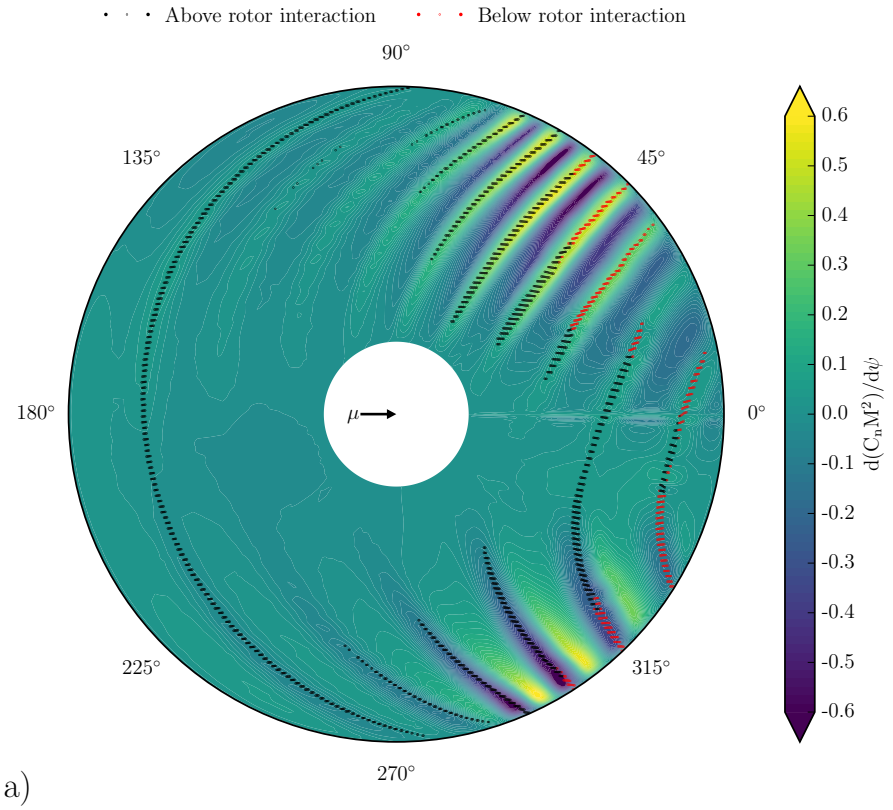

a)

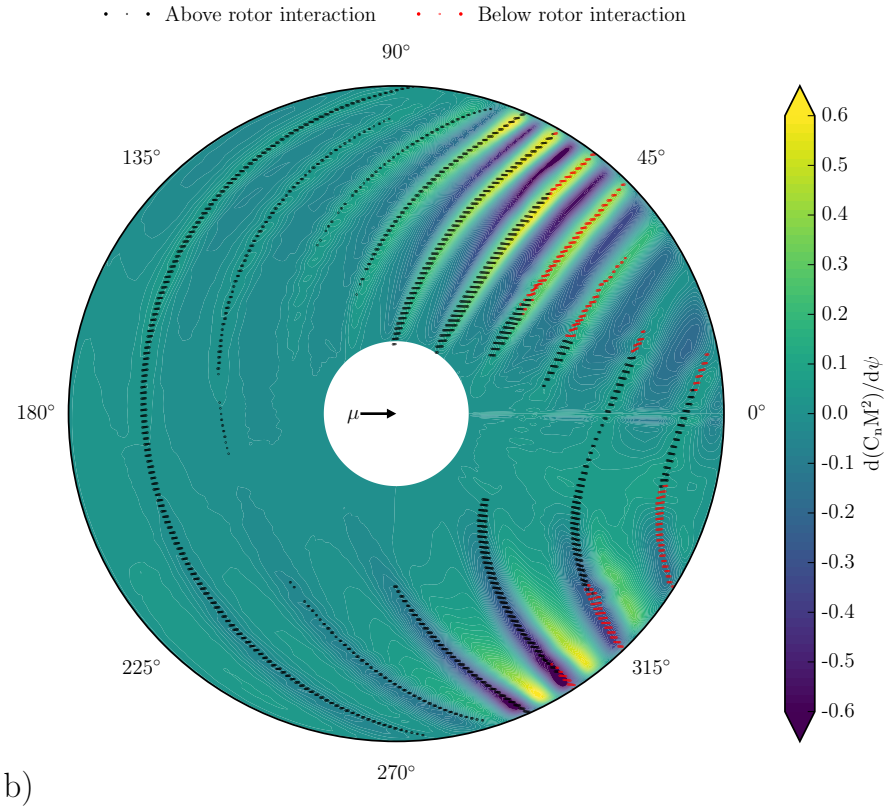

b)

Figure 6.17: Calculated normal force coefficient time derivative and BVI locations, baseline (BL): (a) fuselage interference, (b) isolated rotor.

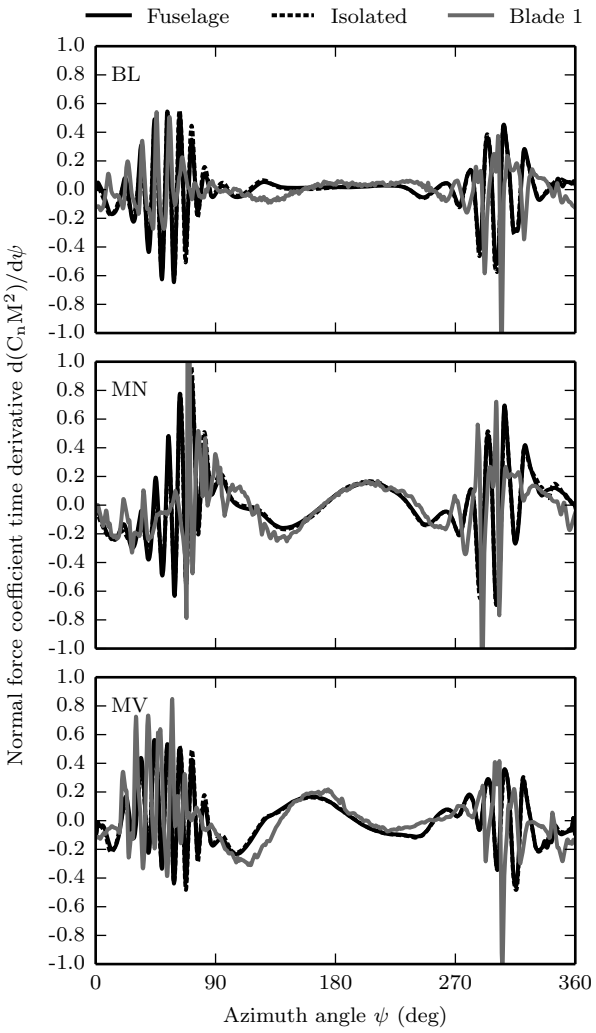

Figure 6.18: Calculated time derivative of normal force coefficient at $r = 0.87R$ with fuselage interference and isolated rotor. Comparison with experimental measurements from Ref. 207.

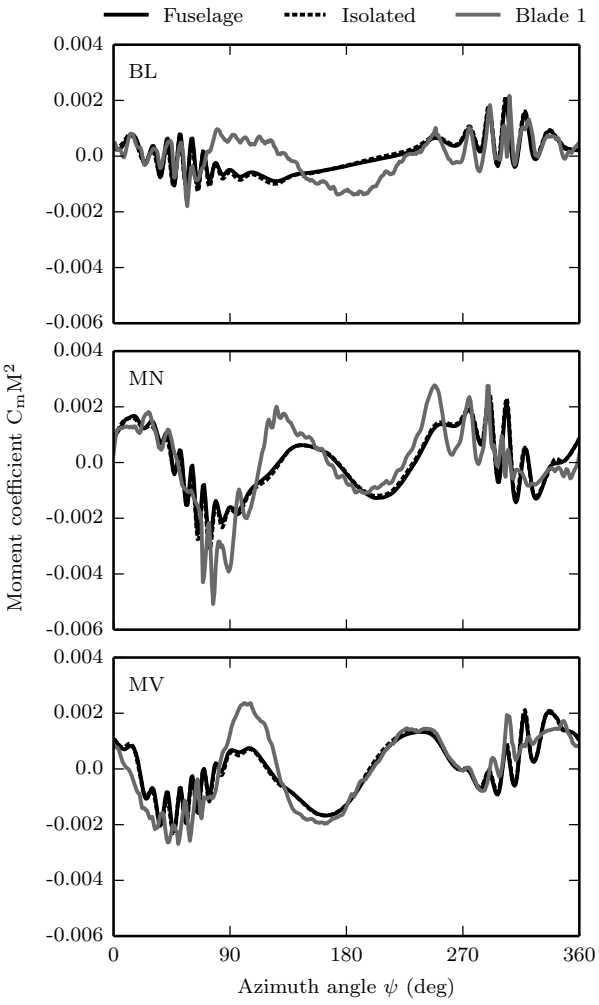

Figure 6.19: Calculated moment coefficient at $r = 0.87R$ with fuselage interference and isolated rotor, mean value removed. Comparison with experimental measurements from Ref. 207.

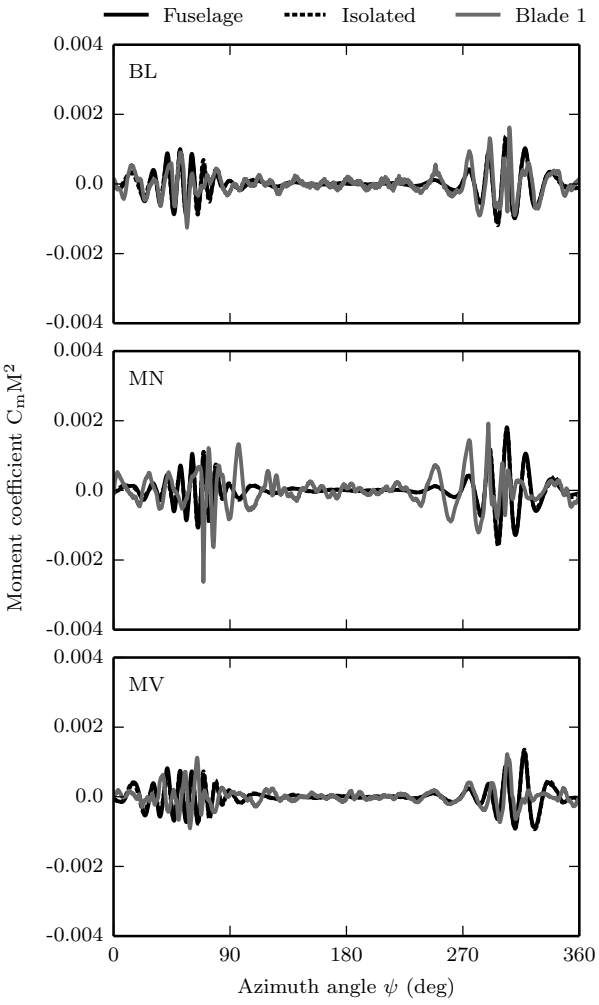

Figure 6.20: Calculated moment coefficient at $r = 0.87R$ with fuselage interference and isolated rotor, 10/P high-pass filtered. Comparison with experimental measurements from Ref. 207.

Chapter 7

Results and Discussion: Effect Flexible Modelling

The necessity of using elastic blade modelling in the analysis of hingeless rotor blades was suggested by Shupe (Refs. 24, 25), who analysed the effect of the inclusion of the second flap mode on the rotor hub loads. It was found that the second flap mode was highly excited under non-uniform inflow distributions, such as the ones found in forward flight.

This chapter presents the assessment of the effect of elastic blade modelling on the performance of the HART II rotor. The present methodology deploys flap-lag-torsion coupled modes of vibration. As a result the introduction of a mode of vibration does not include the isolated effect of one DOF. Instead it incorporates the contribution of the dominant DOF along with smaller contributions of the other DOFs. The previously used descending condition is used because of the high level of non-uniformity found in the inflow. For the assessment of the effect of flexible modelling on the aeroelastic behaviour of the rotor, the number of modes of vibration included in the analysis is varied. A minimum of one mode of vibration, which corresponds to the first lag mode, and a maximum of ten modes of vibration are used. The latter corresponds to the reference case used previously. Results are presented for all aspect of the rotor operation, ranging from rotor trim angles and dynamic response to aerodynamic characteristics.

7.1 Rotor Trim

Control angles. Figure 7.1 presents the evolution of the control pitch angles with the number of modes of vibration employed in the simulation. The control angles have been normalised with their respective reference control angles. It is noted that the reference results were obtained using ten vibration modes. Square, diamond, and triangle markers symbolise collective, lateral cyclic, and longitudinal cyclic angles respectively. In the BL case, the use of only the first mode of vibration (1L) leads to a large overprediction of the cyclic pitch angle and an underprediction of the collective pitch angle. This is associated with the lack of flap motion and torsion twist. As a result, large cyclic pitch angles are required to tilt the TTP and obtain the desire trim conditions. The use of two modes of vibration (1L and 1F) reduces the discrepancies of the cyclic pitch angles by more than 50%. This is due to the capability of the rotor to flap and lag rigidly. Therefore smaller cyclic pitch angles are required to tilt the TTP and match trim conditions. No improvement on the prediction of the collective pitch angle is observed. The use of the third vibration mode incorporates flexibility effects on the flapping motion. Little improvement is identified in the prediction of lateral pitch angle, while the rest of the discrepancies are kept constant or increase. This mode of vibration is highly coupled with the first torsion mode. Hence its consideration alone would lead to considerable errors. The first torsion mode is introduced as the fourth vibration mode. A large improvement in the predictions is obtained consequence of torsion modelling. The computed control angles essentially match the reference ones at this point and the consideration of higher modes of vibration has a small effect on the control angles. The large improvement in the prediction of the collective pitch angle is explained by the effective reduction of the blade pitch angle consequence of the elastic twist. As a result, the collective pitch angle needs to be increased to balance the deficit in thrust. The first torsion mode (1T) is located close to the 4P frequency. Consequently, the model accounts for frequencies up to the 4P which essentially covers all the excitation frequencies present in the operation of the rotor except the BVI. Nevertheless, the effect of BVI on the dynamic response of the rotor is considerably small due to the short duration of these events, which are cancelled out by the inertia of the blade. In the MN and MV cases of study, the same analysis is made. A minimum of four

modes of vibration (1L, 1F, 2F, and 1T) are required to obtain convergence on the trim control angles. The inclusion of the first flap mode greatly improves the prediction of the cyclic pitch angle, as it allows the rotor to flap and tilt. The introduction of the torsion mode has been proven to be highly important, as it reduces the effective pitch angle, this leads to a higher collective pitch angle and coupled torsion flap blade dynamic response.

Power and vibration index. Figure 7.2 presents the evolution of the rotor power required and generalized human vibration index with the number of modes of vibration employed in the simulation. The vibration index quantifies the hub vibrations generated by the rotor and transmitted to the fuselage. It is is defined for a 4 blades rotor in terms of the 4P and 8P amplitude coefficients as shown in Eq 7.1. Where $F_{x,i}$, $F_{y,i}$, and $F_{z,i}$ are the amplitudes of the rotor hub force oscillations and $T_{x,i}$, $T_{y,i}$ the respective torque amplitudes. Note that different weighting factors are given to each of the force and components to better replicate the effect of passenger. This definition was previously used by Lim *et al.* (Ref. 211) for the analysis of active twist technologies.

$$VI = \sum_{i=4P,8P} \frac{\sqrt{(0.5F_{x,i})^2 + (0.67F_{y,i})^2 + F_{z,i}^2}}{W_0} + \frac{\sqrt{T_{x,i}^2 + T_{y,i}^2}}{RW_0} \tag{7.1}$$

In Fig. 7.2 the power and vibration index have been normalised with their respective reference values. Square and diamond markers symbolise power and vibration index respectively. Control pitch angles were observed to converge once the torsion was introduced. However, power and vibration index require more vibration modes. Power required highly depends on the correct prediction of the lag deformations. As a result, a large improvement is obtained with the incorporation of the fifth vibration mode (2L) an a further small change with the ninth mode (3L). However, the amplitude of the latter change is considerably smaller than the absolute value of the power. The vibration index is observed to be much more dependent on the number of vibration modes included in the simulation. The vibration index uses force and torque components of up to 8P. Consequently, the modes of vibration used must cover the frequency spectrum up to the 8P frequency. Fig **??** showed that the seventh mode of vibration $4F$ has a slightly higher frequency than the 8P frequency. That means that at least the seven first modes of vibration need to be used to obtain a converged solution of the vibration index, which is confirmed in Fig. 7.2.

7.2 Elastic Deformations

The proposed methodology calculates the dynamic response of the rotor as the modal superimposition of the responses of the blade on the individual modes of vibration. As a result, elastic deformations are highly dependent on the number of vibration modes used in the calculation. In this section the effect of flexibility modelling on the motion of the blade is quantified by measuring the elastic deformation of the blade tip relative to the undeformed rotor blade. Predictions obtained with a minimum of one vibration mode and a maximum of ten vibration modes are compared with the experimental measurements to assess the predictive capability.

Elastic flap deflections. Flap tip elastic deformations are measured in the out of plane direction relative to the undeformed preconed rotor. Figure 7.3 presents the elastic flap deformations in the BL, MN, and MV cases of study. Elastic flap deflections have been normalised with the rotor radius. Silver, grey, and black lines correspond to elastic deflections predicted with different number of vibration modes. The line label refers to the number of vibration modes and the dominant mode of the highest mode, i.e., 4-1T refers to the simulation carried out with four modes of vibration and the fourth mode is the first torsion mode. Experimental measurements of each blade from Ref. 207 are symbolised with open markers. A strong once-per-rev oscillation in the flapping deflection is observed in the BL case. The use of one vibration mode results in zero flapping which represents an infinitely stiff rotor blade in flap. If the first flap mode is added, the solution is better approximated. However, the first torsion mode is required to essentially modify the control angles and the dynamic response of the rotor. A small improvement in the predictions is observed when the sixth vibration mode is included. However, solutions obtained with more than six vibration modes show little difference and the solution is considered to be converged. This is confirmed in Fig 7.6 where the normalised mean value of the tip flap motion is shown. The converged solution shows an excellent agreement with the experimental measurements, with discrepancies in the range of blade to blade differences.

In the MN case, a 3P flapping component is identified. This is attributed to the inclusion of a 3P HHC. Once again the use of only one mode leads to large errors, as no

flapping is predicted. The incorporation of the first and second flapping modes greatly improved the solution. However the 3P frequency is located higher in the frequency spectrum than the second flap mode and the use of the first torsion mode is required to capture the 3P excitation. A small improvement is obtained with the incorporation of the sixth vibration mode. Little variations are obtained beyond the sixth mode as shown in Fig. 7.6. Overall good agreement is observed between the predicted deflections obtained in the reference case and experimental measurements, with discrepancies in the range of blade to blade differences. The dynamic behaviour of the blade in the MV case is similar to the MN case and a minimum of six vibration modes (including flap, lag, and torsion) are required to correctly capture the elastic deflections. Once again, the flap deflections calculated with the reference setup show excellent agreement with the experimental measurements.

Elastic torsion twist. The elastic tip torsion twist is measured in the pitching direction relative to the pretwist blade with applied control angles. Calculations carried out with a minimum of one and maximum of ten vibration modes and experimental measurements are presented in Fig. 7.4. Silver, grey, and black lines denote elastic torsion predicted with different number of vibration modes. The line label refers to the number of vibration modes and the dominant mode of the highest mode. Experimental measurements of each blade from Ref. 207 are presented with open markers. For the BL case a strong 2P component is observed in the experimental measurements. Two group of computational predictions are distinguished. Simulations with up to the three modes do not predict any torsion. The incorporation of the first torsion mode improves the prediction, but no further improvement is observed as a result of the inclusion of higher modes. This is once again confirmed in Fig. 7.6 for the mean value of the torsion twist, which is approximately constant for the simulation with more than four vibration modes. Despite the inclusion of torsion vibration modes, the converged solution underpredicts the dynamics of torsion.

As a result of the application of HHC, the dynamics of torsion raise significantly as shown in Fig. 7.4 in MN and MV cases. The same two groups of computational predictions previously identified are observed in the HHC cases. If the first torsion mode is not include, no torsion is predicted leading to large discrepancies with the experimental measurements. From Fig. 7.4 it is clear than the first torsion mode dominates the dynamics of torsion

and the inclusion of higher frequency modes do not improve the prediction. Although the amplitude of some of the deformation peaks is underestimated with the reference setup, overall very good agreement in amplitude and phase is found in the cases with HHC.

Elastic lag deflections. Lag deflections are measured relative to the undeformed blade in the in plane direction, with positive sign against rotation. Fig. 7.5 presents the dynamic evolution of the lag deflection, mean removed, for the proposed approach with different number of vibration modes and experimental measurements from Ref. 207. Elastic lag deflections have been normalised with the rotor radius. Silver, grey, and black lines represent elastic deflections predicted with different number of vibration modes. The line label refers to the number of vibration modes and the dominant mode of the highest mode. Experimental measurements of each blade from Ref. 207 are symbolised with open markers. In the BL and MV cases, all the computational solutions virtually superimpose the experimental measurements and lag deflections are independent of the number of modes of vibration. In the MN case, two different groups are identified. If no torsion modes are included the solution is shifted in phase relative to the experimental data. This is essentially due to a change in pitch angle and consequently aerodynamic excitation. Once the first torsion mode is include, the dynamic solutions superimpose the experimental data. However, a large variation in the mean tip elastic tip deflection is observed in Fig. 7.6. A minimum of five modes of vibration, including the second lag mode, is required to obtain a converged solution. Little improvement is obtained if extra modes are added.

7.3 Bending Moments

In an aeroelastic simulation, flap and lag bending moments are highly related to the assumed modes of vibration because of their proportionality with the curvature of the modes. Similarly, torsion moments are proportional to the first spatial derivative of the vibration mode. Consequently, the number of modes of vibration considered in the simulation highly influences the predicted moments. The effect of the flexible blade modelling on the estimation of bending moments is assessed in this section. Experimental measurements of bending and torsion moments were taken at $r = 0.17R$ and $r = 0.33R$ respectively.

Flap bending moments. Figure 7.7 presents the predicted flap bending moments and experimental measurements. The mean value of flap bending moment has been subtracted in every case. Silver, grey, and black lines denote flap bending moments predicted with different number of vibration modes. The line label refers to the number of vibration modes and the dominant mode of the highest mode. Experimental measurements of each blade from Ref. 207 are indicated with open markers. In general the predictions of the proposed approach exhibit little correlation with the experimental measurements. This was previously justified in Section 5.5 and no further comparison of flapping moments with the experimental measurements is done. However, the effect of flexibility modelling on the predicted bending moments is assessed. In the BL case, the use of only the first lag mode is associated with zero flap bending moment, which is a non-physical solution. The incorporation of the first flap mode results on a 1P oscillation of the flap bending moment. The predictions obtained with the second flap mode incorporates higher order content and no further modification of the predicted moments is obtained including higher order vibration modes. For the HHC cases, the first torsion mode is required to capture the 3P frequency content. However, the introduction of higher order modes does not lead to further changes in flap bending moments. Although no modifications in the dynamic content are observed for modes beyond the first torsion mode, the convergence of the mean value of the flapping bending moment requires the use of nine modes of vibration (Fig. 7.10). That includes the first five flapping natural modes.

Torsion moments. The effect of the flexible blade modelling on the torsion bending moment is presented in Fig. 7.8. Silver, grey and black lines represent torsion moments predicted with different number of vibration modes. The line label refers to the number of vibration modes and the dominant mode of the highest mode. Experimental measurements of each blade from Ref. 207 are symbolised with open markers. A low order of magnitude 1P content in the torsion moment is observed in the experimental measurements in the BL case. Two different groups of predictions are distinguished. However, both of them underestimate the dynamics of torsion. The first of these group corresponds to predictions done with up to three modes of vibration. In this case no elastic torsion is obtained. Once the first torsion mode is included, elastic twist is obtained and the addition of higher vibration modes has minimum impact on the torsion moment calculations. In the MN and

MV cases the same two groups of computations are identified. The introduction of the first torsion mode leads to estimations of elastic twist which are not available otherwise. All the predictions made with at least four modes of vibration virtually superimpose and show excellent agreement with the experimental data. This is confirmed in Fig. 7.10 with the mean value of torsion moment, which is observed to almost converge with four modes of vibration, and its prediction only improves when the second torsion mode is included.

Lag bending moments. Figure 7.9 presents the calculated lag bending moments and experimental measurements from Ref. 207. The mean value of lag bending moment has been removed in every case to better show the dynamic content. Silver, grey and black lines denote lag bending moments predicted with different number of vibration modes. The line label refers to the number of vibration modes and the dominant mode of the highest mode. Experimental measurements of each blade from Ref. 207 are presented with open markers. In general the dynamic lag bending moments calculations show little dependence on the number of vibration modes used in the simulation. For the BL and MV cases all the simulations virtually superimpose the experimental measurements. For the MN case, two groups of predictions are distinguished. The first one, without any torsion vibration mode correctly captures the shape and amplitude but it is shifted in phase. The second group, which includes at least one torsion mode virtually superimpose the experimental measurements. Even for the first group the discrepancies are in the range of blade to blade differences and overall excellent agreement for every setup is observed. The trend observed for the dynamic content of the lag bending moment is different to the one of the man value, which is highly dependent on the flexible modelling. A minimum of five modes of vibration, including the second lag mode, are required to obtain a converged solution (Fig. 7.10).

7.4 Wake Geometry

Although the geometry of the wake is not directly linked to the number of assumed vibration modes, the dependence of the loading and elastic deflection of the blade indirectly modifies the vortex system. This dependence is quantified in this section.

Top view. Figure 7.11 presents the top view of the vortical structure predicted

with the proposed approach with different number of vibration modes and experimental measurements from Ref. 207 in the BL case. Dotted, dashed, and solid lines represent tip vortices predicted with rigid blade (1L and 1F), elastic flapping blade with torsion (1L, 1F, 2F, 1T), and fully elastic blade (reference blade with 10 vibration modes) respectively. Experimental measurements have been superimposed as Exp. The colour of the tip vortex refers to the blade number where the vortex was originally released: 1=blue, 2=red, 3=fuchsia, and 4=green. Top and bottom subfigures of Figure 7.11 refer to the vortex system observed for two different azimuth positions of the blade number one: $\psi = 70$deg and $\psi = 20$deg. All prediction virtually superimpose in the top view and only minimal discrepancies are observed in the vortex bundle regions. Very good agreement between the calculations of the present work and experimental measurements is found in the first and fourth quadrants, whilst excellent correlation with the experimental data is observed in the second and third quadrants. The virtual superimposition in the top view of the geometry predictions obtained with different number of vibration modes is repeated in the MN and MV cases and no further details are given.

Side view. The relative vertical distance between the blade and the vortex highly influences the strength of the BVIs. In Fig 7.3 it was shown the dependence of the flapping solution on the number of modes of vibration included in the analysis. The variation of the flap motion consequently changes the releasing point of the tip vortices and loading of the blade, which ultimately determines the downwash strength. The dependency of the vertical position of the tip vortex on the number of vibration modes is now assessed.

Side view: advancing side. Figure 7.14 presents the vortex system predicted with the proposed approach with different number of vibration modes and experimental measurements from Ref. 207 for the lateral plane located on the advancing side. Silver, grey, and black solid lines correspond to tip vortices predicted with rigid blade (1L and 1F), elastic flapping blade with torsion (1L, 1F, 2F, 1T), and fully elastic blade (reference blade with 10 vibration modes) respectively. Experimental measurements have been superimposed as Exp. for conventional rotation direction vortices and Exp. CCW for counter-rotating vortices. The open marker indicates the position of the blade one at emission time. In the BL case, the experimental measurements are located above the present computations by an average of 0.5 chords. The computational underprediction of the vortex location

can be partially justified by the average higher flapping location of the releasing blade. Computations carried out with the reference and elastic setups virtually superimposed and only a small discrepancy is observed at the front of the disk for the rigid setup. It was observed previously in Fig. 7.3 that flap motion predictions for all three setups are close and only at the front and back of the disk the discrepancies are larger. The area with biggest differences in Fig. 7.14 corresponds to area of Fig. 7.3 with larger discrepancies. In the HHC cases, the differences in flapping response between the rigid case and the elastic cases is magnified, this essentially leads to larger variations in vortex releasing points. The application of HHC results in larger excitation of the torsion mode which ultimately changes the loading and downwash. From the above it is expected a larger difference in vortex geometry between the rigid blade setup and both elastic blade setups, which is corroborated in Fig. 7.14. Particularly, for the MN case the agreement between the reference case and the experimental measurements is excellent. For the MV case, dual vortex configurations are not captured. Nevertheless, very good overall correlation between the computation and the experimental dataset is identified.

Side view: retreating side. Figure 7.15 presents the vortex system predicted with the proposed approach with different number of vibration modes and experimental measurements from Ref. 207 for the lateral plane located on the retreating side. Silver, grey, and black solid lines correspond to tip vortices predicted with rigid blade (1L and 1F), elastic flapping blade with torsion (1L, 1F, 2F, 1T), and fully elastic blade (reference blade with 10 vibration modes) respectively. Experimental measurements have been superimposed as Exp. The open marker indicates the position of the blade one at emission time. The vortex geometry obtained with the present work in the BL case exhibits excellent agreement with the experimental measurements in shape and height, and virtual superimposition is observed. A very small discrepancy at the back of the disk between rigid and flexible calculations is observed, which can be attributed to the variation in flap motion and/or difference in downwash. In the MN case, the excellent agreement between the experimental measurements and the elastic predictions is repeated, and virtual superimposition is observed. An overprediction of the vertical location is observed if the rigid setup is considered. This can be caused by the larger discrepancies in flapping predictions previously shown in Fig. 7.3. The trend is revert for the MV case, where a lower position is found for the

rigid case. Despite the relative changes, which will affect the strength of the BVIs, the agreement between the experimental values and the predictions of the proposed method has been proven to be excellent.

7.5 Aerodynamic Loading

The effect of the inclusion of flexibility modelling on the blade dynamic response and wake geometry has been described in the previous sections. These are coupled with the aerodynamic loading of the blade. Hence, variations in aerodynamic loading are expected. This section evaluates the effect of flexible blade modelling on the aerodynamic loading. Computations are compared with experimental measurements from Ref. 207.

Normal force coefficient.. Figure 7.16 presents the evolution of the mean normal force and moment coefficients with the number of modes of vibration employed in the simulation. Both coefficients have been normalised with their reference coefficients. It is noted that the reference results were obtained using ten vibration modes. Square markers symbolise the mean normal force coefficient, which is of interest now. The mean values predicted without torsion modes, three first modes, are about 4% higher than the reference value for the BL case. The incorporation of the first torsion mode reduces the difference to marginal. This is in accordance with the evolution of the collective pitch angle with the number of vibration modes observed in Fig. 7.1. The mean value of normal force coefficient is completely converged once the second torsion mode has been incorporated and no further variations are found. The same trends although of slightly different magnitude are observed for the MN and MV cases. The reference predictions were previously compared with experimental measurements and underpredictions of about 4%, 12%, and 16% were found for BL, MN, and MV respectively. An underprediction of the aerodynamic loading was expected due to the higher mean flap position and dynamic pitch angle of the instrumented blade.

Figure 7.17 presents the calculated dynamic, mean removed, normal force coefficient at $r = 0.87R$ along with the correspondent experimental measurements from Ref. 207. Silver, grey, and black lines correspond to normal force coefficients predicted with different number of vibration modes. The line label refers to the number of vibration modes and the dominant mode of the highest mode. Experimental measurements of the first blade

are denoted by a dotted grey line. In every case, strong high frequency fluctuations in aerodynamic loading associated with BVI are observed at approximately $\psi = 50$deg and $\psi = 300$deg. In the BL case, three main groups of predictions are identified. The first one corresponds to the setup with only the first lag mode. As the blade does not flap, larger control angles are required to fulfil the trim conditions. As a result, the slope of the normal force coefficient at the front of the disk is better predicted. However, the overall shape shows worse correlation with the experimental measurements. The next group to consider is the one composed of simulations with up to three modes of vibration. This predictions are close to the one of the reference setup. Nevertheless substancial differences are observed on the advancing and retreating sides. Once the torsion mode is included, all the predictions virtually superimpose. Overall really good agreement between predictions done with the reference setup and experimental measurements is observed for the low frequency content of the normal coefficient except at the minimum aerodynamic loading location, $\psi = 160$deg, where the predicted value has an offset in phase and amplitude.

Regarding the MN and MV cases, combinations of 2P and 3P oscillations are observed in Fig. 7.17. In order to correctly capture 3P behaviour, modes of vibration with natural frequencies up to the 3P frequency need to be included in the analysis. This is evident in Fig. 7.17 where converged solutions are obtained with four vibration modes for the MN case. The inclusion of more than four vibration modes does not lead to any further change. However, the use of less modes results in discrepancies. This is due to two reasons: the fourth mode of vibration is the first mode of vibration with natural frequency higher than 3P frequency and its inclusion is necessary to cover the main exciting frequencies; and the fourth mode is required to include torsion dynamics in the analysis. Overall very good correlation between code calculations with the reference setup and experimental measurements is observed. Similar results are obtained in the MV case, where converged solutions are obtained with four modes of vibration. The use of less than four modes results in the underprediction of dynamic loading and the neglection of the torsion twist. Nevertheless, the overall agreement between the calculations obtained with the reference setup and the experimental measurements is very good.

Figure 7.18 presents the high frequency content, 10P high-pass filtered, of the calculated normal force coefficient. The calculated values are compared with experimental

measurements from Ref. 207. Silver, grey, and black lines denote normal force coefficients predicted with different number of vibration modes. The line label refers to the number of vibration modes and the dominant mode of the highest mode. Experimental measurements of the first blade are presented with a dotted grey line. In the BL case, two different groups are identified depending on the number of vibration modes used. The first one comprises the predictions done with up to three modes and the second one is composed of those simulations with four or more modes. Within each group, the simulations virtually superimpose. However, simulations without torsion show a further overprediction of the oscillations amplitude.

Regarding the MN case, two groups are again identified: simulations with the first torsion mode and higher order modes superimpose the reference setup. Calculations with less than four modes of vibration present higher oscillation peaks than those of the previous group. As a result the strength of the BVI is further overestimated. In the MV case, correlations obtained without torsion result in larger BVI amplitudes than those obtained accounting for torsional dynamics. The lack of difference between simulations carried out with four and ten modes of vibration reaffirms the independence of the very high frequency phenomena, BVI, from the relatively low dynamics of the rotor. As a result, any difference in BVI strength is caused by a variation in BVI miss distance and not the dynamics of the blade itself.

Figure 7.19 presents the time derivative of the normal force coefficient calculated at $r = 0.87R$ along with the correspondent experimental measurements from Ref. 207. Silver, grey, and black lines correspond to time derivatives of the normal force coefficient predicted with different number of vibration modes. The line label refers to the number of vibration modes and the dominant mode of the highest mode. Experimental measurements of the first blade are denoted by a dotted grey line. Similarly to the normal force coefficient, two groups of computations are distinguished: predictions with a maximum of three modes of vibration and calculations with the first torsion mode. The reference setup, which uses ten modes of vibration does not show any difference relative to the simulation carried out with four modes of vibration. However, if the first torsion mode is not employed, the dynamic response of the rotor changes modifying the BVI miss distance and the time derivative of the normal force coefficient. Predictions obtained with and without the first torsion mode

exhibit the same phase angle. However, the amplitude of the oscillations vary between setups. In the BL case, both groups overpredict the amplitude of the time derivative on the advancing side by approximately the same magnitude. The agreement between the phase angle of the computations and experimental measurements is excellent. On the retreating side computations show a phase offset relative to the experimental data and the incorporation of the torsional dynamics results in a reduction on the retreating side time derivatives. In the MN case, the largest differences between computations are identified between $\psi = 0$deg and $\psi = 60$deg, where the time derivatives are reduced as a result of the inclusion of the first torsion mode in the analysis. Nevertheless, the correlation with the experimental data on advancing side is fair. The agreement is greatly improved on the retreating side where minimum differences between computations are identified. Regarding the MV case, the incorporation of torsional dynamics is associated with a reduction in aerodynamic loading time derivative on both BVI locations. The agreement between the reference setup and the experimental measurements is good for the magnitude and phase on the advancing side while the strongest interaction on the retreating side is not captured. Overall good agreement bewtween the reference setup and the experimental data has been identified. Two groups of computations have been observed: those with and without torsional dynamics. The inclusion of the first torsion modes results in the reduction of the aerodynamic loading time derivatives.

Moment coefficient. Figure 7.16 presents the evolution of the mean normal force coefficient and moment coefficient with the number of modes of vibration employed in the simulation. Both coefficients have been normalised with their reference coefficients. It is noted that the reference results were obtained using ten vibration modes. Diamond markers symbolise the mean moment coefficient, which is of interest now. Marginal differences in mean value result from the use of extra modes of vibration in the BL case. In the MN case, two different cases are observed. If the first torsion mode is not include, discrepancies of approximately 1% are observed relative to the reference setup. Once the first torsion is included the differences relative to the case with ten modes is minimum. Regarding the MV case, computations without the first torsion mode exhibit a relative error of about 0.6%. The incorporation of the fourth mode reduces the discrepancies to marginal.

The dynamic content of the moment coefficient at $r = 0.87R$ is presented in Fig. 7.20 for

the proposed method and experimental data. Silver, grey, and black lines denote moment coefficients predicted with different number of vibration modes. The line label refers to the number of vibration modes and the dominant mode of the highest mode. Experimental measurements of the first blade from Ref. 207 are presented with a dotted grey line. In the BL case, high frequency oscillations associated with BVIs are superimposed to the 2P oscillation. Minimum differences between all the setups are observed on the low frequency content. Results obtained with three or more modes of vibration virtually superimpose. This is explained by the magnitude of the third natural frequency, which is higher than the 2P frequency. As a result, the system is allowed to respond in frequencies at least as high as the excitation frequency. This is no longer valid for the HHC cases, where the 3P exciting frequency is larger than the third natural frequency. Therefore, the first torsion mode needs to be added to allow the blade to oscillate with a frequency at least as high as the dominant forcing one. This is observed in Fig. 7.20, where a clear distinction between computations obtained with and without the first torsion mode is identified. The use of four or more modes of vibration consequently results on a better agreement with the experimental data.

Figure 7.21 presents the high frequency content, 10P high-pass filtered, of the calculated moment coefficient. Silver, grey, and black lines denote moment coefficients predicted with different number of vibration modes. The line label refers to the number of vibration modes and the dominant mode of the highest mode. Experimental measurements of the first blade from Ref. 207 are presented with a dotted grey line. BVIs are clearly observed on the advancing and retreating sides. Similarly with the analysis made for the high frequency content of the normal force coefficient, two groups of predictions are identified. The first one comprises calculations with up to three modes of vibration, whilst the second on is composed of simulations including four or more modes. In the BL case, excellent agreement between predictions of both groups and experimental values is observed in magnitude and phase. A minimum reduction in the amplitude of the BVIs is observed when torsion dynamics is including in the analysis. Regarding the MN case, the magnitude of the BVIs matches the experimental measurements. However, there is a phase difference in the calculated moment coefficient and minimum discrepancies between code prediction are found. In the MV case, the magnitude of the interactions are correctly captured with

the reference setup on the advancing side with a phase discrepancy. In contrast, on the retreating side the phase angle is accurately modelled and the magnitude of only one of the vortex interactions is not matched with the reference case. The prediction of the latter is better prediction without torsion, which can be associated to a smaller BVI miss distance consequence of the different trim state.

The main effect of the inclusion of high order dynamics on the analysis is the modification of the low frequency behaviour, which effectively changes the trim state and wake geometry. Ultimately, this modifies blade angle of attack and the BVIs miss distance. A minimum use of four vibration modes, which include flap, lag, and torsion vibration modes, is crucial for the correct prediction of the aerodynamic loading.

7.6 Conclusions

A large effort was made to create a novel mathematical formulation for the modelling of coupled flap/lag bending and torsion vibration characteristics of rotor blades. The effect of coupled flexible blade modelling on different aspects of the rotor operation has been extensively presented in this chapter.

In the first place, the effect of flexible modelling on the trim state was assessed. A minimum of four modes of vibration were required to obtain a reliable solution of the control angles. The incorporation of more modes of vibration showed little improvement. The inclusion of torsion dynamics was identified as critical for the correct modelling of the rotor dynamic behaviour, and consequently the control angles. Regarding the prediction of rotor power, a minimum of nine modes of vibration were required to obtain a converged solution. This means that up to the third lag mode was needed. The human vibration index was found to be highly dependent on the level of flexibility modelling used and a minimum of seven modes of vibration were required to make the vibration index independent of the number of modes.

In the second place, the elastic deflections were shown to be highly dependent on the level of flexibility used to model the rotor blades. The deployment of rigid blades in flap and lag (first two modes of vibration) led to large discrepancies in flap tip deflections. The addition of the second flap mode improved the results. However, the incorporation

of the first torsion mode was observed to be essential to obtain estimations closer to the experimental measurements. The subsequent addition of extra modes of vibration resulted on the further improvement of the prediction. However, the magnitude of the incremental change for modes of vibration higher than the sixth one (third flapping mode) was found to be marginal. The elastic twist required a minimum of four coupled modes of vibration to obtain accurate predictions and a marginal change was identified when the eight mode was added. Regarding the lag displacement two different tendencies were identified. The first one, associated with the dynamic deflection, showed very weak relation between the deflection and the number of modes used. Depending on the case one or fourth modes of vibration were required. The second one, linked to the mean value of lag deflection, was found to be highly dependent on the number of vibration modes used in the analysis. A minimum of six modes of vibration were required to obtain a converged solution and a marginal improvement in the solution was found as a consequence of the addition of the ninth mode.

In the third place, a strong relation between bending and torsion moments and the level of flexible modelling was found. The calculation of flap bending moments required a minimum of six modes of vibration to obtain converged solutions in mean value and dynamic content. The addition of higher order content beyond the sixth mode was found to have a marginal effect on the flap bending moments. Regarding torsion moments, the use of less than four modes of vibration led to large errors in torsional moments. The use of higher order content was found to add marginal changes and only the inclusion of the eight mode generated a tangible improvement in the prediction of the mean value and dynamic content. The dynamic lag bending moment was found to be quite independent of flexibility effects and the use of four modes of vibration led to converged solutions. Although of small magnitude, an further improvement in the prediction was observed when the sixth mode of vibration was considered. A minimum of five modes of vibration were necessary for the correct calculation of the mean value of lag bending moment.

In the fourth place, the relation between blade flexible modelling and the geometry of the wake was analysed. Marginal differences in the geometry of the wake were observed in the top view for all analysed cases. A small change in the vertical position of the vortex systems was identified as a consequence of the inclusion of flexible modelling. It was

mainly associated to different flapping position analysed previously.

In the last place, the dependence of the aerodynamic loading on flexible modelling was evaluated. The modification of the low frequency behaviour was identified as the main effect of the inclusion of high order dynamics on the analysis, which effectively changed the trim state and wake geometry. Ultimately, this was observed to modify blade angle of attack and the BVIs miss distance. A minimum use of four vibration modes, which include flap, lag, and torsion vibration modes, was found to be necessary for the correct prediction of the aerodynamic loading.

From the above, it can be concluded that the inclusion of blade flexible modeling has its larger effect on the dynamic response of the rotor: elastic deformations, bending moments, and torsion moments. Depending on the specific DOF and property, up to nine modes of vibrations were necessary to obtain fully converged solutions. However, the use of four DOF led to reasonably well converged solutions. Aerodynamic loading were found to be fairly dependent on the dynamic response of the rotor blades. However, rotor trim angles, power required and vibration index were found to be highly dependent on the bending and torsion moments. Consequently, successful predictions of them were demonstrated to require flexible modelling with high order content.

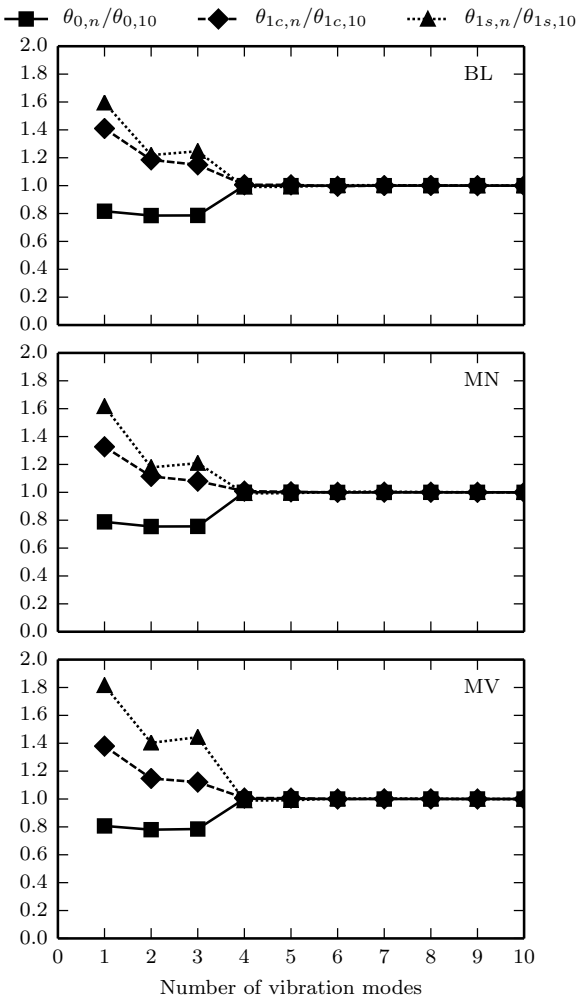

Figure 7.1: Effect of flexibility on calculated control angles.

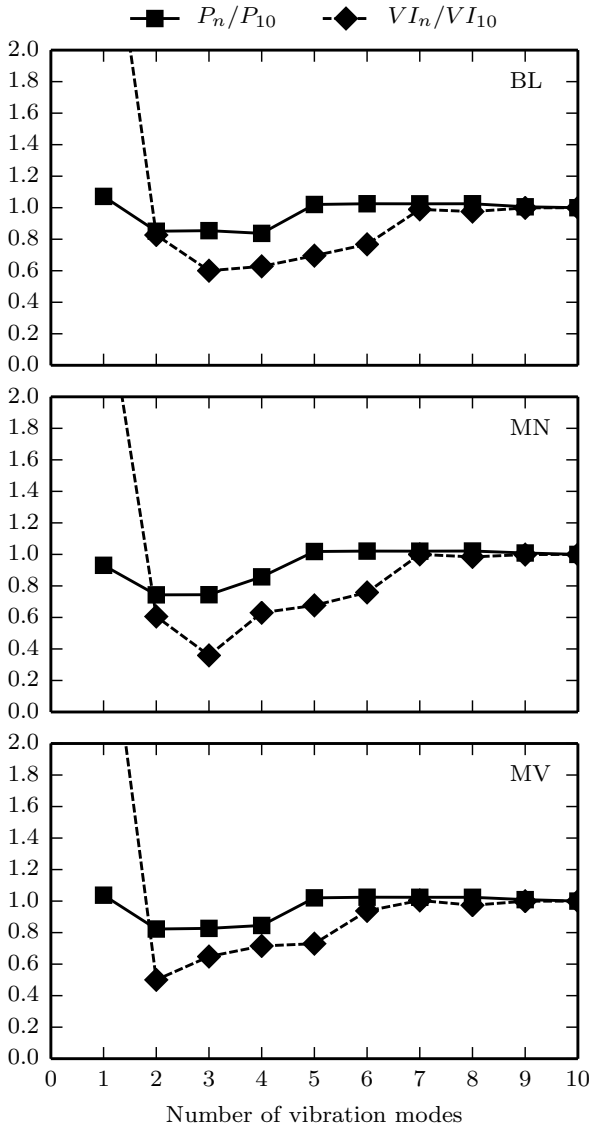

Figure 7.2: Effect of flexibility on calculated rotor power required and vibration index.

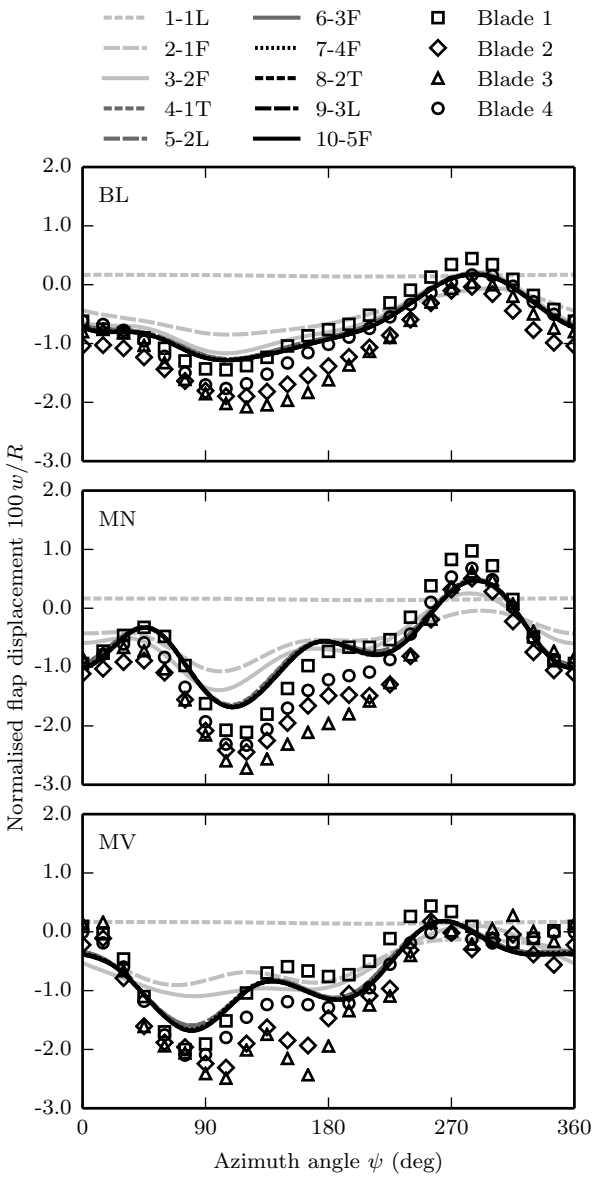

Figure 7.3: Effect of flexibility on calculated blade tip elastic flapping motion relative to precone. Comparison with experimental measurements from Ref. 207.

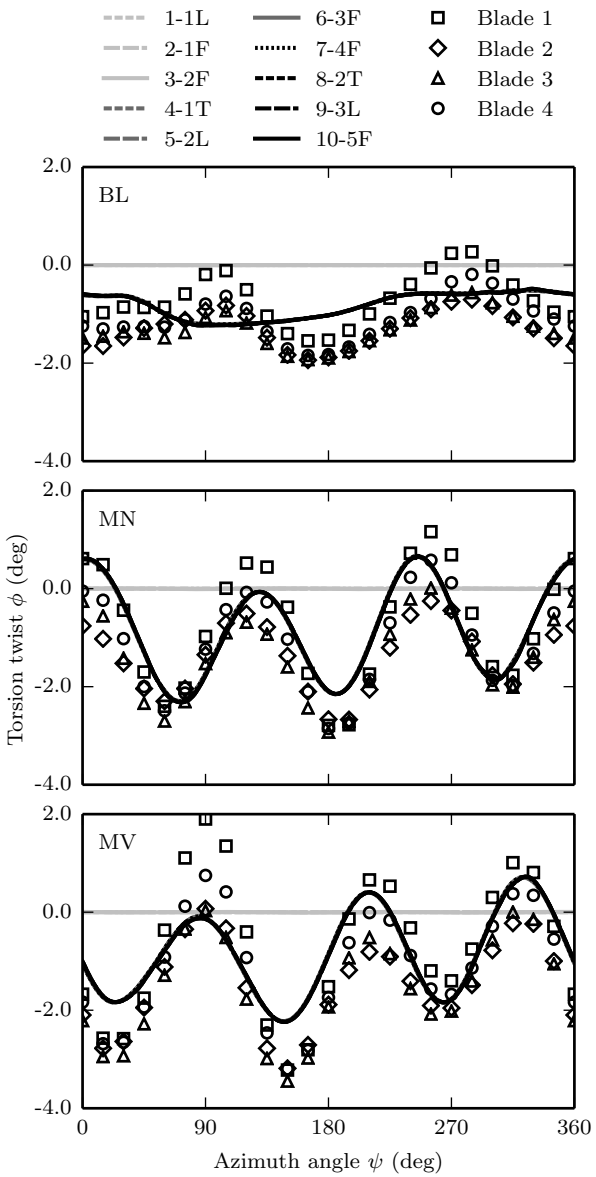

Figure 7.4: Effect of flexibility on calculated blade tip elastic torsion motion relative to control and pretwist. Comparison with experimental measurements from Ref. 207.

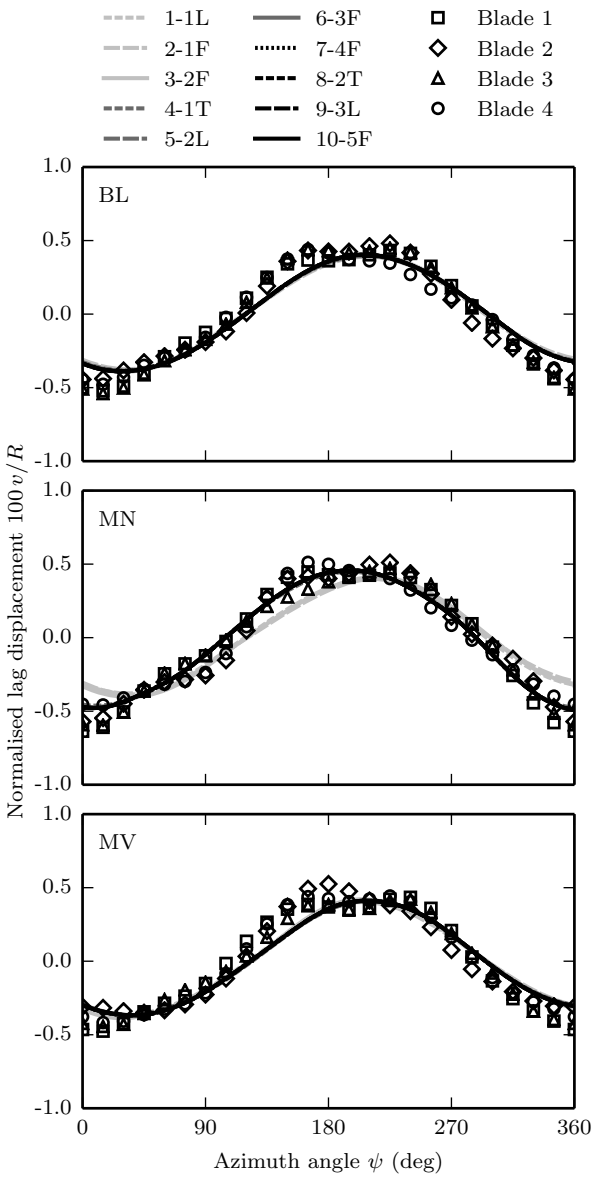

Figure 7.5: Effect of flexibility on calculated blade tip elastic lag motion, mean value removed. Comparison with experimental measurements from Ref. 207.

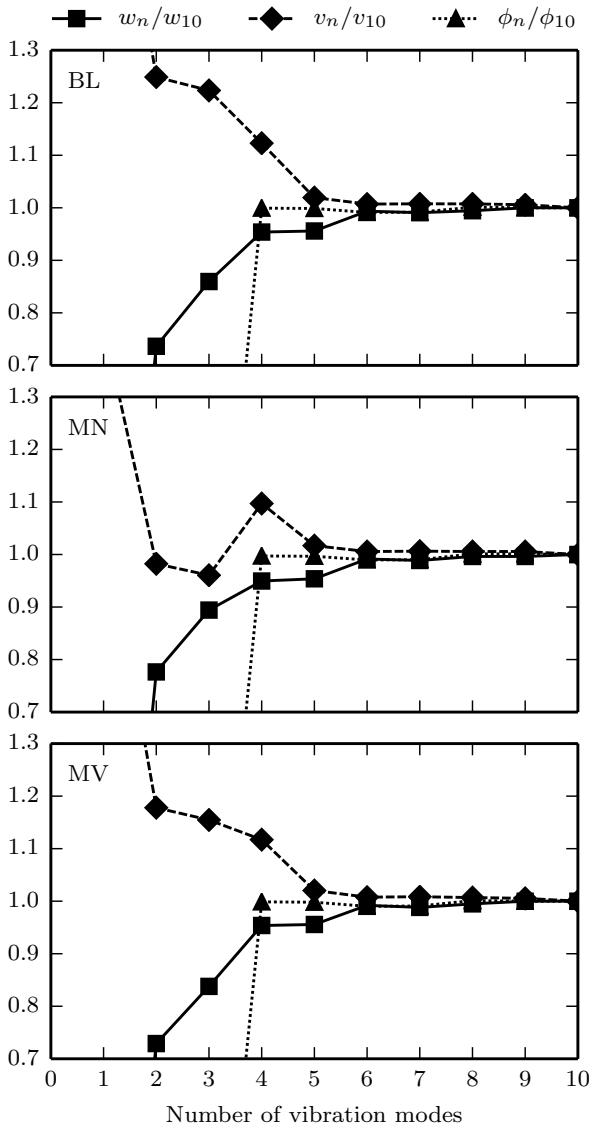

Figure 7.6: Effect of flexibility on calculated mean values of tip elastic flap, lag, and torsion motions.

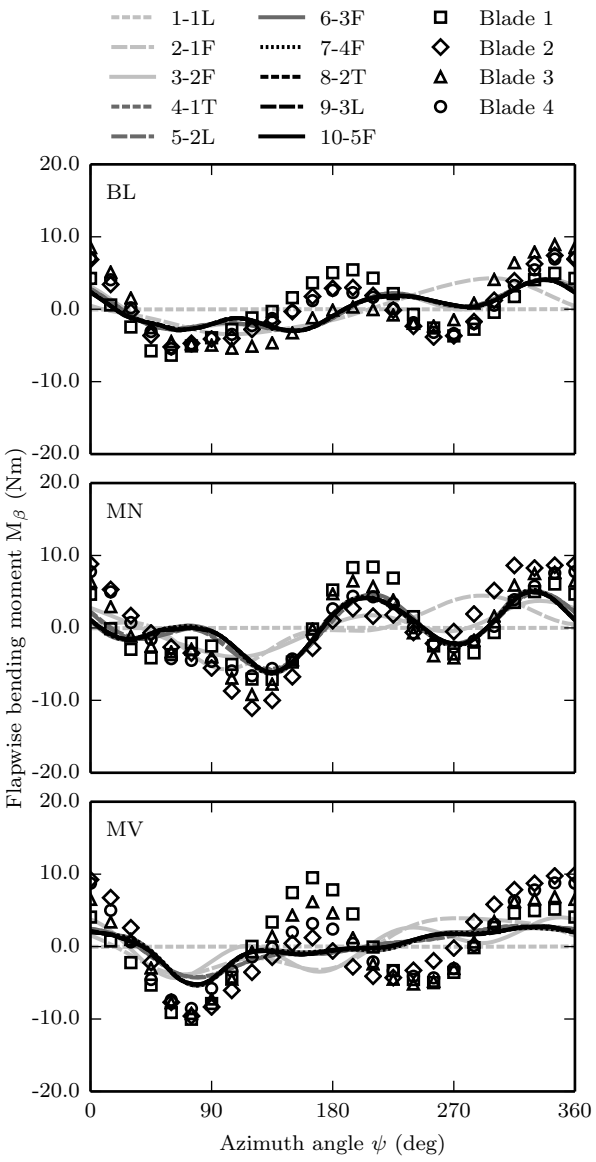

Figure 7.7: Effect of flexibility on calculated flapping bending moments at $r = 0.17R$, mean value removed. Comparison with experimental measurements from Ref. 207.

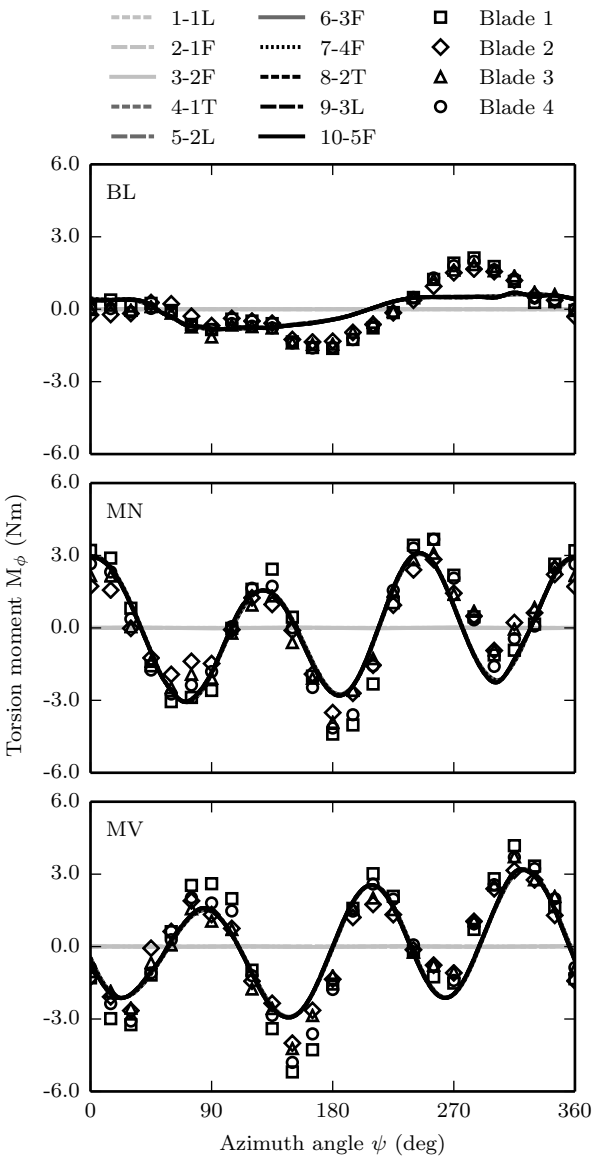

Figure 7.8: Effect of flexibility on calculated torsion moments at $r = 0.33R$, mean value removed. Comparison with experimental measurements from Ref. 207.

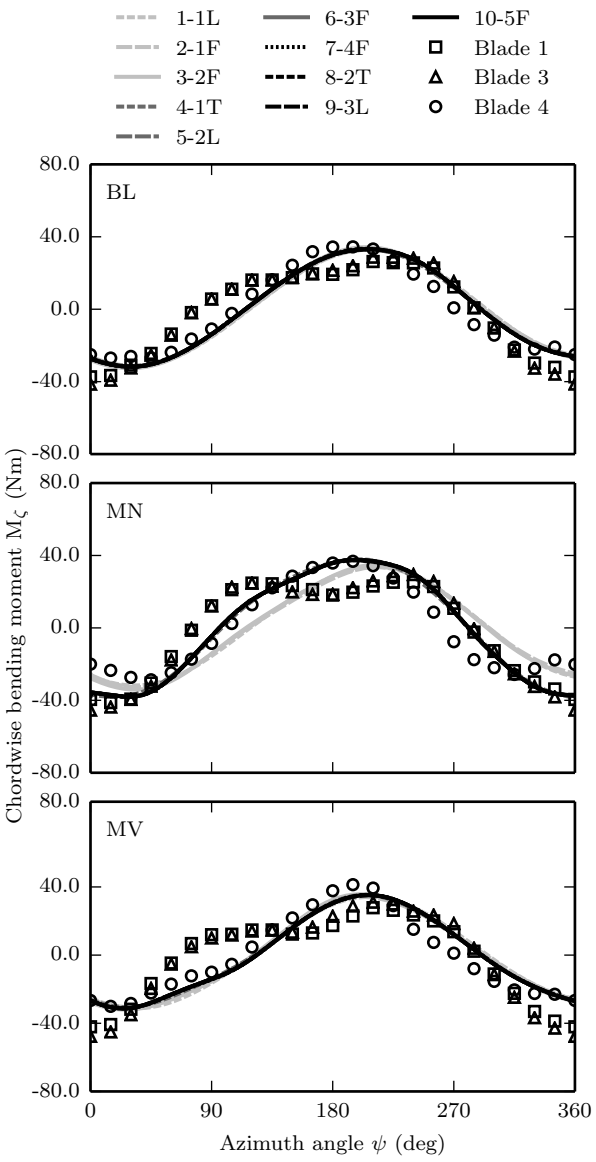

Figure 7.9: Effect of flexibility on calculated lag bending moments at $r = 0.17R$, mean value removed. Comparison with experimental measurements from Ref. 207.

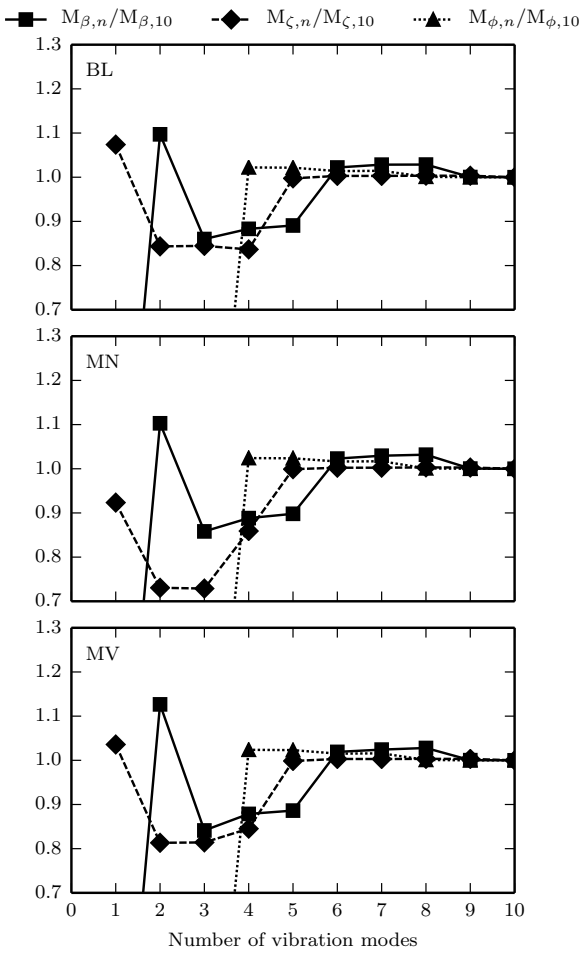

Figure 7.10: Effect of flexibility on calculated mean values of flap bending at $r = 0.17R$, lag bending at $r = 0.17R$, and torsion at $r = 0.33R$ moments.

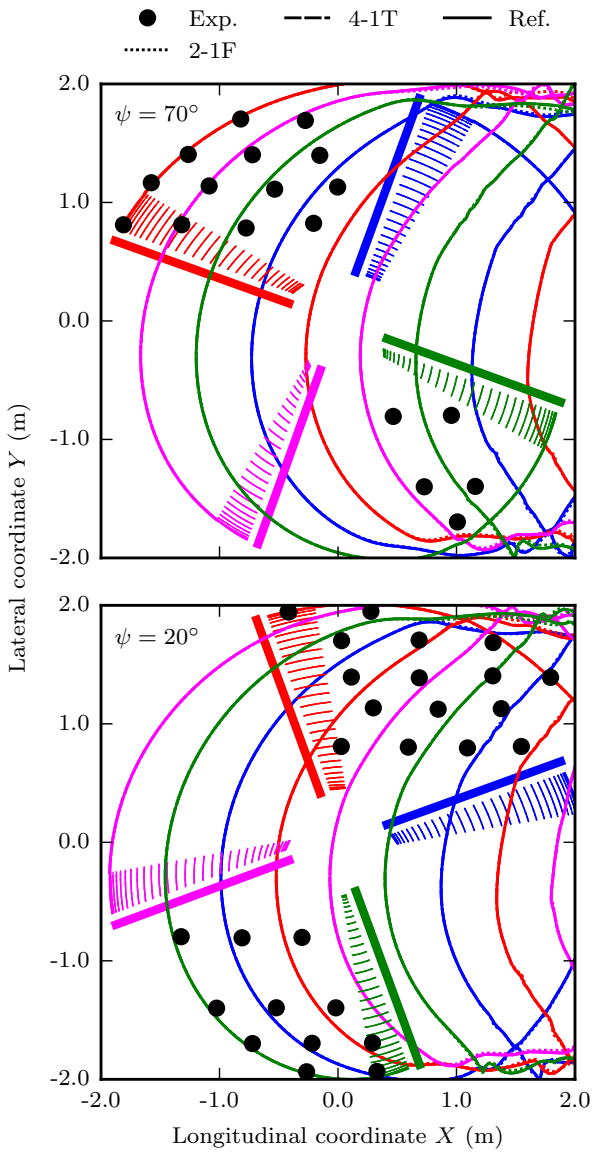

Figure 7.11: Top view of the calculated wake geometry. Effect of flexibility - baseline (BL). Comparison with measurements from Ref. 207.

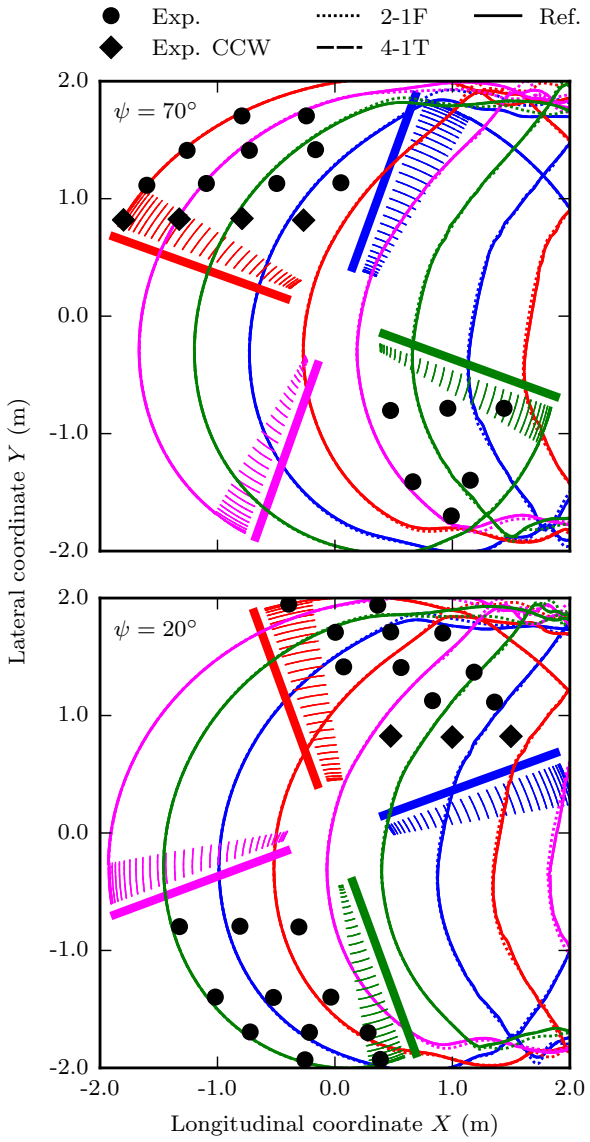

Figure 7.12: Top view of the calculated wake geometry. Effect of flexibility - minimum noise (MN). Comparison with experimental measurements from Ref. 207.

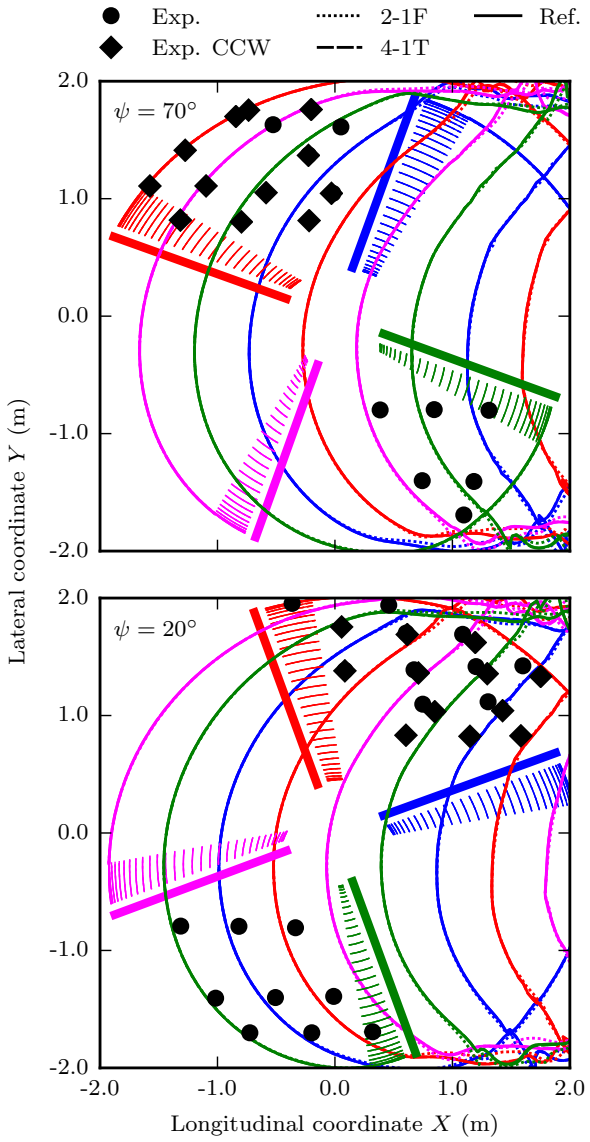

Figure 7.13: Top view of the calculated wake geometry. Effect of flexibility - minimum vibration (MV). Comparison with experimental measurements from Ref. 207.

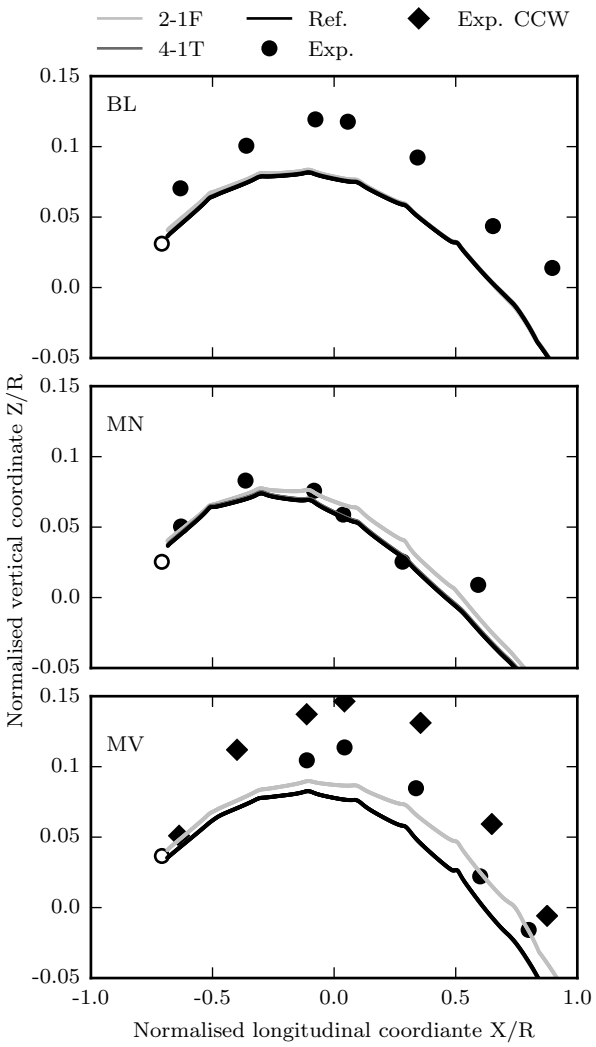

Figure 7.14: Side view of the calculated wake geometry. Effect of flexibility - $y/R = 0.7$. Comparison with experimental measurements from Ref. 207.

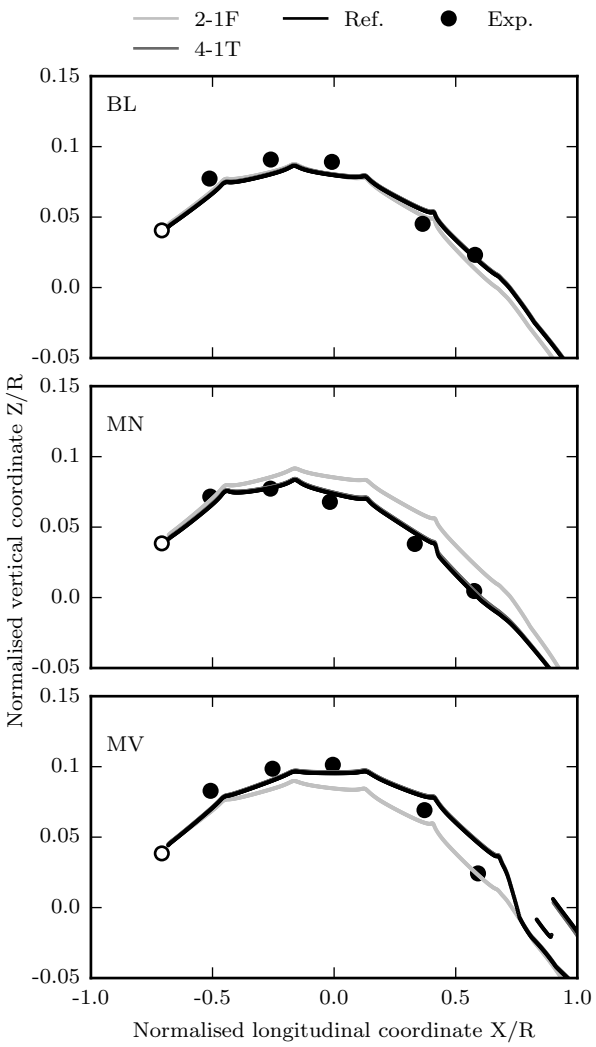

Figure 7.15: Side view of the calculated wake geometry. Effect of flexibility - $y/R = -0.7$. Comparison with experimental measurements from Ref. 207.

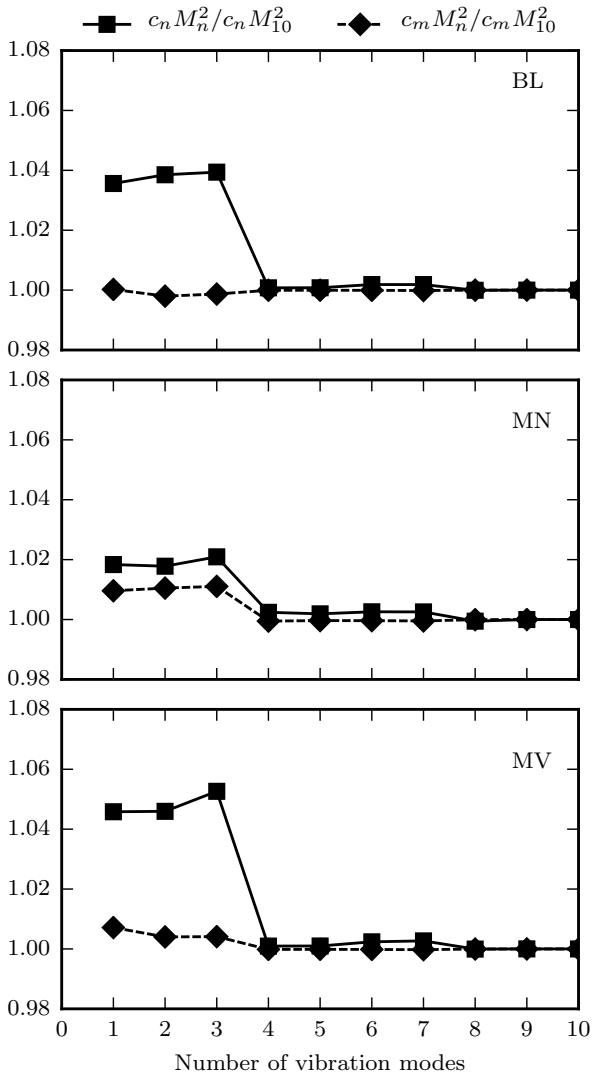

Figure 7.16: Effect of flexibility on calculated normalised mean aerodynamics coefficients at $r = 0.87R$.

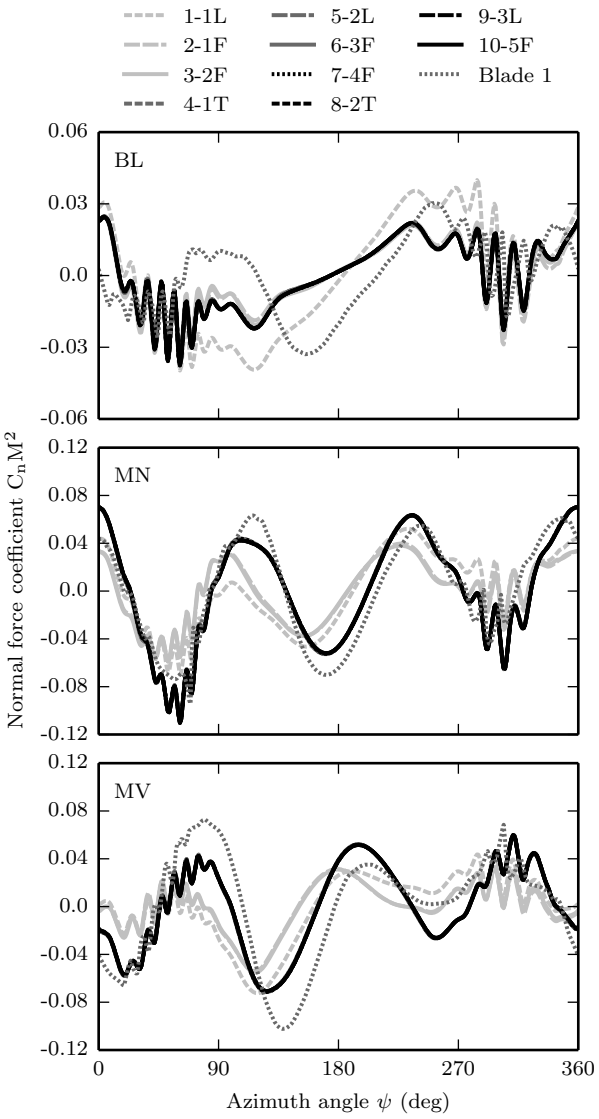

Figure 7.17: Effect of flexibility on calculated normal force coefficient at $r = 0.87R$, mean value removed. Comparison with experimental measurements from Ref. 207.

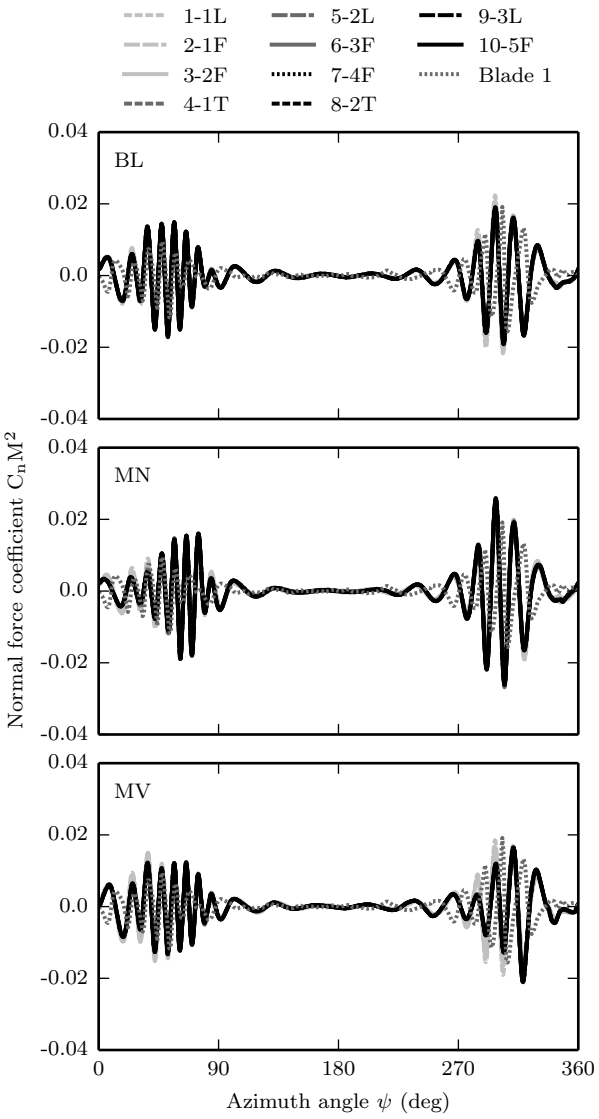

Figure 7.18: Effect of flexibility on calculated normal force coefficient at $r = 0.87R$, 10/P high-pass filtered. Comparison with experimental measurements from Ref. 207.

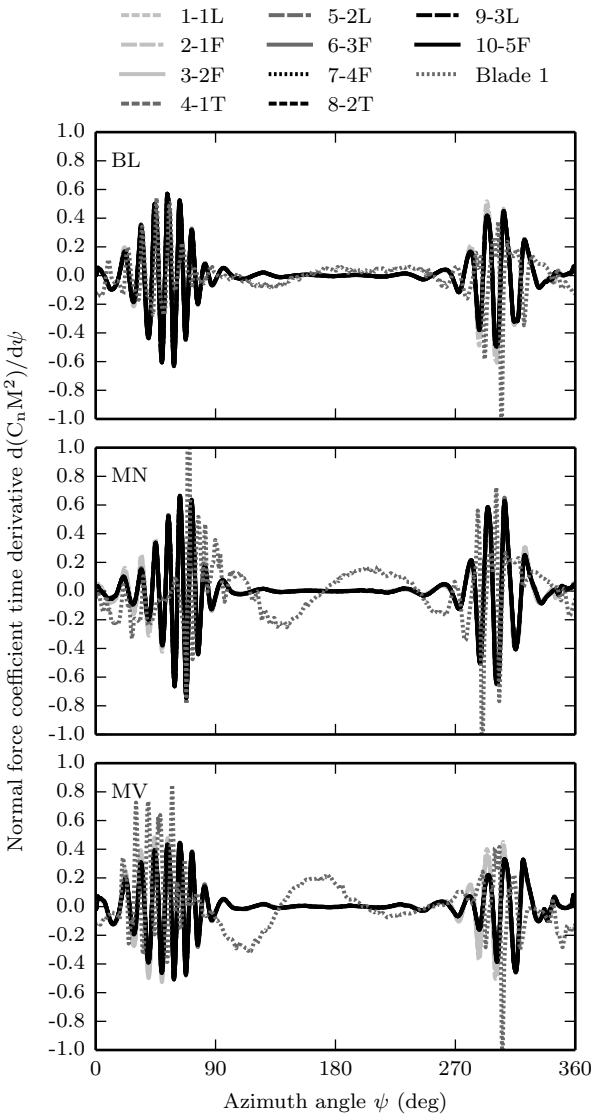

Figure 7.19: Effect of flexibility on calculated time derivative of normal force coefficient at $r = 0.87R$. Comparison with experimental measurements from Ref. 207.

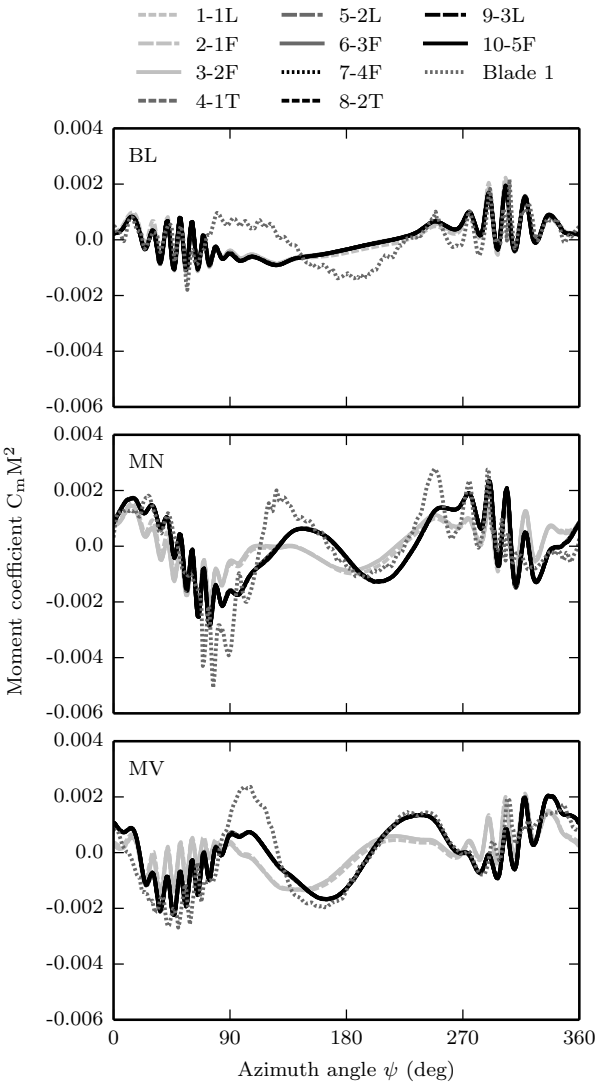

Figure 7.20: Effect of flexibility on calculated moment coefficient at $r = 0.87R$, mean value removed. Comparison with experimental measurements from Ref. 207.

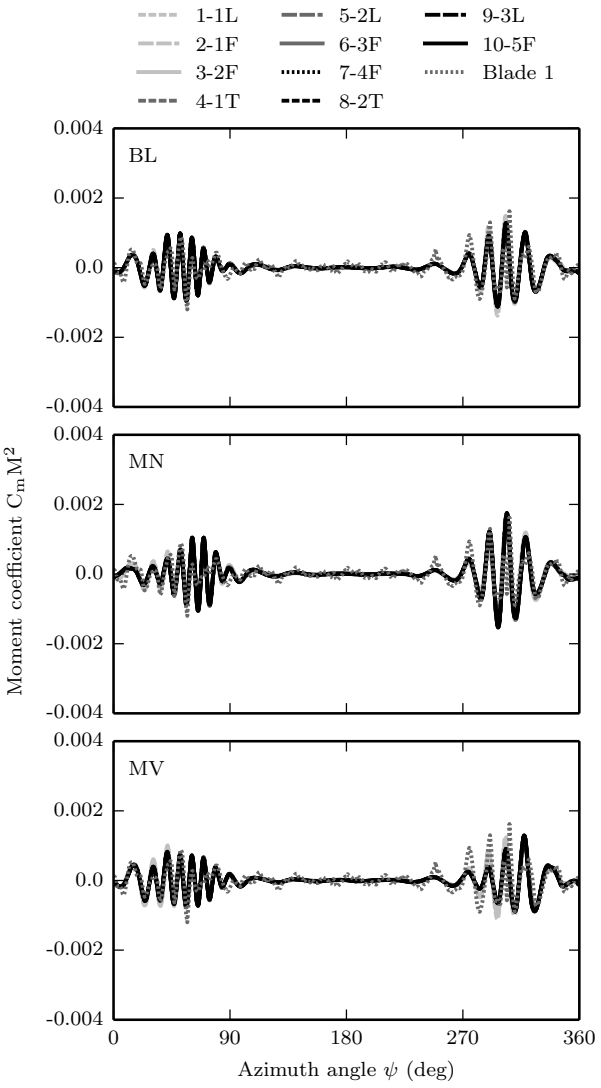

Figure 7.21: Effect of flexibility on calculated moment coefficient at $r = 0.87R$, 10/P high-pass filtered. Comparison with experimental measurements from Ref. 207.

Chapter 8

Conclusions

This chapter summarises the most significant findings and conclusions drawn individually in each chapter and assesses the achievement of the objectives outlined in Chapter 1. Moreover, the contribution to the knowledge resulting from the completion of this research project is discussed. In the last place, suggestions for future work are made.

Chapter 1 described the increasing concern about the continuous rise in chemical pollutant and noise emissions levels and the depletion of fossil fuels. This concern has placed the aviation industry into a difficult position, where its expected growth is compromised by its environmental impact. Vision 2020 and Flightpath 2050 are two governmental initiatives to reduce the environmental footprint of the aviation industry. Three different paths were identified to meet the goals targeted by these initiatives. The first one is the reduction of the number of flight operations, which is not feasible due to the expected growth in operations. The second one is the optimisation of the operational procedures. However, its potential is limited. The third one is the development of novel aircraft configurations which are more efficient and quieter than the last generation. Within the helicopter industry the last option requires the development of conceptual configurations such as the tilt-rotor and compound helicopter. The inherent complexity of these configurations, where multiple interactions between components are present, has made their development long and highly expensive.

Within this context, the relevance of simulations tools able to predict the complex behaviour of the rotorcraft is evident. This projects aims to lay the foundations of a

comprehensive rotorcraft code for the analysis of conceptual configurations. Due to the complexity of the interactions present in their operation, a model approaching the third Padfield level of hierarchy has been found to be necessary. However, high fidelity tools are associated with computational overhead which makes its use for multidisciplinary optimisation not possible. Therefore, a trade off between fidelity and computational cost has to be made.

8.1 Achievement of the Objectives

Development of a computational framework for the aeroelastic simulation of rotorcraft propulsion systems

Objective. Within the context of the development of a third level of Padfield's hierarcy simulation tool able to model new rotorcraft configurations, the main objective of this research work was defined in Chapter 1 as: *development of a computational framework for the aeroelastic simulation of rotorcraft propulsion systems.* A series of features were specified as requirements for the developed simulation frameworks, these are:

- The simulation tool must be able to accurately simulate and predict the aerodynamic flowfield and the unsteady loads generated by the rotor and transferred to the fuselage.
- The developed framework must be easily expandable to account for potential interactions with other rotors, auxiliary lift surfaces, and fuselage bodies.
- It must be able to provide low and high frequency aerodynamic loading for the integration of an ongoing project on noise emission calculation.
- It must provide accurate predictions of rotor power required. This feature permits to use the code as a validation and tuning tool for lower order model developments.
- It must be applicable to the design process. Consequently, a detailed aeroelastic analysis is required.

- It must be applicable to multidisciplinary optimisation methodology. Hence, the computational cost must be kept low.

The successful fulfilment of the required features and consequently, the objective, lays the foundations of the comprehensive rotorcraft code for the analysis of conceptual configurations.

Tasks performed and conclusions drawn. The aeroelastic simulation of a rotor blade involves the mathematical and computational modelling of different interrelated areas. For some of these areas, mathematical and numerical methods are readily available. However, the progress carried out up to date in some of the other areas is not enough and further work has been required. In order to tackle the problem more efficiently, each of the fields of study was treated separately and later coupled and integrated into the simulation framework. The specifications set for the computational tool require the development of models approaching the third level of Padfield's hierarchy while keeping the computational cost low. This has required to pay special attention to numerical methods for enhanced stability, acceleration techniques, and code optimisation for parallel computing. As previously mentioned, each of the areas are tackled separately. Thus, a series of individual goals were set in Chapter 1:

1. **Goal:** *Formulation of a computationally efficient method for the rapid estimation of the coupled natural frequencies and modes of vibration of modern rotor blades*

   Approach followed: A mathematical formulation for modelling of coupled flap-lag bending and torsion vibration characteristics of helicopter rotor blade has been presented. The model has been formulated based on the application of Lagrange's equation of motion to the three-dimensional kinematics of a non-uniform rotating blade. Spatial solutions of classical theories have been deployed as assumed deformation functions to enhance the computational efficiency of the method. The method has been reduced to a set of closed-form integral expressions compatible with different structural boundary conditions. The effect of different geometrical parameters on the coupling between modes of vibration has been assessed. The dependence of the method's prediction on the gyroscopic matrix has been evaluated. The predictive capability of the proposed method has been examined by comparing its predictions with experimental measurements, finite element analyses results, and

multi-body dynamics calculations for three different rotor blades. The comparison showed that:

- The methodology exhibits excellent numerical performance with definite fast convergence.
- The method was shown to have excellent computational performance and fully coupled modes were estimated in a fraction of a second.
- The predictions obtained with the present method demonstrated to show excellent and in some cases very good agreement with experimental data, FEA results, and multi-body dynamics calculations.
- The effect of gyroscopic coupling was assessed, and it was identified as critical for configurations with high values of precone angle.

2. **Goal:** *Development of an analytical formulation for the aeroelastic modelling of flexible rotor blades with coupled modal characteristics*

   Approach followed: An existing analytical formulation for the aeroelastic modelling of flexible rotor blades has been modified to make it suitable for its use along coupled flap-lag bending and torsion modal characteristics. The flexible treatment of the three-dimensional kinematics of rotor blades was enhanced by better accounting for torsional velocity and acceleration effects. Additionally, coupling terms arising in the three-dimensional kinematics were better modelled. These terms were identified in the method for the rapid estimation of the coupled natural frequencies and modes of vibration to play a relevant role. The developed kinematic formulation was discretised in the time domain using two second-order accurate backward-difference approximations which highly improved the stability of the method. These equations were used to obtain the aerodynamic and inertia loading, which were incorporated into a flap-lag-torsion coupled predictor-corrector aeroelastic time-marching method.

   The developed aeroelastic modelling formulation was coupled with a free-vortex wake inflow model, an unsteady blade element aerodynamic model, and an efficient trim method to build a cost effective aeroelastic simulation framework.

3. **Goal:** *Implementation of an unsteady free-vortex wake aerodynamic model for the estimation of the unsteady rotor inflow*

   Approach followed: A relaxation free-vortex wake model based on the pseudo-implicit, predictor-corrector method proposed by Bagai and Leishman (Ref. 102) has been implemented in the present work to generate the rotor disk inflow. Its superior convergence characteristics made this option an optimum choice. The method is optimised to be executed in parallel and coupled to a numerical acceleration scheme based on velocity field interpolation to enhance its computational performance. The current implementation accounts for a near wake region with multiple trailing vortices and a far wake with root and tip vortices. A vortex roll-up model, a viscous diffusion model based, an unsteady blade aerodynamic model, and a fuselage aerodynamic interference model have been coupled in the solution with the free-vortex wake model.

   The implemented free-vortex wake model was assessed, when coupled with the rest of the aeroelastic model, for a small scale rotor operating in descending conditions. These conditions constitute a challenge for the prediction of wake geometries. The main conclusions drawn are:

   - The implemented free-vortex wake model has not shown any instability or lack of convergence in the cases analysed.
   - Its implementation with computational enhancement techniques reduced its execution time by up to 97% for a given discretisation level.
   - Wake geometries predicted with the implemented model have been shown to have very good agreement with experimental measurements and others code calculations.

4. **Goal:** *Implementation of computational enhancement techniques for the minimisation of the computational overhead associated with the free-vortex wake model*

   Approach followed: Two computational enhancement techniques have been implemented in the free-vortex wake model to minimise its computational overhead. The implementation of the inflow model was optimised for parallel execution, and

later parallelism within a shared memory multiprocessing machine enabled. As a result, simulations have been considerable accelerated in low end personal computer. Additionally, a numerical acceleration scheme based on velocity field interpolation has been implemented. These technique reduces the number of Biot-Savart's law evaluations while keeping the prediction accuracy. The acceleration scheme has been optimised as well for parallel execution. The implementation of both techniques has shown the following advantages:

- It has been demonstrated that the use of parallel execution alone, without velocity interpolation, resulted in execution time reductions of up to 82% for an eight cores CPU.
- It has been shown that the use of velocity interpolation alone, without parallel execution, resulted in require computational time reductions of up to 89%.
- The combination of both techniques resulted in reductions of the execution time of up to 97%. Converged solutions (full aeroelastic model with trim procedure) can be obtained in 49min, 13min and 3min for $\Delta\psi = 2$deg, $\Delta\psi = 5$deg, and $\Delta\psi = 10$deg as azimuth discretisation levels.
- The computational efficiency attained using these techniques places this method next to lower order methods in terms of computational cost.

5. **Goal:** *Implementation of a computationally efficient fuselage aerodynamic interference model to prove the ability of the framework to capture flow interactions*

   Approach followed: A computationally efficient semiempirical analytical fuselage formulation originally proposed by Van der Wall *et al.* (Ref. 187) has been implemented in the present work. The current implementation directly modifies the rotor disk inflow and wake geometry. As a result of the modification of the inflow, the rest of the aspects of the rotor operation varied. Consequently, the rotor inflow and geometry were further re-adapted.

   - It has been demonstrated that the inclusion of the fuselage has a large effect on the cyclic control angles.

- It has been shown that the change in wake geometry, consequence of the presence of the fuselage, can modify the BVIs miss distance. Therefore, the strength of the interactions is influenced by the fuselage model.
- The necessity of a fuselage model has been justified by the coupled response of the whole rotor to the change in inflow conditions caused by the fuselage.
- The capability of the free-vortex wake model to capture the interference of the fuselage has been proven. This proves its expandability to account for multirotor interactions.

6. **Goal:** *Implementation of an unsteady blade aerodynamic model able to accurately estimate low and high frequency unsteady aerodynamics*

   Approach followed: An unsteady blade aerodynamic model based on Leishman-Beddoes indicial response method (Ref. 174, 189, 190) has been implemented in the present work. It provides time evolutions of lift, drag, and moment coefficients due to an effective angle of attack and pitch rate and their time derivatives. The successful implementation of the method has been assessed by comparing the predicted aerodynamic loading with experimental measurements and other code's calculations. Favourable comparison of the low and high frequency aerodynamic loading has been presented. The latter is specially important for the correct modelling of BVIs and the associated noise emission.

7. **Goal:** *Integration of the previous areas into a cost effective aeroelastic simulation framework*

   Approach followed: The previously discussed modules: coupled modal characteristics, three-dimensional kinematics of elastic blade, free-vortex wake inflow model, fuselage aerodynamic interference model, and unsteady blade aerodynamic model have been integrated in a cost effective time-marching manner. A predictor-corrector time-marching scheme has been used to obtain the dynamic response of the rotor. The use of this scheme resulted in better numerical stability, which enabled the use of larger azimuth discretisations, reducing the computational overhead. Additionally, the time-marching aeroelastic method has been optimised for parallel computation

leading to a further improvement in the computational efficiency.

The predictive capability of the framework has been extensively assessed by comparing its results with experimental measurements and a second code's calculations for the HART II rotor undertaking descend:

- The computational efficiency of the code has been strongly enhanced, leading to large reductions in computational execution times, see previous point: *Implementation of computational enhancement techniques for the minimisation of the computational overhead associated with the free-vortex wake model.*
- Excellent agreement between the modal characteristics of the rotor blade predicted and experimental measurements has been demonstrated.
- Trim control angles and power required predictions have been proven to exhibit excellent agreement with the experimental data.
- Excellent correlation between the elastic deflection experimentally measured with the calculations of this method has been identified.
- Very good and in some cases excellent agreement between computed bending and torsion moments and experimental measurements has been shown.
- A mixture of very good and excellent correlations has been observed between the predicted aerodynamic loading and the experimental measurements. The favourable comparison during the complex flight condition test has proven the predictive capability for aeroelastic and noise purposes.
- Wake geometries predicted with the implemented model have been demonstrated to have very good and in some cases excellent agreement with experimental measurements and others code calculations.

From the above, it can be concluded that the general objective and the individual goals set in Chapter 1 have been successfully achieved.

8.2 Contribution to Knowledge

The main contribution of this work has been the successful development of a computational framework for the aeroelastic simulation of rotorcraft propulsion systems. The developed framework has been demonstrated to be able to accurately simulate and predict the aerodynamic flowfield and the unsteady loads generated by the rotor and transferred to the fuselage. The framework is easily expandable to account for potential interactions with other rotors, auxiliary lift surfaces and fuselage bodies, as shown in Chapter 6 for the fuselage aerodynamic interference. The simulation tool has been proven to be able to provide high fidelity low and high frequency aerodynamic loading, including blade vortex interactions. The latter enables the calculation of impulsive noise, which is an ongoing research project in the institution. The frameworks has been identified to provide accurate predictions of rotor power required, which enables its use as a validation tool for lower order models. The developed framework approximates the third level of Padfield's hierarchical paradigm, providing detailed aeroelastic information necessary for design purposes. The addition of parallel computing and an acceleration scheme has resulted in a highly computationally efficient tool which was proven to generate fully converged solutions in less than an hour for a really fine azimuthal resolution. If a slightly coarser discretisation is used, the solution is obtained in only 3.2min with a low end personal computer. The low computational cost makes this tool suitable for multidisciplinary optimisation methodologies.

The features of the developed framework successfully lays the foundations of a comprehensive rotorcraft code for conceptual configurations. The broader comprehensive code could potentially model rotorcraft configurations such as tilt-rotor, compound helicopter, coaxial helicopter, and conventional helicopter. The addition of a computational model for the noise emissions calculations has been enabled by the development of a rotor aeroelastic simulation tool able to calculate the low and high frequency aerodynamic loading responsible for the loading noise.

In addition to the computational tool itself, contribution was made in each of the individual areas previously described. These can be summarised as:

- A mathematical formulation for the modelling of coupled flap-lag bending and torsion

vibration characteristics of helicopter rotor blade has been developed and presented. The method has been reduced to a set of closed-form integral expressions compatible with different structural boundary conditions. The effect of different geometrical parameters on the coupling between modes of vibration has been assessed. The predictive capability of the proposed method has been extensively evaluated by comparing its predictions with experimental measurements, finite element analyses results, and multi-body dynamics calculations for different rotor blades.

- An existing analytical formulation for the aeroelastic modelling of flexible rotor blades has been modified to make it suitable for its use along with coupled flap-lag bending and torsion modal characteristics. The adapted methodology has been proven to give aeroelastic predictions which exhibit very good or excellent agreement with experimental data.

- A relaxation type free-vortex wake aerodynamic model has been implemented and optimised for computational efficiency. It has been further enhanced with parallel computing and coupled to a numerical acceleration scheme based on velocity field interpolation. The implemented method has shown definitive convergence for the cases analysed, large reductions in computational overhead have been attained, and very good agreement of its predictions with experimental measurements has been observed for the cases tested.

- Two computational enhancement techniques have been implemented in the free-vortex wake model to minimise its computational overhead. The combination of both techniques resulted in reductions of the execution time of up to 97%. Converged solutions have been obtained in 49min, 13min, and 3min for $\Delta\psi = 2$deg, $\Delta\psi = 5$deg, and $\Delta\psi = 10$deg as azimuth discretisation levels. The computational efficiency attained using these techniques places this method next to lower order methods in terms of computational cost.

- A computationally efficient semiempirical analytical fuselage formulation has been implemented. The effect of the inclusion of fuselage aerodynamic interference on the performance of the rotor has been addressed. The necessity of accounting for

interference effects has been proven. The ability of the free-vortex wake model to capture interferences has been demonstrated, which increases the level of confidence on the capability to model multirotor interactions.

- An investigation of the effect of flexible blade modelling on different aspects of the rotor operation has been carried out. Although its effect on the wake has been quantified as small, it highly influences the dynamic behaviour of the rotor blade. Consequently the fluctuating loads transferred to the fuselage and the rotor power have been found to be highly dependent on the type of structural blade modelled. The inclusion of flexibility was demonstrated to lead to predictions closer to the experimental measurements.

- An unsteady blade aerodynamic model was implemented. It was proven to accurately predict low and high frequency aerodynamic loading. A favourable comparison with experimental measurements has been presented. The ability to calculate high frequency aerodynamic loading enables the calculation of impulsive noise in the broader comprehensive rotorcraft code.

- All these modules were successfully integrated into a cost effective aeroelastic simulation framework. The superior stability of the developed approach along with the code optimisation for parallel computing results in a drastic reduction of the computational cost.

Furthermore, a large contribution to the Clean Sky project was made in parallel to the completion of this research project. The author was actively involved in the activities undertaken by the Technology Evaluator of Clean Sky, regarding rotorcraft performance modelling activities with the GRC-ITD. The Rotorcraft Mission Energy Management Model (RMEM) developed at Cranfield University was successfuly integrated into the Clean Sky developed Phoenix platform. A comprehensive assessment of the fuel burn, and gaseous and noise emissions was carried out for novel rotorcraft technologes at mision, operational, and airport level.

8.3 Future Work

As it was stated in Chapter 1, this project aimed to lay the foundations of a comprehensive rotorcraft code for conceptual configurations. Different lines of work can be outlined for the simulation framework of the propulsion system itself and the potential comprehensive rotorcraft code.

- Enhancement of the unsteady blade aerodynamic model.
  - The current methodology does not distinguish between variations in angle of attack originated by the movement of the blade and those generated by non-uniform flowfield. Certain overpredictions in the magnitude of the high frequency aerodynamic loading have been observed, this could potentially be corrected by the separation of both effects in the formulation.
  - The implemented formulation has been demonstrated to successfully model the unsteady behaviour of the blade. The addition of a dynamic stall model to the model could potentially improve the prediction at high angles of attack or under stall dynamic conditions.

- Dual-vortex configurations were experimentally observed in one of the cases tested. The present methodology does not account for this kind of vortex configurations. An investigation of the potential of adding an extra vortex to the far wake should be assessed. A trade-off will be presented between the extra computational cost and the increase in the accuracy. This trade-off should be studied in depth.

- The implemented fuselage aerodynamic model was proven to be highly efficient due to its analytical nature. However, a set of model constants is required for each fuselage studied. The calculation of these constants relies on the availability of aerodynamic data for the specific fuselage. The computation of these aerodynamic characteristics for different fuselages will enhance the model making it more versatile.

- The most potential line of future work is the integration of the developed framework into a comprehensive rotorcraft code.

- The developed simulation tool provides the values of hub forces and moments required by the flight dynamics code. Consequently, the core capability has been already built and only the addition of a tail rotor model to the flight dynamics code would be required for a conventional helicopter configuration.
- The simulation framework developed has been proven to account for interactions between the rotor and the fuselage. It is theoretically equally capable of accounting for interactions between rotors. Therefore, the development of a multirotor comprehensive rotorcraft code with aeroelastic simulation of the rotors is a feasible line of research. Minimum changes to the frames of reference and blade kinematics are required to model clockwise a rotating rotor. Additionally, the aerodynamic interaction of other rotors on a given rotor is accounted by simple superimposition in the forcing term of the free-vortex wake governing equation.
- The potential conceptual configuration comprehensive code could include a noise emissions model. The information required to obtain thickness and loading noise can be directly obtained from the developed framework. New rotorcraft configurations could potential reduce noise emissions and the developed platform would be able to estimate it and possibly optimise its design for minimum noise production.

References

[1] "Global Market Forecast 2017-2036 "Growing Horizons"," Technical report, Airbus, 2017.

[2] Group, A. T. A., "Air Transport Action Group (ATAG) - Facts & Figures," 2016, [Online; accessed 24-June-2017].

[3] Leggett, J. A., Elias, B., and Shedd, D. T., "Aviation and the European Union's Emission Trading Scheme," *Congressional Research Service*, Vol. 9, 2012.

[4] Kampa, M. and Castanas, E., "Human Health Effects of Air Pollution," *Environmental pollution*, Vol. 151, No. 2, 2008, pp. 362–367.

[5] "The Environmental Effects of Civil Aircraft in Flight," Short report, The Royal Commission on Environmental Pollution, 2002.

[6] Karamolegkos, K., Goulos, I., Pachidis, V., Stevens, J., Smith, C., Thevenot, L., and d'Ippolito, R., "Helicopter Mission Analysis Using a Mutidisciplinary Simulation Framework," *ASME Turbo Expo 2014: Turbine Technical Conference and Exposition*, American Society of Mechanical Engineers, 2014.

[7] d'Ippolito, R., Stevens, J., Pachidis, V., Berta, A., Goulos, I., and Rizzi, C., "A Multidisciplinary Simulation Framework for Optimization of Rotorcraft Operations and Environmental Impact," *2nd International Conference on Engineering Optimization*, September.

[8] Goulos, I., Pachidis, V., d'Ippolito, R., Stevens, J., and Smith, C., "An Integrated Approach for the Multidisciplinary Design of Optimum Rotorcraft Operations," *Journal of Engineering for Gas Turbines and Power*, Vol. 134, No. 9, 2012, pp. 091701.

[9] JTI, C. S., "Clean Sky JTI (Joint Technology Initiative) home page," 2017, [Online; accessed 24-June-2017].

[10] "Flightpath 2050, Europe's Vision for Aviation," Technical report, High Level Group on Aviation Research - European Comission, 2011.

[11] Clarke, J.-P., "The Role of Advanced Air Traffic Management in Reducing the Impact of Aircraft Noise and Enabling Aviation Growth," *Journal of Air Transport Management*, Vol. 9, No. 3, 2003, pp. 161–165.

[12] Goulos, I., Giannakakis, P., Pachidis, V., and Pilidis, P., "Mission Performance Simulation of Integrated Helicopter–Engine Systems Using an Aeroelastic Rotor Model," *Journal of Engineering for Gas Turbines and Power*, Vol. 135, No. 9, 2013, pp. 091201.

[13] Fakhre, A., Pachidis, V., Goulos, I., Tashfeen, M., and Pilidis, P., "Helicopter Mission Analysis for a Regenerated Turboshaft," *ASME Turbo Expo 2013: Turbine Technical Conference and Exposition*, American Society of Mechanical Engineers, 2013.

[14] Goulos, I., Hempert, F., Sethi, V., Pachidis, V., d'Ippolito, R., and d'Auria, M., "Rotorcraft Engine Cycle Optimization at Mission Level," *Journal of Engineering for Gas Turbines and Power*, Vol. 135, No. 9, 2013, pp. 091202.

[15] Fakhre, A., Goulos, I., Tzanidakis, K., Pachidis, V., and d'Ippolito, R., "A Multidisciplinary Approach for the Comprehensive Assessment of Integrated Rotorcraft-Powerplant Systems at Mission Level," *ASME Turbo Expo 2014: Turbine Technical Conference and Exposition*, American Society of Mechanical Engineers, 2014.

[16] Goulos, I., Mohseni, M., Pachidis, V., D'Ippolito, R., and Stevens, J., "Simulation Framework Development for Helicopter Mission Analysis," *Proceedings of ASME Turbo Expo 2010: Power for Land, Sea, and Air*, American Society of Mechanical Engineers, 2010.

[17] Goulos, I., *Simulation Framework Development for the Multidisciplinary Optimisation of Rotorcraft*, Ph.D. thesis, Cranfield University, 2012.

[18] Brooker, P., "Civil aircraft design priorities: air quality? climate change? noise?" *The Aeronautical Journal*, Vol. 110, No. 1110, 2006, pp. 517–532.

[19] Padfield, G. D., *Helicopter Flight Dynamics*, John Wiley & Sons, 2008.

[20] Castillo Pardo, A., Pachidis, V., Stevens, J., Smith, C., Thevenot, L., and d'Ippolito, R., "Clean Sky Technology Evaluator - On the Environmental Impact of Green Rotorcraft Technologies," *Greener Aviation Conference 2016*, October 2016.

[21] Stevens, J., Smith, C., Thevenot, L., d'Ippolito, R., Gires, E., Castillo Pardo, A., and Pachidis, V., "Clean Sky Green Rotorcraft New Technologies - Maximizing Noise and Emissions Benefits," *Proceedings of the 42nd European Rotorcraft Forum*, September 2016.

[22] Smith, C., Pachidis, V., Castillo Pardo, A., Gires, E., Stevens, J., Thevenot, L., and d'Ippolito, R., "Achieving Rotorcraft Noise and Emissions Reduction for 'Clean Sky' - The Measurement of Success," *5th CEAS Air & Space Conference*, September 2015.

[23] Castillo Pardo, A., Goulos, I., and Pachidis, V., "Modelling and Analysis of Coupled Flap-Lag-Torsion Vibration Characteristics Helicopter Rotor Blades," *Proceedings of the Institution of Mechanical Engineers, Journal of Aerospace*, Vol. 231, No. 19, 2016, pp. 1804–1823.

[24] Shupe, N. K., "A Study of the Dynamic Motions of Hingeless Rotored Helicopters." Tech. Rep. TR ECOM-3323, US Army Electronics Command, 1970.

[25] Curtiss Jr, H. C. and Shupe, N. K., "A Stability and Control Theory for Hingeless Rotors," *27th Annual Forum of the American Helicopter Society, Washington, DC*, 1971.

[26] Lewis, W. D., "An Aeroelastic Model Structure Investigation for a Manned Real-Time Rotorcraft Simulation," *Proceedings of the 49th Annual Forum*, American Helicopter Society, May 1993.

[27] He, C. and Lewis, W. D., "A Parametric Study of Real Time Mathematical Modeling Incorporating Dynamic Wake and Elastic Blades," *Proceedings of the 48th Annual Forum*, American Helicopter Society, June 1992.

[28] Du Val, R. W., "A Real-Time Blade Element Helicopter Simulation for Handling Qualities Analysis," *15th Annual European Rotorcraft Forum*, September 1989.

[29] Peters, D. A., Boyd, D. D., and He, C. J., "Finite-State Induced-Flow Model for Rotors in Hover and Forward Flight," *Journal of the American Helicopter Society*, Vol. 34, No. 4, 1989, pp. 5–17.

[30] Peters, D. A. and He, C. J., "Correlation of Measured Induced Velocities with a Finite-State Wake Model," *Journal of the American Helicopter Society*, Vol. 36, No. 3, 1991, pp. 59–70.

[31] Turnour, S. R. and Celi, R., "Modeling of Flexible Rotor Blades for Helicopter Flight Dynamics Applications," *Journal of the American Helicopter Society*, Vol. 41, No. 1, 1996, pp. 52–66.

[32] Kim, F. D., Celi, R., and Tischler, M. B., "Forward Flight Trim Calculation and Frequency Response Validation of a High-Order Helicopter Simulation Model," *Journal of Aircraft*, Vol. 30, No. 6, 1991, pp. 854–863.

[33] Spence, A. M. and Celi, R., "Coupled Rotor-Fuselage Dynamics and Aeroelasticity in Turning Flight," *Journal of the American Helicopter Society*, Vol. 40, No. 1, 1995, pp. 47–58.

[34] Celi, R., "Steady Stall and Compressibility Effects on Hingeless Aotor aeroelasticity in High-G Turns," *Vertica*, Vol. 14, No. 4, 1990, pp. 509–530.

[35] Drees, J. M., "A Theory of Airflow Through Rotors and its Application to some Helicopter Problems," *Journal of the Helicopter Association of Great Britain*, Vol. 3, No. 2, 1949, pp. 79–104.

[36] Chunduru, S. J., Subramanian, S., and Gaonkar, G. H., "Dynamic Stall and Wake Effects on Trim and Stability of Hingeless Rotors with Experimental Correlation," *Journal of the American Helicopter Society*, Vol. 42, No. 4, 1997, pp. 370–382.

[37] Petot, D., "Differential Equation Modeling of Dynamic Stall," *La Recherche Aerospatiale(English Edition)*, , No. 5, 1989, pp. 59–72.

[38] Ganguli, R., Chopra, I., and Weller, W. H., "Comparison of Calculated Vibratory Rotor Hub Loads with Experimental Data," *Journal of the American Helicopter Society*, Vol. 43, No. 4, 1998, pp. 312–318.

[39] Milgram, J., Chopra, I., and Straub, F., "Rotors With Trailing Edge Flaps: Analysis and Comparison with Experimental Data," *Journal of the American Helicopter Society*, Vol. 43, No. 4, 1998, pp. 319–332.

[40] Nagabhushanam, J. and Gaonkar, G., "Hingeless-Rotor Aeromechanical Stability in Axial and Forward Flight With Wake Dynamics," *Journal of the American Helicopter Society*, Vol. 44, No. 3, 1999, pp. 222–233.

[41] Theodore, C. R., *Helicopter Flight Dynamics Simulation with Refined Aerodynamic Modeling*, Ph.D. thesis, University of Maryland, College Park, 2000.

[42] Bagai, A., Leishman, J. G., and Park, J., "Aerodynamic Analysis of a Helicopter in Steady Maneuvering Flight Using a Free-Vortex Rotor Wake Model," *Journal of the American Helicopter Society*, Vol. 44, No. 2, 1999, pp. 109–120.

[43] Kim, F. D., Celi, R., and Tischler, M. B., "High-Order State Space Simulation Models of Helicopter Flight Mechanics," *Journal of the American Helicopter Society*, Vol. 38, No. 4, 1993, pp. 16–27.

[44] Brown, R. E. and Houston, S. S., "Comparison of Induced Velocity Models for Helicopter Flight Mechanics," *Journal of Aircraft*, Vol. 37, No. 4, 2000, pp. 623–629.

[45] Timoshenko, S. P., "On the Correction for Shear of the Differential Equation for Transverse Vibrations of Prismatic Bars," *The London, Edinburgh, and Dublin Philosophical Magazine and Journal of Science*, Vol. 41, No. 245, 1921, pp. 744–746.

[46] Vlasov, V. Z., *Thin-Walled Elastic Beams*, National Science Foundation and Department of Commerce, 1961.

[47] Houbolt, J. C. and Brooks, G. W., "Differential Equations of Motion For Combined Flapwise Bending, Chordwise Bending, and Torsion of Twisted Nonuniform Rotor Blades," Technical Note NACA/TN-3905, NACA, February 1957.

[48] Bielawa, R. L., "Aeroelastic Analysis for Helicopter Rotor Blades with Time-Variable, Nonlinear Structural Twist and Multiple Structural Redundancy: Mathematical Derivation and Program User's Manual," Technical Report NASA/CR-2638, NASA, October 1976.

[49] Hodges, D. H. and Dowel, E. H., "Nonlinear Equations of Motion for the Elastic Bending and Torsion of Twisted Nonuniform Rotor Blades," Technical Note NASA/TN-7818, NASA, December 1974.

[50] Hodges, D. H. and Ormiston, R. A., "Stability of Elastic Bending and Torsion of Uniform Cantilever Rotor Blades in Hover with Variable Structural Coupling," Technical Note NASA/TN-8192, NASA, April 1976.

[51] Crespo Da Silva, M. R. M. and Hodges, D. H., "Nonlinear Flexure and Torsion of Rotating Beams, with Application to Helicopter Rotor Blades-I. Formulation," *Vertica*, Vol. 10, No. 2, 1986, pp. 151–169.

[52] Hodges, D. H., Ormiston, R. A., and Peters, D. A., "On the Nonlinear Deformation Geometry of Euler-Bernoulli Beams," Technical Paper NASA/TP-1566, NASA, April 1980.

[53] Hodges, D. H., "Nonlinear Equations for Dynamics of Pretwisted Beams Undergoing Small Strains and Large Rotations," Technical Paper NASA/TP-2470, NASA, May 1985.

[54] Epstein, M. and Murray, D. W., "Large Deformation In-Plane Analysis of Elastic Beams," *Computers & Structures*, Vol. 6, No. 1, 1976, pp. 1–9.

[55] Hegemier, G. and Nair, S., "A Nonlinear Dynamical Theory for Heterogeneous, Anisotropic, Elastic Rods," *AIAA Journal*, Vol. 15, No. 1, 1977, pp. 8–15.

[56] Hodges, D. H., "Proper Definition of Curvature in Nonlinear Beam Kinematics," *AIAA journal*, Vol. 22, No. 12, 1984, pp. 1825–1827.

[57] Hodges, D. H., "Finite Rotation and Nonlinear Beam Kinematics," *Vertica*, Vol. 11, No. 1/2, 1987, pp. 297–307.

[58] Cosserat, E. and Cosserat, F., "Théorie des Corps Déformables," *Paris*, 1909.

[59] Ericksen, J. L. and Truesdell, C., "Exact Theory of Stress and Strain in Rods and Shells," *Archive for Rational Mechanics and Analysis*, Vol. 1, No. 1, 1957, pp. 295–323.

[60] Green, A. E. and Laws, N., "A General Theory of Rods," *Proceedings of the Royal Society of London. Series A. Mathematical and Physical Sciences*, Vol. 293, No. 1433, 1966, pp. 145–155.

[61] Cohen, H., "A Non-Linear Theory of Elastic Directed Curves," *International Journal of Engineering Science*, Vol. 4, No. 5, 1966, pp. 511–524.

[62] Whitman, A. B. and DeSilva, C. N., "A Dynamical Theory of Elastic Directed Curves," *Zeitschrift für angewandte Mathematik und Physik ZAMP*, Vol. 20, No. 2, 1969, pp. 200–212.

[63] Simo, J. C. and Vu-Quoc, L., "On the Dynamics in Space of Rods Undergoing Large Motions — a Geometrically Exact Approach," *Computer methods in applied mechanics and engineering*, Vol. 66, No. 2, 1988, pp. 125–161.

[64] Antman, S. S. and Warner, W. H., "Dynamical Theory of Hyperelastic Rods," *Archive for Rational Mechanics and Analysis*, Vol. 23, No. 2, 1966, pp. 135–162.

[65] Berdichevskii, V. L., "Equations of the Theory of Anisotropic Inhomogeneous Rods," *Soviet Physics Doklady*, Vol. 21, 1976, p. 286.

[66] Berdichevskii, V. L., "On the Energy of an Elastic Rod," *Journal of Applied Mathematics and Mechanics*, Vol. 45, No. 4, 1981, pp. 518–529.

[67] Parker, D. F., "An Asymptotic Analysis of Large Deflections and Rotations of Elastic Rods," *International Journal of Solids and Structures*, Vol. 15, No. 5, 1979, pp. 361–377.

[68] Pleus, P. and Sayir, M., "A Second Order Theory for Large Deflections of Slender Beams," *Zeitschrift für angewandte Mathematik und Physik ZAMP*, Vol. 34, No. 2, 1983, pp. 192–217.

[69] Berdichevskii, V. L., "Variational-Asymptotic Method of Constructing the Nonlinear Shell Theory," *Theory of shells*, 1980, pp. 137–161.

[70] Hodges, D. H., Atilgan, A. R., Cesnik, C. E. S., and Fulton, M. V., "On a Simplified Strain Energy Function for Geometrically Nonlinear Behaviour of Anisotropic Beams," *Composites Engineering*, Vol. 2, No. 5, 1992, pp. 513–526.

[71] Hodges, D. H., Lee, B. W., and Atilgan, A. R., "Application of the Variational-Asymptotical Method to Laminated Composite Plates," *AIAA journal*, Vol. 31, No. 9, 1993, pp. 1674–1683.

[72] Murthy, V., "Dynamic Characteristics of Rotor Blades," *Journal of Sound and Vibration*, Vol. 49, No. 4, 1976, pp. 483–500.

[73] Surace, G., Anghel, V., and Mares, C., "Coupled Bending-Bending-Torsion Vibration Analysis of Rotating Pretwisted Blades: an Integral Formulation and Numerical Examples," *Journal of Sound and Vibration*, Vol. 206, No. 4, 1997, pp. 473–486.

[74] Fasana, A. and Marchesiello, S., "Rayleigh-Ritz Analysis of Sandwich Beams," *Journal of sound and vibration*, Vol. 241, No. 4, 2001, pp. 643–652.

[75] Hodges, D. H., "Vibration and Response of Nonuniform Rotating Beams with Discontinuities," *Journal of the American Helicopter Society*, Vol. 24, No. 4, 1979, pp. 43–50.

[76] Goulos, I., Pachidis, V., and Pilidis, P., "Lagrangian Formulation for the Rapid Estimation of Helicopter Rotor Blade Vibration Characteristics," *Aeronautical Journal*, Vol. 118, No. 1206, 2014, pp. 861–901.

[77] Goulos, I., Pachidis, V., and Pilidis, P., "Helicopter Rotor Blade Flexibility Simulation for Aeroelasticity and Flight Dynamics Applications," *Journal of the American Helicopter Society*, Vol. 59, No. 4, 2014, pp. 1–18.

[78] Goulos, I., Pachidis, V., and Pilidis, P., "Flexible Rotor Blade Dynamics for Helicopter Aeromechanics Including Comparisons with Experimental Data," *Aeronautical Journal*, Vol. 119, No. 1213, December 2014, pp. 301–342.

[79] Goulos, I. and Pachidis, V., "Real-Time Aero-elasticity Simulation of Open Rotors with Slender Blades for the Multidisciplinary Design of Rotorcraft," *Journal of Engineering for Gas Turbines and Power*, Vol. 137, No. 1, 2015, pp. 012503.

[80] Mangler, K. W., "Calculation of The induced Velocity Field of a Rotor," Tech. Rep. 2247, Royal Aircraft Establishment, February 1948.

[81] Mangler, K. and Squire, H. B., "The Induced Velocity Field of a Rotor," Tech. Rep. ARC R & M 2642, 1950.

[82] Ormiston, R. A., "An Actuator Disc Theory for Rotor Wake Induced Velocities," *AGARD Specialists' Meeting on the Aerodynamics of Rotary Wings*, September 1972.

[83] Pitt, D. M. and Peters, D. A., "Theoretical Prediction of Dynamic-Inflow Derivatives," *6th European Rotorcraft and Powered Lift Aircraft Forum*, September 1980.

[84] Peters, D. A. and HaQuang, N., "Dynamic Inflow for Practical Applications," *Journal of the American Helicopter Society*, Vol. 33, No. 4, 1988, pp. 64–68.

[85] Peters, D. A., Karunamoorthy, S., and Cao, W.-M., "Finite State Induced Flow Models. I-Two-Dimensional Thin Airfoil," *Journal of Aircraft*, Vol. 32, No. 2, 1995, pp. 313–322.

[86] Peters, D. A. and He, C. J., "Finite State Induced Flow Models. II-Three-Dimensional Rotor Disk," *Journal of Aircraft*, Vol. 32, No. 2, 1995, pp. 323–333.

[87] Morillo, J. A. and Peters, D. A., "Velocity Field Above a Rotor Disk by a New Dynamic Inflow Model," *Journal of aircraft*, Vol. 39, No. 5, 2002, pp. 731–738.

[88] Howlett, J. J., "UH-60A Black Hawk Engineering Simulation Program: Volume I-Mathematical Model," Contractor Report NASA/CR-166309, NASA, December 1981.

[89] Theodore, C. and Celi, R., "Helicopter Flight Dynamic Simulation with Refined Aerodynamics and Flexible Blade Modeling," *Journal of Aircraft*, Vol. 39, No. 4, 2002, pp. 577–586.

[90] Ribera, M. and Celi, R., "Simulation Modelling in Steady Turning Flight with Refined Aerodynamics," *31st European Rotorcraft Forum*, September 2005.

[91] Landgrebe, A. J., "An Analytical and Experimental Investigation of Helicopter Rotor Hover Performance and Wake Geometry Characteristics," Technical Report USAAMRDL TR 71-24, U.S. Army Air Mobility Research and Development Laboratory Fort Eustis, June 1971.

[92] Landgrebe, A. J., "The Wake Geometry of a Hovering Helicopter Rotor and its Influence on Rotor Performance," *Journal of the American Helicopter Society*, Vol. 17, No. 4, 1972, pp. 3–15.

[93] Kocurek, J. D. and Tangler, J. L., "A Prescribed Wake Lifting Surface Hover Performance Analysis," *Journal of the American Helicopter Society*, Vol. 22, No. 1, 1977, pp. 24–35.

[94] Egolf, T. A. and Landgrebe, A. J., "Helicopter Rotor Wake Geometry and its Influence in Forward Flight. Volume 1: Generalized Wake Geometry and Wake Effect on Rotor Airloads and Performance," Contractor Report NASA CR-3726, NASA, October 1983.

[95] Beddoes, T. S., "A Wake Model for High Resolution Airloads," *2nd International Conference on Rotorcraft Basic Research*, February 1985.

[96] Clark, D. R. and Leiper, A. C., "The Free Wake Analysis," *Journal of the American Helicopter Society*, Vol. 15, No. 1, 1970, pp. 3–11.

[97] Scully, M. P., *Computation of Helicopter Rotor Wake Geometry and its Influence on Rotor Harmonic Airloads*, Ph.D. thesis, Massachusetts Institute of Technology, 1975.

[98] Bliss, D., Quackenbush, T., and Bilanin, A., "A New Methodology for Helicopter Free Wake Analysis," *Proceedings of the 38th Annual Forum*, American Helicopter Society, May 1983.

[99] Bliss, D., Wachspress, D., and Quackenbush, T., "A New Approach to the Free Wake Problem for Hovering Rotors," *Proceedings of the 41st Annual Forum*, American Helicopter Society, May 1985.

[100] Crouse, G. L., Leishman, J. G., and Bi, N., "Theoretical and Experimental Study of Unsteady Rotor/Body Aerodynamic Interactions," *Journal of the American Helicopter Society*, Vol. 37, No. 1, 1992, pp. 55–65.

[101] Crouse, G. L. and Leishman, J. G., "A New Method for Improved Rotor Free-Wake Convergence," *31st AIAA Aerospace Sciences Meeting and Exhibit*, January 1993.

[102] Bagai, A. and Leishman, J. G., "Rotor Free-Wake Modeling Using a Pseudo-Implicit Technique—Including Comparisons with Experimental Data," *Journal of the American Helicopter Society*, Vol. 40, No. 3, 1995, pp. 29–41.

[103] Bagai, A. and Leishman, J. G., "Rotor Free-Wake Modeling Using a Pseudoimplicit Relaxation Algorithm," *Journal of Aircraft*, Vol. 32, No. 6, 1995, pp. 1276–1285.

[104] Vatistas, G. H., Kozel, V., and Mih, W., "A Simpler Model for Concentrated Vortices," *Experiments in Fluids*, Vol. 11, No. 1, 1991, pp. 73–76.

[105] Bagai, A. and Leishman, J. G., "Free-Wake Analysis of Tandem, Tilt-Rotor and Coaxial Rotor Configurations," *Journal of the American Helicopter Society*, Vol. 41, No. 3, 1996, pp. 196–207.

[106] Bagai, A. and Leishman, J. G., "Adaptive Grid Sequencing and Interpolation Schemes for Helicopter Rotor Wake Analyses," *AIAA journal*, Vol. 36, No. 9, 1998, pp. 1593–1602.

[107] Scully, M. P., "A Method of Computing Helicopter Vortex Wake Distortion," Technical Report ASLR TR 138-1, Massachusetts Institute of Technology, June 1967.

[108] Landgrebe, A. J., "An Analytical Method for Predicting Rotor Wake Geometry," *Journal of the American Helicopter Society*, Vol. 14, No. 4, 1969, pp. 20–32.

[109] Bliss, D. B., Teske, M. E., and Quackenbush, T. R., "A New Methodology for Free Wake Analysis Using Curved Vortex Elements," Contractor Report NASA CR-3958, NASA, December 1987.

[110] Bhagwat, M. J. and Leishman, J. G., "Stability, Consistency and Convergence of Time-Marching Free-Vortex Rotor Wake Algorithms," *Journal of the American Helicopter Society*, Vol. 46, No. 1, 2001, pp. 59–71.

[111] Bhagwat, M. J. and Leishman, J. G., "Technical Note: Accuracy of Straight-Line Segmentation Applied to Curvilinear Vortex Filaments," *Journal of the American Helicopter Society*, Vol. 46, No. 2, 2001, pp. 166–169.

[112] Horn, J. F., Bridges, D. O., Wachspress, D. A., and Rani, S. L., "Implementation of a Free-Vortex Wake Model in Real-Time Simulation of Rotorcraft," *Journal of Aerospace Computing, Information, and Communication*, Vol. 3, No. 3, 2006, pp. 93–107.

[113] Datta, A., Nixon, M., and Chopra, I., "Review of Rotor Loads Prediction with the Emergence of Rotorcraft CFD," *Journal of the American Helicopter Society*, Vol. 52, No. 4, 2007, pp. 287–317.

[114] Berezin, C. and Sankar, L., "An Improved Navier-Stokes/Full-Potential Coupled Analysis for Rotors," *Mathematical and Computer Modelling*, Vol. 19, No. 3-4, 1994, pp. 125–133.

[115] Berkman, M. E., Sankar, L. N., Berezin, C. R., and Torok, M. S., "Navier-Stokes/Full Potential/Free-Wake Method for Rotor Flows," *Journal of aircraft*, Vol. 34, No. 5, 1997, pp. 635–640.

[116] Bangalore, A. K., Moulton, M. A., and Caradonna, F. X., "The development of an overset/hybrid method for rotorcraft applications," *AHS Specialists' Meeting for Rotorcraft Aerodynamics and Aeroacoustics*, American Helicopter Society, October 1997.

[117] Yang, Z., Sankar, L. N., Smith, M. J., and Bauchau, O., "Recent Improvements to a Hybrid Method for Rotors in Forward Flight," *Journal of Aircraft*, Vol. 39, No. 5, 2002, pp. 804–812.

[118] Moulton, M. A., Bridgeman, J. O., and Caradonna, F. X., "Development of an Overset/Hybrid CFD Method for the Prediction of Hovering Performance," *Proceedings of the 53rd Annual Forum*, American Helicopter Society, May 1997, pp. 1088–1101.

[119] Strawn, R. C. and Barth, T. J., "A Finite-Volume Euler Solver for Computing Rotary-Wing Aerodynamics on Unstructured Meshes," *Journal of the American Helicopter Society*, Vol. 38, No. 2, 1993, pp. 61–67.

[120] Park, Y. M., Nam, H. J., and Kwon, O. J., "Simulation of Unsteady Rotor-Fuselage Interactions Using Unstructured Adaptive Meshes," *Proceedings of the 59th Annual Forum*, American Helicopter Society, May 2003.

[121] Steger, J., Dougherty, F., and Benek, J., "A chimera Grid Scheme", Advances in Grid Generation, Edited by KN Ghia and U. Ghia, FED," *American Society of Mechanical Engineers*, Vol. 5, 1983.

[122] Benek, J., Donegan, T., and Suhs, N., "Extended Chimera Grid Embedding Scheme with Application to Viscous Flows," *19th Fluid Dynamics, Plasma Dynamics and Laser Conference*, AIAA, June 1987.

[123] Harten, A., Engquist, B., Osher, S., and Chakravarthy, S. R., "Uniformly High Order Accurate Essentially Non-Oscillatory Schemes, III," *Journal of computational physics*, Vol. 71, No. 2, 1987, pp. 231–303.

[124] Hariharan, N. and Sankar, L., "High-Order Essentially Nonoscillatory Schemes for Rotary-Wing Wake Computations," *Journal of Aircraft*, Vol. 41, No. 2, 2004, pp. 258–267.

[125] Hall, C. M., *High-Order Accurate Simulations of Wake and Tip Vortex Flowfields*, Ph.D. thesis, The Pennsylvania State University, 1998.

[126] Boelens, O., der Ven, H. v., Oskam, B., and Hassan, A., "Boundary Conforming Discontinuous Galerkin Finite Element Approach for Rotorcraft Simulations," *Journal of Aircraft*, Vol. 39, No. 5, 2002, pp. 776–785.

[127] Steinhoff, J., Yonghu, W., Mersch, T., and Senge, H., "Computational Vorticity Capturing-Application to Helicopter Rotor Flows," *Proceedings of the 30th Aerospace Sciences Meeting and Exhibit*, AIAA, January 1992, p. 56.

[128] Wang, C., Bridgeman, J., Steinhoff, J., and Wenren, Y., "The Application of Computational Vorticity Confinement to Helicopter Rotor and Body Flows," *Proceedings of the 49th Annual Forum*, American Helicopter Society, May 1993, pp. 557–557.

[129] Wenren, Y. and Steinhoff, J., "Application of Vorticity Confinement to the Prediction of the Wake of Helicopter Rotors and Complex Bodies," *Proceedings of the 17th Applied Aerodynamics Conference*, AIAA, June 1999, p. 3200.

[130] Dietz, W., "Application of Vorticity Confinement to Compressible Flow," *Proceedings of the 42nd Aerospace Sciences Meeting and Exhibit*, AIAA, January 2004, p. 718.

[131] Brown, R. E., "Rotor Wake Modeling for Flight Dynamic Simulation of Helicopters," *AIAA journal*, Vol. 38, No. 1, 2000, pp. 57–63.

[132] Brown, R. E. and Line, A. J., "Efficient High-Resolution Wake Modeling Using the Vorticity Transport Equation," *AIAA journal*, Vol. 43, No. 7, 2005, pp. 1434–1443.

[133] Johnson, W., "A Comprehensive Analytical Model of Rotorcraft Aerodynamics and Dynamics. Part 1. Analysis Development," Technical Memorandum NASA TM-81182, NASA, 1980.

[134] Johnson, W., "A Comprehensive Analytical Model of Rotorcraft Aerodynamics and Dynamics. Part 2. User's Manual," Technical Memorandum NASA TM-81183, NASA, 1980.

[135] Johnson, W., "Technology Drivers in the Development of CAMRAD II," *Proceedings of the Aeromechanics Specialists Conference, San Francisco, California*, American Helicopter Society, 1994.

[136] Johnson, W., "Rotorcraft Dynamics Models for a Comprehensive Analysis," *Proceedings of the 54th Annual Forum of the American Helicopter Society*, Vol. 54, American Helicopter Society, 1998, pp. 452–471.

[137] Johnson, W., "A General Free Wake Geometry Calculation For Wings and Rotors," *Proceedings of the 51st Annual Forum*, American Helicopter Society, 1995.

[138] Johnson, W., "Influence of Wake Models on Calculated Tiltrotor Aerodynamics," *Proceedings of Aerodynamics, Acoustics, and Test and Evaluation Technical Meeting*, American Helicopter Society, 2002.

[139] Lim, J. W., Yu, Y. H., and Johnson, W., "Calculation of Rotor Blade-Vortex Interaction Airloads Using a Multiple-Trailer Free-Wake Model," *Journal of Aircraft*, Vol. 40, No. 6, 2003, pp. 1123–1130.

[140] Lim, J. and van der Wall, B. G., "Investigation in the Effect of a Multiple Trailer Free Wake Model for Descending Flights," *Proceedings of the 61st Annual Forum*, American Helicopter Society, 2005.

[141] Hennes, C., Lopes, L., Shirey, J., Erwin, J., and Brentner, K., "PSU-WOPWOP 3.3. 3 User's Guide," *The Pennsylvania State University, University Park, PA, USA*, 2009.

[142] Sim, B. and Lim, J., "Blade-vortex Interaction (BVI) Noise and Airload Prediction Using Loose Aerodynamic/Structural Coupling," *Proceedings of the 62nd Annual Forum*, American Helicopter Society, may 2007.

[143] Williams, J. F. and Hawkings, D. L., "Sound Generation by Turbulence and Surfaces in Arbitrary Motion," *Philosophical Transactions of the Royal Society of London A: Mathematical, Physical and Engineering Sciences*, Vol. 264, No. 1151, 1969, pp. 321–342.

[144] Bauchau, O. A., "DYMORE user's manual," *Georgia Institute of Technology, Atlanta*, 2007.

[145] Squire, H., "The Growth of a Vortex in Turbulent Flow," *Aeronautical Quarterly*, Vol. 16, No. 03, 1965, pp. 302–306.

[146] Peters, D. A. and Barwey, D., "A General Theory of Rotorcraft Trim," *Mathematical Problems in Engineering*, Vol. 2, No. 1, 1996, pp. 1–34.

[147] Bauchau, O. A., Bottasso, C. L., and Nikishkov, Y. G., "Modeling Rotorcraft Dynamics with Finite Element Multibody Procedures," *Mathematical and Computer Modelling*, Vol. 33, No. 10-11, 2001, pp. 1113–1137.

[148] Zaki, A., Reveles, N., Smith, M., and Bauchau, O., "Using Tightly-Coupled CFD/CSD Simulation for Rotorcraft Stability Analysis," *Proceedings of the 66th Annual Forum*, American Helicopter Society, May 2010.

[149] Reveles, N., Smith, M. J., Zaki, A., and Bauchau, O., "A Kriging-Based Trim Algorithm for Rotor Aeroelasticity," *37th European Rotorcraft Forum*, Agustawestland, September 2011.

[150] Zaki, A. A., *Using Tightly-Coupled CFD/CSD Simulation for Rotorcraft Stability Analysis*, Ph.D. thesis, Georgia Institute of Technology, 2012.

[151] Benoit, B., Kampa, K., von Grunhagen, W., Basset, P., and Gimonet, B., "HOST, a General Helicopter Simulation Tool for Germany and France," *Proceedings of the 56th Annual Forum*, Vol. 56, American Helicopter Society, 2000, pp. 1110–1131.

[152] Toulmay, F., "Modèle d'étude de l'aérodynamique du rotor," *Model for Computation of Rotor Aerodynamics), Rapport Eurocopter-France no*, Vol. 371, 1986.

[153] Michéa, B., Desopper, A., and Costes, M., "Aerodynamic Rotor Loads Prediction Method with a Wree wake for Low Speed Descent Flights," *Tiré à part- Office national d'études et de recherches aerospatiales*, 1992.

[154] Rahier, G. and Delrieux, Y., "Blade-Vortex Interaction Noise Prediction Using a Rotor Wake Roll-Up Model," *Journal of Aircraft*, Vol. 34, No. 4, 1997, pp. 522–530.

[155] Spiegel, P., Rahier, G., and Michéa, B., "Blade-Vortex Interaction Noise-Prediction and Comparison with Flight and Wind Tunnel Tests," Tech. rep., ONERA, 1992.

[156] Spiegel, P. and Rahier, G., "Theoretical Study and Prediction of BVI Noise Including Close Interactions," *International Specialists' Meeting on Rotorcraft Basic Research*, Vol. 1, American Helicopter Society, March 1991.

[157] van der Wall, B. G., "Analytic Formulation of Unsteady Profile Aerodynamics and its Application to Simulation of Rotors," Tech. Rep. ESA TT 1244, DLR, 1992.

[158] von Grünhagen, W., "Bestimmung der gekoppelten Schlagbiege-, Schwenkbiege- und Torsionsschwingungen für beliebige Rotorblätter mit Hilfe der Finite-Element-Methode (Computation of the Coupled Flap Bending, Lag Bending and Torsion Oscillations for Arbitrary Rotor Blades with the Aid of the Finite Element Method)," *DFVLR IB*, 1980, pp. 154–80.

[159] Leiss, U., "A Consistent Mathematical Model to Simulate Steady and Unsteady Rotor-Blade Aerodynamics," Tech. Rep. USAAMRL TR 72-67, US Army Air Mobility Research and Development Laboratory, 1984.

[160] Wagner, H., "Über die Entstehung des dynamischen Auftriebes von Tragflügeln," *ZAMM-Journal of Applied Mathematics and Mechanics/Zeitschrift für Angewandte Mathematik und Mechanik*, Vol. 5, No. 1, 1925, pp. 17–35.

[161] Küssner, H. G., "Zusammenfassender Bericht über den instationären Auftrieb von Flügeln," *Luftfahrtforschung*, Vol. 13, No. 12, 1936, pp. 410–424.

[162] Bisplinghoff, R. L., Ashley, H., and Halfman, R. L., *Aeroelasticity*, Courier Dover Publications, 2013.

[163] Petot, D., Arnaud, G., Harrison, R., Stevens, J., Dieterich, O., van der Wall, B. G., Young, C., and Széchényi, E., "Stall Effects and Blade Torsion — An Evaluation of Predictive Tools," *Journal of the American Helicopter Society*, Vol. 44, No. 4, 1999, pp. 320–332.

[164] van der Wall, B. G. and Geissler, W., "Experimental and Numerical Investigations on Steady and Unsteady Behaviour of a Rotor Airfoil with a Piezoelectric Trailing Edge Flap," *Proceedings of the 55th Annual Forum*, Vol. 1, American Helicopter Society, May 1999, pp. 963–976.

[165] van der Wall, B. G. and Yin, J., "DLR's S4 Rotor Code Validation with HART II Data: the Baseline Case," American Helicopter Society, October 2007.

[166] van der Wall, B. G. and Göpel, C., *Über den Einfluß der Rotorversuchsstände ROTEST und ROTOS auf die Rotordurchströmung im DNW*, Ph.D. thesis, TU Braunschweig, 1991.

[167] van der Wall, B., "Helicopter Rotor BVI Airloads Computation Using Advanced Prescribed Wake Modelling," *29th Applied Aerodynamics Conference*, AIAA, June 2011, p. 3374.

[168] van der Wall, B. G. and Roth, M., "Free-Wake Analysis on Massively Parallel Computers and Validation with HART Test Data," *Proceedings of the 53rd Annual Forum*, American Helicopter Society, May 1997.

[169] Yin, J. and Delfs, J., "Improvement of DLR Rotor Aeroacoustic Code (APSIM) and its Validation with Analytical Solution," *Proceedings of the 29th European Rotorcraft Forum*, Royal Aeronautical Society, September 2003.

[170] Yin, J. and Ahmed, S., "Aerodynamics and Aeroacoustics of Helicopter Main-Rotor/Tail-Rotor Interaction," *Proceedings of the 5th Aeroacoustics Conference and Exhibit*, AIAA, May 1999, p. 1929.

[171] Bir, G., Chopra, I., Kim, K., Wang, J., Smith, E., Vellaichamy, S., Ganguli, R., Nixon, M., and Torok, S., "University of Maryland Advanced Rotorcraft Code (UMARC) Theory Manual," *UM-Aero Report*, Vol. 92, No. 02, 1992.

[172] Chopra, I. and Bir, G., "University of Maryland Advanced Rotor Code: UMARC," *Proceedings of the Aeromechanics Specialists Conference*, American Helicopter Society, January 1994.

[173] Weissinger, J., "The Lift Distribution of Swept-Back Wings," Technical Memorandum NACA TM 1120, NACA, 1947.

[174] Leishman, J. G. and Beddoes, T., "A Semi-Empirical Model for Dynamic Stall," *Journal of the American Helicopter society*, Vol. 34, No. 3, 1989, pp. 3–17.

[175] Gopalan, G., Sitaraman, J., Baeder, J., and Schmitz, F., "Aerodynamic and Aeroacoustic Prediction Methodologies with Application to the HART II Model Rotor," *Proceedings of the 62nd Annual Forum*, American Helicopter Society, May 2006.

[176] Leishman, J. G., Bhagwat, M. J., and Bagai, A., "Free-Vortex Filament Methods for the Analysis of Helicopter Rotor Wakes," *Journal of aircraft*, Vol. 39, No. 5, 2002, pp. 759–775.

[177] Bhagwat, M. J. and Leishman, J. G., "Generalized Viscous Vortex Model for Application to Free-Vortex Wake and Aeroacoustic Calculations," *Proceedings of the 58th Annual Forum*, Vol. 58, American Helicopter Society, June 2002, pp. 2042–2057.

[178] Datta, A., *Fundamental Understanding, Prediction and Validation of Rotor Vibratory Loads in Steady-Level Flight*, Ph.D. thesis, 2004.

[179] Chen, P. C., Baeder, J. D., Evans, R. A., Niemczuk, J. B., and Ross, P. A., "Active Twist Smart Rotor Technology for Blade-Vortex Interaction Noise Reduction," *1999 Symposium on Smart Structures and Materials*, International Society for Optics and Photonics, March 1999, pp. 37–49.

[180] Zhao, J., Prasad, J., and Peters, D. A., "Rotor Dynamic Wake Distortion Model for Helicopter Maneuvering Flight," *Journal of the American Helicopter Society*, Vol. 49, No. 4, 2004, pp. 414–424.

[181] Goulos, I., "An Improved Analytical Approach for Modeling the Effect of Rotor Wake Curvature Using Finite-State Induced Flow Models," *Journal of the American Helicopter Society*, Vol. 61, No. 3, 2016, pp. 1–16.

[182] Macmillan, W., *Development of a Modular-Type Computer Program for the Calculation of Gas Turbine Off-Design Performance*, Ph.D. thesis, Cranfield University, 1974.

[183] Ortiz-Carretero, J., Castillo Pardo, A., Pachidis, V., and Goulos, I., "Assessment of the Effect of Environmental Conditions on Rotorcraft Pollutant Emissions at Mission Level," *ASME Turbo Expo 2017: Turbomachinery Technical Conference and Exposition*, American Society of Mechanical Engineers, June 2017.

[184] Ortiz-Carretero, J., Castillo Pardo, A., Goulos, I., and Pachidis, V., "Impact of Adverse Environmental Conditions on Rotorcraft Operational Performance and Pollutant Emissions," *Journal of Engineering for Gas Turbines and Power*, Vol. 140, No. 2, 2018, pp. 021201.

[185] Tisseur, F. and Meerbergen, K., "The Quadratic Eigenvalue Problem," *SIAM Review*, Vol. 43, No. 2, 2001, pp. 235–286.

[186] Benner, P., Mehrmann, V., and Xu, H., "A Numerically Stable, Structure Preserving Method for Computing the Eigenvalues of Real Hamiltonian or Symplectic Pencils," *Numerische Mathematik*, Vol. 78, No. 3, 1998, pp. 329–358.

[187] van der Wall, B. G., Bauknecht, A., Jung, S. N., and You, Y. H., "Semi-Empirical Physics-based Modeling of Fuselage-Rotor and Fuselage-Wake Interferences for Comprehensive Codes," *Proceedings of the 70th Annual Forum*, American Helicopter Society, May 2014.

[188] Montgomerie, B., "Methods for Root Effects, Tip Effects and Extending the Angle of Attack Range to+-180°, with Application to Aerodynamics for Blades on Wind Turbines and Propellers," Scientific Report FOI-R-1305-SE, Swedish Defence Research Agency, 2004.

[189] Leishman, J. G., "Aeroacoustics of 2-D and 3-D Blade Vortex Interaction Using the Indicial Method," *Proceedings of the 52nd Annual Forum*, Vol. 2, American Helicopter Society, 1996.

[190] Leishman, J., "Subsonic Unsteady Aerodynamics Caused by Gusts Using the Indicial Method," *Journal of Aircraft*, Vol. 33, No. 5, 1996, pp. 869–879.

[191] Leishman, G. J., *Principles of Helicopter Aerodynamics*, Cambridge University Press, 2006.

[192] Beddoes, T., "Practical Computation of Unsteady Lift," *Proceedings of the 8th European Rotorcraft Forum*, Association Aeronautique et Astronautique de France, 1982.

[193] Leishman, J. G., "Two-Dimensional Model for Airfoil Unsteady Drag Below Stall," *Journal of Aircraft*, Vol. 25, No. 7, 1988, pp. 665–666.

[194] Clough, R. W. and Penzien, J., *Dynamics of Structures, Berkeley: Computers & Structures*, Inc, 1995.

[195] Titurus, B. and Lieven, N., "Integration of Hydraulic Lag-Damper Models with Helicopter Rotor Simulations," *Journal of Guidance, Control, and Dynamics*, Vol. 33, No. 1, 2010, pp. 200–211.

[196] Bousman, W. G., Young, C., Toulmay, F., Gilbert, N. E., Strawn, R. C., Miller, J. V., Maier, T. H., Costes, M., and Beaumier, P., "A Comparison of Lifting-Line and CFD Methods with Flight Test Data from a Research Puma Helicopter," Technical Memorandum NASA/TM-110421, NASA, October 1996.

[197] van der Wall, B. G., Burley, C. L., Yu, Y., Richard, H., Pengel, K., and Beaumier, P., "The HART II Test - Measurement of Helicopter Rotor Wakes," *Aerospace Science and Technology*, Vol. 8, No. 4, 2004, pp. 273–284.

[198] Schneider, O., "Analysis of SPR Measurements from HART II," *Aerospace Science and Technology*, Vol. 9, No. 5, 2005, pp. 409–420.

[199] van der Wall, B. G., "A Comprehensive Rotary-Wing Data Base for Code Validation: the HART II International Workshop," *Aeronautical Journal*, Vol. 115, No. 1164, 2011, pp. 91.

[200] van der Wall, B. G., "2nd HHC Aeroacoustic Rotor Test (HART II)-Part I: Test Documentation," Tech. Rep. DLR-IB 111-2003/31, DLR, 2003.

[201] van der Wall, B. G. and Burley, C. L., "2nd HHC Aeroacoustic Rotor Test (HART II)-Part II: Representative Results," Tech. Rep. DLR-IB 111-2005/03, DLR, 2005.

[202] "Technical Documentation for Rotorblades acc. to Dwg." MBB Technical Documentation Report DSK2-01017-00, 1998.

[203] Jung, S. N., You, Y. H., Dhadwal, M. K., Hagerty, B. P., Riemenschneider, J., and Keimer, R., "Blade Property Measurement and Its Assessment on Air/Structural Loads of HART II Rotor," *Proceedings of the 70th Annual Forum*, American Helicopter Society, May 2014.

[204] Sharpe, D. L., "An Experimental Investigation of the Flap-Lag-Torsion Aeroelastic Stability of a Small-Scale Hingeless Helicopter Rotor in Hover," Technical Paper NASA/TP-2546, NASA, January 1986.

[205] Srinivasan, A. V., Cutts, D. G., Shu, H. T., Sharpe, D. L., and Bauchau, O. A., "Structural Dynamics of a Helicopter Rotor Blade System," *Journal of The American Helicopter Society*, Vol. 35, No. 1, May 1990, pp. 75–85.

[206] Furchert, R., "Bestimmung der Eigenfrequenzen und Eigenformen von 3 Rotorblättsa des Rotorversuchsstands (Determination of Natural Frequencies and Mode Shapes of 3 Rotor Blade Sets of the RotorTest Rig)," Tech. Rep. DLR-IB 111-292/11, DLR, 1992.

[207] van der Wall, B. G., Lim, J. W., Smith, M. J., Jung, S. N., Bailly, J., Baeder, J. D., and Boyd Jr, D. D., "The HART II International Workshop: an Assessment of the State-of-the-Art in Comprehensive Code Prediction," *CEAS Aeronautical Journal*, Vol. 4, No. 3, 2013, pp. 223–252.

[208] Uhle, H., "Windkanalmessungen am Profil NACA 23012 mit Original und Modifizierter Hinterkante (Wind Tunnel Measurements of the Airfoil NACA 23012 with Original and Modified Trailing Edge)," Tech. Rep. MBB TN D127-2/71, 1971.

[209] Dadone, L. U., "U.S. Army Helicopter Design Datcom Volume I - Airfoil)," Tech. Rep. USAAMRDL CR 76-2, Boeing Vertol Company, 1976.

[210] van der Wall, B. G., Lim, J. W., Smith, M. J., Jung, S. N., Bailly, J., Baeder, J. D., and Douglas Boyd, D. J., "An Assessment of Comprehensive Code Prediction State-of-Art Using the HART II International Workshop Data," *Proceedings of the 68th Annual Forum*, American Helicopter Society, May 2012.

[211] Lim, J. W., Boyd Jr, D. D., Hoffman, F., van der Wall, B. G., Kim, D.-H., Jung, S. N., You, Y. H., Tanabe, Y., Bailly, J., Lienard, C., et al., "Aeromechanical Evaluation of Smart-Twisting Active Rotor," *Proceedings of the 40th European Rotorcraft Forum*, Royal Aeronautical Society, September 2014.

Appendix A

This appendix enumerate the journal articles and conference publications of the author published or accepted for publication during the completion of this project.

Journal Articles

- Castillo Pardo, A., Goulos, I., Pachidis, V., Modelling and Analysis of Coupled Flap-Lag-Torsion Vibration Characteristics for Helicopter Rotor Blades, *Proceedings of the Institution of Mechanical Engineers, Journal of Aerospace*, Vol. 231, No. 19, 2016, pp. 1804-1823.

- Ortiz-Carretero, J., Castillo Pardo, A., Goulos, I., Pachidis. V., Impact of Adverse Environmental Conditions on Rotorcraft Operational Performance and Pollutant Emissions, *Journal of Engineering for Gas Turbine and Power*, Vol. 140, No. 2, 2018, pp. 021201.

Conference Proceedings

- Castillo Pardo, A., Pachidis, V., Stevens, J., Smith, C., Thevenot, L., d'Ippolito, R., Clean Sky Technology Evaluator - On the Environmental Impact of Green Rotorcraft Technologies, *Greener Aviation Conference 2016*, Brussels, Belgium, 2016.

- Ortiz-Carretero, J., Castillo Pardo, A., Pachidis, V., Goulos, I., Assessment of the Effect of Environmental Conditions on Rotorcraft Pollutant Emissions at Mission Level, *Proceedings of the ASME Turbo Expo 2017*, Charlotte, NC, USA, 2017.

- Stevens, J., Smith, C., Thevenot, L., d'Ippolito, R., Gires, E., Castillo Pardo, A., Pachidis, V., Clean Sky Green Rotorcraft New Technologies - Maximizing Noise and Emissions Benefits, *Proceedings of the 42nd European Rotorcraft Forum*, Lile, France, 2016.

- Smith, C., Pachidis, V., Castillo Pardo, A., Gires, E., Stevens, J., Thevenot, L., d'Ippolito, R., Achieving Rotorcraft Noise and Emissions Reduction for 'Clean Sky' - The Measurement of Success, *5th CEAS Air & Space Conference*, Delft, The Netherlands, 2015.